FEASIBILITY OF USING ULTRASONIC SHEAR WAVES TO ASSESS CERVICAL REMODELLING DURING THE GESTATION PERIOD

BY:

Laura María Peralta Pereira

A THESIS SUBMITTED TO UNIVERSITY OF GRANADA
IN PARTIAL FULFILMENT OF THE REQUIREMENTS FOR THE DEGREE OF
DOCTOR OF PHILOSOPHY

ADVISOR:

Dr. Guillermo Rus Carlborg

Department of Structural Mechanics & Hydraulic Engineering
University of Granada
Granada (Spain)

May 2015

Editor: Universidad de Granada. Tesis Doctorales
Autor: Laura María Peralta Pereira
ISBN: 978-84-9163-833-9
URI: http://hdl.handle.net/10481/50941

Feasibility of using ultrasonic shear waves to assess cervical remodelling during the gestation period

El doctorando Laura María Peralta Pereira y el director de la tesis Dr. Guillermo Rus Carlborg, garantizamos, al firmar esta tesis doctoral, que el trabajo ha sido realizado por el doctorando bajo la dirección del director de la tesis y hasta donde nuestro conocimiento alcanza, en la realización del trabajo, se han respetado los derechos de otros autores a ser citados, cuando se han utilizado sus resultados o publicaciones.

En Granada, a 30 de abril de 2015

Director de la Tesis	Doctorando
Fdo.: GUILLERMO RUS CARLBORG	Fdo.: LAURA MARÍA PERALTA PEREIRA

Summary

Prematurity affects 11% of the births and is the main cause of infant mortality. On the opposite case, late in pregnancy, labour has to be induced in approximately 23% of the pregnancies worldwide. However, it fails in 32% of the induced births, which is associated with fetal suffering. Both conditions are related to precocious and/or delayed cervical ripening. Quantitative and objective information about the temporal evolution of the cervical ripening may provide the development of a complementary method to identify cases at risk of preterm delivery and to assess the likelihood of successful induction of labour, therefore allowing an efficient intervention. So far, however, no reliable clinical tool is available for quantitative and objective evaluation of cervical maturation. In current clinical practice, this biomechanical status is only subjectively assessed by digital palpation. In the past decade, different methods have been proposed to assess the pregnant cervix. Nonetheless, all of them were unsuccessful in objectively quantifying the histological, biochemical and mechanical changes that characterise the cervical remodelling during gestation. Among them, elastography has recently received particular attention in a quest for meaningful information on the degree of cervical stiffness/softness that may anticipate delivery much earlier than state-of-the-art geometry-based tests. Nevertheless, its potential application to assess the full complexity of cervical tissue still remains unclear. During gestation, in the so called cervical remodelling, several changes progressively occur in the structure of the cervical tissue. An increase in the hydration, disorganisation of collagen network and decrease in elasticity are observed. The collagen structure disorganisation is particularly complex: collagen fibres turn thicker and more wavy as the gestation progresses, while pores between collagen fibres become larger and separated. Notwithstanding, the link between stiffness and the cervical remodelling is not yet fully understood.

In this thesis, the basic principles of solid mechanics are introduced to provide a connection between shear waves and cervical remodelling, facing towards the gestational assessment and its possible application to predict preterm birth and successful labour induction by shear wave elastography. In particular, we explore the feasibility of ultrasonic shear waves to assess the pregnant cervix. To this end, this thesis combines both experimental and numerical approaches. On the one hand, we evaluate the capability and reliability of shear wave elastography to assess cervical maturation in healthy pregnant women for first time. After showing its sensitivity to the cervix, a better insight into remodelling processes

is the next proposed challenge achieved throughout this dissertation. For this purpose, we propose an animal model, in particular sheep, which allows to objectively define time control over the cervical maturation and provides physiologically relevant data that can then be connected to the elastographic measurements. The cervical ripening was induced by injecting dexamethasone in some animals, while a group stood as control. Then, the artificially induced cervical maturation was monitored using shear wave elastography during 24 hours. Moreover, histological analyses and two-photon excitation microscopy, combining both Second Harmonic Generation and Two-photon Fluorescence microscopy contrasts, were used to investigate, at the microscopic scale, the architecture of cervical tissue. This study provides an insight about the cervical remodelling and the mechanical properties that are perceptible in elastography.

On the other hand, a numerical approach has been developed to provide insight into the multi-scale problem and biochemical variables. The hypothesised link between shear waves and the hierarchical structure of cervical tissue, which is evidenced by the animal study, is analysed by a multi-scale computational model using the finite difference time domain technique to simulate shear wave propagation. As a third contribution, the key role of viscoelastic dissipation mechanisms in the interaction between shear waves and tissue micro-architecture is evidenced and studied in detail. First, a comparative study of the macro-scale viscoelastic moduli is developed, which manifests that a Maxwell model best describes shear waves-tissue interactions, contrarily to common belief in literature. In addition, computational models were used to analyse the influence of wave design parameters (i.e., excitation frequency) to optimally interrogate the relevant viscoelastic properties.

The last contribution of this thesis is a numerical histo-mechanical model used to link the variations of microscopic histological characteristics (both morphological and biochemical) with the macroscopic tissue-scale mechanical properties measurable by shear waves. We propose a multi-scale approach, which aims at describing the cervical remodelling, and combines three elements: collagen morphology, wave-tissue interactions and constitutive mixture theory. Parametric simulations were carried out for a broad range of mechanical and geometrical parameters that characterise the cervical extracellular matrix, showing that histological features can be quantitatively related to mechanical properties. This work provides valuable knowledge about the mechanisms that take place in normal pregnancy, which will allow a better understanding of the cervical mechanical remodelling and lead to better methods of diagnosis of preterm birth and successful induction of labour.

Resumen

El parto prematuro afecta al 11% de los nacimientos y es la principal causa de mortalidad infantil. Por otro lado, al final de la gestación, el parto tiene que ser inducido en aproximadamente el 23% de los embarazos en todo el mundo. Sin embargo, la inducción falla en el 32% de los partos inducidos, lo que se asocia con el sufrimiento fetal. Ambas condiciones, el parto prematuro y el éxito del parto provocado, están relacionadas con la maduración precoz y/o tardía del cuello uterino. La información cuantitativa y objetiva sobre la evolución temporal de la maduración cervical puede proporcionar un método complementario para identificar los casos en riesgo de parto prematuro y para evaluar la probabilidad de éxito de la inducción del parto, y por tanto, permitir una intervención eficiente. Hasta ahora, sin embargo, no hay ninguna herramienta clínica fiable para cuantificar objetivamente el proceso de maduración del cuello uterino. En la práctica clínica actual, este estado biomecánico se evalúa subjetivamente mediante palpación digital. En la última década, se han propuesto diferentes métodos para evaluar el estado del cuello uterino durante el embarazo. Sin embargo, ninguno de estos métodos ha tenido éxito en cuantificar objetivamente los cambios histológicos, bioquímicos y mecánicos que caracterizan el proceso de remodelación que el cuello del útero sufre durante la gestación. Entre los métodos propuestos para tal fin, recientemente, la elastografía ha recibido especial atención. Esta técnica podría proporcionar información significativa del grado de rigidez del cuello uterino, lo que puede anticipar el momento del parto mucho antes que los métodos basados sólo en medir la geometría del órgano. Sin embargo, su posible aplicación al tejido del cuello uterino sigue sin estar clara del todo. Durante la gestación, en el proceso de remodelación del cuello del útero, varios cambios se producen progresivamente en la estructura del tejido cervical. Se produce un aumento en la hidratación del tejido, desorganización en la red de colágeno y disminución de la elasticidad. La desorganización de la estructura de colágeno es particularmente compleja: las fibras de colágeno se vuelven más gruesas y más onduladas a medida que la gestación progresa, mientras que los poros entre las fibras de colágeno aumentan y las fibras se separan. Sin embargo, el vínculo entre la rigidez del tejido y la remodelación del cuello uterino aún no se comprende.

En esta tesis, se usan los principios básicos de la mecánica de sólidos para proporcionar una conexión entre las ondas utrasónicas de cizalla y el proceso de remodelación del cuello uterino, con la finalidad de evaluar el curso de la gestación y la posible aplicación de la elastografía basada en ondas mecánicas de cizalla para predecir el parto prematuro y el

éxito de la inducción del parto. En particular, se explora la viabilidad de las ondas ultrasónicas de cizalla para evaluar el cuello uterino en embarazadas. Para ello, esta tesis combina un enfoque experimental y numérico. Por un lado, por primera vez, en este trabajo se evalúa la capacidad y fiabilidad de la elastografía basada en ondas de cizalla para estimar la maduración cervical en las mujeres embarazadas. Después de demostrar la sensibilidad de la aplicación de esta técnica en el cuello del útero, el próximo reto que se aborda en esta tesis es proporcionar información valiosa para comprender el proceso de remodelación cervical. Con tal fin, se emplea un modelo animal, concretamente ovejas, que permite definir y controlar objetivamente el tiempo de la maduración cervical y proporciona datos fisiológicamente relevantes que pueden ser conectados a las medidas de elastografía. En este estudio, se indujo el parto mediante una inyección de dexametasona en un cierto número de animales, mientras que el resto se usó como control. A continuación, la maduración cervical inducida artificialmente mediante la dexametasona se monitorizó durante 24 horas usando elastografía basada en ondas de cizalla. Por otra parte, la arquitectura del tejido cervical a escala microscópica se investigó combinando análisis de histología y microscopía, que incluyen técnicas no lineales de imagen del segundo armónico y de excitación de dos fotones Este estudio animal proporciona una visión sobre la remodelación del cuello uterino y las propiedades mecánicas que son perceptibles en la elastografía.

Por otro lado, se ha desarrollado un modelo numérico para proporcionar información sobre el problema multi-escala y las variables bioquímicas. La hipótesis de la relación existente entre las ondas de cizalla y la estructura jerárquica del tejido del cuello uterino previamente mostrada por el estudio animal, se analizan mediante modelo computacional multi-escala en el que se usa la técnica de las diferencias finitas para simular la propagación de las ondas ultrasónicas de cizalla. Como tercera contribución de esta tesis, el papel clave del mecanismo de disipación de energía viscoelástico por la interacción entre las ondas de cizalla y la micro-arquitectura del tejido se evidencia y estudia en detalle. En primer lugar, se realiza un estudio comparativo de los módulos viscoelásticos que describen el comportamiento del tejido a nivel de la macro-escala. Las evidencias mostradas en esta tesis sugieren que el modelo de Maxwell es el que mejor describe las interacciones entre el tejido cervical y las ondas de cizalla, contrariamente a la creencia común en la literatura. Igualmente, usando modelos computacionales, se analiza la influencia de los parámetros de diseño de las ondas de cizalla (como la frecuencia de excitación) para interrogar de manera óptima las propiedades viscoelásticas de interés.

La última contribución de esta tesis es un modelo histo-mecánico numérico que se utiliza para vincular los cambios de las propiedades histológicas microscópicas (tanto morfológicas y bioquímicas) con las propiedades mecánicas del tejido a escala macroscópica medibles mediante las ondas de cizalla. Se propone un enfoque multi-escala que tiene como objetivo describir la remodelación del cuello uterino durante la gestación y que combina tres elementos: la morfología del colágeno, las interacciones de las ondas de cizalla con el tejido y la teoría de mezclas. Se realizó un estudio paramétrico usando una amplia gama

de valores de los parámetros mecánicos y geométricos que caracterizan la matriz extracelular cervical, que muestra que las características histológicas pueden ser cuantitativamente relacionadas con las propiedades mecánicas. Finalmente, esta tesis aporta valiosa información sobre los mecanismos que se producen en el embarazo normal, lo que permitirá una mejor comprensión de la remodelación mecánica que sufre el cuello del útero y conducirá a mejores métodos de diagnóstico para el parto prematuro y el éxito de la inducción del parto.

Acknowledgments

First of all, I would like to thank my advisor Dr. Guillermo Rus, head of the Nondestructive Evaluation Laboratory of the Department of Structural Mechanics and Hydraulic Engineering, for giving me the opportunity to start my scientific career in such an exciting research field. His particular enthusiasm about science and his valuable advices have played an imperative role in the successful of this project and in my research career.

I am very grateful to the different institutions and universities that have received me as an invited scientist during my international graduate program. There is a piece of work from all of them in this dissertation. First, thanks to professor Nader Saffari, head of the Ultrasonics group in the Department of Mechanical Engineering (UCL). Not only because I always felt welcome at UCL during the several times I have worked there, but also because he gave me the chance to learn from him. He has taught and passed me down his research vision. Secondly, I cannot forget Dr. Marie Muller, assistant professor of Department of Mechanical and Aerospace Engineering in North Carolina State University, to whom I owe enormous gratitude. Her valuable and expertise advices are included in this work. She is responsible, in part, for the success of this thesis. Finally, thanks to the rest of institutions, in particular to all the great people who work there and have contributed and collaborated with me on this work. They are: Institut Langevin, where we designed and analysed the shear wave elastography experiments; Institut National de la Recherche Agronomique (INRA), where the animal experiments were carried out; Institut Fresnel (Aix-Marseille University), who processed the SHG and 2PF images; and San Cecilio University Hospital in Granada, where we performed the women study.

Also, I thank all of my colleagues of the Nondestructive Evaluation Laboratory. We have had a lot of enjoyable experiences and memories that made this work easier.

Finally, thanks are due to my family, for their constant support and patience. Specially to my parents and my boyfriend, who encouraged me to face every single problem I have found through this work. I am in debt to them for their comprehension during these years. And I have to end with my brother, Antonio. He is the best "scientific reference" I know.

This work has been supported by the Ministry of Economía y Competitividad of Spain through FPI grant BES-2011-044970 within Project number DPI2010-17065.

Abbreviations

ABC	Absorbing boundary conditions
ACTH	Adrenocorticotropic hormone
ARF	Acoustic radiation force
ARFI	Acoustic radiation force imaging
BEM	Boundary element method
CCI	Cervical consistency index
CE	European Community CE marking
CGA	Cervical gland area
CI	Confidence interval
CL	Cervical length
DTI	Diffusion tensor imaging
ECM	Extracellular matrix
EI	Elastographic index
EIA	Enzyme-immunoassay
FDA	Food and drugs administration
FDTD	Finite difference time domain
FEM	Finite element method
FP	Forward problem
FT	Fourier transform
GA	Gestational age
GAG	Glycosaminoglycan
GLY	Glycine
HA	Hyaluronic acid
HES	Hematoxylin-eosin-saffron
HYP	Hydroxyproline
INRA	Institut National de la Recherche Agronomique
IP	Inverse problem
IQR	Interquartile range
K-V	Kelvin-Voigt
LIF	Light-induced fluorescence
MDG	Millennium Development Goal

MI	Mechanical index
MR	Magnetic resonance
MRI	Magnetic resonance imaging
NO	Nitric oxide
NOS	Nitric oxide synthase
PDF	Probability density function
PG	Prostaglandin
PGE2	Prostaglandin E2
PGEM	Prostaglandin E metabolite
PGF	Prostaglandin F
PGHS	Prostaglandin H2 synthase
PIP	Probabilistic inverse problem
PRO	Proline
pSWE	Point shear wave elastography
PTB	Preterm birth
QUS	Quantitative ultrasound
ROE	Region of excitation
ROI	Region of interest
SE	Strain elastography
SHG	Second harmonic generation
SLRP	Small-leucine-rich-proteoglycans
SNR	Signal-to-noise ratio
SSI	Supersonic shear imaging
SWE	Shear wave elastography
SWS	Shear wave speed
TE	Transient elastography
TI	Thermal index
WHO	World Health Organization
X-link	Cross link
1D	One dimension
2D	Two dimensions
3D	Three dimensions
2PF	Two-Photon fluorescence

List of Symbols

Symbol	SI	Description
E	[Pa]	Young's modulus
λ	[Pa]	Lamé's first constant
μ	[Pa]	Lamé's second constant or shear elasticity
ρ	[kg/m^3]	Density
c_s	[m/s]	Shear wave velocity
K	[Pa]	Bulk modulus
ν	[-]	Poisson's ratio
σ	[N]	Stress
ε	[-]	Strain
F	[Pa/m]	Magnitude of the acoustic radiation force
Ω	[Np/m]	Acoustic absorption coefficient
I	[W/m^2]	Intensity of the acoustic beam
c	[m/s]	Wave velocity
ω	[rad/s]	Angular frequency
p	[Pa]	Hydrostatic pressure
$\dot{\gamma}$	[-]	Rate of shear deformation
t	[s]	Time variable
η	[Pa s]	Dynamic shear viscosity
η^V	[Pa s]	Dynamic volume or bulk viscosity
φ	[rad]	Wave phase
σ^*	[N]	Complex stress
ε^*	[-]	Complex strain
G^*	[Pa]	Complex dynamic modulus
G'	[Pa]	Storage modulus
G''	[Pa]	Loss modulus
μ_1, μ_2	[Pa]	Shear elasticity in Zener model
γ	[s^{-1}]	Resistance coefficient or attenuation
$\Delta x, \Delta y$	[m]	Finite difference in space
Δt	[s]	Finite difference in time
f	[Hz]	Frequency
ϕ	[^{o}]	Angle between collagen fibres and wave propagation
L_0	[m]	Fibre length
ζ	[%]	Concentration of ECM constituent
k	[m^{-1}]	Wave number

Symbol	Description
σ_{ij}	Cartesian components of the stress tensor
ε_{ij}	Cartesian components of the strain tensor
c_{ijkl}	Cartesian components of the elasticity tensor
x, y, z	Cartesian component
X, Y, Z	Cartesian axis
δ_{ij}	Kronecker symbol
σ_M	Spherical stress tensor
ε_M	Volumetric strain tensor
τ_{ij}	Cartesian components of the deviator or deviatoric part of the stress tensor
d_{ij}	Cartesian components of the deviator or deviatoric part of the strain tensor
u_i	Cartesian components of the displacement vector
v_i	Cartesian components of the particle velocity vector
$E_{rel}(t)$	Relaxation modulus
$C_{crp}(t)$	Creep compliance
j	Imaginary number
$H(t)$	Heaviside step function or unit step function
δ	Dirac delta function
$\mathscr{L}$	Laplace transform
α	Significance criterium in statistical power
ES	Effect size in statistical power
N	Number of samples
p	p-value
r	Pearson regression coefficient
R^2	Coefficient of determination
f_i	Volume force densities
σ^2	Variance
dl	Infinitesimal arc-length of a fibre
ℓ	Random variable that describes the stretch at which the fibre becomes mechanically active
$\overline{\ell}$	Expected value of ℓ
χ^2	Chi-square distribution
β	Beta function
(a, b)	Shape parameters of Beta function
Γ	Gamma function
$\mathscr{P}$	Probability function
A	Wave amplitude
θ	Model parameters
$c_i(\omega)$	Estimated shear phase velocity
$\tilde{c}_i(\omega, \theta)$	Modeled shear phase velocity by rheological law
$\chi(\theta)$	Cost functional
$\hat{\theta}$	Estimated model parameters
N_p	Number of individuals in a population
N_g	Number of generations

Symbol	Description
P_s	Fraction of surviving individuals
P_t	Probability of tournament
P_c	Probability of crossover
P_m	Probability of mutation
S_m	Scale of mutation
M	Set of model parameters
$\mathbf{M}$	Manifold of possible set of model parameters
$\mathcal{C}$	Model class
Q	Set of configurations
q_i	Independent configuration
$\mathcal{Q}$	Manifold of possible configurations
s	Spatial media that define the configuration
C	Set of shear phase velocities
$\mathcal{C}$	Manifold of possible shear phase velocity
$p(\dots)$	Probability
$\mathcal{N}$	Normal distribution
κ	Normalization constant
σ	Standard deviation

Why does this magnificent applied science which saves work and makes life easier bring us so little happiness?
The simple answer runs: Because we have not yet learned to make sensible use of it.

Albert Einstein
in an address at Caltech, 1931.

Contents

List of Figures

List of Tables

Part I

INTRODUCTION

1

Context and motivation

Cervical biomechanics is a key controlling element of Preterm birth (PTB), which is the leading cause of death in children under 5 years of age [4]. Addressing preterm birth was an urgent priority for reaching Millennium Development Goal (MDG) 4, calling for the reduction of child deaths by two-thirds by 2015. Although countries made great progress in improving child survival, MDG-4 was only achieved by a few countries [4, 5]. For the post-2015 era, a new set of country targets to complete the unfinished work of the health MDG are being formulated. These objectives include a renewed target of reducing to 20 or fewer the child mortality under 5 years per 1000 live-births by 2035; and the Newborn Action Plan target calls for all countries to aim at reducing to fewer than 10 newborn deaths per 1000 live-births by 2035 [4, 6]. Therefore, reducing PTB is one of the priorities to achieve these targets.

According to World Health Organization (WHO 2014) [7], every year an estimated 15 million babies are born preterm in the world, and this number is rising each year. Between them, unfortunately almost one million die due to complications of PTB and babies who survive are at risk of its morbidity consequences. Preterm birth is defined as a labour that occurs at a gestational age of less than 37 completed weeks ($<$ 259 days), and is characterised by the association of uterine contractions and cervical modifications leading to the delivery of a preterm infant. Although PTB is a heterogeneous syndrome, most preterm births happen spontaneously, and always has a common denominator of cervical softening, shortening and dilatation. Better understanding of the causes and mechanisms will advance the development of solutions to prevent PTB. In this context, pregnancy and childbirth are

critical windows of opportunity for providing effective interventions to reduce mortality and disability due to PTB [8].

On the other hand, a post-term pregnancy is defined as a pregnancy that reaches or goes beyond 42 weeks' gestation ($\geq$ 294 days). Compared with term pregnancies and those delivered at 40 weeks' gestation, post-term pregnancies have been associated with higher perinatal mortality rates and higher rates of induced labour, fetal distress in labour, meconium staining of the amniotic fluid and operative delivery, along with other complications related to the mother, such an increased risk of labour dystocia, perineal injury and caesarean delivery [9]. Two general approaches exist for the management of post-term pregnancy: elective induction of labour and expectant management with serial fetal monitoring. Induction of labour, compared to expectant management, has a good evidence that is associated with reduced perinatal mortality, without an increase in the rate of caesarean section [10, 11]. Induction of labour is defined as the process of artificially stimulating the uterus to start labour. It is usually performed by administering oxytocin or prostaglandins to the pregnant woman or by manually rupturing the amniotic membranes [12]. Nowadays, labour has to be induced in approximately 23% of the pregnancies worldwide [13]. However, it fails in 32% of the induced pregnancies. As a consequence, caesarean section is performed. Caesarean delivery not only carries operative risks, but also increases risks for future pregnancies [14].

Both PTB and post-term pregnancy that requires induction of labour are associated with early and/or delayed cervical ripening. Hence, the control of this cervical maturation has been considered for the last 30 years as one of the most pressing problems in obstetrics [15, 16]. So far, however, no reliable clinical tool is available for quantitative and objective evaluation of cervical softness. In current clinical practice, this biomechanical status is only assessed by digital palpation, using a subjective scoring system introduced by Bishop [17]. Nevertheless, it is a poor predictor to determine eligibility for caesarean section after failed induction [18] and is not useful for assessing risk of PTB prediction [19]. In the past decade, some studies have reported that transvaginal sonographic measurement of cervical length appears to be a better predictor than the Bishop score, but this technique remains limited for the prediction of cervical ripening. As a consequence, it results as a poor indicator of preterm labour [20, 21] and for the need for caesarean delivery [22, 23]. The measured geometrical changes yield a low percentage of accurate predictions. Furthermore, they provide a limited anticipation of the cervix ripening and are insufficient to assess mechanical changes [16].

Elastography has recently been used in obstetrics and gynecology in a quest for meaningful information on the degree of cervical stiffness/softness, which in addition to cervical length, may provide a complementary method to identify cases at risk of preterm delivery and assess the likelihood of successful induction of labour. Quasi-static elastography is an imaging technique where displacements are generated by a hand-induced displacement of the tissue using the probe. The displacement and the generated strain in the tissue are then estimated using two-dimensional correlation of ultrasound images, and the resulting strain is represented as a colour map. Lately, many authors have proposed quasi-static

elastography as a new method for assessment of the softening of cervical tissue [24–27], but these studies concluded that quasi-static elastography has a limited interest for cervical assessment. Indeed, the resulting colour map is only a qualitative description of the relative strain distribution, far away from a quantitative description of the actual stiffness of the tissue. Despite the simplicity and compatibility of the technique with standard equipment, measurements are dependent on the transducer pressure applied by the operator and this technique would be more useful if measurements could be standardised between subjects. Therefore, quasi-static elastography cannot reliably quantify cervical stiffness so far and cannot be used to predict preterm delivery. Absolute values of cervical stiffness are necessary for an objective assessment of the cervical mechanical state, and the subsequent diagnosis of PTB or predictor for induction success [16, 28].

As opposed to static elastography, dynamic elastography is based on the propagation of shear waves within the tissue. Shear wave speed estimation has minimal dependence on user interaction and enables the targeting of a specific area of evaluation. A shear wave is generated and propagated within the tissue. In a homogeneous tissue, measuring its speed allows the quantification of stiffness. Although it has been successfully applied in the diagnosis and classification of tumours and/or cancer in other tissues as breast or liver [29, 30], its potential application to cervical tissue still remains unclear. Some assumptions are made that are inappropriate for the cervix: tissue is considered as homogeneous, isotropic and semi-infinite [31]. Notwithstanding, cervical tissue is anisotropic, heterogeneous and its architecture small relative to the shear wavelengths that are characteristic in dynamic elastography. Indeed, uterine cervix is a soft tissue, that is a distribution of cells embedded in an extracellular matrix (ECM), formed mainly by fibrillar collagen, whose organisation varies along gestation to allow dilation at term [1]. In addition, measurements made in this manner introduce artefacts that are difficult to correct given the fairly limited state of knowledge on the cervical-tissue mechanics. Shear wavelength may condition the wave-collagen interactions in the cervix, and therefore viscoelastic properties. Currently, all elastography techniques are characterised by a limited frequency band, below a few kHz [32], and the resulting wavelength is therefore considerably larger than the cervix architecture.

The cervix undergoes important changes throughout the gestation period in a process called cervical remodelling. During this cervical maturation several changes occur in the tissue (both biomechanically and morphologically). An increase in the hydration, disorganisation of collagen network and decrease in elasticity can be observed. The collagen structure disorganisation is particularly complex: collagen fibres turn thicker and more wavy as the gestation progresses in a transition from relatively straight fibres to wavy fibres, while pores between collagen fibres become larger and separated [33–35]. However, the link between stiffness and cervical remodelling is not yet fully understood. Understanding the mechanisms that take place in normal pregnancy will allow a better comprehension of the

cervical remodelling and lead to better methods for PTB diagnosis and successful induction of labour.

In particular, determining the viscoelastic properties could provide a sensitive characterisation of the micro-structural constitution of soft tissues and could reveal changes in the structure of the cell organisation [36]. However, viscoelastic parameters of cervical tissue have scarcely been studied so far in medical diagnosis [37], but the few available results suggest that viscoelastic properties are particularly sensitive to the gestation process [38–40]. Shear wave elastography is a promising but not yet fully understood tool to assess the cervical mechanics. Thus, a sound knowledge of the tissue microstructure and its interactions with shear waves is needed. As the long-term objective is to translate viscoelastic measurements into descriptions of ECM properties and pregnancy states, the relationships between stromal ECM features and viscoelastic measurements must be clearly understood. In this thesis, we intend to evaluate the application of shear wave elastography to assess cervical ripening. We aim at linking variations at the microscopic histo-biomechanical levels that characterise cervical ripening with mechanical properties assessed by shear waves, to finally evaluate the feasibility of shear wave elastography to be a complementary diagnostic tool for preterm birth and labour induction success.

2 Objectives

Nowadays objectively assessing the cervical ripening is still a challenge due to the complex nature of cervical tissue and its mechanical remodelling during pregnancy [41, 42]. The cervical softening is of particular importance; indeed, uterine contractions do not yield delivery if the cervix is firm [43]; and a soft cervix is associated with preterm delivery, even without contractions [44, 45]. However, its current clinical assessment is totally subjective, based on digital examination [17, 18]. Several methods have been proposed to evaluate the pregnant cervix, however none of them is capable of objectively detecting the changes (histological, biochemical and mechanical) in the uterine cervix before the cervical shortening has already occurred [46]. In contrast, shear wave elastography might achieve this target [47, 48]. However, its potential application to cervical tissue still remains unclear. Understanding the mechanisms that take place in normal pregnancy will allow a better comprehension of the cervical mechanical remodelling and lead to better methods of diagnosis of PTB and successful induction of labour. To this end, this thesis aims at understanding the relation between shear waves and cervical remodelling, and explore how shear wave elastography can address it. To reach this main target, several particular research steps are formulated on the basis of some research hypothesis, which are listed and commented below:

1. Elastography, which aims to map tissue stiffness or elasticity, provides an additional and clinically relevant information about the tissue mechanics. Shear wave elastography is based on the propagation of shear waves remotely within the tissue to quantify the tissue elasticity [49]. As opposed to quasi-static elastography, shear wave speed estimation has minimal dependence on user interaction and enables the targeting of a specific area of evaluation [50].

Hypothesis 1: Cervical stiffness progressively decreases during pregnancy and not in the same way throughout the cervix, which may present softer areas during gestation and thus be more sensitive in assessing the cervical mechanical state. Shear wave elastography can objectively quantify this decrease in cervical stiffness and its spatial variability.

➥***Research objective 1*:** Evaluate the shear wave elastography feasibility, sensitivity and capability for assessing cervical ripening.

2. Cervical softening occurs in a gradual fashion throughout gestation, much earlier than geometrical changes as shortening [51]. During the cervical remodelling several changes progressively occur in the cervical ECM. An increment in the hydration, disorganisation of collagen network and decrease in elasticity have been observed [1, 2]. The collagen structure disorganisation is particularly complex: collagen fibres turn thicker and more wavy as the gestation progresses in a transition from relatively straight fibres to wavy fibres, while pores between fibres become larger and separated [34, 39].

   Hypothesis 2: This softening is governed by changes in tissue micro-architecture, predominated by morphological changes in fibrillar collagen as alignment, waviness and thickness. Furthermore, each phase and constituent of the cervical extracellular matrix contributes to the ultrasound-sensitive mechanical properties of the tissue. A mechanical cervical description based on micro-structural changes will provide a complementary tool to objectively assess the cervical ripening.

   ➥***Research objective 2*:** Propose a modelling approach to describe the histo-biomechanical changes of the cervical extracellular matrix during pregnancy and link them with shear wave propagation characteristics.

3. Measurement of shear wave speed, dispersion, attenuation and nonlinear effects provides an objective description of tissue softness and microstructure. Whereas compressibility is predominantly governed by the fluid phase of the tissue, the shear stiffness is highly dependent on collagen fibre organisation [52].

   Hypothesis 3: Coupled mechanical parameters of complex tissue can be simultaneously reconstructed from ultrasonic shear wave transmission measurements by a model-based inverse problem. An appropriate rheological model, able to capture the features of interest, provides information on how the different scales are linked to each other and finally, helps to extract mechanical properties from shear wave propagation.

   ➥***Research objective 3*:** Evaluate the feasibility of elementary rheological models to describe the viscoelastic behaviour of cervical tissue and explore the possibility of quantifying both cervical elasticity and viscosity from shear wave velocities.

3

The uterine cervix

The aim of this chapter is to supply the basic knowledge of the cervix, its structure, functions and composition that support this thesis. This chapter reviews in detail the literature related to cervical tissue, paying particular attention to the structure and mechanics. The components of its extracellular matrix (ECM) and how each of them changes during pregnancy are fully explained. In addition, collagen network, its role and function are thoroughly discussed in the context of cervical mechanics in non-pregnant and pregnant states. Finally, current methods applied to evaluate the pregnant cervix, based on the cervical remodelling assessment, are described.

3.1 Anatomy and histology

The uterine cervix is a dense fibrous organ that is located at the end of the female uterus. The cervix is roughly cylindrical, although the overall shape is extremely variable between women; in the non-pregnant nulliparous it is approximately 3 cm in length and 2 cm in diameter. However, it has been observed to increase in size as a result of parity or infections, and decrease following the menopause [53]. The passage between the uterus and the vagina is the endocervical canal. It is fusiform in shape, flattened from front to back, and broader at the middle third than at extremity. The opening into the uterus is called the *internal os* and the opening that bulges into the vagina is called the *external os*. Figure 3.1 shows the localisation of the cervix in the female pelvic region during the non-pregnant state.

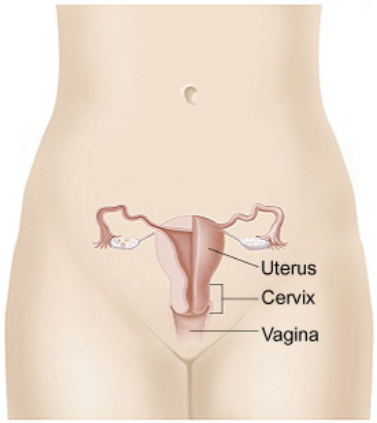

Figure 3.1: *The location of the cervix during the non-pregnant state*[1].

As opposed to the uterus, which is mainly composed of smooth muscle, the cervix is made of a dense fibrous connective tissue. In the non-pregnant state, the cervix acts as a barrier to infection, and during pregnancy it takes a mechanical role. It is responsible for keeping the fetus inside the uterus until the end of gestation, and during birth serves as the channel through which the fetus passes to the outside world. This unique "valve" behaviour is consequence of an extensive remodelling that occurs from early gestation to the postpartum period. This cervical remodelling is thoroughly described in Section 3.2.

3.1.1 Cervical structure: Extracellular matrix

The composition of cervical tissue consists of a distribution of cells, mostly fibroblast and smooth muscle cells, embedded in an ECM. The cellular content is typically around 5-10% per weight, quite low compared to the uterus. The ECM supplies strength and rigidity to resist mechanical load and provides a scaffold for cell attachment and migration. It is composed of a dense, hydrated and highly cross-linked collagen network embedded in a viscous proteoglycan ground substance, which is interlaced with the protein elastine. These biochemical components exist on varying length scales from the nanometre to the millimetre and act together in a cooperative nature to give the cervix its tensile and compressive strength [53].

The main constituent of the cervical ECM is fibrillar collagen, which represents the 85% of dry tissue. Cervical collagen consists of type I (70%), type II (30%) and some small percentage of type IV that is found in the basement membranes. The ground substance is composed by interstitial fluid/water (around 75-80% of the tissue), proteoglycans and glycosaminoglycans (GAGs), which represent between 0.2% and 1.5% of the dry tissue. Finally, the cervical ECM has a small composition of mature and cross-linked elastin, ranging between 0.9% and 2.5% of dry tissue weight [1]. These constituents are discussed individually in the following subsections, especially in regard to tissue mechanics.

[1]Reproduced from *http://www.fairviewebenezer.org*.

Many biochemical and mechanical changes take place during the cervical remodelling in pregnancy, and the structure and composition of cervical ECM undergo several changes. At this point it is convenient to clarify that, in this section, the biochemical composition of cervical ECM refers only to non-pregnant state or early pregnancy (first-trimester). The cervical remodelling will be described later in Section 3.2.

Collagen

Type I and II collagens are the main components in the ECM of the human cervix. They belong to fibrillar collagen subfamily. Collagen molecules are composed of a spatial arrangement of three polypeptide chains (α-chains), which exhibit a repeating triplet amino acid sequence $(\text{GLY-X-Y})_n$, where GLY is glycine, and X and Y can be any amino acid, but usually these positions are occupied by proline (PRO) and hydroxyproline (HYP). This triplet amino acid sequence, known as tropocollagen, forms the fundamental structure unit in fibril-forming collagens and results in triple helical domains of 300 nm in length and with a diameter of 1.5 nm. In classical fibrillar collagen, multiple collagen molecules packed together form fibrils and multiple fibrils arranged in bundles form a collagen fibre (see Figure 3.2). The self assembling of tropocollagen to form fibrils gives a characteristic band appearance to collagen that can be seen in atomic force microscopy, electron microscopy, and can also be inferred from X-ray diffraction [54]. The fibril assembly is stabilised by covalent cross-links between adjacent tropocollagen molecules. In addition to these strong covalent bonds there are weaker non-covalent cross-link interactions between fibrils which help to maintain the integrity of the structure.

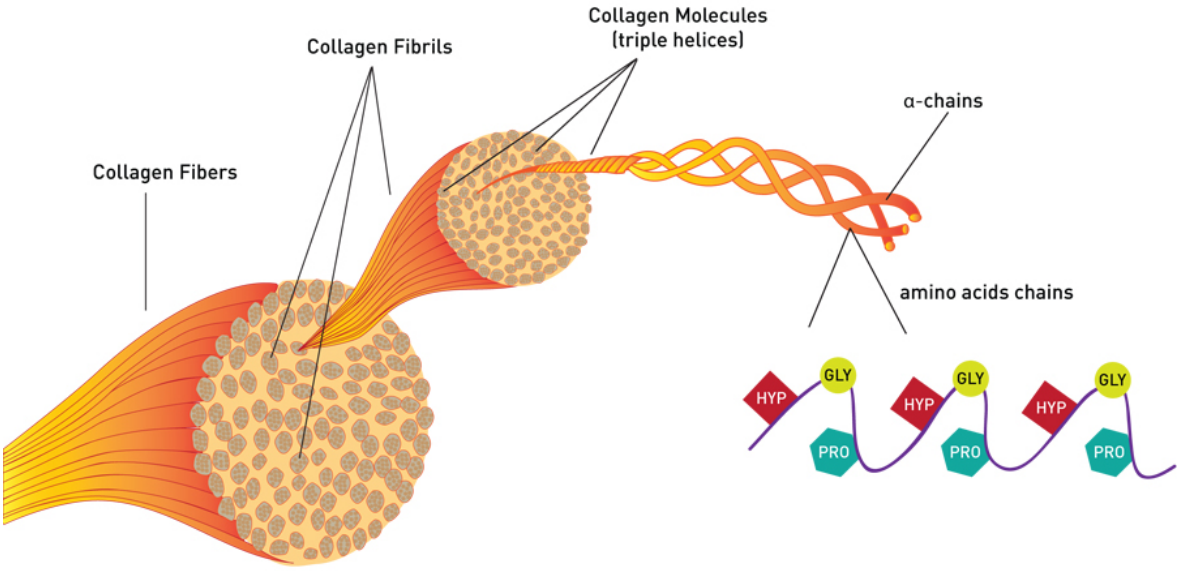

Figure 3.2: *Schematic view of hierarchical characteristics of fibrillar collagen, ranging from the amino acid sequence level at nanoscale up to the scale of collagen fibrils at micro-scale.*[2].

[2]Reproduced from *http://world.gold-collagen.com*.

The strength of cervical ECM is determined by the content and organisation of its collagen [1]. Early studies have shown that the collagen structure has a preferred orientation to resist cervical effacement and dilation [55–57]. Collagen fibre bundles arrange themselves within the cervix according to anatomical directions. Using X-ray, Aspden [55] investigated the collagen organisation in the cervix and the relationship with its mechanical function. The study showed that in non-pregnant state human cervix has three zones of organised collagen with gradual transition between them. The innermost and outermost zones of stroma contain collagen fibrils preferentially aligned in the longitudinal direction (parallel to the cervical canal), whereas the middle zone contains collagen fibres preferentially aligned in the circumferential direction, i.e. surrounding the cervical inner canal. These three zones are schematically represented in Figure 3.3. A posterior study [56] confirmed these preferential orientations by using magnetic resonance (MR) diffusion tensor imaging (DTI). These preferentially aligned fibres are responsible for the typical anisotropic behaviour of the tissue, and they provide strength both longitudinally and circumferentially with respect to the cervical canal [55, 56].

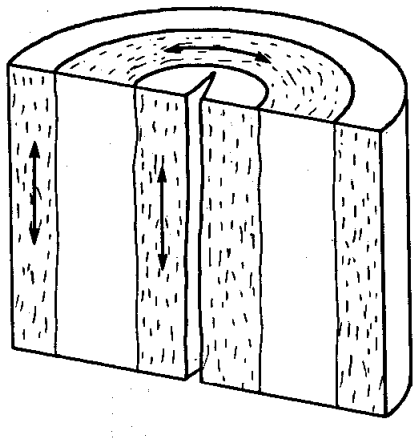

Figure 3.3: *Schematic representation of collagen organisation in the human cervix. The middle zone contains collagen fibres preferentially aligned in the circumferential direction, while in the outer and inner parts the fibres are aligned in the longitudinal direction*[3].

In many connective tissue types, as the cervical one, when the collagen fibres are observed in between crossed polarisers in the optical microscope, they present an undulating appearance [2, 57–59]. This wavy configuration of the fibrils at the microscopic level imparts a high degree of elasticity to soft tissues, enabling them to be stretched repeatedly longitudinally without damaging the underlying structure at the nano and molecular levels [60]. Thus, both preferred alignment directions and the waviness of fibres play an important role, determining the general mechanical behaviour of the tissue [61]. The crimped collagen fibres can be observed in Figure 3.4.

[3]Reproduced from Aspden [55].

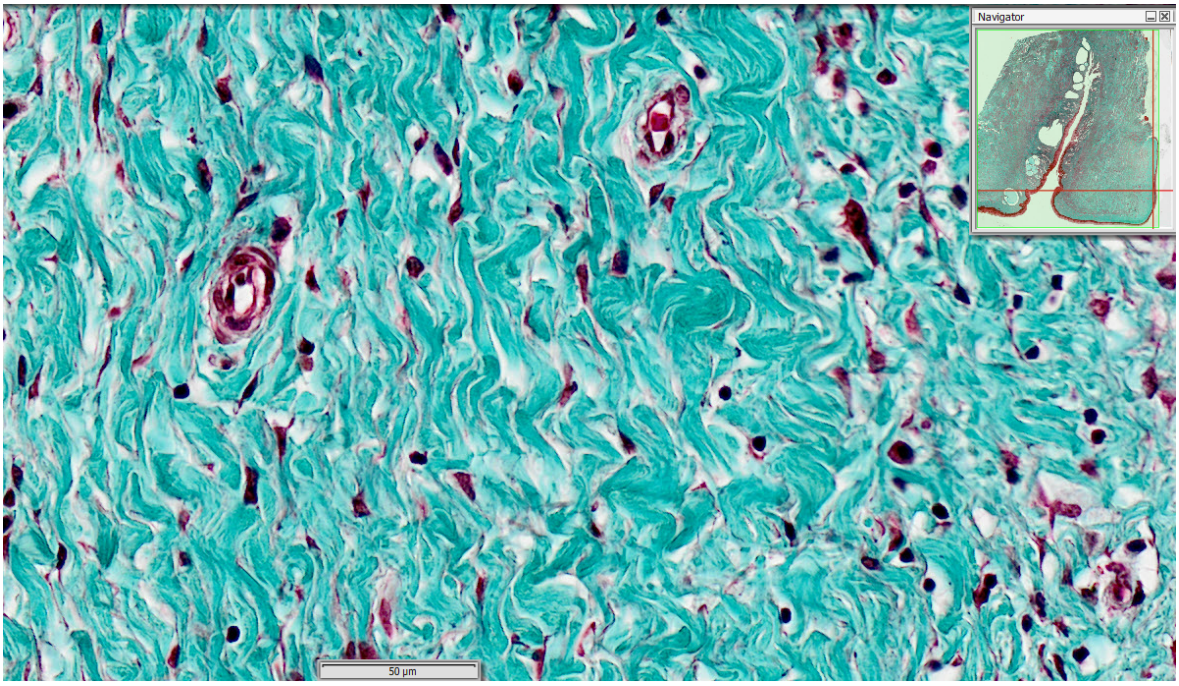

Figure 3.4: *Undulating appearance of collagen fibres in cervical tissue observed in the optical microscope.*

Elastin

Elastic fibres are another main component of the ECM. They confer elasticity, allowing both stretch and elastic recoil. The major protein of mature elastic fibres is elastin. The cervical stroma has a small composition of mature and cross-linked elastin ranging between 0.9% and 2.9% of dry tissue weight, which does not change during pregnancy [3, 62]. It is present in the walls of blood vessels and parallel to collagen fibres in the stroma. Orientation of the elastic fibres within the cervix has been described in detail in previous studies [63], which showed that elastic fibres are noted to be sparsely distributed in the cervical stroma. They are orientated from the *external os* to the periphery and from there in a band upwards towards the *internal os*, where they become sparse in that area of the cervix that contains the greatest amount of smooth muscle, just below the *internal os*.

There are several reasons to think it is unlikely that elastic fibres significantly contribute to the initial strength of the collagenous matrix [1]. First, single elastin fibres display significant lower Young's moduli, at least several orders of magnitude, than collagen fibrils (0.3-1.5 MPa for elastin fibres [64] *vs* 200-500 MPa for hydrated collagen fibrils [60]). Second, the volume fraction of collagen in the cervical ECM is 20 times higher than elastin protein. Rather, it is more likely that elastic fibres play a complementary role to collagen [1]. Therefore it is believed that elastin plays a major role following parturition, by restoring cervical shape after marked deformation associated with vaginal delivery [3].

Proteoglycans and glycosaminoglycans

Proteoglycans are macromolecules that contain a core protein with at least one covalently linked GAG chain. Proteoglycans can be classified into families according to location (i.e., cell surface *vs* ECM) and core protein properties [1]. GAGs are long linear polymers of sulfated polysaccharides composed of repeating disaccharide units. There are essentially 3 types of sulfated GAG chains: (i) dermatan sulfate; (ii) heparin and heparan sulfate, and (iii) keratan sulfate. The simplest GAG is hyalunoric acid (HA). HA is a free GAG chain with no sulfate groups and no core protein.

In the cervical ECM, the GAGs are represented either in the form of proteoglycans such as dermatan sulfate in decorin, or they are embedded in the matrix without core protein as in the case of hyaluronic acid. The major proteoglycan in human cervix is decorin (dermatan sulfate proteoglycan). It is located in the ECM and belong to the family of small-leucine-rich-proteoglycans (SLRP). This family is characterised by a relatively small core protein and a centrally located leucine-rich domain. In the cervical ECM, decorin accounts for 76% in GAG content, heparan sulfate represents the 13% and the remaining 11% is HA [3].

Between the several properties of the GAGs, there are some related to cervical structural function. They have a high fixed negative charge that renders them hydrophilic. As a consequence, they attack water into the tissue causing an osmotic swelling pressure, acting as lubricants or force damping mechanics to allow the tissue sustains compressive forces. Furthermore, it is known that GAGs influence collagen fibril formation and spacing. In particular, decorin regulates the fibril formation by binding its core to the collagen fibrils in the cervix, maintaining a uniform collagen fibril diameter and consistent collagen fibril distance [65]. In the cervical stroma, the role of HA is to imbibe fluid to maintain the osmotic welling pressure, counteracting the volume restoring forces of the cross-linked collagen [66]. During pregnancy, the amount of GAGs changes in association with cervical remodelling, which will be discussed in more detail in the following section.

3.2 Cervical remodelling during pregnancy

From early pregnancy to the postpartum period the cervix suffers an extreme remodelling process, which involves properly timed biochemical cascade interactions between the cellular component and ECM. Cervical remodelling can be roughly divided into four distinct but overlapping phases termed softening, ripening, dilation and postpartum repair [39]. The cervical softening refers to the remodelling that occurs slowly over the course of gestation and is related to biochemical and mechanical properties changes. Some authors define it as the first measurable decline in the tensile strength or tissue compliance compared with non-pregnancy [1, 39], but despite the progressive softening, cervical competence is maintained during this phase. The cervical ripening is a more accelerated phase characterised by loss of integrity and ability to remain closed. Because it is defined in terms of loss of structural function of the cervix, it therefore not only involves tissue softening but also shape

changes (i.e., effacement, dilation, shortening). As any "structural failure", cervical ripening is due to the combination of external loading conditions (uterine contractions, uterine growth, intrauterine pressure, membrane adhesion), structure geometry (cervical anatomy) and material (tissue) properties [1]. At the end of the pregnancy, the ripened cervix is able to sufficiently dilate and allow passage of fetus. Finally, a process of cervical repair occurs after parturition so that a successful pregnancy cycle can be repeated.

Many authors have investigated the biomechanical changes associated with cervical remodelling during pregnancy in both animal and human models [33–35, 67, 68]. However, this complex process is not yet fully understood. On the tissue level, the main compositional and structural changes of the cervical ECM will be described in this section.

3.2.1 Tissue hydration

It is confirmed by several studies that the water content during cervical maturation increases by approximately 5% at late in pregnancy [2, 15, 67]. This water increment modifies the mechanics of the cervix. A previous study has shown that alter the hydration level of cervical tissue samples substantially modified the stiffness of the material response [69]. Interstitial fluid flow is thought to control the short-term, non-equilibrium properties of soft tissue. The mechanical properties of the cervix will be described with more details in Section 3.3.

3.2.2 Collagen

Cervical maturation is associated with a disorganisation of the collagen network. Since collagen is the main constituent of cervical ECM, the disorganisation of these collagen fibres might have a major impact on weakening the tensile strength of the cervix. During pregnancy, the solubility of collagen considerably increases, from 37% in non-pregnant tissue to 80% in the third trimester [2]. Collagen solubility measures the organisation and stability of collagen fibrils. Changes in the solubility characteristics of collagen depend on the number of covalent cross-links between collagen triple helices that is required for the formation of stable collagen fibrils. Softening is characterised by a reduced collagen cross-linking. Increased collagen solubility has been correlated with cervical softening in both animals and humans [34, 69]. Furthermore, cervical insufficiency has been correlated to increasing collagen solubility [70, 71]. However, studies disagree on the collagen content. While some authors state that the collagen content does not decrease during pregnancy [2, 3], others claim that it can decrease up to 40% [67, 72].

Morphological studies have shown that the collagen network, which is preferably aligned in the non-pregnant cervix [55, 56], disorients and disrupts during the cervical softening [39]. Morphology studies using multiple imaging modalities corroborate it. The fibril anisotropy of the cervix and its disorganisation have been depicted by X-ray [55] and diffusion tensor imaging [56], in non pregnant tissue, and by 2 photon excitation microscopy [2, 73] in both pregnant and non pregnant tissues. A recent study, using optical coherence tomography, shows that the collagen fibres still maintain their preferential direction circling

around the inner cervical canal, but they are more disorganised and dispersed around the main fibre direction in the pregnant samples [74].

The collagen fibres themselves have a characteristic wave and crimp that influence the mechanical material response. Along with the fibre disorientation, the collagen network suffers additional changes during gestation. In particular, the collagen fibre size progressively increases from early to late pregnancy and pores between collagen fibres become larger and farther apart, probably as a result of the loss of collagen cross-linking and changes in the ECM proteins [39]. These morphological changes in the collagen bundles have been mainly measured in rodent tissue [33, 34, 75] and in some human tissue studies [2]. Their results emphasis the intrinsic relation between the cervix stage and collagen morphology and organisation. The importance of the collagen remodelling has also been highlighted after pregnancy [76].

3.2.3 Proteoglycans and glycosaminoglycans

Currently the content of the ground substance and the role of the GAGs still remain to be fully determined. Numerous studies have noted a change in GAG concentrations during pregnancy [2, 67, 77]. HA, heparan sulfate and acidic GAG content increase in the postpartum cervix compared to the non-pregnant state. Deparan sulfate (primarily associated with decorin) is the only GAG that has been found to decrease with cervical remodelling [77]. These changes in the composition of GAGs in the cervical ECM alter collagen structure and packing, and thus cervical mechanics.

Many studies evidence the important role of HA in cervical ripening. Nevertheless, its role in cervical softening is still unclear. Term pregnancy is associated with a significant increase in HA concentration. The affinity of HA for water molecules indicates that an increase in HA concentration causes an increase in tissue hydration. In earlier studies, higher HA content was found to be associated with increasing collagen inter-fibrillar spacing and networking disorganisation [78]. On the other hand, HA is implicated in the increased cervical inflammation. This increasing production of inflammatory cytokines, which may signal migration of inflammatory cells into the cervical stroma, an important feature of cervical ripening [1].

Term pregnancy is associated with a 40%-50% decrease in decorin concentration, which is postulated to decrease stability of the collagen network [77]. The reduction of dermatan sulfate at the onset of labour suggests that it may promote flexibility and distensibility to the ripened cervix associated with disruption of the collagen fibres organisation [3].

3.3 Biomechanical assessment of the uterine cervix in pregnancy

Currently, no method is capable of objectively detecting the changes (histological, biochemical and mechanical) in the uterine cervix before the cervical shortening has already occurred [42, 46]. Thus, characterising the biomechanics of the cervical tissue still reminds a challenge. The biomechanical changes in cervical tissue during pregnancy, described in the

previous section as cervical remodelling, have motivated new methods to assess the pregnant cervix. Measuring the micro-structural disorganisation and increased water content might offer an opportunity for early detection of PTB or for prediction of failed induction of labour. Consequently, current methods are based on the quantification of mechanical or optical properties associated with increased hydration, loss of organisation in collagen structure and cervical softening

Only a reliable characterisation of longitudinal changes over the course of the gestation will set up cervical biomarkers to predict spontaneous PTB or induction of labour success, which are the final targets of all applications. The main *in-vivo* methods for biomechanical testing of the uterine cervix are briefly explained in the following sections. Adopting the classification previously proposed by Feltovich *et al.* [41], we group the different methods depending on the feature that they attempt to assess, i.e. tissue hydration, collagen structure or tissue elasticity. Elastography is only briefly presented here because Chapter 4 is aimed at describing all these techniques and their application to cervical tissue.

3.3.1 Tissue hydration testing

The methods classified under this term are based on the fact that tissue hydration increases during gestation in the cervix. They aim at detecting this raise in the water content and relating it to the cervical ripening.

Acoustic attenuation

This method estimates the attenuation within the uterine cervix. Although the measurement of the acoustic attenuation primarily address tissue hydration, it can also report about the collagen structure. It has been proposed that the ultrasonic attenuation of the cervix should decrease as a consequence of the cervical ripening, since the spaces between fibres increase and fill with water, GAGs and enzymes. Studies in phantoms and animal models have shown that attenuation parameters can be accurately measured [79, 80]. However, *in-vivo* experiments performed in rats did not show any significant effect of ultrasonic attenuation with gestational age [79]. Posterior results in humans suggested that ultrasonic attenuation decreases with increasing gestational age, nevertheless, the high variability of the estimated attenuation coefficient within the cervix may undermine the application of the technique [80]. Not more promising results were reported by MacFarlin *et al.* [38] in an *in-vivo* study carried out in 42 pregnant women. They found a positive association between attenuation and time to delivery, but not with gestational age or cervical length. Furthermore, the results presented high variability.

This method has the advantages that it is quantitative and easy to perform. However, the high variability between subject and the manually election of the ROI make a standardised comparison between subjects difficult. Finally, the method relies on the election of homogenous ROIs since tissue inhomogeneity violates the assumptions of the used attenuation algorithm [38].

Electrical impedance

This method relies on that higher hydration reduces the electrical resistivity and increases light absorption. The electrical impedance of the cervix is calculated by the placement of electrodes on the cervix and measures the voltage required to obtain a specific current through the tissue. A first study in women demonstrated that pregnant cervices presented lower values of electrical impedance than the non pregnant ones [81]. Later, the method was applied to 86 pregnant women before labour induction [82]. Patients with a favourable cervix showed higher hydration represented as lower values of resistivity. However, in a posterior study performed by Gandhi *et al.* [83] contradictory results were found. They found higher impedance values in the term-pregnant women than in first trimester women and in non pregnant women. Finally, a recent study showed low predictive values for vaginal delivery [84]. The authors suggested that the results may reflect that the method only evaluates the most superficial layer of the distal cervix and consequently concluded that it does not offer clinical utility at present.

T2-weighted magnetic resonances images

This method uses T2-weighted magnetic resonance images of the cervix to calculate an intensity index. The background is that an increment in the hydration produces changes in the signal intensity of the images. Different authors have applied MRI to assess *in-vivo* the pregnant cervix [85–87]. They found that the signal intensity of the cervical stroma increased with the gestational age, and a higher signal intensity was associated with a shorter time interval to delivery [85]. Its application to predict the risk of PTB was studied by de Tejada *et al.* [87] in a prospective cohort study on 100 women. They found that the risk of spontaneous preterm delivery increased in women with low cervical stromal differentiation on MRI. However, despite its predictive value and is non-invasive nature [87], the authors concluded that this test may be clinically useless, due to limited practical and cost issues. Indeed, the cervical stromal differentiation is as predictive as the cervical length, but in contrast, measure of the cervical length is easier and less costly to obtain by ultrasound imaging [87].

3.3.2 Collagen structure testing

These techniques are aimed at quantitatively determining the changes in the ECM during pregnancy, particularly the loss of organisation in collagen structure.

Collagen light-induced fluorescence or collascope

The collascope is a probe that measures the insoluble cross-linked collagen by light-induced fluorescence (LIF) in the cervix, which is then analysed in a computer system to obtain a fluorescence spectrum. Its target is to measure the drop in the amount of cross-linked collagen during the cervical remodelling [88, 89]. The collascope was used to weekly investigate the relation between gestational changes of light-induced fluorescence and the time-to-delivery interval in a study that included pregnant patients beginning at 24-40 weeks' gestation and

patients in labour [90]. Cervical LIF was found to significantly decrease as gestational age increases. The authors concluded that LIF may be a useful tool to identify patients in whom delivery is imminent. A posterior study reported that cervical LIF was a measure of the drop in the amount of cross-linked collagen after application of prostaglandins [91]. This effect was observed only in patients with a prior high cross-linked collagen and the authors suggested that the technique may help distinguish women who would benefit from pre-induction ripening. However, this method seems not to be sensitive to micro-structural changes occurring early in pregnancy, since it did not detect changes prior to 25 weeks' gestation [89].

This method is non-invasive, easy to perform and provides an objective measure of collagen cross-links. Nevertheless, it requires specialised and fairly cumbersome equipment and only evaluates the superficial layer of the distal cervix.

Cervical gland area

The background of this method is that the absence of normal mucosal glands of the cervix (cervical gland area, CGA) is due to biochemical changes in the connective tissue in relation to cervical maturation [92]. Cervical glands are seen by a hyper-echoic or hypo-echoic segment around the cervical mucosa on conventional ultrasound imaging. The first study that showed that the relationship between the absence of CGA and cervical maturation was performed by Yoshimatsu *et al.* [93]. Results showed that CGA detection rate was significantly lower in threatened preterm labor than in normal pregnancy. Another prospective cohort study carried out on 338 women found that the absence of detection of CGA was a better predictor of PTB than the cervical length and the presence of cervical funnelling [94]. A recent study demonstrated that an absent CGA reflects high HA levels in the cervix with threatened preterm delivery [95]. However, results suggested that HA was not predictive for preterm delivery and thus, neither CGA could be. Although the method uses standard imaging techniques, which made it easy to apply, all authors have pointed as a main limitation the subjective evaluation of the presence or absence of the CGA.

Near-infrared spectroscopy

Near-infrared spectroscopy is used to non-invasively assess the optical properties of cervical tissue, characterised by absorption and scattering. The optical properties are sensitive to the tissue concentration of light-absorbing molecules and light-scattering structures. Thus, the optical properties of the cervix should change because of alterations in the biochemical composition of the ECM. This method has been applied to assess cervical ripening in normal pregnancies [96, 97]. A probe with seven near-infrared diode lasers transmits light with different wavelengths to the distal part of the uterine cervix, and the wavelength dependence of absorption is used to calculate absorption and scattering properties. Scatter power presented significant differences between the second and the third trimester and showed an increase as a function of the gestational age [96]. Opposite results were reported by Baños *et al.*, who found a decrease in total scatter power after induction of cervical ripening using

misoprostol. These contradictory results question the relevance of the technique in assessing the cervical tissue.

3.3.3 Tissue elasticity testing

The cervical softening during gestation has triggered the development of the methods presented in this section. The common goal of these methods is to evaluate, in particular quantify, the cervical stiffness/softness.

Elastography

Elastography aims to quantitatively assess the elasticity by an induced-displacement of the tissue. Attending to the force used to generate the displacements in the tissue the different methods are divided in quasi-static or dynamic methods. Quasi-static methods have been widely applied to assess the pregnant cervix, but their limitations to objectively assess cervical elasticity have been reported by several authors [25, 27]. In contrast, dynamic methods based on the shear wave propagation seem to provide promising results [47, 98]. All elastography techniques as well as their application to cervical tissue will be described in details in Chapter 4, and thus they are omitted here.

Aspiration

The aspiration method measures the vacuum (negative pressure) required to displace the tissue for a given distance, and thus estimate the stress-strain curve of the tissue. It allows a quantitative, *in-situ* and *in-vivo* mechanical characterisation of the tissue. A predefined suction pressure in a pipette (8 mm diameter) is applied on the anterior cervical lip, causing tissue aspiration (maximum 4 mm). A mini-camera estimates amount of deformation after suction. The obtained value of the closing (suction) pressure is a measure of the stiffness of the tissue. The first application to cervical tissue was performed by Mazza *et al.* [28], who texted *ex-vivo* and *in-vivo* non pregnant cervices. The reported variability between subjects suggested that the method was not as useful as expected. However, posterior studies in pregnant women showed promising results [51, 99, 100], which were consistent with the cervical remodelling. Stiffness in early pregnancy (first trimester) is significantly lower than in the non pregnant cervix. Further, the negative pressure needed to deform the cervix decreases during gestation, indicating a decrease in stiffness. After delivery (average 6 weeks postpartum) consistency returns to the level of early pregnancy [51, 66].

One of the disadvantages of this technique is that it only evaluates a relatively small part of the tissue, i.e., the superficial layer of the cervix's distal part. Consequently, no conclusions can be drawn about the mechanical properties of the middle or the proximal parts, and thus the measurement cannot adequately address cervical heterogeneity.

Mean gray-level histogram

The mean gray-level histogram addresses differences between the anterior and posterior cervical wall obtained with conventional ultrasound imaging. The principle is that a hard anterior lip absorbs more ultrasound beam, thus shadowing the posterior lip, which then

appears echo-poor [101–104]. A grayscale histogram is obtained from a midsection of the anterior and posterior cervix, and both histograms are compared. A more echogenic anterior than posterior lip indicates a harder cervix. A first study [103] carried out on 68 women suggested that the mean gray scale value was the single best predictor of preterm delivery between the evaluated factors (Bishop score, cervical length, parity and uterine contractions) [103]. In a posterior study, the histograms were associated with the Bishop score and the method showed a sensitivity of 71% to identify a hard cervix [101]. However, a most recent sensitivity study of the method reported poor inter-observer reliability and the authors concluded that the mean gray-level histogram should currently not be applied in clinical practice [102]. Furthermore, there is poor physical relationship between the shear modulus (stiffness) of a material and its acoustic scattering properties (that cause echogenicity in grayscale images) [41].

Cervical distensibility

These methods estimate the distensibility of the uterine cervix using different devices [105–107]. The *cervicotonometer* was designed and proposed by Cabrol *et al.* to measure the distensibility index of the uterine cervix [105]. Using a speculum the *cervicotonometer* is introduced into the cervical canal and then, it opens. Finally the size of the opening of the cervical canal and the force used to obtain it are simultaneously measured. The cervical distensibility index is defined as the slope of the force-length curve. In the first application of the device results showed an increase in cervical distensibility at the end of gestation and a dramatic decrease in the postpartum period [105]. After that, its possible application to predict spontaneous PTB and the post-term delivery were tested in two different studies [108, 109]. The cervical distensibility index had 100% sensitivity and 34% specificity to predict spontaneous PTB, while for post-term delivery the sensitivity and the specificity were 80% and 79%, respectively.

Previously to the *cervicotonometer*, the distensibility of the cervix was measured by Kiwi *et al.* by using a compliant ballon [106]. The compliant ballon (length 3-4 cm) is placed in the cervical canal and filled with 50 ml water at a rate of 12 ml/min. Then, the pressure inside the balloon is recorded. The distensibility of the cervix is expressed as elastance (mmHg/mL). The results from this study showed that in non-pregnant women the elastance was higher in women without prior second trimester abortions than to those with prior second trimester abortions [106].

The most recent mechanical test data for pregnant cervix is the device called *EndoFlip* [107]. The *EndoFlip* is a 1-m-long probe (diameter 2.8 mm) with a 12-cm-long cylindrical polyester urethane bag mounted on the tip. The probe is connected to an infusion pump that fills saline solution up to 50 ml into and out of the bag. Sensors spaced at 0.5-cm intervals along the probe are used to determine 16 serial diameters of the bag. Tissue stiffness is calculated from the geometric profiles and expressed as the pressure-strain elastic modulus at each sensor site [107]. Because of the positioning of the device in the inner canal, it was able to capture the deformation behaviour from the *internal* to the *external os*. A preliminary

study showed that the highest pressure-strain elastic modulus was always found in the middle part of the cervical canal and was significantly higher for early pregnant women than term-pregnant women. Finally, a stiffness variability was reported along the cervical length only in early-pregnant women.

The main disadvantage of all distensibility methods is that they are invasive, as they involve instrumentation in the cervical canal and thus, they may never be clinically useful. However, they are able to give valuable physiological information about the uterine cervix that may serve as good standards against which non-invasive methods could be contrasted.

4

Ultrasound elastography: basic principles and techniques

Elastography has gradually become a powerful medical imaging technique as it offers real time qualitative, quantitative and functional information on the inner structure of soft tissues. The goal of elastography is to map tissue stiffness or elasticity, which provides an additional and clinically relevant information on the tissue mechanics. Various techniques have been developed using different modalities, employing different tissue excitations, and extracting different parameters of tissue motion.

In this chapter, the different ultrasound elastography techniques are briefly described. We distinguish between quasi-static and dynamic methods, which are the two main forms of elastography that have been established in clinical practice [110]. Special attention is paid to shear wave elastography (SWE), which constitutes the core of this dissertation. Finally, a literature review about the applications of ultrasound elastography to cervical tissue is provided at the end of this chapter.

4.1 Background

The origin of elastography comes from "palpation", which has been traditionally used to detect cancerous tumours [111]. Palpation is the practice of feeling the stiffness of patient's tissues or organs with the practitioner's hands. Currently, it is still a valuable clinical practice, which however shows important limitations. Its application is limited to organs accessible

to the practitioner's hands, it provides limited disease detectability and spatial discrimination, and the interpretation of the information is totally subjective. Consequently, has been developed with the aim to address these challenges.

Since the 70's elastography has gradually become a widely applied medical imaging technique [112]. All elastography techniques rely on the same fundamentals: by inducing motion in the tissue a mechanical characterisation is possible if the resulting displacements are followed. Various techniques have been developed employing different mechanical excitations (static compression, monochromatic or transient vibration), generated by different ways (externally or internally) and extracting different parameters of tissue motion (strain, displacements or shear wave speed). Finally, different imaging modalities can be used to estimate the resulting tissue displacements: ultrasound or magnetic resonance imaging (MRI). In this chapter, only ultrasound elastography is described.

From the physical point of view, the elasticity of soft tissues is expressed by the elastic modulus, either Young's modulus (E) or shear modulus (μ). Currently, in the commercial available technologies, these moduli are typically estimated with respect to the measured quantity of tissue deformation using one of the following approaches: (i) calculate E using the Hooke's law; (ii) calculate E or μ from the measurement of the shear wave speed (SWS). Longitudinal waves propagate very quickly in soft tissues (~ 1500 m/s), enabling to image the body at high frequencies. Their velocity depends on the bulk modulus, K. In contrast, shear wave velocity, c_s, is slower in soft tissues ($\sim 1 - 50$ m/s) and is directly related to the medium shear modulus,

$$c_s = \sqrt{\frac{\mu}{\rho}} \tag{4.1}$$

where ρ is the medium density and the relationship between the elastic moduli is established as $\mu = \dfrac{3KE}{9K - E}$. While K varies no more than 12% over the whole range of soft tissues, μ varies by a factor of more than 10^5. This provides the potential for images with enormous tissue contrast, if they can be obtained with relatively good signal-to-noise-ratio (SNR) [52]. In soft tissues, the high water content makes the tissue quasi-incompressible (Poisson's ratio, $\nu \approx 0.5$) and the Young's modulus can be approximated as: $E = 3\mu$. Under this approximation, in a homogeneous region of tissue, isotropic and non-viscous, shear wave speed can thus be used to quantitatively map the Young's modulus ($E = 3\rho c_s^2$). Although this is the assumption that commercial dynamic methods usually follow, some clear limitations exist. Soft tissues are naturally viscoelastic materials, and thus shear wave velocity becomes a function of frequency. This could lead to differences in shear wave speeds measured with different imaging systems. Along with the viscosity, other issues of dynamic elastography will be discussed in the course of this thesis, particularly focusing on the application to cervical tissue.

4.2 Quasi-static methods

Quasi-static elastography or strain elastography (SE) was introduced for first time in 1991 by Ophir *et al.* [113]. In the SE, the tissue deformations are induced by an external palpation with the probe or by endogenous stress such as cardiovascular movements. The technique is based on the Hooke's law, $\sigma = E\varepsilon$, which states that for homogenous and isotropic material, the deformation, ε, is directly proportional to the uni-axially applied stress, σ, where E is the Young's modulus of the material. The displacements and the local strains are usually derived from the ultrasonic backscatter signals before and after compression by the 2D correlation of the ultrasound pre and post-compression data (see Figure 4.1). The result is a qualitative deformation gradient map, called elastogram. The elastogram is a representation of the pattern of strain, which is inversely related to tissue stiffness and can be assessed subjectively. It is easy to interpret following the physical principle that the lower the Young's modulus of a material, the higher the strain or deformation.

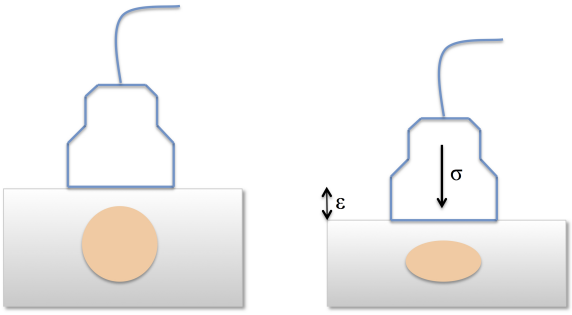

Figure 4.1: *Strain elastography principle. An static axial compression, σ, is applied to the tissue to get a deformation, ε. Before and after compression states are shown.*

This technique has the advantage of being relatively easy to implement. Nevertheless, it presents some limitations: displacements are manually generated using the probe and thus it is difficult to compress deep organs; the boundary conditions are not taken into account to calculate the resulting elastogram; nearly uniform stress must be applied in order to interpret the images; the applied stress is highly operator dependent; and since the applied stress is unknown, the technique does not allow to quantitatively estimate the local Young's modulus or stress/strain ratio and the resulting elastogram provides only a qualitative description of the relative strain distribution. To face the challenge of transmitting stress to deep organs, strain induced by either cardiovascular pulsation or respiration can be used [114]. Even if it may allow its application to deeper organs such as liver [115], the rest of limitations still have to be taken account.

Notwithstanding, SE has been efficiently applied to breast lesion characterisation and widely validated by many authors [116, 117]. If a reference healthy tissue can be found

and experienced the same stress as the target region, then, the calculated ratio can provide a semi-quantitative analysis [110]. Many commercial implementations of quasi-static elastography have been developed by different companies as Hitachi®[1] or Siemens®[2].

4.2.1 Artefacts in strain imaging

There are many factors other than tissue elasticity that influence strain images or elastograms due to the fact that the stress is not homogeneously distributed within the tissue and tissue elasticity is nonlinear. Typical artefacts presented in strain elastography are coming from different sources [50]. The size of the transducer can limit stress and strain penetration and homogeneity in tissue stress. Areas close to the probe depict less strain because of the friction than when a good lubricant is applied. Stress-concentration artefacts are consequence of the artificial overstrain in soft tissues when they are adjacent to hard tissue. Finally, the apparent positions of structures in the strain image may be slightly displaced with respect to the corresponding structures in the conventional B-mode image.

Image interpretation can minimise the artefacts influence. There are some recommendations listed by Bamber *et al.* [50] that should be followed to obtain good quasi-static strain images:

- Close proximity of the target to the transducer ($< 3 - 4$ cm)
- Nearly homogeneous tissue
- No anatomical planes that allow slip movement anterior to or within the imaged region
- Some distance to tissue boundaries
- No structures present (e.g. large veins) that would damp the shear stress
- A broad stress source (in 2D) relative to the width of the imaged region
- Knowing the position of the stress source with respect to the imaged region
- A limited number of diagnostic targets

4.3 Dynamic methods

Dynamic elastography methods were developed to overcome the SE limitations and, particularly, to obtain quantitative elasticity maps. They are based on the propagation of shear waves within the tissue, which can be generated by a vibrating force (sonoelastography) [118], a given frequency shift (vibroacoustography) [119], a short impulsion (transient elastography) [120] or acoustic radiation force (ARFI and SWE) [49, 121]. In a homogeneous tissue, measuring shear wave speed allows the quantification of stiffness. Dynamic elastography can produce a quantitative and higher resolution elasticity map compared to quasi-static methods. The use of shear waves, however, requires a more complex system, able to generate the shear waves and to image the small displacements induced by the shear waves.

[1] http://www.hitachi-medical-systems.com.
[2] http://www.healthcare.siemens.com.

At this point, since different terms are used in the literature, it is convenient to clarify the terminology that we follow in this thesis. Here, the term shear wave elastography (SWE) only refers to methods that make images of shear wave speed using radiation force excitation, even though all dynamic methods use shear waves. This terminology is commonly used in the literature. In acoustic radiation force imaging the tissue displacements are mapped, but no the shear wave speed. When ARFI is used to estimate shear wave velocity, the technique is called ARFI quantification or point shear wave elastography (pSWE), because it is a point measure in a specific region of interest (ROI) and not an image. Transient elastography (TE) also measures shear wave speed without creating an image but, since it uses a surface mechanical force rather than acoustic radiation force, it has not been classified here under the term SWE.

4.3.1 Sonoelastography

Sonoelastography is a method that combines continuous mechanical vibrations and real-time ultrasound Doppler imaging. It was proposed for detection of hard lesions [118, 122] and also for the study of tissue viscoelastic properties [123]. In sonoelastography, a low-frequency vibration (less than 1 kHz) is generated by an external source, such as an audio speaker or a piston shaker, which is brought into close contact with the tissue [124]. After that, Doppler techniques are used to estimate the vibration amplitude and phase within a ROI. The result is usually a greyscale image, where high vibrations are bright and lower vibrations are dark. This technique relies on the hypothesis that stiffer areas would vibrate at much lower amplitude than softer ones. Or in other words, when a region of uniform tissue contains a hard inclusion there is a local decrease in the peak vibration amplitude at the hard inclusion. Hence, in the resulting image, the higher the elasticity the darker the colour and the lower the vibration amplitude.

However, this simplified approach does not take into consideration the undesirable effects caused by diffraction, dissipation and stationary waves. Furthermore, interpreting the shear wave velocity maps can be difficult because of the sensitivity to the boundary conditions. It is important to establish a uniform background within an organ since it produces only a relative image contrast related to local hardness.

4.3.2 Vibroacoustography

Vibroacoustography is a dynamic elastography technique based on the ultrasound radiation force [119]. The acoustic radiation force (ARF) is a volumetric force created by transfer of momentum within the medium due to absorption and scattering mechanisms [125, 126]. The magnitude of the applied acoustic radiation force (F) can be related to the acoustic absorption (Ω) and speed of sound in the tissue (c) and the temporal average intensity of the acoustic beam at a given spatial location (I) as described in [127],

$$F = \frac{2\Omega I}{c} \tag{4.2}$$

Vibroacoustography uses two continuous sources, at close frequencies, ω_1 and $\omega_2 = \omega_1 + \Delta\omega$. The acoustic interactions of the two beams produce an oscillating radiation force in a small region around the joint focal point, where the amplitude of the field oscillates at the frequency difference $\Delta\omega$, typically in the low kHz range or less. This force causes the object to vibrate and as a result an acoustic emission field is produced in the surrounding medium. The sound waves generated by the vibration of the object are detected by a hydrophone tuned to the frequency difference $\Delta\omega$ and filtered by a band-pass filter centred at the same frequency (see Figure 4.2).

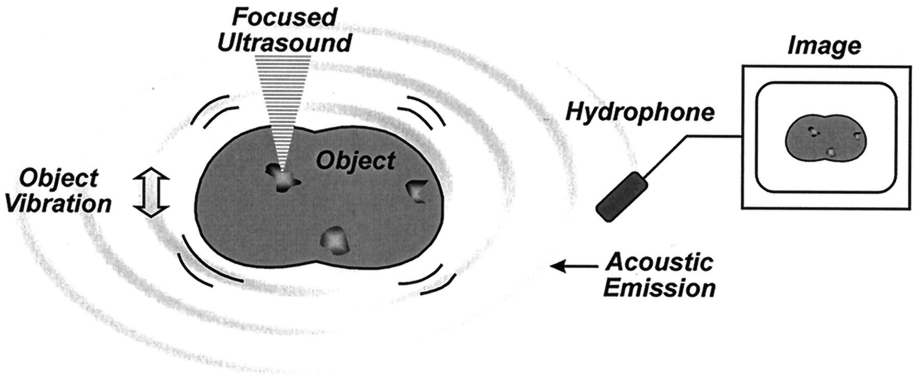

Figure 4.2: *Principle of ultrasound-stimulated vibroacoustography*[3].

In order to build a 2D image, the confocal transducers sweep out the entire area in raster scanning by moving the focal spot and recording the response at each point of the image. Covering the entire image by the radiation force produces a considerable deposit of energy within the medium and a relatively long acquisition time, which makes its application difficult in real-time and *in-vivo*. In addition, the measured parameter depends on the radiation force and the stiffness and geometry of the vibrating object [31].

This technique has been applied to a variety of targets including vessels, phantoms, lesions and contrast agents [119, 128, 129]. Although the monochromatic excitation elastography techniques offer a quantitative mapping of the tissue elasticity, the disadvantage of the monochromatic vibrations lies in the impossibility to separate the compressional waves from the shear waves, an aspect that can affect the shear wave speed estimation. This aspect motivated the development of new elastography techniques, in which the tissue excitation was transient instead of monochromatic.

4.3.3 Transient elastography

Several techniques relies on the propagating shear waves resulting from a transient (impulsive or short tone burst) tissue excitation, whose displacement history along the central axial line can be extracted by ultrasonic techniques. This allows the global estimation of the tissue shear wave velocity and therefore the tissue elasticity. All these techniques that generate

[3]Reproduced from Fatemi and Greenleaf [119].

shear wave from a transient impulse have the advantage that allow to separating the compressional wave (which propagates very fast) from the slower shear wave without taking into account the boundary conditions. In this dissertation, following the currently terminology used in literature, we use the term transient elastography (TE) only for the technologies that generate shear waves from a vibrating external push, and thus techniques based on acoustic radiation force are classified under another term.

The TE consists of generating a transient impulse on the medium by an external mechanical excitation and recording the shear wave that propagates within the medium by using an ultrasound transducer [120, 130]. First, a shear wave and a spherical shear wave are generated by a controlled external mechanical excitation, using a piston that "punches" the body surface. The displacements generated within the medium by the shear wave are estimated by correlating the back-scattered echo signals using a mono-dimensional ultrasound transducer (5 MHz) more than one thousand times (repetitions) per second [130]. Finally, the shear phase wave velocities are retrieved from a spectral analysis around the displacement central frequency, leading to an estimation of Young's modulus using Equation (4.1) and considering the medium homogeneous and non viscous.

The technique has been commercialised as *Fibroscan*® (manufactured by Echosense[4]) and permits to characterise the liver fibrotic state by giving a global score based on the mean elasticity. Its effectiveness in the evaluation of chronic liver diseases allows a reduction of more than 50% of liver biopsies [131, 132].

A few years later, the 1D transient elastography was extended to 2D, allowing a complete 2D Young's modulus map of the medium [133]. An ecographic device used for acoustics time reversal experiments (process of re-focalizing acoustic waves) was adapted to perform ultrafast imaging based on ultrasound plane wave emission [120]. A vibrator was fixed to the ultrasound imaging array, which is then used as an impactor to generate a quasi-plane shear wave. Once the movie of the propagating shear wave is reconstructed, the wave equation is inverted to recover a map of Young's modulus. However, the device was bulky, heavy and difficult to use in practice [31].

4.3.4 Acoustic radiation force imaging

The acoustic radiation force imaging (ARFI) was introduced by Nightingale *et al.* [134]. This method uses focused ultrasound to generate localised displacement of a few microns via an ARF impulse within the tissue, but unlike vibroacoustography, ARFI only uses one localised ultrasound beam. The transfer of momentum from the propagating acoustic wave to the tissue occurs over the duration of the acoustic pulse. In addition to vibrating at the ultrasonic frequency, the tissue within the region of excitation (ROE, or region where the ultrasound waves propagate and are absorbed) is deformed in response to a focused ARF excitation, and shear waves propagate away from the ROE [125]. Through the use of longer duration acoustic pulses ($0.05 - 1$ ms) than are typically used in diagnostic ultrasound ($<$

[4]http://www.fibroscan.com.

0.02 ms), transient soft tissue deformation on the order of microns (10^{-6} m) can be generated in vivo [135]. The displacement generated by the ARF is then mapped, within the focal region of each push within a specified ROI, at a known time after cessation of the push using ultrasonic correlation based methods (before and after the push application). The measured displacement is displayed as a qualitative elastogram within a small box. The same transducer is used to generate the force impulse and to monitor the resulting tissue displacement. The tissue displacement response within the region of the push is directly related to the magnitude of the applied force and inversely related to the tissue stiffness [121, 134]. The resulting images of tissue displacements depict similar information to the images generated in SE.

The technique has been demonstrated in breast [136] and prostate [137], and has been implemented in a commercial elastography system as *VirtualTouch Imaging*^{TM} (Siemens[5]). Since only the displacements are displayed, this technique cannot be used to quantitatively estimate the Young's modulus. Measured parameters are influenced by the geometry of the tissue and the beam. Nevertheless, compared to SE, ARFI methods are less user-dependent (i.e. more uniaxial) than those in hand-induced strain imaging, the ARFI images have also been shown to have better resolution, suffer less from stress concentration artefacts, possess better transfer of shear modulus contrast to image contrast, exhibit improved SNR at depth and be less influenced by the presence of slip movement anterior to the imaged region [50, 135]. Another advantage of the techniques based on ARF is that they can be applied almost everywhere, in anywhere where an imaging system can focus.

The displacements induced by radiation force can be generated at multiple locations and combined to build a complete quantitative map of tissue stiffness, but like in vibroacoustography, this increases the time needed to build one entire image [138] as well as the tissue temperature due to multiple pushing. After acquiring an image, time is need to allow the transducer to cool before another image may be generated.

The velocity of the shear wave generated by the ARF can be quantified in a small ROI and consequently, converted to elastic modulus [139]. This is implemented in the method known as ARFI quantification or point shear wave elastography (pSWE) [50]. In this method, the SWS is measured by repeated interrogations with different "track" directions throughout a specified ROI. The resulting is an average value of the SWS. This point measure (no image) is responsible for the name pSWE. Current commercial systems by Siemens and Philips[6]are based on this technique.

4.3.5 Shear wave elastography

Shear wave elastography utilises ARF to excite the medium and generate shear waves, but unlike pSWE, SWE produces a quantitative elasticity map of the medium in real time. ARF is applied at a multiple focal zone configuration in which each focal zone is interrogated

[5]http://www.healthcare.siemens.com.
[6]http://www.healthcare.philips.com.

in rapid succession, leading to a cylindrically shaped shear wave extending over a larger depth, enabling real-time shear wave images to be formed. This multiple focal zone approach has been termed supersonic shear imaging (SSI) [49]. The technique can be subdivided into two basic steps as follows:

- *The Mach-cone creation*. Ultrasound beams are successively focused at different depths to create spherical waves at each focal point (see Figure 4.3). The different generated spherical waves interfere constructively along a Mach-cone (quasi-plane on the imaging plane and cylindrical in three dimensions) creating two quasi-plane shear wave fronts propagating in opposite directions in the imaging plane [49]. The constructive spherical wave interference increases the shear wave amplitude and the SNR. In the imaging plane, the plane wave front allows the simplification of propagation hypotheses, which is of great interest for the inverse problem. Only one Mach-cone is needed to generate the quasi-plane shear wave fronts that travel across the medium to cover the entire ROI.
- *Ultrafast Imaging*. Ultrasound plane waves are generated to track the shear wave displacement along the entire imaging plane with very good temporal resolution in one single acquisition typically up to 5000 frame per second. Hence, there is no need to repeat the acquisition several times to acquire the entire displacement field. This allows, not only imaging in real-time, which makes the examination easier, but also averaging the very rapidly acquired images to improve image quality [31].

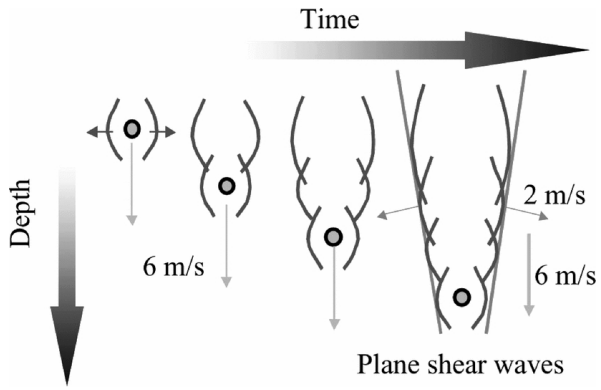

Figure 4.3: *Generation of a supersonic shear source. Ultrasound beams are successively focused at different depths. Each burst creates pushes by radiation pressure at focus that induces a shear wave. The constructive interferences of the shear waves form a supersonic Mach cone (in which the speed of the source is greater than the speed of the generated wave) and a quasi-plane shear wave is created*[7].

The Young's modulus maps are then reconstructed by estimating the velocity of the shear wave between two points of the image, using a time of flight algorithm. This technique has been implemented on a commercial diagnostic imaging called $Aixplorer^{TM}$ (Supersonic Imagine®[8]).

[7] Reproduced from Bercoff, Tanter and Fink [49].
[8] http://www.supersonicimagine.com.

In this thesis, we propose SWE to objectively assess the cervical ripening. The experimental studies presented in this dissertation have been performed by using the $Aixplorer^{TM}$ system. A great advantage is that it does not require additional set-up and can be performed during routine medical examination. The $Aixplorer^{TM}$ ultrasound system has received *FDA* (Food and Drugs Administration) and *CE* (European Community) clearances for *in-vivo* applications to obstetrics.

4.3.6 Others technologies

Currently a new modality of transient elastography, based on the propagation of torsional waves, is being developed [140]. The tissue elasticity is estimated from the shear wave velocity using a transducer capable of transmitting and receiving torsional ultrasound waves. The advantage of such a transducer is that it allows to easily separate compressional and shear waves. In contrast to commercial shear transducers, torsional movement guarantees no compressional wave generation at the boundary of the transducer, which is critical in quasi-fluids where compressional waves mask shear waves. The first prototype of the torsional transducer has been testing *in-vitro* with encouraging results.

4.3.7 Artefacts in shear wave imaging

Some simplifying assumptions are employed in all of the dynamic methods described here to estimate the elastic modulus. Biological tissues are more complex than the elasticity description presented in Section 4.1, which assumes that the medium is linear elastic, homogeneous, isotropic, semi-infinite and continuos. However, soft tissues in general, exhibit viscoelastic behaviour. As a consequence, the force-deformation relationship is usually both nonlinear and time dependent. Pressure leads high SWS artefact near the surface due to localised pre-stress which causes the superficial tissue to stiffen because of this nonlinear character of tissue. Moreover, biological tissues present anisotropy, i.e., both SWS and elasticity vary spatially and depend on the measurement direction. When the assumption of homogeneity in not satisfied inside the ROI, incorrect SWS can be estimated, leading to artefacts. Variations in either tissue density or SWS may cause scattering, reflection and refraction of shear-waves.

On the other hand, there are some factors related to the shear wave generation and propagation that affect data quality and may produce speed errors. Some of these factors, which must be taken account, are: strength of the push, variations in attenuation, absorption and reflection of the pushing beam, ultrasound scatterer density, tissue continuity, very high or very low SWS, and shear wave scattering, reflection or refraction [50]. Typical artefacts arise from shear wave reflections at structural interfaces and can result in a non real elasticity values, care is needed in interpreting them. Scattering results in shear wave attenuation and in a dependency on the vibration frequency of SWS. Finally, at tissue surfaces, near boundaries interfaces and within thin layers, mechanical waves may propagate as a guided wave that

follows the structure and travel with a speed different to that of a pure shear-wave. This can invalidate the assumed relationship between their speed and elastic modulus.

Although a full characterisation of the artefacts associated with SWE has yet to be conducted, there are some recommendations that may help to minimise these artefacts. To avoid shear wave reflections it is helpful to exclude structural boundaries that are visible on B-mode from the measurement region. A minimal compression application during imaging may reduce the nonlinearity effect and guarantees the reproducibility in the measurements. Finally, the most important is a deep understanding of the shear wave-tissue interactions. This understanding may help to take account the artefacts, gain additional information and give to elastography the ability to image extra tissue characteristics.

4.4 Application to cervical tissue

Measuring the cervical stiffness might be useful in the prediction of preterm delivery or successful induction of labor. For that purpose, elastography has recently been used in obstetrics and gynaecology in a quest for meaningful information on the degree of cervical stiffness/softness. Between the different elastography techniques, quasi-static or SE has been applied the most.

The first elastography measurement in pregnant cervical tissue was performed by Thomas *et al.* [141]. Using SE they calculated an elasticity tissue quotient (a ratio of the percentage of soft tissue to that of stiffer tissue) and correlated it with age and duration of pregnancy. Although this preliminary study showed promising results, a posterior study [142] demonstrated no correlation of the tissue quotient with gestational age.

After that, the feasibility of quasi-static methods to evaluate the cervical stiffness during pregnancy was studied by different authors [25, 27]. In both studies cervical strain from a hand-induced displacement was estimated. Molina *et al.* [25] evaluated the reproducibility of the technique in 112 pregnant women over four different ROIs of the cervix. Measurements were reliable and reproducible in all the cases, except in the area that received the force of the transducer directly. They concluded that measurements obtained by elastography may be a mere reflection of the force being applied by the transducer to different parts of the cervix. In a posterior study, Hernandez-Andrade *et al.* analysed the associations between cervical strain assessed in two different regions and maternal characteristics in 262 pregnant women. Their results suggested spatial variability in the stiffness, and a stronger relationship between cervical strain and cervical length than with gestational age. Finally, similar finding were reported, and both studies agree that it was premature to suggest that quasi-static elastography can reliably reflect changes associated with cervical ripening. Measurements are highly dependent on the pressure applied by the practitioner, and the technique would be more useful if measurements could be standardised between subjects. In fact, the lack of a standard is currently one of the challenges for the clinical use of SE. Recent works have been dedicated to discuss about this standardisation [16, 143, 144]. Different approaches to control the loading applied to the cervix have been proposed, such

as limiting the induced probe displacement [25], controlling the compression by a "pressure bar" [27] or using a reference elastomer material [145]. The resulting elastogram not only reflects the tissue elasticity, but also several factors that influence it. A recent work [146] shows that the cycle phase (compression or relaxation) and the derivative pitch (ROI where the displacements are assessed) influence the strain values calculated by SE.

The standardisation of the applied pressure has motivated alternative methodologies to assess the tissue strain, although they are often called quantitative elastography, all of them use quasi-static methods (continuum force) to induce the tissue deformation and thus do not quantitatively calculate the elasticity [146–148]. These methods aim to measure the maximum deformability of the cervix. The cervix is manually compressed with the probe until no further cervical deformation is observed in the B-mode image (maximum deformation). Then, the maximum deformability of the cervix is quantified as the ratio of the anterior-posterior distance (thickness) before (reference configuration) and after compression application (compressed configuration), measured in a sagittal plane of the cervix. Notwithstanding they do not use the conventional elastogram or strain map to determine the cervical consistency, still measure strain under an unknown pressure and consequently cannot quantify the Young's modulus. These studies have shown repeatability and reliability between the measurements and associations between tissue strain, gestational age and cervical length [146–148]. However, the tissue strain dependence on the applied force is still a main issue, along with it is not possible to quantify the absolute value of the elastic modulus. The heterogeneity of the cervix, its nonlinear nature and the election of the ROI to assess the strain are open questions [146, 149].

The unclear results from SE to assess the cervical consistency have led to the application of shear waves. Recently, *ex-vivo* measurements of shear wave speed were carried out by Carlson *et al.* [48, 150] in human hysterectomy samples. They aimed to explore the spatial variability within the cervix and the feasibility of SWS to identify ripened cervices. Their results were promising and SWS was sensitive enough to differentiate between ripened and unripened cervical tissue. Furthermore, spatial variability of SWS was confirmed too. The heterogeneity of the cervix makes the spatial location of the estimate very important, and thus an overall characterisation of the cervical stiffness is needed to objectively quantify the cervical ripening and in final application diagnose PTB or guide the artificial labour induction. In their work, Carlson *et al.* only got an average value of the SWS in a specified ROI. Moreover, no absolute quantification of the elastic modulus has been done yet. According to their results, while SWS varies from approximately 1.2 to 5.5 m/s over the cervix, the elastic modulus should vary more than 80 kPa. This makes the elasticity a more sensible variable to assess cervical stiffness/softness and thus, more valuable biomarker for physicians [16]. The purpose of this dissertation is evaluate the feasibility of SWE to assess cervical ripening. To our knowledge, the first applications of SWE to cervical tissue are reported in this thesis.

4.4.1 Elastography to diagnose preterm birth

A soft cervix early in pregnancy increases the risk of PTB. However, currently assessing the cervical softening is subjective. Because of that, particular effort has been dedicated to the possible application of elastography to diagnose PTB [26, 151–155]. Unfortunately, as it has been previously reported, all studies concluded that SE may be too user-dependent to be a reliable clinical tool.

The first work that aimed to predict PTB using cervical strain was performed by Parra-Saavedra *et al.* They proposed a strain-based index (cervical consistency index, CCI) to assess the cervical stiffness. The CCI introduced for first time the method to measure the maximum deformability of the cervix. The cervix was progressively compressed using the probe until no further shortening of the anteroposterior diameter could be observed. The CCI measures the ratio of the anteroposterior cervical diameter compressed and uncompressed. Although the results showed that CCI seemed to be a better predictor of PTB than the cervical length, the standardisation of the technique was pointed as a potential limitation. Similar results were reported by Kobbing *et al.* [152]. All concluded that expert operators, trained to perform the measurements, are needed. Moreover a deeper knowledge about cervical ripening may help to place the ROI, which is of further importance.

No more successful finding were reported by employing the resulting elastograms from SE [26, 151, 155]. The position of the ROI where to estimate the strain significantly influences the results. Results showed that elastography measurements were stronger associated with PTB in certain cervical regions than others, where even no association was found. The common conclusion of all studies is that absolute values of cervical stiffness are necessary to reliably predict the PTB.

4.4.2 Elastography to predict induction of labour success

Induction of labour is needed in several obstetric situations. Cervical assessment is important to predict whether the induction would succeed or fail. As PTB, the success of induction of labour is associated with cervical ripening. Consequently, the same methods have been applied to evaluate it and SE has been widely applied [24, 156–159].

In the first application of elastography to the induction success [24], the authors used a numerical scale called the elastographic index (EI), which was the value depicted in the resulting elastogram. The EI ranged from 0 to 4, hard to soft tissue, represented in colour in the elastogram. The cervical deformation was achieved due to movement generated by the patient's breathing and arterial pulsation, and no hand-induced displacements. Even though the authors claimed that no additional pressure was applied to the cervix and measurements were not operator-dependent, there is always a remaining pressure to guarantee the contact between the probe and the cervix, which is impossible to avoid. Contradictory results were found in the different assessed cervical parts, which may support the hypothesis of Molina *et al.* and the EI may be a mere reflection of the force being applied by the transducer to different parts of the cervix.

Further studies presented contradictory results. While the combination of elastography and cervical length is proposed by some authors as more predictive method for success of induction [156], Pereira *et al.* [159] suggest that the angle of progression and elastographic score are unlikely to be useful in prediction of vaginal delivery and induction-to-delivery interval. The possible usefulness of cervical elastography in the prediction of labor induction failure was confirmed by the "maximum deformability of the cervix method" too [157].

The application of a reference elastomer material to approximately estimate the Young's modulus does not solve the user-dependence of the technique [158]. Furthermore, the reference cap reduces the quality of the B-mode image, which sometimes makes it difficult to see the anatomy of the uterine cervix. Finally, even though this study shows a significant association between the cervical dilation time and the approximate Young's modulus, absolute values are impossible to assess.

Recently, the shear wave velocity has been proposed as an objective method to predict the success of labour induction [47]. The study included 20 women to whom the labour was induced. A miniaturised probe attached to the clinician's finger was used to punctually estimate the SWS. They detected differences in softening pre- and post- cervical ripening. Nevertheless, because of the applied technology (pSWE), the velocity only can be estimated in a single point, which furthermore due to the shortening of the cervix, it was not guaranteed to be assessed always in the same place. The heterogeneity of the cervix would request more attention. Much work remains to corroborate these preliminary results over more areas the cervix, in a larger sample and the findings should be confirmed by employing a conventional transvaginal probe that could be used in regular clinical practice. Finally, like in the previous *ex-vivo* study [48, 150], the reduced variability of the SWS during cervical ripening supports that the elastic modulus may be a more valuable biomarker for physicians. The quantitative elasticity map generated by SWE in real-time may provide more complete information about the cervical ripening.

5 Theoretical background

This chapter is aimed to briefly outline the field of linear viscoelasticity and the basic rheology to model this constitutive behaviour. In Section 5.1, the constitutive equations for both elasticity and viscoelasticity are presented. Section 5.2 exposes the principal features of viscoelastic materials. Finally, the simplest and most usual rheological models, which will be used over the course of the methodology in this thesis, are described in Section 5.3.

5.1 Continuum mechanics

Rheology is a science dealing with deformation and flow of matter. Relationships between stresses and deformations are the fundamental concepts of continuum mechanics, which are briefly discussed in this section. Constitutive equations for both elastic and viscoelastic materials are presented below.

5.1.1 Elasticity

Elasticity is the physical property of a material that deforms under stress and returns to its original shape after being deformed. The elasticity of materials is described by a stress-strain curve. For a pure elastic material, this curve is the same for the loading and unloading process, and the stress only depends on the current strain, not on its history.

The classical theory of elasticity deals with the mechanical properties of elastic solids for which the stress is directly proportional to the stress in small deformations. Their constitutive law is based on Hooke's law,

$$\sigma_{ij} = c_{ijkl}\varepsilon_{ij} \tag{5.1}$$

where $i, j = x, y, z$ are the cartesian components of the stress tensor σ_{ij}, and the strain tensor ε_{ij}, and c_{ijkl} is the elasticity tensor. If the material is isotropic, the elasticity tensor c_{ijkl} is then isotropic,

$$\sigma_{ij} = \lambda \delta_{ij} \varepsilon_{kk} + 2\mu \varepsilon_{ij} \tag{5.2}$$

where δ_{ij} is the Kronecker symbol, and λ and μ are the Lamé constants, which describe the behaviour of linear-elastic, isotropic materials. The relations between the Lamé constants and the engineering moduli are,

$$\lambda = \frac{E\nu}{(1+\nu)(1-2\nu)}, \quad \mu = \frac{E}{2(1+\nu)} \tag{5.3}$$

where E and ν denote the Young modulus and the Poisson ratio, respectively.

It is a common and useful practice to divide the stress tensor into two components: spherical and deviatoric parts,

$$\sigma_{ij} = -p\delta_{ij} + \tau_{ij} \tag{5.4}$$

where $-p = \frac{1}{3}\sigma_{kk}$ is the hydrostatic pressure, $\sigma_M = -p\delta_{ij}$ is the spherical stress tensor, and $\tau_{ij} = \sigma_{ij} - \frac{1}{3}\sigma_{kk}\delta_{ij}$ is the deviator or deviatoric part of the stress tensor. The spherical part represents the volume change and the deviatoric one the shape change. In the same way, the strain tensor can be split also into spherical and deviatoric parts,

$$\varepsilon_{ij} = -V\delta_{ij} + d_{ij} \tag{5.5}$$

where $-V = \frac{1}{3}\varepsilon_{kk}$, $\varepsilon_M = -V\delta_{ij}$ represents the volumetric part and $d_{ij} = \varepsilon_{ij} - \frac{1}{3}\varepsilon_{kk}\delta_{ij}$ is the deviatoric part of the strain tensor.

Therefore, for an elastic isotropic material, the Hook's law relates the deviatoric part of stress and strain with shear modulus,

$$\tau_{ij} = 2\mu d_{ij} \tag{5.6}$$

and the hydrostatic part of stress and strain with bulk modulus K,

$$\sigma_{kk} = 3K\varepsilon_{kk} \tag{5.7}$$

with $K = \lambda + \frac{2}{3}\mu$, $\sigma_{ij} = \tau_{ij}$ for $i \neq j$ and $d_{ij} = \varepsilon_{ij}$ for $i \neq j$.

5.1.2 Viscosity

The Newtonian model of fluid response is based on three assumptions:

(a) shear stress is proportional to the rate of shear strain in a fluid particle;

(b) shear stress is zero when the rate of shear strain is zero;

(c) the stress to rate-of-strain relation is isotropic, that is, there is no preferred orientation in the fluid.

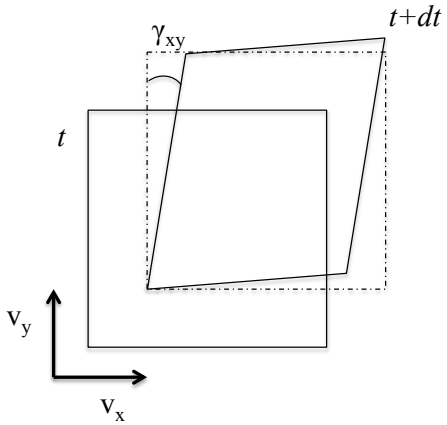

Figure 5.1: *Schematic representation of shear deformation in a fluid particle.*

To implement the Newtonian assumptions we consider first a typical shear term in the tensor, e.g $\sigma_{xy} = \tau_{xy}$. Figure 5.1 depicts the deformation of a fluid particle as it moves between time t and time $t + dt$. In this interval the shear stress σ_{xy} produces in the fluid particle an incremental angular strain γ_{xy}, which rate is,

$$\frac{d\gamma_{xy}}{dt} = \frac{dv_x}{dy} + \frac{dv_y}{dx} \tag{5.8}$$

Taking account the Newtonian assumptions (a) and (b) thus require that,

$$\tau_{xy} = \eta \frac{d\gamma_{xy}}{dt} = \eta \left(\frac{dv_x}{dy} + \frac{dv_y}{dx} \right) \tag{5.9}$$

where the coefficient of proportionality η is the viscosity coefficient, and is a property of the fluid. Thus in general, the basic constitutive relation for viscosity is defined by the Newton's law of liquids as,

$$\tau_{ij} = \eta \left(\frac{dv_i}{dx_j} + \frac{dv_j}{dx_i} \right) \text{ with } i \neq j \tag{5.10}$$

where the coefficient η is the same in all three shear stresses because a Newtonian fluid is isotropic. Finally, considering the compatibility equation $\varepsilon_{ij} = \frac{1}{2}\left(u_{i,j} + u_{j,i}\right)$, the Newton's law for fluids relates the deviatoric part of stress and strain with viscosity as,

$$\tau_{ij} = 2\eta \dot{d}_{ij} \tag{5.11}$$

In the same way, for a general viscous material where fluid compressibility is essential, it is possible to define a volume or bulk viscosity coefficient η^V that relates the spherical part of stress and strain as,

$$\sigma_{kk} = 3\eta^V \varepsilon_{kk} \tag{5.12}$$

5.2 Viscoelastic materials

Soft tissues are typical viscoelastic materials. Viscoelasticity is the property of materials that exhibit both viscous and elastic characteristics when undergoing deformation. Or in other words, a viscoelastic material is any material that dissipates energy when is subjected to stress or strain, and thus the relationship between stress and strain depends on time. Viscoelastic materials are characterised by its memory; the material "remembers" and is forever responding to earlier loads, i.e. they present hysteresis. The stress-strain curve reveals that for a viscoelastic material the loading process is different than in the unloading process. Moreover, they possess important characteristic properties that will be described in detail below. In the time domain, viscoelastic material creep or relax and propagating waves decay and disperse. In the frequency domain, constitutive relations are functions of frequency.

Only the purely mechanical theories are outlined here, and thermodynamic variables such as temperature and entropy are excluded. Without loss of generality, the concepts are discussed in a one-dimensional formulation and the elastic constants defined in this chapter refer to shear elasticity. More details can be found in most of the books on viscoelasticity [160, 161].

5.2.1 Relaxation, creep and complex modulus

The relationship between relaxation, creep and complex modulus links the time and frequency domain. These typical features that characterise viscoelastic material are briefly outlined below.

Stress relaxation

We define the stress relaxation as the observed decrease in stress in response to a constant amount of strain generated in the material. Experimentally, in a stress relaxation test, at time t_0 a constant strain ε_0 acts as "input" to the material that is maintained for a sufficiently long time period. In a viscoelastic material, the resulting time-dependent stress is decreasing until a plateau is reached at some later time. The relaxation modulus is defined a the ratio of the stress function and the constant strain, $E_{rel}(t) = \sigma(t)/\varepsilon_0$, where usually the constant strain is defined as the unit step (that is, $\varepsilon_0 = 1$).

In a stress relaxation test, viscoelastic solids gradually relax and reach an equilibrium stress greater than zero (i.e., $\lim_{t\to\infty} E_{rel}(t) = E_{rel,\infty} > 0$), while for viscoelastic fluids the stress vanishes to zero (i.e., $\lim_{t\to\infty} E_{rel} = 0$).

Creep

In a creep test, at time t_0 a viscoelastic material is loaded with a constant stress σ_0 that is maintained for a sufficiently long time period. The resulting time-dependent strain is increasing. Analogous with relaxation modulus, the creep compliance is defined as the ratio of strain to constant stress, $C_{crp}(t) = \varepsilon(t)/\sigma_0$, where usually the constant stress is defined as the unit step (i.e., $\sigma_0 = 1$).

In a creep test, the resulting strain for viscoelastic solids increases until it reaches a nonzero equilibrium value (i.e., $\lim_{t\to\infty} C_{crp}(t) = C_{crp,\infty}(t) > 0$), while for viscoelastic fluids the resulting strain increases without bound as time increases.

Creep and relaxation are both manifestations of the same molecular mechanisms, and one should expect that E_{rel} and C_{crp} are related. However, in general $E_{rel}(t) \neq 1/C_{crp}(t)$. In particular, the relaxation response moves toward its equilibrium value more quickly than does the creep response.

Dynamic loading: stress-strain phase lag

Creep and stress relaxation tests are convenient for studying material response at long times (minutes to days), but less accurate at shorter times (seconds and less). Dynamic tests, in which the stress (or strain) resulting from a sinusoidal strain (or stress) is measured, are often well-suited for filling out the short-time range of viscoelastic response. We illustrate these ideas with a discussion of the stress resulting from a sinusoidal strain. Note that the discussion of the strain resulting from sinusoidal stress can proceed similarly by just interchanging the role of stress and strain.

In a typical dynamic test carried out at a constant temperature, the material is subjected to a sinusoidally varying strain,

$$\varepsilon(t) = \varepsilon_0 \sin(\omega t) \tag{5.13}$$

where ε_0 is the amplitude, and ω is the angular frequency. The response of stress as a function of time t depends on the characteristics of the material which can be separated into several categories:

- A purely elastic solid. This materials follow the Hook's law of solid, and thus the stress is proportional to the strain at all the time,

  $$\sigma(t) = \mu\varepsilon_0 \sin(\omega t) \tag{5.14}$$

  Therefore, for pure elastic solids the response of stress caused by strain is immediate. That is, the stress is in phase with the strain, as it is depicted in Equation (5.14).
- A purely viscous material. For this kind of material, the constitutive equation is the Newton's law of liquids, $\sigma(t) = \eta\dfrac{d\varepsilon}{dt}$, and the stress is proportional to the strain rate,

  $$\sigma(t) = \eta\omega\varepsilon_0 \cos(\omega t) \tag{5.15}$$

  That it can be written as,

  $$\sigma(t) = \eta\omega\varepsilon_0 \sin(\omega t + \frac{\pi}{2}) \tag{5.16}$$

  Equation (5.16) shows that, in a purely viscous liquid the stress amplitude is linear in the strain amplitude: $\sigma_0 = \eta\omega\varepsilon_0$, which is dependent on the frequency ω. The stress is out of phase with the strain, and strain lags stress by a $\pi/2$ rad phase lag.

- A viscoelastic solid. When a viscoelastic material is subjected to a sinusoidally varying strain as the one defined in Equation 5.13, a steady state will eventually be reached in which the resulting stress is also sinusoidal, having the same angular frequency but retarded in phase by an angle φ; this is analogous to the delayed strain observed in creep experiments. The stress lags the strain by the phase angle φ, and this is true even if the stress rather than the strain is the controlled variable. For the sinusoidally varying strain defined in Equation (5.13), the cyclic stress is written as,

$$\sigma(t) = \sigma_0 \sin(\omega t + \varphi) \tag{5.17}$$

  where the phase shift φ is between 0 and $2/\pi$ and the stress amplitude σ_0 depends on the frequency ω. By an identity of trigonometry, we can rewrite Equation (5.17) as,

$$\sigma(t) = \sigma_0 \cos(\varphi) \sin(\omega t) + \sigma_0 \sin(\varphi) \cos(\omega t) \tag{5.18}$$

  Thus the stress is the sum of an in-phase response and out-of-phase response.

It is a common practice in engineering to use complex variables to describe the sinusoidal response of viscoelastic materials. If instead of defining the strain history as in Equation (5.13), we specify the complex strain as $\varepsilon^* = \varepsilon_0 e^{j\omega t}$, then we obtain the following complex stress,

$$\sigma^* = \sigma_0 e^{j(\omega t + \varphi)} \tag{5.19}$$

The complex stress can be written as,

$$\sigma^* = G^* \varepsilon^* \tag{5.20}$$

where G^* is called the complex dynamic modulus, and is defined by,

$$G^* = \frac{\sigma_0}{\varepsilon_0} e^{j\varphi} = \frac{\sigma_0}{\varepsilon_0} \cos(\varphi) + j \frac{\sigma_0}{\varepsilon_0} \sin(\varphi) \tag{5.21}$$

The real and the imaginary parts of the complex dynamic modulus are referred as $G' = \frac{\sigma_0}{\varepsilon_0} \cos(\varphi)$ and $G'' = \frac{\sigma_0}{\varepsilon_0} \sin(\varphi)$, respectively. G' is called the storage modulus and corresponds to the in-phase response, which is a measure of the energy stored and recovered per cycle. The out-phase of the response is the loss modulus G'', which is a characterisation of the energy dissipated in the material by internal damping.

5.3 Constitutive models of linear viscoelasticity

The characteristic feature of linear viscoelastic materials is that the stress is linearly proportional to the strain history, and it is important to note that the property of linearity of response does not refer to the shape of any material response curve. Linear viscoelasticity is usually applicable only for small deformations and/or linear materials. Thus, infinitesimal strain theory should be employed for this case. In a simple way, linear viscoelastic behaviour

can be described as a linear combinations of springs, which model the elastic component, and dashpots, which represents the viscous component. These are known as rheological models. Figure 5.2 shows a schematic representation of both elements.

Figure 5.2: *Schematic representation of the Hookean spring and the Newtonian dashpot.*

The constitutive equation for a material which responds as a linear elastic spring of stiffness μ is,

$$\sigma = \mu\varepsilon \quad \text{or} \quad \frac{d\varepsilon}{dt} = \frac{1}{\mu}\frac{d\sigma}{dt} \tag{5.22}$$

The spring models the instantaneous bond deformation of the material, and its magnitude will be related to the fraction of mechanical energy stored reversibly as strain energy. The response of this material to a creep-recovery test is to undergo an instantaneous elastic strain upon loading, to maintain that strain so long as the load is applied, and then to undergo an instantaneous de-straining upon removal of the load. Thus, in this case we have no creep and no relaxation so the creep compliance and the relaxation modulus are constant functions.

On the other hand, the entropic uncoiling process is fluid-like in nature, and can be modelled by a "Newtonian dashpot" (see Figure 5.2). By definition, the dashpot responds with a strain-rate proportional to stress:

$$\sigma = \eta\frac{d\varepsilon}{dt} \tag{5.23}$$

where η is the viscosity of the material. This is the typical response of many fluids; the larger the stress, the faster the straining. The strain due to a suddenly applied load can be obtained by integrating this constitutive equation. Note that, in the dashpot model, the strain is seen to increase linearly and without bound so long as the stress is applied. However, when the load is removed, there is no stress to move the piston back through the fluid, so that any strain built up is permanent.

This rheological/mechanical analogue approach results in a linear ordinary differential equation with constant coefficients relating stress and its rates of finite order with strain and its rates of the form,

$$a_0\sigma + a_1\frac{d\sigma}{dt} + a_2\frac{d^2\sigma}{dt^2} + \cdots + a_n\frac{d^n\sigma}{dt^n} = b_0\varepsilon + b_1\frac{d\varepsilon}{dt} + b_2\frac{d^2\varepsilon}{dt^2} + \cdots + b_n\frac{d^n\varepsilon}{dt^n} \tag{5.24}$$

where the constant coefficients a_i, b_i, with $i = 0, 1, 2, \ldots, n$ are related to the elastic modulus and viscosity of the material which are usually determined from physical experiments. A complete statement of the constitutive equation obtained from using of mechanical analogs

then consists of both an equation of this form and a set of appropriate initial conditions. The three basic models that are typically used to model linear viscoelastic materials are the Maxwell model, the Kelvin-Voigt model and the Zener model. Each of these models differs in the arrangement of these springs and dashpots elements.

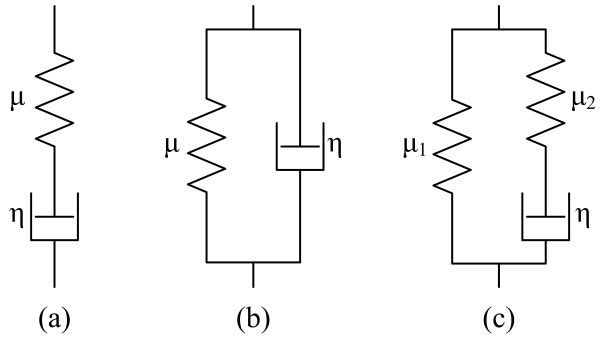

Figure 5.3: *Schematic representation of the (a) Maxwell, (b) Kelvin-Voigt and (c) Zener models.*

5.3.1 The Maxwell model

The Maxwell model shown in Figure 5.3 is a mechanical model in which a spring and a dashpot are connected in series. In this model, the total strain is the sum of the strain in the spring (ε_1) and the strain in the dashpot (ε_2). Furthermore, equilibrium requires that the stress be the same in both elements and equal to the imposed stress. We have, then, the three following equations,

$$\varepsilon_1 = \frac{\sigma}{\mu},\ \dot{\varepsilon_2} = \frac{\sigma}{\eta},\ \varepsilon = \varepsilon_1 + \varepsilon_2 \tag{5.25}$$

where the over-dot denotes time differentiation $\dot{\varepsilon} = \dfrac{d\varepsilon}{dt}$. Because the spring and the dashpot are subject to the same stress, the model is also known as an iso-stress model. Combining these equations we get the general constitutive equation of Maxwell model,

$$\dot{\varepsilon} = \frac{\dot{\sigma}}{\mu} + \frac{\sigma}{\eta} \tag{5.26}$$

Stress relaxation

In the stress relaxation test, the material is subjected to a constant strain ε_0 at time t_0. Letting the imposed constant strain defined as $\varepsilon(t) = \varepsilon_0 H(t - t_0)$ and the initial condition $\sigma(0) = 0$, where $H(t)$ is the Heaviside step function or the unit step function, Equation (5.26) can be written as,

$$\varepsilon_0 \delta(t - t_0) = \frac{\dot{\sigma}}{\mu} + \frac{\sigma}{\eta} \tag{5.27}$$

where $\delta(t)$ is the Dirac delta function. Let $\hat{\sigma}(s) = \mathscr{L}\{\sigma(t)\}(s)$ where $\mathscr{L}$ denotes the Laplace transform. Then taking the Laplace transform of both sides of the above differential equation we obtain,

$$\hat{\sigma}(s) = \varepsilon_0 \frac{e^{-t_0 s}}{\frac{1}{\eta} + \frac{1}{\mu} s} = \mu \varepsilon_0 \frac{e^{-t_0 s}}{s + \frac{\mu}{\eta}} \tag{5.28}$$

and taking the inverse Laplace transform we can find the relaxation function for the Maxwell model,

$$\sigma(t) = \mu e^{-\frac{\mu}{\eta}(t-t_0)} \varepsilon_0 H(t-t_0) \tag{5.29}$$

Therefore, the relaxation modulus is $E_{rel}(t) = \mu e^{-\frac{\mu}{\eta}t}$. Note that $\frac{\eta}{\mu}$ is physically the time needed for the stress to fall to its initial value or relax. This parameter is called relaxation time. The shorter the relaxation time, the more rapid the stress relaxation. The smaller the relaxation time, the faster the relaxation process, even though total relaxation takes theoretically an infinite time. The stress relaxation function of Maxwell model is represented in Figure 5.4.

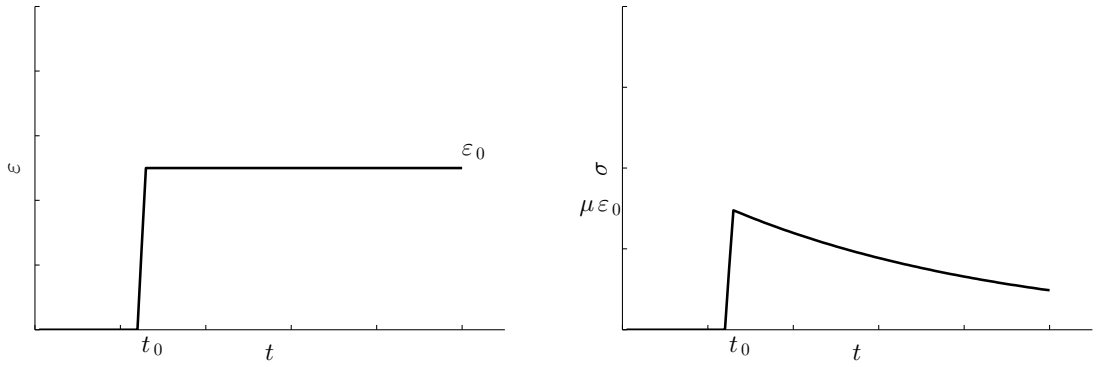

Figure 5.4: *Stress relaxation function of Maxwell model.*

Creep-recovery response

Physically, when the Maxwell model is subjected to a stress, σ_0, the spring will stretch immediately and the dashpot will take time to react. The creep function corresponds to the creep that occurs under the imposition of a constant stress given by $\sigma(t) = \sigma_0 H(t-t_0)$ and $\varepsilon(0) = 0$. With this stress function, Equation (5.26) can be written as,

$$\hat{\varepsilon}(s) = \frac{\sigma_0}{\eta} H(t-t_0) + \frac{\sigma_0}{\mu} \delta(t-t_0) \tag{5.30}$$

Then taking the Laplace transform of both sides of the above differential equation we have that

$$\dot{\varepsilon} = \frac{\sigma_0}{\eta} \frac{e^{-t_0 s}}{s^2} + \frac{\sigma_0}{\mu} \frac{e^{-t_0 s}}{s} \tag{5.31}$$

Finally, we find the creep function taking the inverse Laplace transform,

$$\varepsilon(t) = \left[\frac{1}{\mu} + \frac{1}{\eta}(t-t_0) \right] \sigma_0 H(t-t_0) \tag{5.32}$$

The creep compliance is then, $C_{crp}(t) = \frac{t}{\eta} + \frac{1}{\mu}$. When the load is removed, the spring again reacts immediately, but the dashpot has no tendency to recover. Hence there is an

immediate elastic recovery σ_0/μ, with the creep strain due to the dashpot remaining. In other words, the Maxwell model predicts creep, but not of the ever-decreasing strain-rate type. There is no an elastic recovery, but there is the elastic response and permanent strain. This is one of the limitation of the Maxwell model, to represent the creep response of a solid material, which does not increase without bound as depicted in Figure 5.5. Despite this limitation, the Maxwell model predicts that stress decays exponentially with time (see Figure 5.4), which is accurate for many materials.

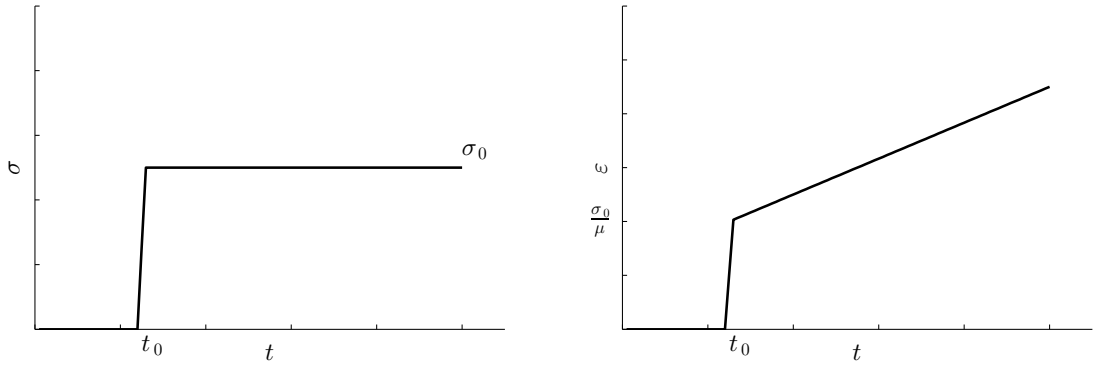

Figure 5.5: *Creep function of Maxwell model.*

Dynamic loading

Let be the strain and the stress, $\varepsilon(t) = \varepsilon_0 e^{j\omega t}$ and $\sigma(t) = \sigma_0 e^{j(\omega t+\varphi)}$. Then substituting them into Equation (5.26), we can obtain the complex dynamic modulus as,

$$G^* = \frac{\sigma_0}{\varepsilon_0} e^{j\varphi} = \frac{\mu(\eta\omega)^2}{\mu^2 + (\eta\omega)^2} + j\frac{\mu^2\eta\omega}{\mu^2 + (\eta\omega)^2} \tag{5.33}$$

Thus, the storage and the loss moduli of the Maxwell model are,

$$G' = \frac{\mu(\eta\omega)^2}{\mu^2 + (\eta\omega)^2}, \quad G'' = \frac{\mu^2\eta\omega}{\mu^2 + (\eta\omega)^2} \tag{5.34}$$

Note that the loss modulus achieves its maximum value at the frequency $\omega = \dfrac{1}{\tau}$, where $\tau = \dfrac{\eta}{\mu}$ is the relaxation time.

5.3.2 The Kelvin-Voigt model

The Kelvin-Voigt model (K-V) consists of a spring and dashpot in parallel, as shown in Figure 5.3. It is assumed there is no bending in this type of parallel arrangement, so that the

strain experienced by the spring is the same as that experienced by the dashpot. This leads to the following equations,

$$\varepsilon = \frac{\sigma_1}{\mu},\ \dot{\varepsilon} = \frac{\sigma_2}{\eta},\ \sigma = \sigma_1 + \sigma_2 \tag{5.35}$$

where σ_1 is the stress in the spring and σ_2 is the dashpot stress. Because the two elements are subject to the same strain, the model is also known as an iso-strain model. Eliminating σ_1 and σ_2, we get the constitutive law of K-V model,

$$\sigma = \mu\varepsilon + \eta\dot{\varepsilon} \tag{5.36}$$

Stress relaxation

The stress relaxation function corresponds to the solution of Equation (5.36) when the strain is constant, $\varepsilon(t) = \varepsilon_0 H_0(t - t_0)$, and the initial stress is $\sigma(0) = 0$,

$$\sigma(t) = \mu\varepsilon_0 H_0(t - t_0) + \eta\varepsilon_0\delta(t - t_0) \tag{5.37}$$

Setting the strain to be a constant ε_0, the constitutive law defined by Equation (5.36) reduces to $\sigma = \mu\varepsilon_0$. Thus the stress is taken up by the spring and is constant, so there is in fact no stress relaxation over time. The relaxation modulus is $E_{rel}(t) = \mu + \eta\delta(t)$. Actually, in order that the K-V model undergoes an instantaneous strain of ε_0, an infinite stress needs to be applied, since the dashpot will not respond instantaneously to a finite stress. Figure 5.6 shows the stress relaxation function for the K-V model.

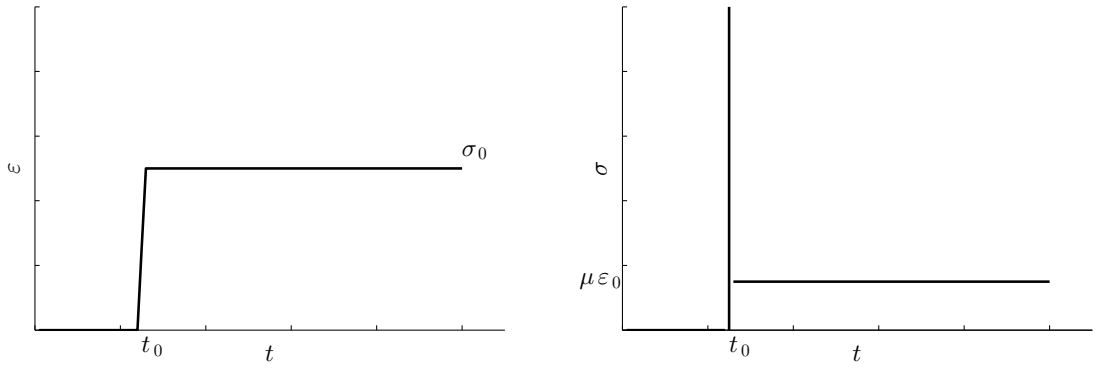

Figure 5.6: *Stress relaxation function of Kelvin-Voigt model.*

Creep-recovery response

The creep function of K-V is represented in Figure 5.7. It is the solution $\varepsilon(t)$ to Equation (5.36) corresponding to $\sigma(t) = \sigma_0 H(t - t_0)$ and $\varepsilon(0) = 0$,

$$\varepsilon(t) = \frac{1}{\mu}\left[1 - e^{-\frac{\mu}{\eta}(t-t_0)}\right]\sigma_0 H(t - t_0) \tag{5.38}$$

If a load σ_0 is applied suddenly to the K-V model, the spring will want to stretch, but is held back by the dashpot, which cannot react immediately. Since the spring does not change length, the stress is initially taken up by the dashpot. The creep curve thus starts with an initial slope σ_0/η. Some strain then occurs and so some of the stress is transferred from the dashpot to the spring. The slope of the creep curve is now σ_2/η, where σ_2 is the stress in the dashpot, with σ_2 ever-decreasing. In the limit when $\sigma_2 = 0$, the spring takes all the stress and thus the maximum strain is σ_0/μ. The creep compliance is now,

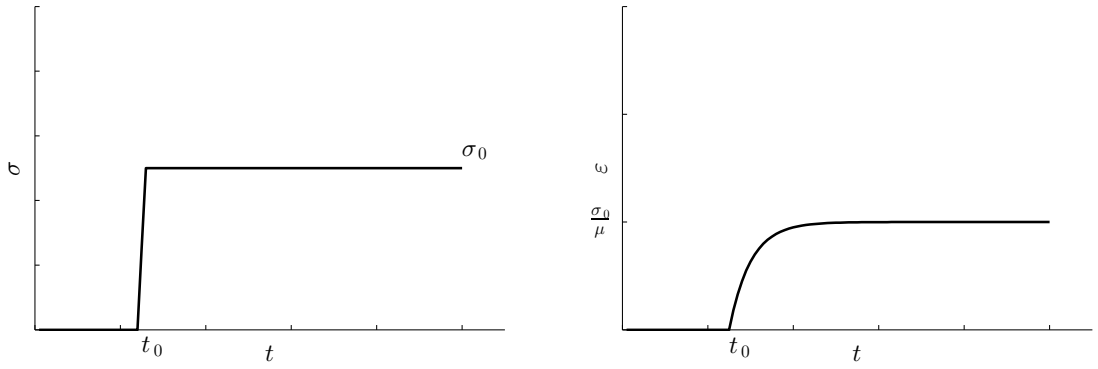

Figure 5.7: *Creep function of Kelvin-Voigt model.*

$$C_{crp}(t) = \frac{1}{\mu}\left(1 - e^{-\frac{\mu}{\eta}t}\right) \tag{5.39}$$

In contrast to Maxwell model, here the time taken for the creep strain to accumulate is called the retardation time, $\tau = \dfrac{\eta}{\mu}$. The shorter the retardation time, the more rapid the creep straining. Despite the accuracy of K-V model in modelling creep, the model has limitations in its ability to describe the commonly observed relaxation of stress in numerous strained viscoelastic materials.

When the Kelvin model is unloaded, the spring will want to contract but again the dashpot will hold it back. The spring will however eventually pull the dashpot back to its original zero position given time and full recovery occurs. There is a transient-type creep and an-elastic recovery, but no instantaneous or permanent strain.

Dynamic loading

Letting the strain and the stress, $\varepsilon(t) = \varepsilon_0 e^{j\omega t}$ and $\sigma(t) = \sigma_0 e^{j(\omega t+\varphi)}$ and substituting them into Equation (5.36), we can find the complex dynamic modulus,

$$G^* = \frac{\sigma_0}{\varepsilon_0} e^{j\varphi} = \mu + j\eta\omega \tag{5.40}$$

Hence, the storage and the loss moduli are,

$$G' = \mu, \;\; G'' = \eta\omega \tag{5.41}$$

5.3.3 The Zener model

The Maxwell and K-V model are thus the simplest viscoelastic bodies. The K-V model exhibits an exponential (reversible) strain creep but no stress relaxation; it is also referred to as the retardation element. The Maxwell model exhibits an exponential (reversible) stress relaxation and a linear (non reversible) strain creep; it is also referred to as the relaxation element. It is expected that more realistic material responses can be modelled using more elements. The Zener model, also known as the standard linear solid, is a particular case of the generalised Maxwell model composed of a Maxwell model in parallel with a spring (see Figure 5.3). The additional spring provides an "equilibrium" stiffness that remains after the stresses in the Maxwell arm have relaxed away as the dashpot extends.

In the Zener model, the Maxwell arm and the parallel spring experience the same strain, and the total stress is the sum of the stress in each arm. Then, the stress-strain relationship is given by,

$$\sigma + \tau_\varepsilon \dot{\sigma} = \mu_1(\varepsilon + \tau_\sigma \dot{\varepsilon}) \tag{5.42}$$

where we have defined $\tau_\varepsilon = \dfrac{\eta}{\mu_2}$ and $\tau_\sigma = \eta\dfrac{\mu_1+\mu_2}{\mu_1\mu_2}$.

Stress relaxation

As usual, the stress relaxation function $\sigma(t)$ is obtained by solving Equation (5.42) with $\varepsilon(t) = \varepsilon_0 H(t-t_0)$ and $\sigma(0) = 0$,

$$\sigma(t) = \left[\mu_1 + \mu_2 e^{-\frac{t-t_0}{\tau_\varepsilon}}\right] \varepsilon_0 H(t-t_0) \tag{5.43}$$

Figure 5.8 shows the stress relaxation function of the Zener model. In this case, the relaxation modulus is $E_{rel}(t) = \mu_1 + \mu_2 e^{-\frac{t}{\tau_\varepsilon}}$, which is just that of the Maxwell model shifted upward by an amount μ_1.

Creep-recovery response

As in the previous cases, the creep function is obtained by solving Equation (5.42) for $\varepsilon(t)$ given a constant stress $\sigma(t) = \sigma_0 H_0(t-t_0)$ and $\varepsilon(0) = 0$. Using the Laplace transform as

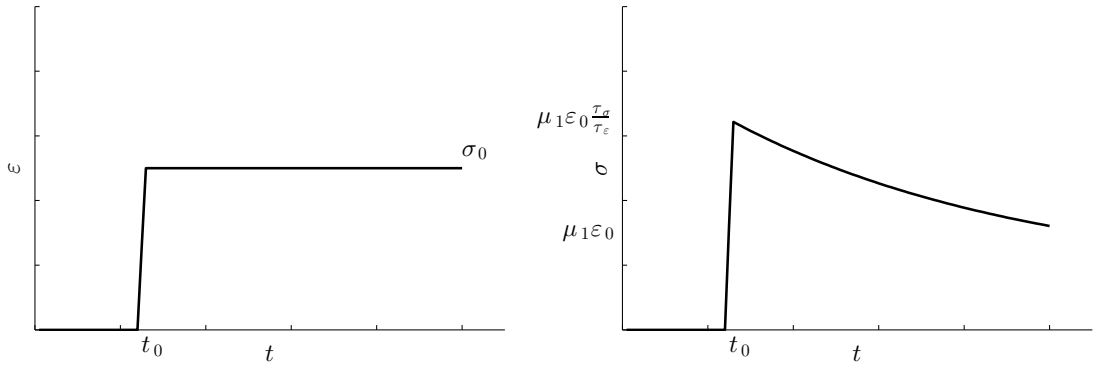

Figure 5.8: *Stress relaxation function of Zener model.*

above in finding the stress function, we have,

$$\varepsilon(t) = \frac{1}{\mu_1}\left[1 + \left(\frac{\tau_\varepsilon}{\tau_\sigma} - 1\right) e^{-\frac{t-t_0}{\tau_\sigma}}\right] \sigma_0 H(t - t_0) \tag{5.44}$$

The creep function of Zener model is despited in Figure 5.9. This model is able to predict both creep and relaxation responses.

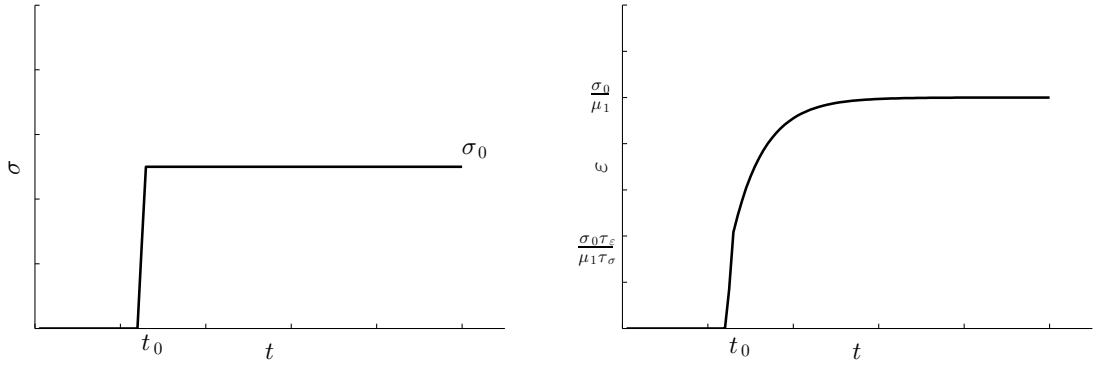

Figure 5.9: *Creep function of Zener model.*

Dynamic loading

Finally, letting the strain and the stress, $\varepsilon(t) = \varepsilon_0 e^{j\omega t}$ and $\sigma(t) = \sigma_0 e^{j(\omega t+\varphi)}$ and substituting them into Equation (5.42), we can find the complex dynamic modulus,

$$G^* = \frac{\sigma_0}{\varepsilon_0} e^{i\varphi} = \frac{\mu_1(t + \tau_\sigma\tau_\varepsilon\omega^2)}{1 + (\tau_\varepsilon\omega)^2} + j\frac{\mu_1(\tau_\sigma - \tau_\varepsilon)\omega}{1 + (\tau_\varepsilon\omega)^2} \tag{5.45}$$

being the storage and loss moduli then,

$$G' = \frac{\mu_1(t + \tau_\sigma \tau_\varepsilon \omega^2)}{1 + (\tau_\varepsilon \omega)^2}, \quad G'' = \frac{\mu_1(\tau_\sigma - \tau_\varepsilon)\omega}{1 + (\tau_\varepsilon \omega)^2} \tag{5.46}$$

Hence, the Zener model combines aspects of the Maxwell and K-V models.

Part II

METHODOLOGY

6

In-vivo assessment of cervical stiffness during pregnancy in women

This chapter describes the material and methods used over the course of an *in-vivo* study in pregnant women. The main goal of this study was to evaluate the feasibility of shear wave elastography (SWE) to provide quantitative information on the evolution of the cervical stiffness along normal pregnancy. Section 6.1 outlines the study design and population. In Section 6.2, the cervical stiffness quantification using SWE is described. Finally, Section 6.3 presents the statistical methods.

6.1 Cohort

The study was designed according to the Declaration of Helsinki. The local ethical committee in human investigation (Comité de ética en investigación humana de la Universidad de Granada and Comisión de ética e investigación sanitaria del hospital universitario San Cecilio de Granada) approved it.

The experimental study was carried out at San Cecilio University Hospital in Granada, and included 42 women with uncomplicated singleton pregnancies at a median value of 27.5 (from 6 to 41) weeks' gestation. The population size was estimated *a priori* by a statistical power analysis [162]. A regression analysis with desired power of 80%, significance criterion as two-sides $\alpha = 0.05$, and supposing the recommended medium effect size $ES = 0.30$, leads to a sample size of $N = 29$.

Non-inclusion criteria were communication problems, multiple gestation, prior surgery on the cervix (e.g. conization or cerclage), and not treated premalignant or malignant

changes on the cervix. All the subjects included in the study had agreed by signing the informed written consent and the patient information. Gestational age (GA) at delivery and neonatal outcome data were acquired by telephone verbal report from the patient that delivered at a different hospital (n=3).

6.2 Stiffness quantification

Elastography was performed by an ultrafast scanner (Aixplorer^{TM}, SuperSonic Imagine, Aix-en-Provence, France). Cervical stiffness was quantified by two expert operators trained to perform the SWE measurements using a 7-MHz conventional endocavitary ultrasonic probe (SE 12-3, Supersonic Imagine, Aix-en-Provence, France). Both operators performed the examination in a standardised pattern. The women were asked to empty their bladder and were placed in the dorsal lithotomy position. The vaginal probe was placed in the anterior fornix of the vagina and a sagittal view of the cervix, with the echogenic endocervical mucosa along the length of the canal, was obtained. A schematic view of the transvaginal ultrasound exam is shown in Figure 6.1.

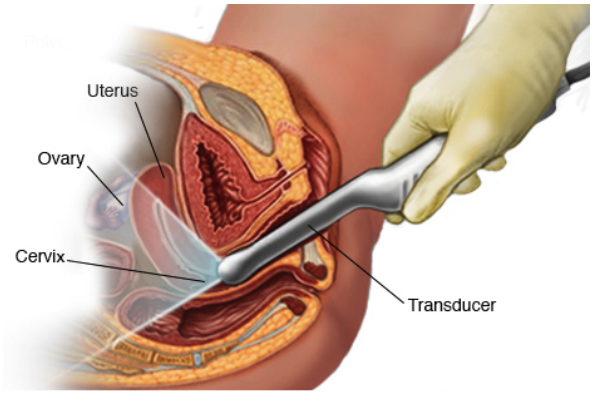

Figure 6.1: *Schematic representation of the transvaginal ultrasound exam*[1].

Elastographic images of the cervix were generated after taking care to avoid any movements in the ultrasound probe. An ultrasound coupling gel was applied to the probe to ensure good impedance matching and to facilitate the introduction of the probe through the vagina. A paired image with a conventional B-mode image from the cervix side by side with an elastrographic colour map was acquired in all the patients (see Figure 6.2). Cervical length (CL) was quantitatively assessed based on the conventional B-mode images and following the Fetal Medicine Foundation criteria (www.fetalmedicine.com).

During the whole examination, thermal index (TI) and mechanical index (MI) were kept lower than the food and drugs administration (FDA) thresholds. During ultrasound acquisition, so-called B-mode imaging, values of TI and MI were 0.2 and 1.4 respectively. In elastography mode, TI and MI where 0.4 and 1.6 respectively. The total duration of the stiffness measurement using SWE was a few minutes (less than 5 minutes).

[1]Reproduced from *Mayo Foundation for Medical Education and Research (http://www.mayoclinic.org)*.

Four regions of interest (ROI) in the cervix were selected to assess the stiffness: external and superior lip (Region A1), internal and superior lip (Region A2), internal and inferior lip (Region A3) and external and inferior lip (Region A4), as shown in Figure 6.2. A circle, 6 mm in diameter, was then placed in each of the four regions and the machine automatically displayed a stiffness value for each circle (mean value and standard deviation), quantifying the elasticity in pressure units (kPa).

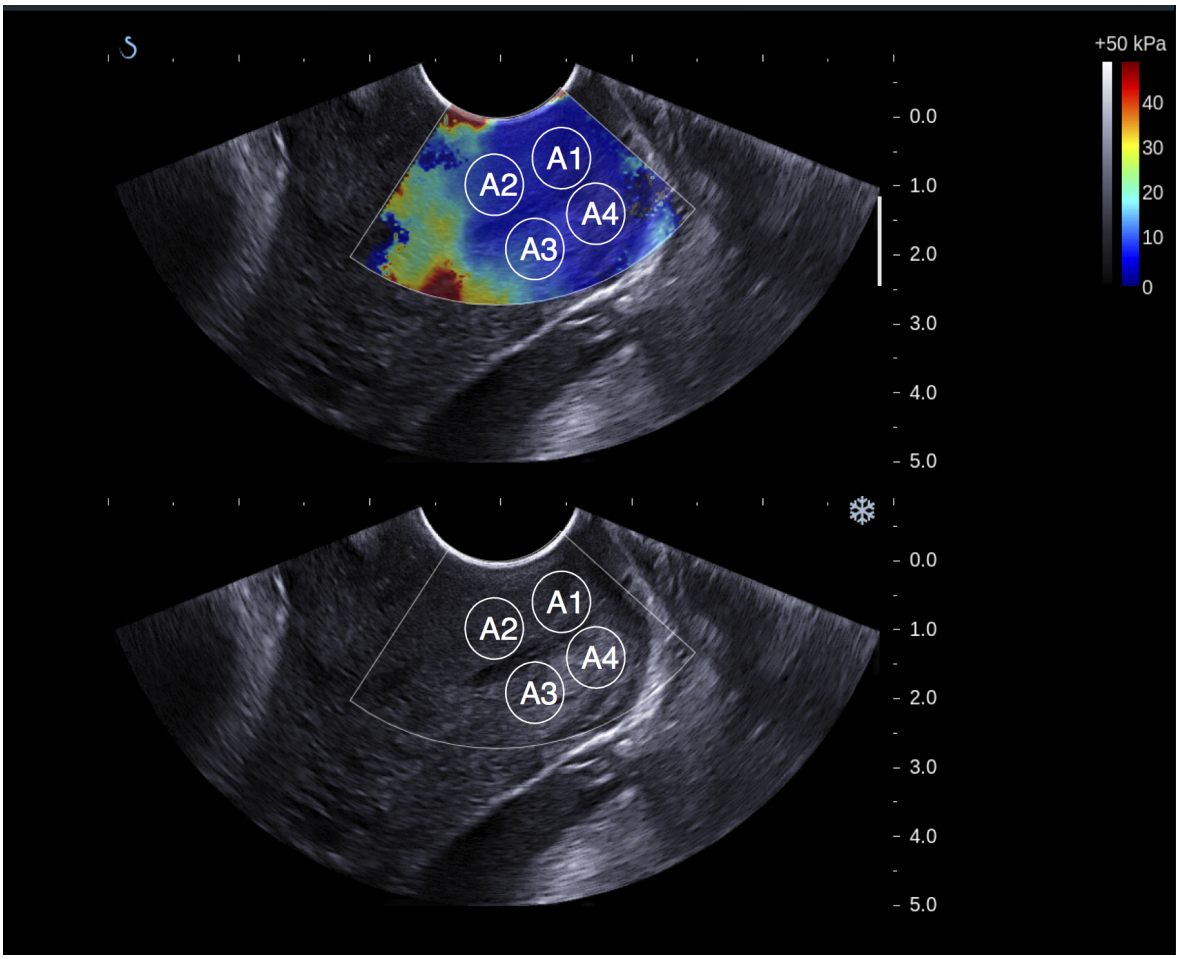

Figure 6.2: *Elastographic and B-mode images of the cervix. The circles indicate the ROI selected to assess the stiffness. Region A1: external and superior cervical lip. Region A2: internal and superior cervical lip. Region A3: internal and inferior cervical lip. Region A4: external and inferior cervical lip.*

Cervical elastographic measurements were carried out twice by a single operator in all the women, and these data were used for intra-observer analysis. A second operator also performed a single measurement of cervical elastography and this was compared to the first measurement made by the previous operator to determine the inter-observer reproducibility. All the measurements were performed offline on stored images, with the operator blinded to previous measurements, and the placement of the ROI within the elastographic image for the stiffness measurement was determined by following only anatomical criteria,

on the conventional B-mode image. This allowed an objective and reproducible positioning of the ROI for stiffness quantification.

6.3 Statistical analysis

Changes of stiffness values throughout gestation were evaluated. Regression analysis was used to determine the relationship between GA, interval time from elastography examination to delivery and CL with cervical stiffness in the four selected regions.

The ANOVA test with Bonferroni correction was performed to compare differences between the mean of the stiffness values in the four different regions selected. The Bonferroni correction allows to control the familywise error rate in the multiple comparison problem.

Inter and intra-operator agreement for stiffness values were assessed using the Cronbach's Alpha statistic. It describes the expected correlation of two tests that measure the same [163]. *A priori* interpretation of the alpha statistic was based on the following distribution: excellent, 0.91-1.0; good, 0.81-0.90; acceptable, 0.71-0-8; questionable, 0.61-0.70; poor, 0.51-0.60; and unacceptable < 0.50 [164].

Data were analysed using the statistical software SPSS 22.0 (SPSS Inc., Chicago, IL, USE). All results are expressed as median [quartile 1 - quartile 3]. Data were considered statistically significant for $p < 0.05$. P-values below 0.0005 are indicated as $p = 0.000$.

7

In-vivo evaluation of cervical remodelling during induced ripening in an animal model

This chapter describes the material and methods used over the course of an *in-vivo* study in pregnant sheep. The aim of this study was to link micro-structural changes in cervical tissue during induced ripening with cervical elasticity quantified using shear wave elastography. Understanding the mechanisms that take place in normal pregnancy will allow a better understanding of the cervical remodelling and lead to better methods of diagnosis of preterm birth and successful induction of labor. Unfortunately, having objectively defined time control over the cervical maturation may be difficult in humans. Animal models, in particular sheep, have been largely used for the exploration of mechanisms of cervical function and parturition [165]. Their size similar to humans enables the use of tools developed for humans, their physiology has been well explored and they enable accurate and easy control of the variables.

In this thesis, we propose an assessment of the evolution of cervical stiffness and its relationship with the micro-architecture of the tissue, during the artificially induced cervical maturation process, using pregnant sheep as a model. Section 7.1 exposes the study design and the experimental protocol. In Section 7.2, the cervical stiffness quantification using SWE is described. Section 7.3 presents the prostaglandin assay to confirm the induced cervical maturation. Section 7.4 describes the material and methods to asses the integrity of the tissue at the micro-scale. The histological analysis and two-photon excitation microscopy are presented in Subsections 7.4.1 and 7.4.2, respectively. Finally, Section 7.3 outlines the statistical analysis tools.

7.1 Animal model

The experiment was performed in accordance with the International Guiding Principles for Biomedical Research involving Animals as promulgated by the Society for the Study of Reproduction and in accordance with the European Convention on Animal experimentation. The local ethical committee (named: Comethea, registered under ethical committee N^o45 in the French national register) approved the experimental design, which was registered under N^o 00264.01).

The study was conducted on 9 pregnant ewes (Ile de France breed) maintained at the National Agricultural Research Institute (Institut National de la Recherche Agronomique, INRA) during spring of 2014. Their gestational age was 127 days (term = 145 days in sheep). Food and water were provided *ad libitum* throughout the experiment (24 hours). Animals were randomly allocated to one of two groups: dexamethasone (n = 5) or control group (n = 4). Each ewe received an ear-tag for permanent identification.

7.1.1 Induction of cervical ripening

The cervical ripening was induced by administrating 8 ml (2 mg) of dexamethasone (Dexadreson®, Intervet) intramuscularly to the animals that were in the induced group. Nothing was administered to induce the labour in the control group.

Parturition is believed to be initiated when adrenocorticotropic hormone (ACTH) from the fetal pituitary gland causes a release of cortisol from the fetal adrenal cortex. The fetal cortisol reduces placental progesterone production and increases placental estrogen production, resulting in release of prostaglandin F (PGF) from the uterus [166]. Consequently, uterine activity increases, the corpus luteum undergoes luteolysis, and parturition is initiated. Dexamethasone is a synthetic corticoid, which mimics fetal cortisol, and has been successfully used to induce parturition in sheep. It is a reliable and predictable method to induces lambing within 30 hours of injection [165–167].

7.2 Shear wave elastography

Figure 7.1 shows a schematic representation of the ultrasound examination on time. All animals were examined every 4 hours for 24 hours using ultrasound transvaginal examination.

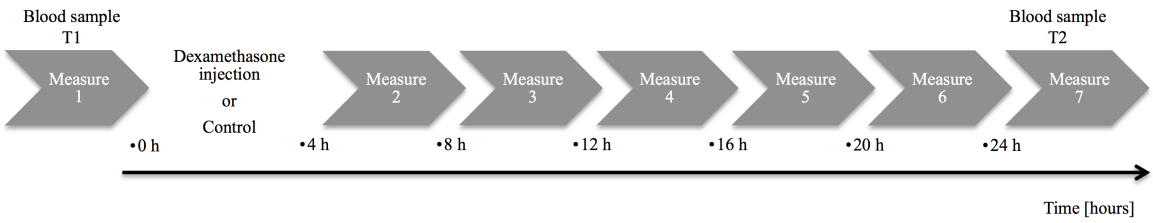

Figure 7.1: *Schematic representation of the ultrasound images acquisition on time.*

The animal was removed from the pen where all ewes were kept, and received a sedation, 1mg (0,2 mL) of acepromazine (Calmivet®, Vetoquinol) intravenously, to avoid any movement and to ensure the good quality of the images. Then, the animal was placed in dorsal recumbency on an artificial insemination table specially designed for use in small ruminants and providing elevation of the hindquarters (see Figure 7.2). Transvaginal ultrasound imaging of the cervix was performed on the animal after applying an ultrasound coupling gel to the probe to ensure good impedance matching and to facilitate the introduction of the probe through the vagina. SWE was performed using a 7-MHz conventional endocavitary ultrasonic probe (SE 12-3, Supersonic Imagine, Aix-en-Provence, France).

Figure 7.2: *In-vivo transvaginal examination of a pregnant sheep.*

7.2.1 Stiffness quantification

The cervical canal of the ewe is characterised by funnel-shaped rings ($N = 3 - 4$), which are not concentrically aligned [168]. The second ring of the cervix was selected to locate the ROI (see Figure 7.3). Based on the measurements of shear wave speed (SWS), the elasticity was quantified in a circular ROI of 5 mm diameter. The second ring was chosen for several reasons: first, because it is a reference point easy to identify in the B-mode image and thus it guarantees quantifying the elasticity always in the same area of the cervix; secondly, because it is close enough to the probe to ensure an efficient generation of the shear waves; and, finally, because it is far enough from both the fetal side and from the vaginal opening to avoid tissue compression from the fetus or from the operator which may artificially generate high stiffness values. The placement of the ROI within the elastographic image for the SWS and stiffness measurements was determined, using exclusively anatomical criteria, on the conventional B-mode image. This allowed an objective and reproducible positioning of the ROI for velocity and stiffness quantification.

For each animal and each measurement SWE was performed by two expert veterinarians. These data were used to determine the inter-observer reproducibility. Both operators were trained to perform the SWE measurement in a standardised pattern and the whole examination did not last more than 5 minutes for each operator. The thermal and mechanical

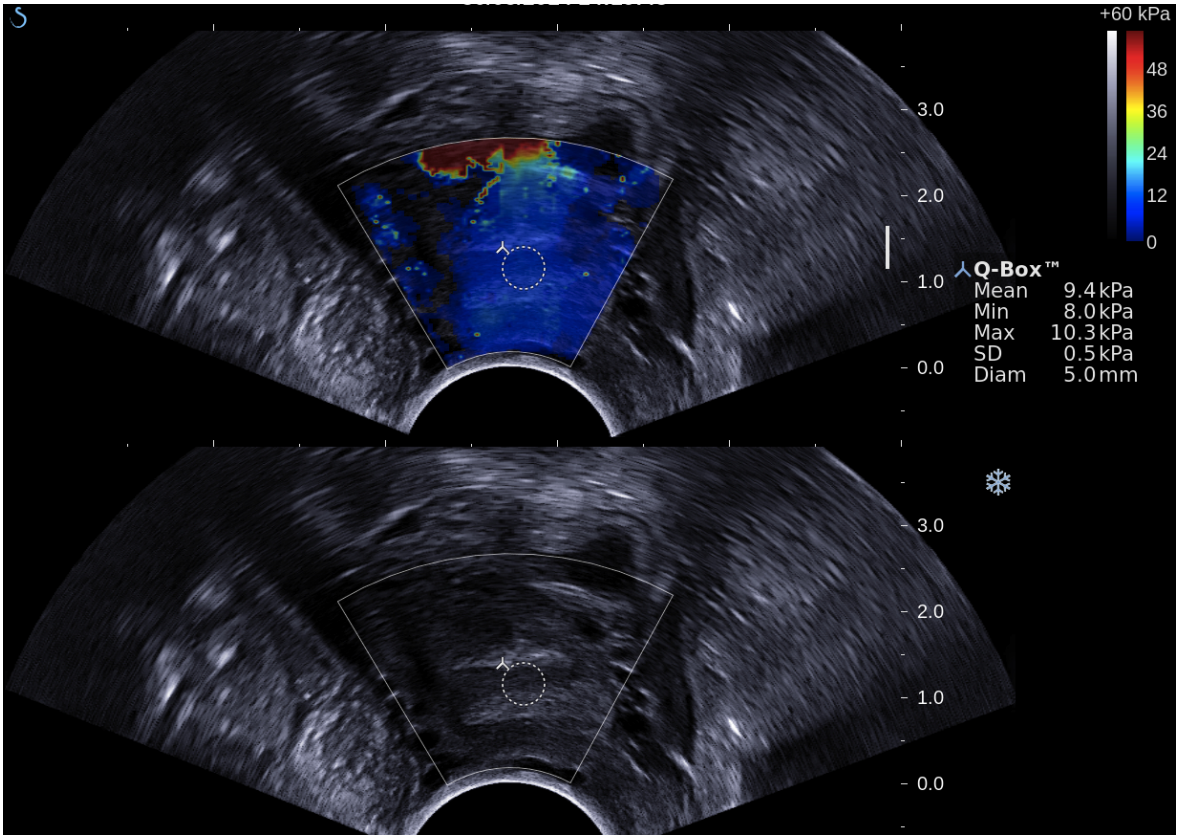

Figure 7.3: *Example of a ROI (white circle) of 5 mm diameter positioned in elastographic image following only anatomical criteria on the conventional B-mode image. The ROI was placed on the second ring of the collagen rings that characterise the sheep cervix.*

index were kept below FDA (Food and Drugs Administration) thresholds. To estimate the intra-observer reproducibility, each practitioner acquired three elastographic images, repositioning the probe every time. The stiffness, calculated in the ROI, and error bars were obtained with the mean and standard deviation of these values, respectively.

7.3 Confirmation of cervical maturation: Prostaglandin Assay

Cervical ripening induced by dexamethasone was confirmed by the significant increase in maternal plasma Prostaglandin E2 (PGE2), as evidenced by the assay of its metabolite PGEM (Prostaglandin E metabolite). Just before birth, the final remodelling of the cervix is driven through the secretion of prostaglandins by the fetoplacental unit. Prostaglandins (PGs) are derived from arachidonic acid and consist of two main families, i.e., PGE and PGF. Upon the increased secretion of cortisol by the fetal adrenals, prostaglandin synthase (PGHS)-2 gene expression in the placenta is up-regulated, resulting in increased production of PGs [169]. In particular, in the cervical region, there is an increased production of PGE2 and subsequent matrix remodelling [169].

The normal parturition process is triggered by the rise in fetal cortisol mimicked here by the injection of dexamethasone to the ewe. This rise is associated with the increased

placental and endometrial activity of the enzyme prostaglandin H2 synthase (PGHS), which closely correlates with the increase in fetal and maternal plasma prostaglandins [169]. PGs are involved in the induction of labour and among the active compounds, PGE2 is known to induce cervical relaxation [170].

For all animals, blood was collected from the jugular vein at the beginning of the experiment, just before the first sedation of the first SWE exam (sample T1), and at the end of the experiment, just before euthanasia (sample T2), as shown in Figure 7.1. Blood serum was stored frozen at -20^{o}C until assay. PGE2 and its metabolites in sheep serum were assayed via the measurement of plasma concentrations of the metabolite Prostaglandin EM (PGEM), using Cayman's Prostaglandin E Metabolite enzyme-immunoassay (EIA) Kit (Item No. 514531, Cayman chemical). In this test, PGE2 and its metabolites are converted to a single and stable derivative (PGEM) that can be easily quantified. PGE2 and PGEM intermediate metabolites from serum (0.5ml) were derived by addition of 0.150 ml of 1 mole/L carbonate buffer and incubated overnight at 37^{o}C. Then 0.200 ml of 1 mole/L phosphate buffer and 0.150 ml of EIA buffer were added to the sample. After acidification to pH 4.00 using 1 mole/L sodium citrate, samples were extracted twice using a mixture of cyclohexane and ethyl acetate (50:50 vol/vol). The organic phase was evaporated under a stream of nitrogen. Samples were then resuspended in the PGEM assay buffer provided in the kit. The PGEM EIA standard was derived following the same procedure. The EIA assay was performed following manufacturer instructions and the EIA plate was read at a wavelength of 410 nm using the EnSpire multimode plate reader (PerkinElmer).

7.4 Assessment of micro-structural remodelling

Histological analyses and two-photon excitation microscopy, combining both Second Harmonic Generation (SHG) and Two-photon Fluorescence microscopy (2PF) contrasts, were used to investigate the structure of cervical tissue at the microscopic scale. Control and dexamethasone animals were studied to assess the cervical remodelling, which is related to the ripening induced by dexamethasone.

Following the last examination, the ewes were humanely slaughtered by electrical stunning followed by exsanguination. Animals were unconscious prior to exsanguination. The uterus was opened, the fetus(es) was (were) immediately euthanised by intra-cardiac injection of a lethal dose of barbiturates (Dolethal®) and a portion of the genital tract including the cervix was collected and fixed in 30% formalin until being processed for histology and optical microscopy analysis.

7.4.1 Histology

A specialist veterinary pathologist identified the second ring structure in the cervix, and then following these medical recommendations, a 7 mm thick transversal section was taken in the cranial third part of the cervix, which grossly corresponds to the second ring. Samples were paraffin-embedded and 6 μm sections were realised for histological evaluation.

Sections were stained using a routine hematoxylin-eosin-saffron (HES). The microscopic evaluation was performed using a light microscope (Eclipse Ni-U, Nikon, Champigny, France[1]) combined with a digital camera (Spot idea camera, Diagnostic Instruments, Sterling Heights, USA[2]). Qualitative analyse of the tissue structures was performed comparing treated and control animals. Using low magnification (x 2), the external perimeter of the cervical mucosa and that of the endocervical lumen were measured on transversal sections. The intra-observer agreement was $> 95\%$ as tested by reproducing this measure 5 times on the same sample.

7.4.2 Second harmonic generation and two-photon fluorescence microscopy

Second Harmonic Generation and Two-photon Fluorescence microscopy are optical microscopy contrasts that are now widely used for label free imaging in tissues at the submicrometric scale. These two processes rely on the excitation of a tissue sample by a pulsed near infra red illumination, with considerable advantages in terms of penetration depth that can reach today up to a millimetre under pure optical excitation. Both types of nonlinear interactions occur in biological tissues without the addition of exogenous contrast agents.

SHG is a second order coherent process in which two lower energy photons are upconverted to exactly twice the incident frequency (half the wavelength) of an excitation laser. Biological SHG imaging was first reported in 1986, when Freund *et al.* [171] investigated the polarity of collagen fibres in rat tail tendon at a resolution of $\sim 50\mu m$. Since then, SHG microscopy has been an increasingly used imaging tool. Its high efficiency and specificity in imaging fibrillar type I collagen has been shown by several authors [171–173]. SHG microscopy has made possible sub-micrometric resolution imaging of complex molecular organisation over millimetre size regions of a tissue, relating for instance collagen morphology to cancer and pathology developments [174–178].

Under two-photon excitation at wavelengths in the range [760nm-950nm], 2PF originates autofluorescence from cell proteins (e.g. amino acids like tryptophan and tyrosine, riboflavins, nicotinamides), cell metabolic activity, but also from collagen and elastin. 2PF has been widely used for imaging cells and tissues [179, 180]. In particular for cervical tissue, is has been used for monitoring collagen re-structuration during pregnancy [89, 181] or for the screening and diagnosis of cervical pre-cancer [182]. As opposite to SHG, 2PF does not require any particular molecular organisation to occur. A major advantage of two-photon microscopy is the possibility to simultaneously combine both 2PF and SHG contrasts, making multi-contrast label-free morphological imaging possible in complex molecular structures. While today 2PF/SHG microscopy is widely exploited as a complementary technique to histological studies in the study of cancers developments and tissue diagnosis, there is however no report yet on the combination of both 2PF/SHG contrasts for the cervix optical imaging. In this work, we apply two-photon excitation microscopy, combining both

[1] http://www.nikon.com/products/instruments/lineup/bioscience/biological-microscopes.
[2] http://www.spotimaging.com.

SHG and 2PF contrasts, to investigate, at the microscopic scale, the integrity of cervix tissues in both control and treated animals.

Experimental setup

The two-photon microscope used for SHG and 2PF imaging is based on an inverted two-photon excitation fluorescence microscope. A Ti:Sapphire laser beam (wavelength 800 nm, pulse duration 150 fs, repetition rate 80 MHz) is directed to galvanometric scanning mirrors (6215H, Cambridge Technology), reflected on a dichroic mirror (770DC, Semrock) and then focused onto the sample by an objective lens (Plan Apo Lambda X 20, NA 0.75, Nikon). The obtained lateral optical resolution is about 460 nm. 2PF/SHG images are obtained by scanning the focused beam in the sample plane using galvanometric mirrors, with a typical dwell time of 50 μs per pixel. The fluorescence light is collected in the backward direction by the same objective lens, spectrally separated (488DC Semrock) and further filtered (2PF: HQ540/80M-2P, Chroma, SHG: 400/40 Semrock). The signals are recorded by analog photo-multipliers (M9110, Hamamatsu). Typical images are performed in 100 μm x 100 μm regions (300 x 300 pixels), stitched together into a final size of a few millimetres. A custom-made Matlab program is used for stitching reconstruction based on an image overlap of 10%.

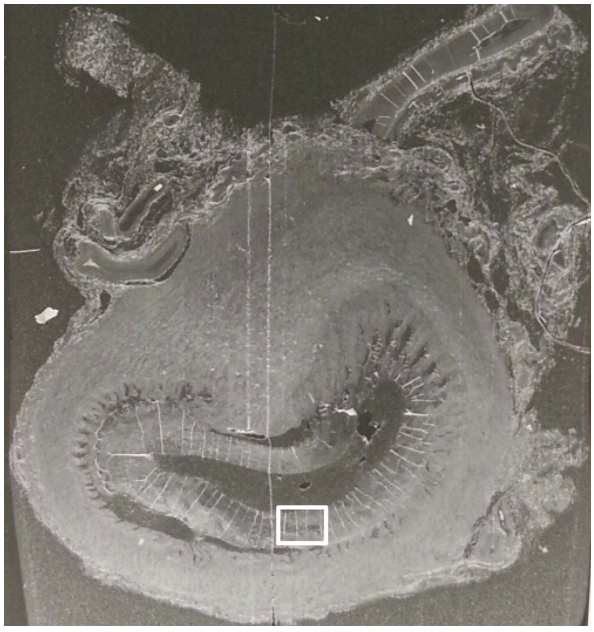

Figure 7.4: *Imaged cervical tissue. The scanned region is box-marked.*

Two-photon microscopy experiments were performed on 6 μm sections taken from the same samples as for histological examination and thus, they approximately correspond to the localisation of the second ring, where the SWE measurements were taken. A 0.17 mm coverslip was placed in order to ensure minimal aberrations in the images. The region of imaging was chosen to cover a size of about 2 mm (two different 2x2 mm^2 regions per animal were recorded), covering the mucosal chorion, mucous plug and submucosa. Figure 7.4 shows the scanned region in a cervix sample. Slices obtained for three different nulliparous

animals were investigated in the case of control and treatment by dexamethasone, while only one multiparous animal was investigated.

To evaluate the morphological changes observed in the SHG images from different animals and regions, in particular the variations in fibre directionality (waviness) in a SHG image, 2D Fourier transforms (FT) of ROIs of about 60 μm size images were investigated. The shape of the characteristic ellipse represented by the 2D FT of each ROI was evaluated using the Matlab® tool *regionprops*. This tool was implemented on a thresholded 2D FT (using an identical thresholding for all FT images), set at 80% of the maximal (center) value of the FT image. The ratio R between minor and major axes of the ellipse fitting of the resulting thresholded FT image was calculated based on the measured lengths (in pixels) of the axes of the ellipse that has the same normalized second central moments as the thresholded FT region.

7.5 Statistical analysis

Elastographic measurements were analysed using the F1 LD F1 model of the nparLD function to calculate an ANOVA-type statistic in order to compare the two groups (control and dexamethasone) globally and at each time point using a post-hoc Wilcoxon rank sum test with a Bonferroni-Hochberg correction [183]. Intra and inter-observer repeatability of measurements were assessed by Bland-Altman analysis [184]. The Bland-Altman plot of the average against the differences of the two measurements was performed and the 95% limits of agreement were calculated for each measurement to examine the agreement and bias between the same and the two different examiners for each measurement.

The results of the PGE2 essay were analysed with a Kruskal-Wallis non-parametric test [185]. For the 2D FT results of the SHG images, a statistical analysis was performed on 10 ROIs measured in two different animals per case (control and treated with dexamethasone), for two different regions (mucosal chorion and submucosa). One-way ANOVA tests (Levene's Test of Homogeneity of Variance, Tukey HSD paired comparison) were performed between the control/treated categories in both regions [185]. A similar statistical analysis was performed on the maximum intensity measured in each ROI image, taken as the average obtained between the 10 pixels of highest intensity in an image.

Statistical analyses were carried out using *R* software (www.r-project.org/, version i386 2.15.2). All results are expressed as median $\pm$ standard deviation. Data were considered statistically significant for $p < 0.05$. P-values below 0.0005 are indicated as $p < 0.000$.

8

Shear wave propagation in cervical tissue: A numerical analysis

To provide insight into the multi-scale problem and biochemical variables existing in the shear wave propagation through the complex structure of cervical tissue, a numerical approach is developed in this thesis. This chapter contains the first step of such a numerical strategy, where shear wave propagations are simulated through cervical tissue using the finite difference time domain technique (FDTD).

This chapter contains a brief description of the applied theory for two dimensional (2D) wave propagation in isotropic viscoelastic structures. The FDTD method and its numerical implementation are presented. Particular emphasis is given to the ability of modelling heterogeneous tissue, where the properties are allowed to vary as a piece-wise constant function at each discretization element.

8.1 Governing equations of the wave propagation motion

In this dissertation, the modelling was restricted to two dimensions for practical reasons. First, because a 3D model would have required a high computational cost. Secondly, because this work aims to present the first fundamental steps directed toward more realistic acoustic models of cervical tissue and a 2D model is able to reproduce them with lower effort than a 3D model. Finally, because theoretical developments may be easier to develop in a 2D framework.

The wave propagation in a 2D viscoelastic medium is described by the equilibrium, constitutive and compatibility equations. The formulation of the equilibrium equations is obtained by applying the linear momentum theorem for each direction of the two dimensional orthonormal basis [186]. This formulation is given in index notation as,

$$\rho u_{i,tt} + \gamma \rho u_{i,t} = f_i + \sigma_{ij,j} \tag{8.1}$$

where $i, j = x, y$ are the cartesian components of the particle displacement vector u_i and of the stress tensor σ_{ij}, f_i are the volume force densities, γ is the resistance coefficient related to the attenuation coefficient [187, 188] and ρ denotes the density of the medium in which the waves propagate. The viscoelastic behaviour or energy dissipation is introduced here by an attenuation term, which is the usual way in the FDTD literature [188, 189].

The relation between the stress and the strain tensors is established with the constitutive equations. The constitutive equations for a linear viscoelastic isotropic material with space dependency can be derived from the Newton's second law and the Hooke's law as follow [190],

$$\sigma_{ij,t} + \gamma \sigma_{ij} = \lambda(x, y)\delta_{ij}\varepsilon_{kk,t} + 2\mu(x, y)\varepsilon_{ij,t} \tag{8.2}$$

where δ_{ij} denotes the Kronecker symbol, ε_{ij}, with $i, j = x, y$, are the cartesian components of the strain tensor, $\varepsilon_{kk} = \varepsilon_{xx} + \varepsilon_{yy}$ is the dilatation (change in volume per unit volume) and $\lambda(x, y)$ and $\mu(x, y)$ are the space-dependent Lamé constants, which describe the behaviour of linear-elastic isotropic materials.
Finally, the kinematic relations establish a relation between the displacement field u_i and the strain vector ε_{ij} as,

$$\varepsilon_{ij} = \frac{1}{2}(u_{i,j} + u_{j,i}) \tag{8.3}$$

8.2 The finite difference time domain technique

Several applicable methods of computer simulation exist, FDTD, boundary elements (BEM), and finite elements (FEM) being the most common, each one with its advantages and limitations. All of them are based on converting the differential equation and boundary conditions into a system of linear equations, by means of the discretization of the whole domain (FDTD and FEM), or of only of its boundary (BEM). Among those, the FDTD method is perhaps the easiest one to implement. The main problem that appears in the simulation of wave propagation is the needed discretization. In order to obtain a good approach to the solution of wave equations, it is necessary to take at least ten discrete elements in each wavelength, which increases the size of the resulting equation system and consequently the computational time. Comparing to the standard FEM, the FDTD has less requirements of storage space and shorter computing time [191]. Finally, the FDTD technique has been widely used to model mechanical waves propagation through several kind of tissues, both hard and soft ones [187, 192].

The FDTD simulation technique is based on the linearized wave equations of continuity and motion written in the time-domain. The fundamental wave equations are discretized directly in their differential notation. Therefore, the spatial and temporal partial derivatives are replaced by central, finite differential quotients [193]. This leads to an explicit linear system of equations. One strong point of this discretization to our particular problem is that allows to model heterogeneous medium by defining the properties that characterise the wave propagation as a piece-wise constant function at each discretization element.

An advantage of using the FDTD simulation technique is that no physical approximations are made; indeed, propagation includes refraction, diffraction, and multiple reflections. Furthermore, the technique allows to simulate the propagation of elastic waves in heterogeneous structures for any geometry described on a regularly spaced cartesian grid. As a consequence, the FDTD simulations can be used both to show the interaction between shear waves and the hierarchical structure of connective tissues, and to study the mechanical properties of soft tissues. The understanding of the effect of cervical structure on an ultrasound signal would allow development of more robust elastographic imaging algorithms which account for the multi-scale nature of the tissue.

8.2.1 Discretization and derivative

Some transformations are applying to the wave equations before discretizing them. Equilibrium, constitutive and compatibility equations (8.1)-(8.3) can be rewritten in function of velocity, $v_i = \dfrac{\partial u_i}{\partial t}$, as,

$$\rho v_{i,t} + \gamma \rho v_i = f_i + \sigma_{ij,j} \tag{8.4}$$

$$\sigma_{ij,t} + \gamma \sigma_{ij} = \lambda(x,y)\delta_{ij}\varepsilon_{kk,t} + 2\mu(x,y)\varepsilon_{ij,t} \tag{8.5}$$

$$\varepsilon_{ij,t} = \frac{1}{2}(v_{i,j} + v_{j,i}) \tag{8.6}$$

The time derivative of the stress components can be expressed in function of the velocities by inserting the kinematic relation (8.6) into the constitutive equation (8.5). The wave motion is then completely described by a set of first-order differential equations,

$$\rho\frac{\partial v_x}{\partial t} + \gamma\rho v_x = f_x + \frac{\partial \sigma_{xx}}{\partial x} + \frac{\partial \sigma_{xy}}{\partial y} \tag{8.7}$$

$$\rho\frac{\partial v_y}{\partial t} + \gamma\rho v_y = f_y + \frac{\partial \sigma_{yx}}{\partial x} + \frac{\partial \sigma_{yy}}{\partial y} \tag{8.8}$$

$$\frac{\partial \sigma_{xx}}{\partial t} + \gamma\sigma_{xx} = (\lambda + 2\mu)\frac{\partial v_x}{\partial x} + \lambda\frac{\partial v_y}{\partial y} \tag{8.9}$$

$$\frac{\partial \sigma_{yy}}{\partial t} + \gamma\sigma_{yy} = (\lambda + 2\mu)\frac{\partial v_y}{\partial y} + \lambda\frac{\partial v_x}{\partial x} \tag{8.10}$$

$$\frac{\partial \sigma_{xy}}{\partial t} + \gamma\sigma_{xy} = \mu\left(\frac{\partial v_x}{\partial y} + \frac{\partial v_y}{\partial x}\right) \tag{8.11}$$

These equations are solved with a finite-difference scheme implemented on a *staggered grid stencil* [193, 194], where velocity and strain/stress variables are defined at alternating positions and times shifted by a half-step in space and time. This configuration is shown in Figure 8.1. One of the attractive features of the staggered-grid approach is that the various difference operators are all naturally centred at the same point in space and time. Thus, the system is not only staggered on a spatial grid but also temporally, so that the velocities are updated independently from the stresses. This allows a very efficient and concise implementation scheme [195].

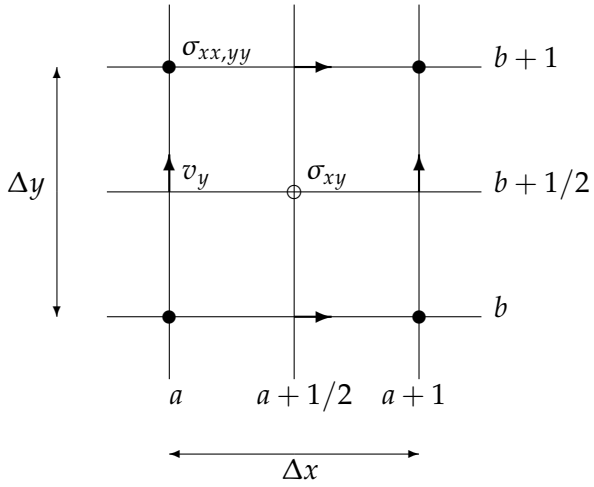

Figure 8.1: *The 2D FDTD grid. The field components are not known at the same location, but offset by a half-step in space and time.*

As shown in Figure 8.1, introducing the finite differences in space, Δx and Δy, and in time, Δt, the wavefield components can be defined as follows in a staggered FDTD grid [193],

$$v_x^{n+1/2}(i,j) = v_x\left[i\Delta x, \left(j+\frac{1}{2}\right)\Delta y; \left(n+\frac{1}{2}\right)\Delta t\right] \tag{8.12}$$

$$v_y^{n+1/2}(i,j) = v_y\left[\left(i+\frac{1}{2}\right)\Delta x, j\Delta y; \left(n+\frac{1}{2}\right)\Delta t\right] \tag{8.13}$$

$$\sigma_{xx}^{n}(i,j) = \sigma_{xx}\left[\left(i+\frac{1}{2}\right)\Delta x, \left(j+\frac{1}{2}\right)\Delta y; n\Delta t\right] \tag{8.14}$$

$$\sigma_{yy}^{n}(i,j) = \sigma_{yy}\left[\left(i+\frac{1}{2}\right)\Delta x, \left(j+\frac{1}{2}\right)\Delta y; n\Delta t\right] \tag{8.15}$$

$$\sigma_{xy}^{n}(i,j) = \sigma_{xy}\left[i\Delta x, j\Delta y; n\Delta t\right] \tag{8.16}$$

With this *staggered grid*, partial differential equations (8.7)-(8.11) can be discretized using centred finite-difference. In each equation, the derivatives are replaced by a difference quotient

of the values of the independent variables at the discrete grid points of the domain,

$$
\begin{aligned}
v^{n+1/2}_{x[a,b+1/2]} &= e^{-\gamma\Delta t} v^{n-1/2}_{x[a,b+1/2]} + \frac{\Delta t}{\rho} f^{n}_{x[a,b+1/2]} \\
&+ e^{-\frac{\gamma\Delta t}{2}} \frac{\Delta t}{\rho\Delta x} \left[\sigma^{n}_{xx[a+1/2,b+1/2]} - \sigma^{n}_{xx[a-1/2,b+1/2]}\right] \\
&+ e^{-\frac{\gamma\Delta t}{2}} \frac{\Delta t}{\rho\Delta y} \left[\sigma^{n}_{xy[a,b+1]} - \sigma^{n}_{xy[a,b]}\right] \qquad (8.17) \\
v^{n+1/2}_{y[a+1/2,b]} &= e^{-\gamma\Delta t} v^{n-1/2}_{y[a+1/2,b]} + \frac{\Delta t}{\rho} f^{n}_{y[a+1/2,b]} \\
&+ e^{-\frac{\gamma\Delta t}{2}} \frac{\Delta t}{\rho\Delta x} \left[\sigma^{n}_{xy[a+1,b]} - \sigma^{n}_{xy[a,b]}\right] \\
&+ e^{-\frac{\gamma\Delta t}{2}} \frac{\Delta t}{\rho\Delta y} \left[\sigma^{n}_{yy[a+1/2,b+1/2]} - \sigma^{n}_{yy[a+1/2,b-1/2]}\right] \qquad (8.18) \\
\sigma^{n}_{xx[a+1/2,b+1/2]} &= e^{-\gamma\Delta t} \sigma^{n-1}_{xx[a+1/2,b+1/2]} \\
&+ e^{-\frac{\gamma\Delta t}{2}} \frac{(\lambda_{[a+1/2,b+1/2]} + 2\mu_{[a+1/2,b+1/2]})\Delta t}{\Delta x} \left[v^{n-1/2}_{x[a+1,b+1/2]} - v^{n-1/2}_{x[a,b+1/2]}\right] \\
&+ e^{-\frac{\gamma\Delta t}{2}} \frac{\lambda_{[a+1/2,b+1/2]}\Delta t}{\Delta y} \left[v^{n-1/2}_{y[a+1/2,b+1]} - v^{n-1/2}_{y[a+1/2,b]}\right] \qquad (8.19) \\
\sigma^{n}_{yy[a+1/2,b+1/2]} &= e^{-\gamma\Delta t} \sigma^{n-1}_{yy[a+1/2,b+1/2]} \\
&+ e^{-\frac{\gamma\Delta t}{2}} \frac{(\lambda_{[a+1/2,b+1/2]} + 2\mu_{[a+1/2,b+1/2]})\Delta t}{\Delta y} \left[v^{n-1/2}_{y[a+1/2,b+1]} - v^{n-1/2}_{y[a+1/2,b]}\right] \\
&+ e^{-\frac{\gamma\Delta t}{2}} \frac{\lambda_{[a+1/2,b+1/2]}\Delta t}{\Delta x} \left[v^{n-1/2}_{x[a+1,b+1/2]} - v^{n-1/2}_{x[a,b+1/2]}\right] \qquad (8.20) \\
\sigma^{n}_{xy[a,b]} &= e^{-\gamma\Delta t} \sigma^{n-1}_{yy[a,b]} \\
&+ e^{-\frac{\gamma\Delta t}{2}} \frac{\mu_{[a,b]}\Delta t}{\Delta y} \left[v^{n-1/2}_{x[a,b+1/2]} - v^{n-1/2}_{x[a,b-1/2]}\right] \\
&+ e^{-\frac{\gamma\Delta t}{2}} \frac{\mu_{[a,b]}\Delta t}{\Delta x} \left[v^{n-1/2}_{y[a+1/2,b]} - v^{n-1/2}_{y[a-1/2,b]}\right] \qquad (8.21)
\end{aligned}
$$

where the damping or resistance coefficient term was modelled as an exponential function $e^{\frac{\gamma dt}{2}}$. These equations represent the numerical value of the corresponding field component at a discrete location in space and time. For example, $v^{n+1}_{x[a,b]}$ stands for the numerical value of the particle velocity v_x at $(x, y) = (a\Delta x, b\Delta y)$ at time $t = (n + 1)\Delta t$.

8.2.2 Boundary conditions

Absorbing boundary conditions (ABC) were used at the borders of the computational grid in order to prevent reflections from the boundaries, and so the grid appears to be unbounded [196]. To minimise artificial reflections from the edges of the computational domain we use a damping expression. An increasing damping term is introduced in the N-elements size boundary around the field of interest. An optimal trade-off between energy absorption of the absorbing layer and problem size was found for an absorbing layer of 30 elements.

The advantages of these boundary conditions are, first, that they absorb energy over a wide range of incident angles, and, second, that they are computationally inexpensive and very simple to implement.

8.2.3 Stability conditions

Possible reasons for numerical errors can be separated into phase and amplitude errors [194]. The first group of errors, which may also be viewed as frequency-dependent velocity errors, is called numerical dispersion and is related to the spatial discretization. The numerical dispersion cannot be completely excluded but can be reduced to an acceptable level by decreasing the lateral step sizes. To prevent these spatial aliasing errors, the shortest wave length of the propagation modes should be sampled at least eight times in order to keep the numerical dispersion at a reasonably low level [197]. This leads to the following criterium for a 2D staggered grid with identical element sizes $\Delta x = \Delta y$,

$$\Delta x \leq \frac{\sqrt{2}}{16} \frac{c_{min}}{f_{max}} \tag{8.22}$$

where c_{min} is the minimum wave velocity and f_{max} the maximum frequency of the propagation modes.

The second group of errors are the amplitude errors. In numerical simulations, if the time step Δt is too large compared to the element size Δx, Δy, it is possible that the calculated amplitude increases exponentially with every time step. In this case, the scheme is said to be unstable. The critical value is the maximum size of the time step Δt. Here, the stability is achieved by the *Courant* condition [194],

$$\Delta t \leq \frac{\Delta x}{\sqrt{2} c_{max}} \tag{8.23}$$

where c_{max} denotes the maximum wave velocity.

9 Modelling the cervical tissue

In this chapter, we propose a spatial model to describe the cervical tissue and feed the FDTD numerical model described in the previous chapter. During the gestation and the cervical remodelling, several changes occur progressively in the structure of the tissue. The proposed model is aimed to quantitatively describe these histological changes, and finally, along with the FDTD model, provide a link to the ultrasonic mechanical properties of cervical tissue. Three different groups of characteristics, independently tunable, describe such a model: morphology at micro-scale, composition and mechanics. They will be described in detail in the following sections.

9.1 Mesoscale morphology model

The central role of collagen in cervical tissue has motivated the development of the spatial model proposed in the present work. The developed synthetic spatial medium is aimed to capture the geometric and morphological features of the collagen, which are primarily responsible for the mechanical behaviour of the cervix. The cervical stroma is modelled as a fibre-reinforced material, made of collagenous fibres surrounded by a matrix. The matrix material is idealised as a hydrogel, i.e. a solution of the different components of the cervical stroma (cells, GAGs and elastin) in water. The geometry of the simulation domain is defined using a 2D regular mapping of the mechanical properties of the considered media: (i) matrix and (ii) collagen fibres.

At non pregnant stage and at early pregnancy, the cervix has three preferred orientated collagen zones of collagen fibrils with gradual transition between them [55–57]. The innermost and outermost zones of the stroma contain collagen fibrils preferentially aligned in the

longitudinal direction, that is parallel to the cervical canal. In the middle zone the fibrils have a preferred orientation in the circumferential direction, i.e. surrounding the cervical inner canal. These preferentially aligned fibres are responsible for the typical anisotropic behaviour of the tissue, and they provide strength both longitudinally and circumferentially with respect to the cervical canal [55]. In this thesis, we propose three 2-D spatial media, as a simplification of the tissue, to model the different zones that characterise the collagen network of cervical tissue [55–57]. We distinguish between longitudinal and transverse profiles, depending on how the collagen fibres are organised within the cervical tissue architecture. In the transverse profile collagen fibres are represented as its cross-section by non-overlapping and randomly distributed circular scatterers. In contrast, in the longitudinal profiles fibres are represented by their longitudinal section. Depending on how the fibres are aligned with respect to the shear waves propagation direction, we propose two longitudinal profiles: longitudinal profile with fibres parallel to the propagation direction ($\phi = 0^o$), and longitudinal profile with fibres perpendicular to the shear waves propagation direction ($\phi = 90^o$). The symbol ϕ represents the angle between fibres and wave propagation direction. Figure 9.1 shows an example of the three synthetic spatial media.

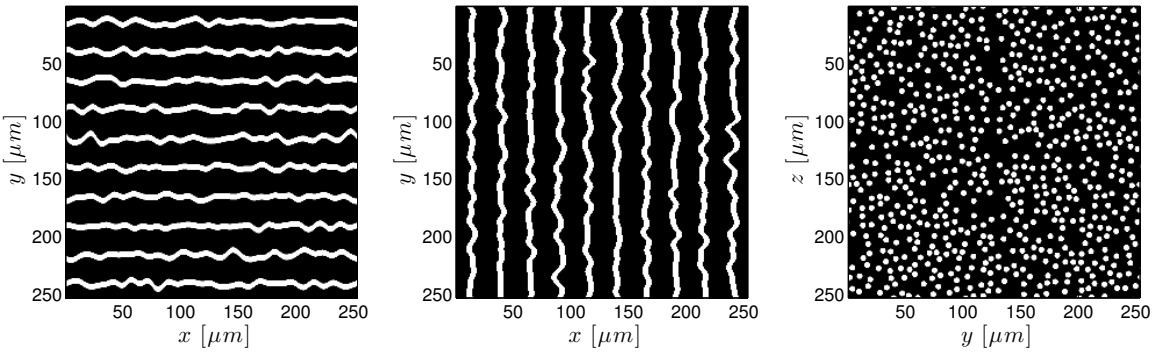

Figure 9.1: *Models used in FDTD simulations: longitudinal section with collagen fibres parallel to shear waves propagation direction ($\phi = 0^o$), longitudinal section with collagen fibres perpendicular to shear waves propagation direction ($\phi = 90^o$) and a transverse section where the collagen fibres are represented as circles in the cross-section. In this example the media consist of a 20% fibre fraction surrounded by a matrix, the fibre thickness is 5 μm, and the standard deviation that characterises the waviness is 15 μm.*

The dimensions of the spatial media were fixed to 250 x 250 μm. This size is large enough to capture the micro-scale architecture of collagen network and also, it allows to keep the computational cost at an acceptable level. The modelling of the fibre morphology and the composition of the ECM are described in the following sections.

9.1.1 Description of fibre waviness

Several studies have demonstrated the collagen influence in the mechanics of soft tissues [1, 61]. Significant effort has been made in determining its mechanical properties at all levels, ranging from single fibres at the nanoscale [198, 199] to a structural element within

a (macroscopic) biological tissue [200, 201]. The main difference between existing microstructural models for crimped collagen fibrils is the assumption of the wave shape at the fibrillar level. While one class of models assumes a predefined planar shape of crimped collagen fibrils like sinusoidal or circular wave forms [202–204], another group is based on statistical distributions of the crimp shape or crimp behaviour of collagen fibrils [205–207].

In this work, a statistical distribution of the fibre waviness is assumed, following the model proposed by Cacho *et al.* [205]. Longitudinal profiles were generated with a randomised algorithm in Matlab®, where the crimped morphology of collagen fibres is described by a Beta distribution characterised by two shape parameters. The election of the distribution function was based on previous numerical tests performed by Elbischger *et al.* [205, 208], which suggest that the probability of the fibre waviness can be satisfactorily approximated by a Beta function. The input values for the algorithm include the size of the profile, collagen fibre thickness, desired values of fibre fraction and the standard deviation that characterises the waviness.

The random crimp of collagen fibres has been described in a previous work by Cacho *et al.* [205]. Let be a set of randomly generated data in an interval of length L_0 on the X-axis such that at any point x within that interval the associated coordinates y and z are independent and normally distributed random variables with zero mean. Under this condition the data generated can be regarded as white Gaussian noise, and characterised by the variance σ^2. As a simplification, it is assumed that the fibre undulates with equal characteristics in all directions orthogonal to the X-axis (i.e. the variances in the Y- and Z-directions are equal).

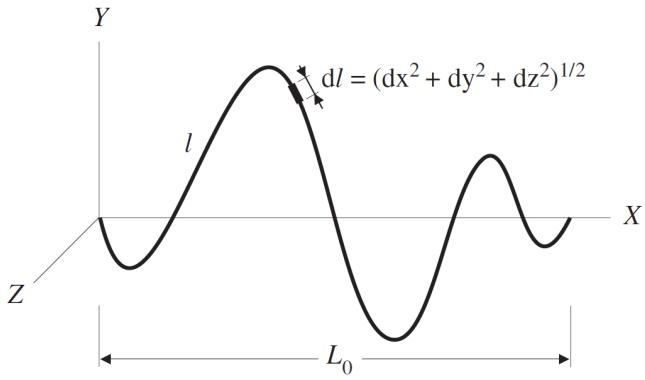

Figure 9.2: *Schematic representation of a single fibre*[1].

The infinitesimal arc-length of the fibre dl is (see figure 9.2):

$$dl = (dx^2 + dy^2 + dz^2)^{1/2} \tag{9.1}$$

It is possible to write $d = dy/dx = dz/dx$, where d is a zero mean, normally distributed random variable whose variance σ_d^2 can be directly related to σ^2. Therefore, it follows that

$$dl = \sqrt{2d^2 + 1}\, dx = \ell\, dx \tag{9.2}$$

[1]Reproduced from Cacho *et al.* [205].

where ℓ is a random variable, which is neither zero mean nor normally distributed.

It is possible to derive the probability density function (PDF) of the variable ℓ. Let us define now $r = 2d^2$, which is a random variable whose distribution is χ^2 with σ_d, and thus,

$$\mathscr{P}(r) = \frac{1}{2\sigma_d^2} e^{\left(-\frac{r}{2\sigma_d^2}\right)},\ r \in [0, \infty) \tag{9.3}$$

From the definitions of ℓ and r it follows that $r = \ell^2 - 1$. Now for $\ell \geq 1$ we may derive the PDF, and from (9.3) we find that,

$$\mathscr{P}(\ell) = \mathscr{P}[r(\ell)] \left|\frac{\partial r(\ell)}{\partial \ell}\right| = \frac{1}{2\sigma_d^2} e^{-\frac{\ell^2-1}{2\sigma_d^2}} |2\ell| \tag{9.4}$$

Therefore, ℓ is always a positive variable and its PDF is,

$$\mathscr{P} = \frac{\ell}{\sigma_d^2} e^{-\frac{\ell^2-1}{2\sigma_d^2}},\ \ell \geq 1 \tag{9.5}$$

Relation (9.1) describes the arc-length at infinitesimal scale within a single fibre. However, it is necessary to establish Equation (9.1) at the fibre level, i.e.,

$$l = \int_{x=0}^{L_0} \ell\, dx \approx \overline{\ell} L_0 \tag{9.6}$$

where $\overline{\ell}$ is a fibre-specific quantity that denotes the mean or expected value of ℓ:

$$\overline{\ell} = \int_{\ell=1}^{\infty} \ell \frac{\ell}{\sigma_d^2} \exp\left(-\frac{\ell^2-1}{2\sigma_d^2}\right) d\ell \tag{9.7}$$

Using the variable change $t = \ell^2/(2\sigma_d^2)$, and applying the incomplete Gamma function ($\Gamma(\alpha, x) = \int_x^\infty t^{\alpha-1} e^{-t} dt$), the mean value can be obtained as,

$$\begin{aligned}
\overline{\ell} &= \int_{\ell=1}^{\infty} \frac{\ell^2}{\sigma_d^2} \exp\left(-\frac{\ell^2-1}{2\sigma_d^2}\right) d\ell \\
&= \sigma_d \sqrt{2\exp(1/\sigma_d^2)} \int_{t=1/(2\sigma_d^2)}^{\infty} t^{1/2} \exp(-t) dt \\
&= \sqrt{2\sigma_d^2 \exp(1/\sigma_d^2)}\, \Gamma\left(\frac{3}{2}, \frac{1}{2\sigma_d^2}\right)
\end{aligned} \tag{9.8}$$

At this point it is important to note that the PDF $\mathscr{P}$ and the mean $\overline{\ell}$ depend only on the variance σ_d^2, which is a (measurable) quantity that can be obtained from the fibre morphology typically observed in micrographs. This quantity is determined by the frequency content of the fibre. This opens the question about the range that should cover sigma σ_d^2, considering that the higher its value, the larger the fibre waviness. A comparison of computer-generated curves with typical fibres, based on images taken through a microscope of the cervical tissue

[209], motivates a restriction of the values of the standard deviation that characterises the waviness to the interval (0, 45).

Numerical tests suggest that $\mathscr{P}(\bar{\ell})$ can be satisfactorily approximated by the Beta function, β, characterised by two shape parameters, a and b,

$$\beta(a,b) = \frac{\Gamma(a)\Gamma(b)}{\Gamma(a+b)} \tag{9.9}$$

where Γ denotes the Gamma function. At this point it is important to note that the PDF and the mean depend only on the variance [210]. Therefore, only the standard deviation is needed to define the waviness.

9.2 Constitutive mixture-theory-based model

During the cervical maturation, the balance of the main constituents of the cervical stroma is continually changing. These composition changes involve the tissue remodelling. In the third trimester of pregnancy water approximately increases 5%, cervical cells raise from 5% to 15%, while GAGs concentration drops 50% and the collagen concentration decreases 30%. The ECM composition at early and at term in pregnancy is summarised in Table 9.1. For more details, see Section 3.2 where the cervical remodelling has been described.

Constituents	*at early* [%]	*at term* [%]
Interstitial fluid (water)	80	$\uparrow$ 85
Dry tissue	20	$\sim$
Collagen	80	$\downarrow$ 30 concentration $\sim$ weight
Elastin	2.5	$\sim$
GAGs	0.2	$\downarrow$ 50 concentration
Cells	5	$\uparrow$ 15

Table 9.1: *Composition of the cervical ECM during gestation. The dry tissue component values are giving in % per dry weight [1–3]. Trends are indicated by: $\uparrow$ (increment), $\downarrow$ (drop) and $\sim$ (no variability).*

The effective mechanical properties inside a pixel are computed from the constituent concentrations ζ_i (%) and mechanical properties (λ_i, μ_i, γ_i, ρ_i), following mixture theory,

$$(\lambda, \mu, \gamma, \rho) = \sum \zeta_i (\lambda_i, \mu_i, \gamma_i, \rho_i) \tag{9.10}$$

Constituent concentrations used in the model are summarised in Table 9.1. The material properties used to simulate the different constituents of the ECM were chosen according to the literature [60, 211–213], and correspond to a realistic range for cervical tissue (see Table 9.2). The considered density values were $\rho = 1000$ kg/m^3 and 1200 kg/m^3, for the matrix and fibre fraction, respectively. The value of the γ resistance coefficient that defines attenuation or the energy loss was set to $\gamma = 940$ s^{-1} in all simulations.

Constituents	*Lamé's first parameter* λ [kPa]	*Lamé's second parameter* μ [kPa]	*References*
Interstitial fluid	$2.2 \cdot 10^6$	5	[212, 214]
Collagen	$1.73 \cdot 10^5$	$7.4 \cdot 10^4$	[60, 215]
Elastin	1300	555	[211]
GAGs	173	74	[213, 216]
Cells	57	14	[216, 217]

Table 9.2: *Mechanical properties values used to simulate the constituents of ECM. These values are used to estimate the mechanical properties by mixture theory that characterise the matrix and the fibre materials in the spatial media.*

9.3 Simulation of the cervical remodelling

In the cervical model, the main histological changes that happen during the cervical remodelling are grouped in three categories: mechanics, morphology and composition. All them can be independently simulated and analysed.

The analysed morphological parameters are related to the collagen fibres. Changes in waviness, thickness and gap between fibres have been simulated. The range of the values used in the simulations are summarised in Table 9.3. Figures 9.3 and 9.4 show the spatial media corresponding to the limit values, i.e. maximum and minimum values of each morphological parameter.

Mechanics [kPa]	*Morphology* [μm]	*Composition* [%]
λ_{matrix}: $(1.65 - 1.76) \cdot 10^6$	waviness: $(5 - 45)$	hydration: $(80 - 85)$
μ_{matrix}: $(7.15 - 7.8)$	diameter: $(3 - 10)$	fibrillar collagen: $(15 - 20)$
λ_{fibres}: $(1.21 - 1.73) \cdot 10^5$	gap: $(1 - 4)$	GAG's: $(0.2 - 1.5)$
μ_{fibres}: $(5.2 - 7.7) \cdot 10^4$		cells: $(8 - 15)$
		elastin: 2.5

Table 9.3: *Ranges of the values of the different parameters, grouped into mechanics, morphology and composition, used in the FDTD simulations. Percentages are given with respect to dry tissue, except hydration and fibrillar collagen that refer to total tissue.*

Each constituent of the ECM is considered individually in the mixture theory-based model. Therefore, the compositional changes have been simulated decreasing or increasing each concentration as shown in Table 9.3. Consequently mechanical properties of the matrix and fibre materials are modified too. Column called mechanics in Table 9.3 shows the range of the mechanical values used to simulate the matrix and the fibre phases in the spatial media.

It is worth noting that, geometry and material properties are independently tuneable, which enables a deep understanding of their specific individual effects. To study the morphological parameters, the remaining parameters, i.e. mechanical properties and composition, are kept constant and set to the values corresponding to early pregnancy. In the same way, the morphology parameters do not vary when the composition and the mechanics are studied.

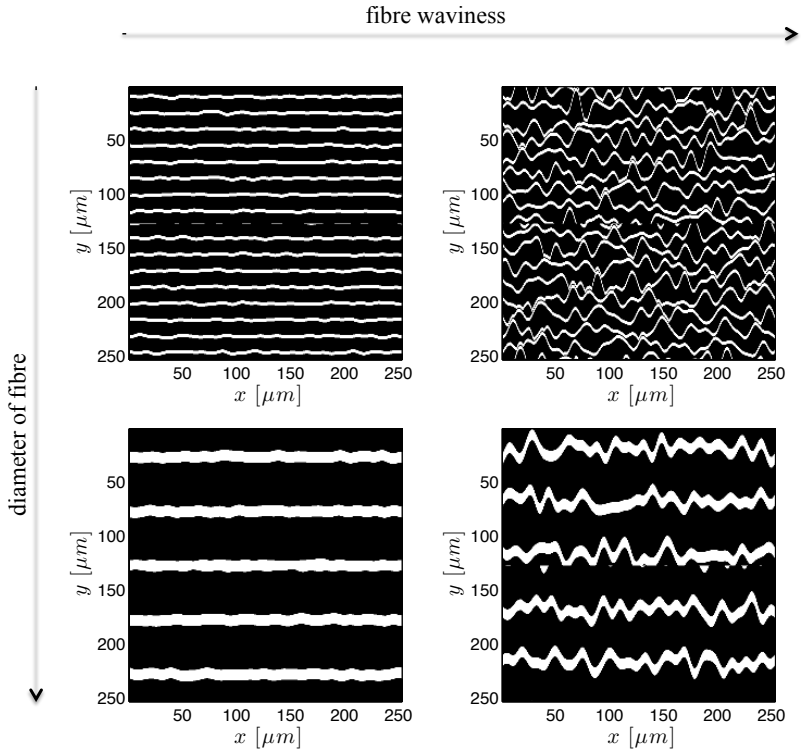

Figure 9.3: *Longitudinal profiles with different morphological parameter values. In this example fibre fraction in the spatial media amounts to 20%. The standard deviation which characterises the waviness ranges from 5 μm to 45 μm; and the diameter of fibre ranges from 3 μm to 10 μm.*

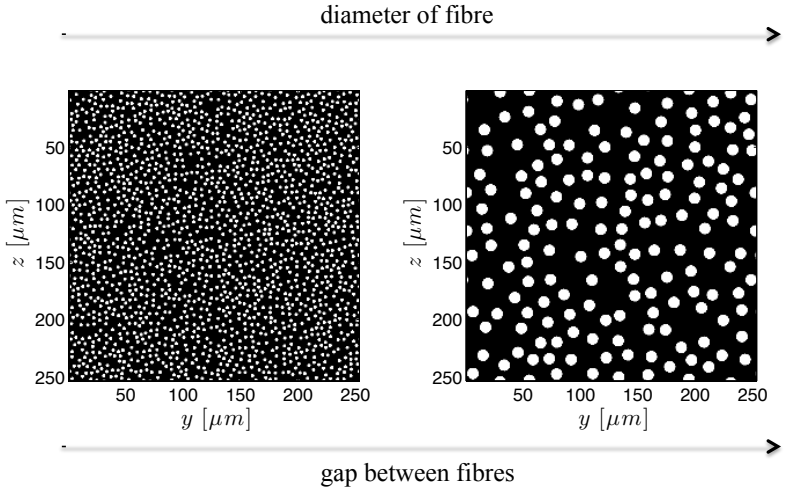

Figure 9.4: *Transversal profiles with different morphological parameter values. In this example fibre fraction in the spatial media amounts to 20%. The diameter of fibre ranges from 3 μm to 10 μm; and the gap between fibres ranges from 1 μm to 4 μm.*

The flowchart of the spatial medium generation by applying the algorithms described in this chapter is depicted in Figure 9.5.

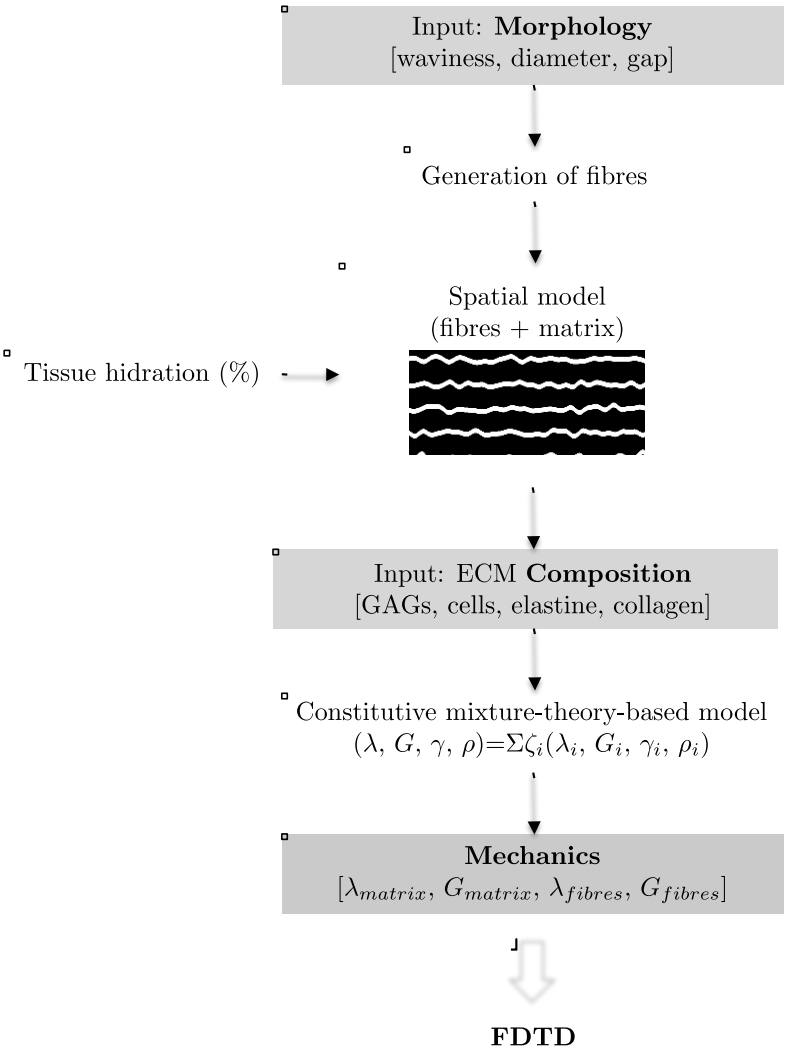

Figure 9.5: *Flowchart of the spatial medium generation and the estimation of its mechanical properties for the FDTD model.*

10

Describing the cervical viscoelasticity

This chapter presents the methods to explore the possibility of quantifying both cervical elasticity and viscosity from shear wave velocity. Section 10.1 describes the algorithm to estimate the shear wave velocity from the FDTD simulations. Then, the viscoelastic parameters can be estimated from the derived dispersion curves. The rheological laws chosen to model the cervical viscoelasticity are exposed in Section 10.2. Finally, Section 10.3 provides the theoretical background for the inverse problem used for first, fitting the phase velocity to the rheological models to estimate both elasticity and viscosity; and second for determining the rheological model, between the three proposed, that best describes the cervical tissue.

10.1 Estimation of the shear wave velocity dispersion curve

From the simulated propagation movie, it is possible to extract the shear wave velocity dispersion curve by a phase difference algorithm, as is depicted in Figure 10.1. From the displacement movie obtained from the FDTD simulation, a first step consists of averaging the tissue velocity field along the height y of the spatial medium. Averaging is a linear operation, which thus does not modify the phase velocity; only amplitude and initial phase are modified. The 3D tissue velocity field $v(x, y, t)$ now turns into a 2D tissue velocity field $v(x, t)$ that fully describes the propagation of the plane wave in the medium along the direction x.

A Fourier transformation of the tissue velocity field $v(x, t)$ in the time domain allows the computation of the phase $\varphi(x, \omega)$ and amplitude $A(x, \omega)$ of the wave at each frequency. For a monochromatic plane wave propagating in the direction x, the phase can be written

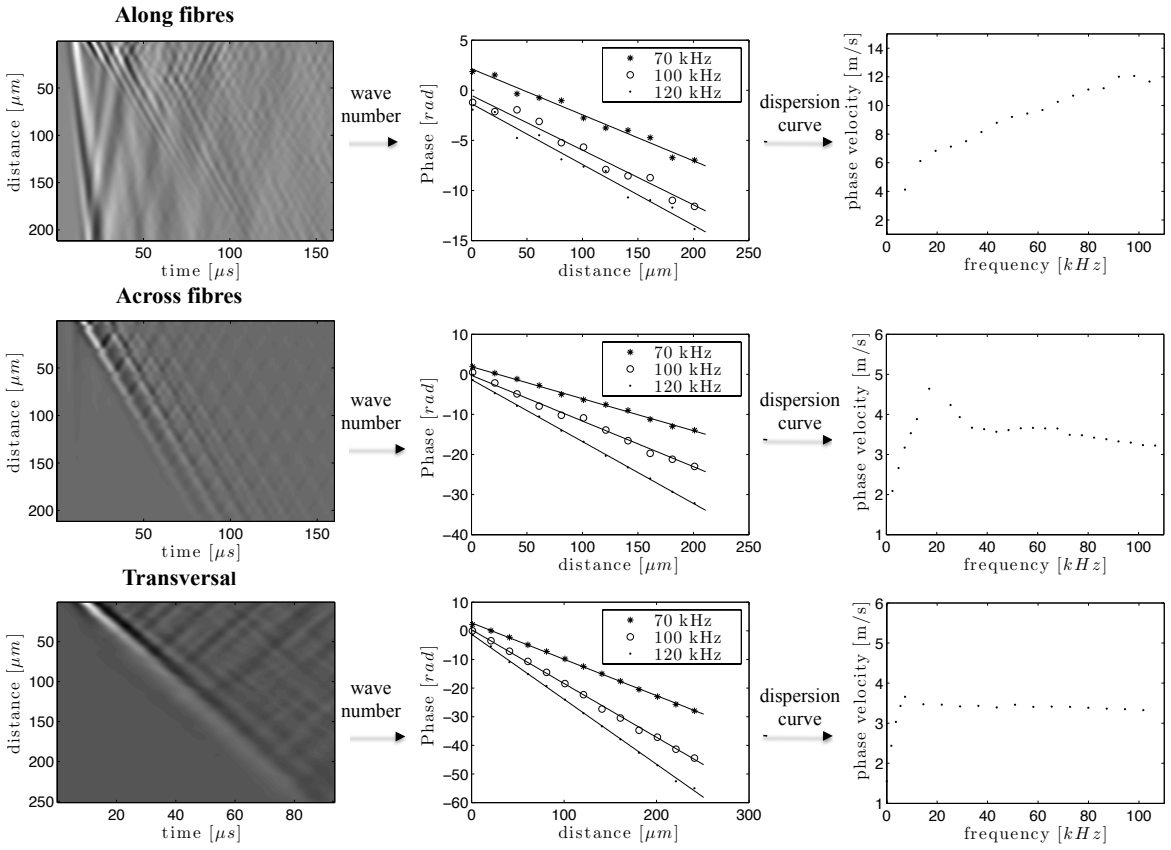

Figure 10.1: *Example of the shear wave dispersion analysis in the spatial media for an excitation frequency of 100 kHz.*

as, $\varphi(x,\omega) = -Re[k(\omega)]x$, where $k(\omega)$ is the complex wave number [218]. Thus, the shear wave phase velocity in this case is,

$$c_s = \omega / Re[k(\omega)] \tag{10.1}$$

where the real part $Re[k(\omega)]$ of the wave number can be estimated from a linear fit of the phase function $\varphi(x,\omega)$ along the propagation distance x [218, 219].

Dispersion curves are plots of shear wave speed (SWS) as a function of angular frequency ω. For mass density ρ, the relationship between SWS and the complex shear modulus is well known to be [220],

$$c_s(\omega) = \frac{\omega}{Re[k(\omega)]} = \sqrt{\frac{2(G'^2 + G''^2)}{\rho\left(G' + \sqrt{G'^2 + G''^2}\right)}} \tag{10.2}$$

where the complex shear modulus $G^* = G' + jG''$ is composed of a shear storage modulus G' and a shear loss modulus G''. The complex modulus can be related to elasticity, μ, and viscosity, η, using rheological models [220]. However, modelling the complex rheological behaviour of soft tissues is a challenging task, where the rheological law must be

able to capture the features of interest. The rheological description of cervical tissue will be described in the following section.

10.2 Viscoelastic modulus estimation

The choice of the rheological model is a priori far from obvious in liquid-like solids such as soft tissues, and different models have been proposed in the literature [219, 221, 222]. Here, the Maxwell, Kelvin-Voigt and Zener models are proposed (see Figure 10.2).

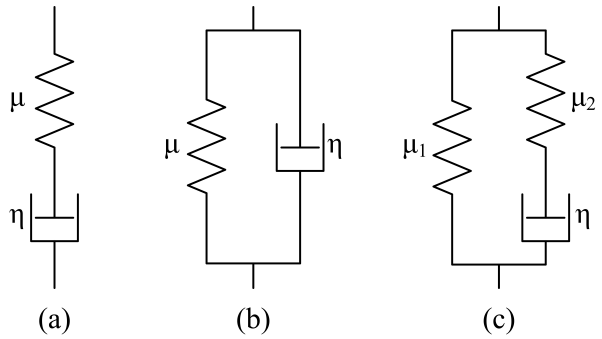

Figure 10.2: *Rheological models used in this study. (a) The Maxwell model is composed by a spring and a dashpot in series. (b) The Kelvin-Voigt model uses a spring and a dashpot in parallel. (c) The Zener model incorporates an extra spring in parallel with a Maxwell's model.*

The Maxwell and Kelvin-Voigt (K-V) rheological models have two parameters that describe the medium in which waves travel as continua characterised by elastic μ and viscous η coefficients. The Maxwell model combines an elastic spring with a viscous dashpot in series to describe tissues as fluid-like media capable of stress relaxation behaviour but no significant creep behaviour. The K-V model is a spring and dashpot placed in parallel, which describes tissues as solids that can creep but show little stress relaxation. Both models were deeply described in Chapter 5. The corresponding complex shear moduli for the Maxwell and K-V models are, respectively,

$$G^{*M} = \frac{j\omega\eta\mu}{\mu + j\omega\eta};\ G^{*K-V} = \mu + j\omega\eta \tag{10.3}$$

The Zener model has three parameters, where a spring μ_1 is placed in parallel with a series spring-dashpot unit (μ_2, η). It is the simplest model that expresses both the stress relaxation and the creep. The complex shear modulus for the Zener model is given by,

$$G^{*Z} = \frac{\mu_1\mu_2 + j\omega\eta(\mu_1 + \mu_2)}{\mu_1 + j\omega\eta} \tag{10.4}$$

Inserting Equations (10.3) - (10.4) into Equation (10.2), the SWS can be expressed, employing the Maxwell, K-V and Zener models, respectively as,

$$c_s^M(\omega) = \sqrt{\frac{2\mu}{\rho\left(1+\sqrt{1+\frac{\mu^2}{\omega^2\eta^2}}\right)}};\ c_s^{K-V}(\omega) = \sqrt{\frac{2(\mu^2+\omega^2\eta^2)}{\rho\left(\mu+\sqrt{\mu^2+\omega^2\eta^2}\right)}} \tag{10.5}$$

$$c_s^Z(\omega) = \frac{\omega}{\sqrt{\frac{\sqrt{A^2+B^2}-A}{2}}};\ \text{with}\begin{cases} A = \dfrac{-\omega^2\rho(\omega^2\eta^2(\mu_1+\mu_2)+\mu_1^2\mu_2)}{\mu_1^2\mu_2^2+\omega^2\eta^2(\mu_1+\mu_2)^2} \\ B = \dfrac{\omega^3\rho\mu_1^2\eta}{\mu_1^2\mu_2^2+\omega^2\eta^2(\mu_1+\mu_2)^2} \end{cases} \tag{10.6}$$

These three laws, described in Equations (10.5)-(10.6), were fitted to the estimated dispersion curves (Equation (10.1)) by an inverse problem (IP). The theoretical background of the IP used to estimate the viscoelastic parameters is described in the following section.

10.3 Inverse problem and rheological law selection

An inverse problem can be defined in opposition to the forward problem (FP). A FP consists of finding the response of a system given a known model. In contrast, an IP consists of retrieving unknown information of the model given the response of a system. Recently, some authors have applied IPs to identify damages or characterise material properties [223–227] defining a corpus of knowledge for reconstructing an unknown part of a system model. The aim of this section is to provide the mathematical basis to the IP and rheological law selection to describe cervical tissue.

10.3.1 Deterministic approach

The fundamental idea of the IP consists of the use of an iterative strategy based on the minimisation of the discrepancy between the simulated dispersion curves $c_i(\omega)$ and the shear phase velocity $\tilde{c}_i(\omega,\theta)$ described by the rheological law, where θ denotes a finite set of model parameters used to describe the rheological law, $\theta = \{\mu,\eta\}$ or $\theta = \{\mu_1,\mu_2,\eta\}$. The discrepancy is represented by a cost functional $\chi(\theta)$ defined as,

$$\chi(\theta) = \frac{1}{N}\sum_{i=1}^{N}\sqrt{(c_i(\omega)-\tilde{c}_i(\omega,\theta))^2} \tag{10.7}$$

where N denotes the number of different frequency observations, $c_i(\omega)$ is the simulated dispersion curve, and $\tilde{c}_i(\omega,\theta) \in \{c_s^M, c_s^{K-V}, c_s^Z\}$ is the shear phase velocity described by the rheological law.

The optimal model parameters $\hat{\theta} = \{\mu,\eta\}$ or $\hat{\theta} = \{\mu_1,\mu_2,\eta\}$, which characterise the rheological laws, are found by a search algorithm that minimises the cost functional $\chi(\theta)$,

by means of a least-square estimation of the residual energy,

$$\hat{\theta} = \arg\min_{\theta} \chi(\theta) \tag{10.8}$$

Genetic algorithms are applied to minimise Equation (10.8), since the cost functional $\chi(\theta)$ is multidimensional and multimodal (i.e., non-convex), implying that it may have more than one local minimum. This algorithm performs a stochastic search through the space of possible solutions and yields a higher probability of finding the global optimum compared to standard iterative gradient-based optimisation algorithms [228]. As a further drawback, note that the convergence of gradient-based algorithms strongly relies on the initial guess. A deeper insight on Genetic algorithms is provided in next section.

Genetic algorithms

The genetic algorithms are an heuristic optimisation technique based on the rules of natural selection and genetics, which simulates the mechanism of survival competitions. First, a population of individuals (called chromosomes) is randomly generated. The population comprises a group of chromosomes that represent possible solutions θ_i ($i = 1, \ldots, N_p$) in a (multidimensional) problem domain. Each solution θ_i is evaluated by computing its cost functional $\chi(\theta)$, for which one FP is solved independently. A new (child) population is formed by stochastically modifying the survivors, applying genetic operators such as tournament and crossover to provide genetic diversity to the population (i.e to ensure that the solution does not fall in local minima). Then, the child chromosomes with higher fitness replace some of their parent chromosomes. The process runs until a stopping criterion (for instance a number of generations N_g) is reached. The choice of N_g , along with the probabilities of the genetic operators, are set so, that the convergence to a global optimum is guaranteed, while establishing a trade-off between the IP error and the computational cost. The termination criterion can of course be modified, for instance by creating some convergence criterion and then ending the iterations when this criterion is met.

A number of parameters have to be adjusted to optimise the computational efficiency of the genetic algorithms and guarantee their good convergence. Table 10.1 summarises the selected configuration parameters used over the course of this dissertation.

Parameters	*Values*
Population size	100
Number of generations	200
Probability of crossover	0.6
Probability of tournament	0.4

Table 10.1: *Configuration parameters of the search algorithm.*

The flowchart of the inverse problem framework by applying genetic algorithms is depicted in Figure 10.3.

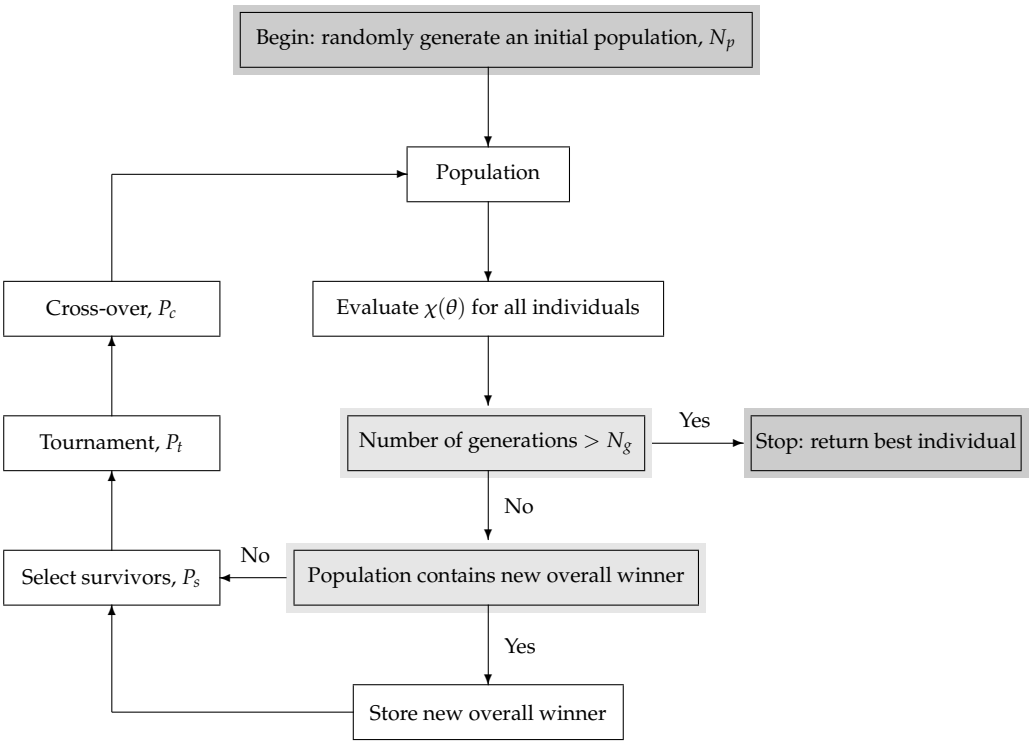

Figure 10.3: *Flowchart of the system identification approach by applying genetic algorithms. User-dependent variables: N_p: Number of individuals in population; N_g: Number of generations; P_s: Fraction of surviving individuals; P_t: Probability of tournament; P_c: Probability of crossover; and S_m: Scale of mutation*[1].

10.3.2 Probabilistic inverse problem

Reconstructing the values of the model parameters has a limited meaning if one considers the existence of intrinsic noise in the measurements, heterogeneity of properties, and even the fact that the model used to idealise the tissue behaviour is just an approximation of reality. To provide a suitable answer instead of deterministic values, probabilistic ones should be provided, which carry information about the degree of uncertainty and the nature of their scattering. This can be solved by treating the input and known data as uncertain up to some degree, and consequently obtaining the solution model in terms of a set of PDF's over each model parameter.

Following the probabilistic formulation of the model-based IP established by Tarantola *et al.* [229], the solution is not a single-valued set of model parameters M. On the contrary, the solution is provided by a PDF $p(M)$ of the values of the model parameters M within the manifold $\mathbf{M}$ of possible values. Here, this formulation is generalised to the case where several model classes $\mathcal{C}$ are candidates to idealise the real input-output system. Including this variable into the IP formulation will allow to derive the model-class selection formulation as a particular case of inverse problem [230, 231].

Bayes' theorem allows to rank the plausibility, in the sense of probability of being true, of the hypothesised models M_j $(j = 1, \ldots, 3)$ conditioned to the simulated observations. In

[1]Reproduced from Bochud [227].

our case, the three hypothesis are the idealised Maxwell, K-V or Zener models respectively, formalised by the functions of velocity $\tilde{c}_j(\omega, \theta)$, in terms of frequency ω and the set of model parameters θ, given in Equations (10.5)-(10.6). The simulated observations are computed by the dispersion curves $C = \{c_i\} \in \mathcal{C}$ at a set of independent configurations $Q = \{q_i\} = \{s, f\}_i \in \mathcal{Q}$, where the parameters that define each configuration are: spatial media, s, and excitation frequencies, f. Thus, this plausibility is defined by,

$$p(M_j|C) = \frac{p(C|M_j)p(M_j)}{p(C)} = \frac{p(C|M_j)p(M_j)}{\sum_j p(C|M_j)p(M_j)} \tag{10.9}$$

where $p(M_j)$ and $p(\theta|q_i, M_j)$ are the *prior* information on hypothesis and configurations, assumed equiprobable and therefore cancelling constants when substituted in the numerator and denominator of Bayes' theorem. Since the term $p(C|M_j)$, usually called evidence, should be independent of the estimated model parameters θ, the marginal joint *likelihood* for all configurations i and over all parameter values $\theta \in \theta$ is,

$$p(C|M_j) = \int_\theta \Pi_i p(c_i|\theta, q_i, M_j)p(\theta|q_i, M_j)d\theta \tag{10.10}$$

The joint probability of independent discrete events i is the product Π_i of their individual probabilities, and the joint probability of a continuous variable θ is its integral [232]. The latter integral is computed numerically by a Sobol quadrature of 10^{12} points [233]. If the simulated dispersion curves are assumed to follow a Gaussian probability distribution with mean equal to the hypothetical modelled velocity at a certain configuration $\tilde{c}_j(\omega, \theta, q_i)$, and standard deviation σ, $C \sim \mathcal{N}(\tilde{c}_j(\omega, \theta, q_i), \sigma)$, the *likelihood* is given by,

$$p(c_i|\theta, q_i, M_j) = \kappa e^{-\frac{1}{2}\sum_{kl}(c_i(\omega_k)-\tilde{c}_j(\omega_k,\theta,q_i))\sigma^{-1}(c_i(\omega_l)-\tilde{c}_j(\omega_l,\theta,q_i))} \tag{10.11}$$

where the standard deviation σ represents the measurement error, which was estimated as $\sigma = 0.5$, and κ is a normalising constant that will cancel out by applying the law of total probability.

Equation (10.9) is evaluated for the possible N observations corresponding to N configurations $q_i = \{s, f\}_i$ defined by: 3 spatial simulation sections, $s = \{$transversal, longitudinal along fibres, longitudinal across fibres$\}$; and the range of excitation frequencies, f.

Part III

RESULTS

11

In-vivo assessment of cervical stiffness during pregnancy in women

This chapter aims at testing the hypothesis on which the first objective of this thesis is based, i.e. evaluate the shear wave elastography feasibility, sensitivity and capability for assessing cervical ripening. Therefore, we *in-vivo* explore that, cervical stiffness progressively decreases during pregnancy and not in the same way throughout the cervix, which may present softer areas during gestation and thus more sensitive to assess the cervical mechanical state. We propose that SWE can objectively quantify this decrease in cervical stiffness and its spatial variability. To achieve that goal, in this chapter, the results of a clinical study performed on 42 healthy pregnant women are shown. Cervical stiffness was quantified in four different regions of the cervix using SWE and the repeatability of the technique was analysed. The measured cervical stiffness was related to gestational age at time of examination, interval from ultrasound examination to delivery and cervical length.

Section 11.1 outlines the characteristics of the study population. In Section 11.2, the statistical results are presented. First, in Subsection 11.2.1 the results of the regression analysis are shown. Subsection 11.2.2 describes the stiffness differences between the four ROI assessed. The reproducibility of the technique and the sensitivity analysis are presented in Subsection 11.2.3. Finally, in Section 11.3, the main findings of this clinical study are discussed.

11.1 Characteristics of the cohort

This preliminary study included forty-two women with uncomplicated singleton pregnancies at a median value of 27.5 (from 6 to 41) weeks' gestation. Maternal and pregnancy characteristics of the population are summarised in Table 11.1. Data are expressed as median (minimum - maximum) or number (%). The preterm rate in our population was 2.38% (n=1). The median gestational age (GA) at delivery was 40.1 (30.3-41.9) weeks. Cervical length (CL) was successful measured in all the patients included in the study. A total of 504 ROIs were analysed for stiffness quantification (42 women x 4 ROI x 3 measurements). One measurement of cervical stiffness in the region A2 (internal and superior lip) and two in the region A3 (internal and inferior lip) were impossible to assess ($n = 3$, 1.79%). Consequently, these measurements had to be rejected from the study. The reasons were the reflections or perturbations of the shear waves in some particular imaging or anatomical configurations (configuration of the bladder), which made it impossible to measure velocity, and consequently no stiffness value was assessed.

Characteristic	*Value*
Total population (number)	42
Maternal age (years)	32.5 (17.0-43.0)
Body mass index (Kg/m2)	25.2 (19.1-31.5)
GA at elastography (weeks)	27.5 (6.0-41.0)
GA at delivery (weeks)	40.1 (30.3-41.9)
Nulliparous (number)	28 (66.7%)
Cervical length (mm)	30.5 (6.0-50.0)
Stiffness A1 (kPa)	6.49 (2.33-30.70)
Stiffness A2 (kPa)	13.97 (4.48-45.50)
Stiffness A3 (kPa)	16.38 (4.70-52.55)
Stiffness A4 (kPa)	8.06 (3.83-27.97)

Table 11.1: *Characteristics of the study population. Data are given as median (range) or n (%).*

11.2 Statistics results

11.2.1 Regression analysis

Regression analysis revealed that cervical stiffness, in the four ROIs, was: (1) a significant predictor of GA at time of examination; (2) a significant predictor of the interval from elastography examination to delivery; and (3) not a predictor of CL. Table 11.2 shows the Pearson correlation coefficients between cervical stiffness in the 4 ROIs (A1, A2, A3 and A4), CL, GA and interval time from elastography examination to delivery. P-values below 0.0005 are indicated as $p = 0.000$. All regression analysis were calculated using the first measurements performed by the operator 1.

In the total population, there were significant associations between cervical stiffness in the four cervical regions and GA and interval time from elastography examination to delivery (Pearson correlation coefficient higher than 0.5 in all cases, $p = 0.000$). Scatterplots of

	cervical length	*gestational age*	*remaining time to delivery*
stiffness A1	$r = 0.259$, $p = 0.098$	$r = -0.672$, $p = 0.000$	$r = 0.670$, $p = 0.000$
stiffness A2	$r = 0.413$, $p = 0.007$	$r = -0.796$, $p = 0.000$	$r = 0.803$, $p = 0.000$
stiffness A3	$r = 0.331$, $p = 0.037$	$r = -0.786$, $p = 0.000$	$r = 0.790$, $p = 0.000$
stiffness A4	$r = 0.057$, $p = 0.720$	$r = -0.567$, $p = 0.000$	$r = 0.573$, $p = 0.000$

Table 11.2: *Pearson correlation coefficient between cervical stiffness, cervical length, gestational age and interval time from elastography examination to delivery.*

the relationship between cervical stiffness assessed in the 4 ROIs (A1, A2, A3 and A4) and interval time from ultrasound examination to delivery and GA, showing linear regression lines and 95% confidence intervals (CI), are depicted in Figures 11.1 and 11.2, respectively

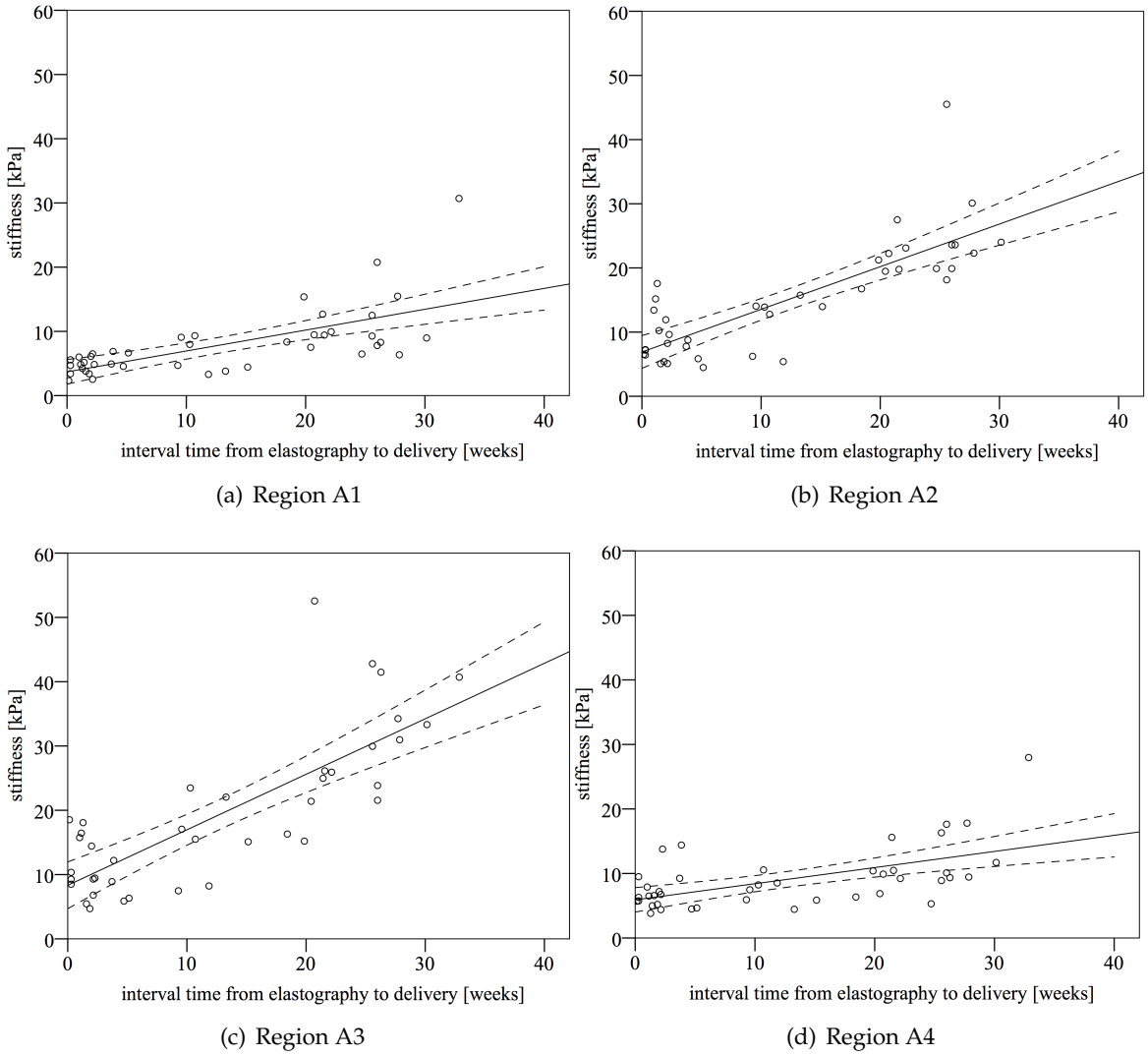

(a) Region A1

(b) Region A2

(c) Region A3

(d) Region A4

Figure 11.1: *Associations between cervical stiffness assessed in the 4 ROIs (A1: external and superior cervical lip; A2: internal and superior cervical lip; A3: internal and inferior cervical lip; A4: external and inferior cervical lip) and interval time from ultrasound examination to delivery. Linear regression (solid line) and 95 % CIs (dashed lines) lines are plotted.*

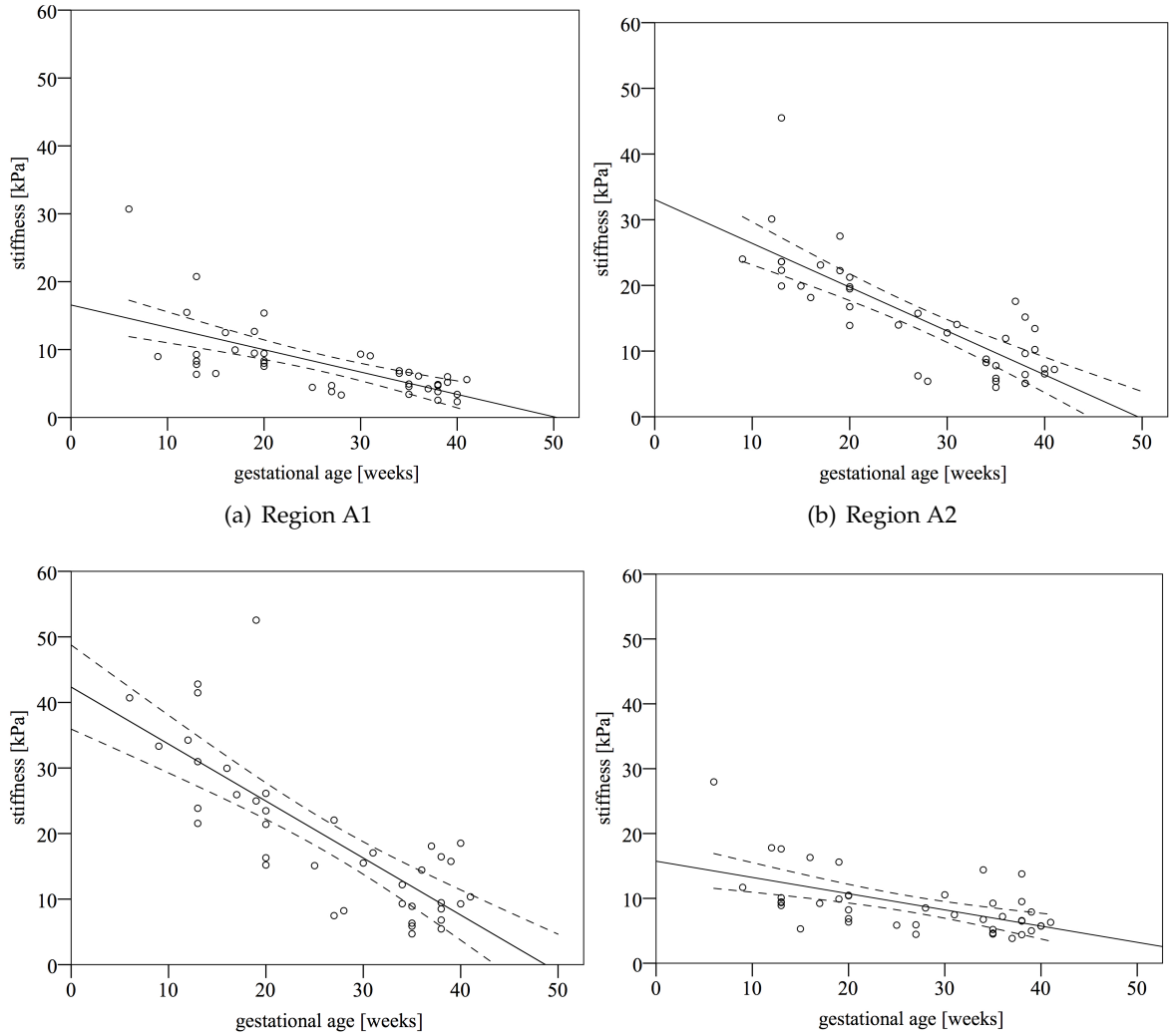

(a) Region A1

(b) Region A2

(c) Region A3

(d) Region A4

Figure 11.2: *Associations between cervical stiffness assessed in the 4 ROIs (A1: external and superior cervical lip; A2: internal and superior cervical lip; A3: internal and inferior cervical lip; A4: external and inferior cervical lip) and gestational age at time of examination. Linear regression (solid line) and 95 % CIs (dashed lines) lines are plotted.*

No high associations ($r < 0.5$ for all cases) and no significant ($p > 0.05$ in external part, regions A1 and A4) were found between cervical length and stiffness. Figure 11.3 shows the correlation between them in the four ROIs. Note that, associations between cervical stiffness in the 4 ROIs and CL are significantly weaker than between stiffness assessed at the same ROI and GA and interval time from elastography examination to delivery.

Associations between gestational age and cervical lenght ($r = -0.434$, $p = 0.004$), and associations between remaining time for delivery and cervical length ($r = 0.455$, $p = 0.002$) are shown in Figure 11.4. They present notably weaker correlations than with cervical stiffness.

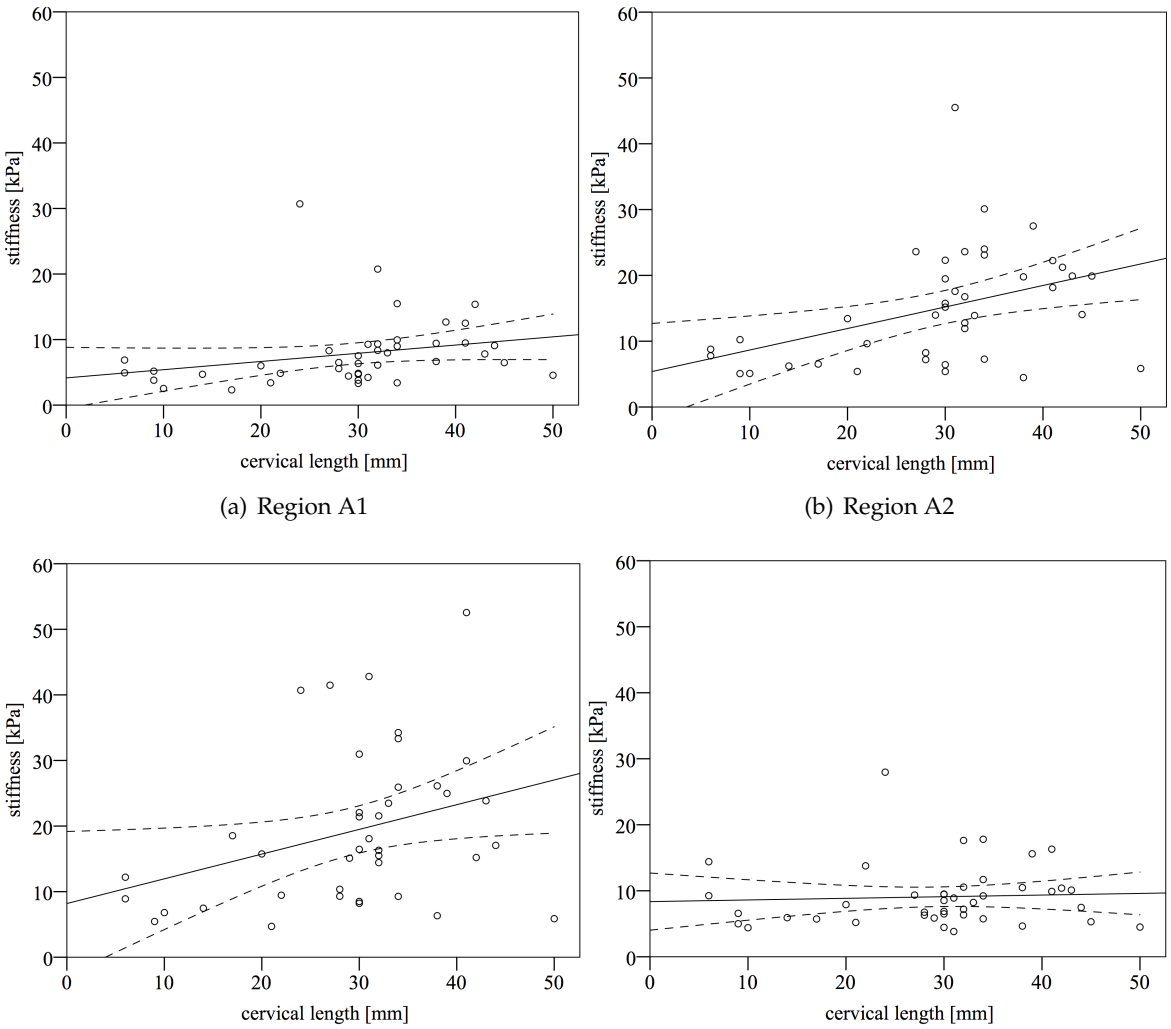

(a) Region A1

(b) Region A2

(c) Region A3

(d) Region A4

Figure 11.3: *Associations between cervical stiffness assessed in the 4 ROIs (A1: external and superior cervical lip; A2: internal and superior cervical lip; A3: internal and inferior cervical lip; A4: external and inferior cervical lip) and cervical length. Linear regression (solid line) and 95 % CIs (dashed lines) lines are plotted.*

11.2.2 Stiffness differences

Stiffness values were significantly different in the four studied regions of the cervix (A1: external and superior cervical lip; A2: internal and superior cervical lip; A3: internal and inferior cervical lip; A4: external and inferior cervical lip). The distribution of the cervical stiffness measured values demonstrated spatial variability both along the length of the cervix (external to internal part) and within its anterior *vs* posterior part. The external part of the cervix was significantly softer than the internal one, and these stiffness values significantly vary in the anterior compared to the posterior cervix (see Table 11.3 and Figure 11.5). This was calculated using the first measurements performed by the operator 1.

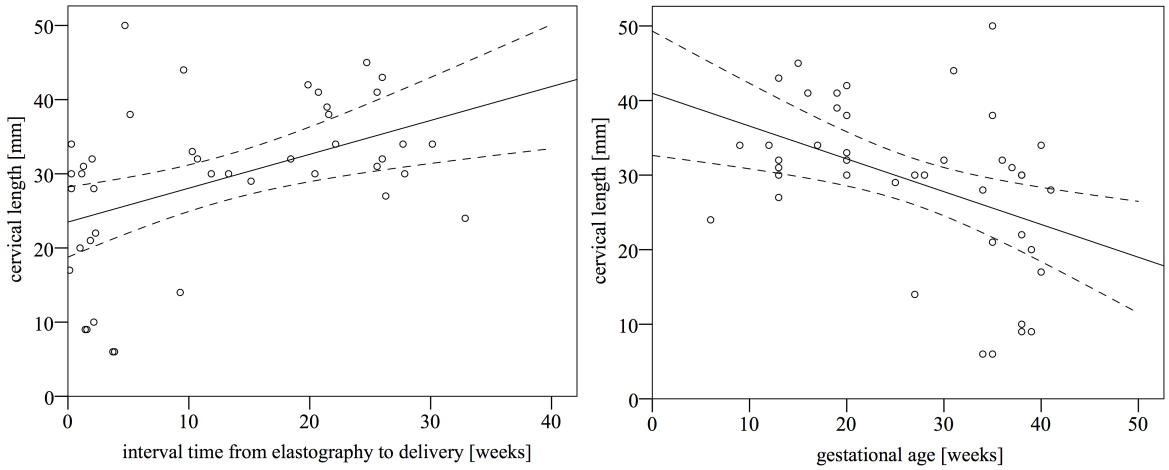

(a) (b)

Figure 11.4: *Associations between CL and interval time from ultrasound examination to delivery (left), and between CL and GA at time of examination (right). Linear regression (solid line) and 95 % CIs (dashed lines) lines are plotted.*

Cervical regions	*Mean difference*	*Standard error*	*95% CI*	*Significance*
A3 - A1	11.345	1.567	8.176 - 14.514	0.000
A3 - A2	3.711	1.004	1.676 - 5.745	0.001
A3 - A4	9.983	1.623	6.700 - 13.267	0.000

Table 11.3: *Mean differences in cervical stiffness measurements between different regions of interest. Region A1: external and superior cervical lip. Region A2: internal and superior cervical lip. Region A3: internal and inferior cervical lip. Region A4: external and inferior cervical lip.*

11.2.3 Sensitivity results

The Cronbach's alpha coefficients were higher than 0.86 and in most cases above 0.9 (see Table 11.4). Therefore, both measurements, intra-operator and inter-operator, were considered at least good (0.81-0.90) and in some areas excellent (> 0.90).

Cervical region	*Intra-operator*	*Inter-operator*
A1	0.931	0.870
A2	0.941	0.936
A3	0.937	0.889
A4	0.897	0.861

Table 11.4: *Cronbach's alpha of elastographic measurements in different regions of the cervix (A1: external and superior cervical lip. A2: internal and superior cervical lip. A3: internal and inferior cervical lip. A4: external and inferior cervical lip.). Concordance analysis of intra and inter-operator measurements.*

11.3 Discussion

One of the objectives of this thesis, which is experimentally addressed in this preliminary study, is to assess the potential of SWE to objectively quantify the cervical stiffness during

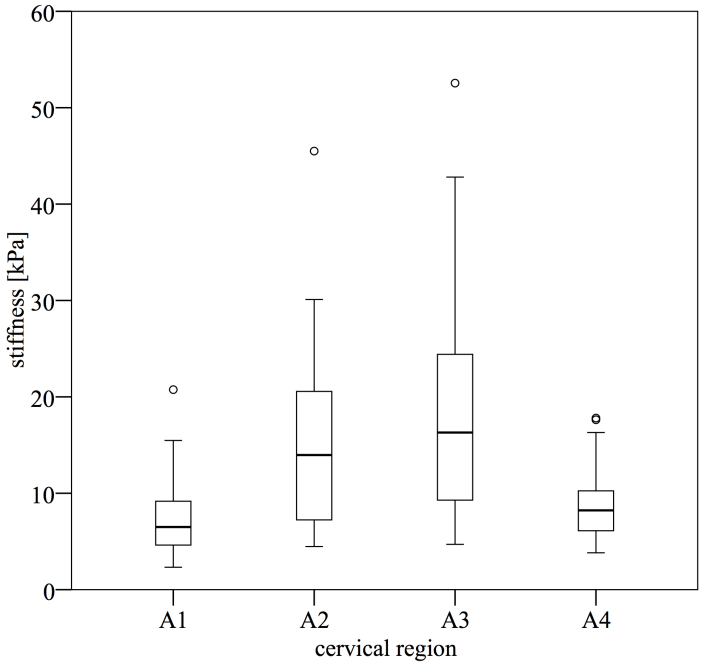

Figure 11.5: *Box-and-whisker plots of cervical stiffness in the four regions: A1(external and superior cervical lip), A2 (internal and superior cervical lip), A3 (internal and inferior cervical lip), A4 (external and inferior cervical lip). Median (lines within boxes), interquartile range (IQR, boxes) and extreme values (whiskers) are shown.*

pregnancy. SWE technique has already been successfully used to characterise the structure and health of different biological soft tissues [30, 234–236]. However, its application to obstetrics had still been unexplored. In a recent study, Gennisson *et al.* [237] assessed the elasticity changes in the myometrium during labour using the same technique, but no absolute value of cervical stiffness was measured until this study. Hence, SWE application to cervical tissue is explored here for first time [98]. Despite shear waves have been already applied to assess differences in ripened *vs.* unripened cervical tissue [47, 48], in those studies only a point measure of shear wave speed (SWS) in a specific region of interest was calculated, since another kind of dynamic elastography (point shear wave elastography, pSWE) was used. Furthermore, no stiffness values were given to describe the cervical maturation. In the present work, results show the sensitivity and capability of SWE to objectively quantify cervical elasticity during normal pregnancy, providing to our knowledge, absolute stiffness values for first time in human cervical tissue. Inter and intra-operator repeatability has been demonstrated. Therefore, data confirm that SWE can objectively quantify cervical stiffness defined by Young's modulus.

Our findings support that stiffness decreases during pregnancy (see Figure 11.2). We found that cervical stiffness significantly decreases with gestational age ($p = 0.000$), being this relation higher in internal (regions A2 and A3, $r = -0.796$ and -0.786, respectively) than external part (regions A1 and A4, $r = -0.672$ and -0.567, respectively). These results agree with previous studies that evaluated cervical softening during pregnancy employing

different techniques based on the distensibility of the tissue or using the aspiration device [51, 106, 107]. All of them found a cervical softening during pregnancy. Or in other words, cervical softening is directly related to the remaining time for delivery, as significant correlations between cervical stiffness and interval time from elastography examination to delivery show (see Figure 11.1).

Our results show weaker correlation of cervical stiffness with CL than with GA. Moreover, correlation between stiffness and CL was only significant in the internal part of the cervix (regions A2 and A3). In a recent study, Wozniak *et al.* [155] found similar correlations between *internal os* stiffness, assessed by quasi-static elastography, and CL. However, the high correlation between stiffness and GA is contrary to a previous result reported by Hernandez-Andrade *et al.* [27], which suggested that cervical tissue strain (an indirect measurement of stiffness) was more strongly associated with CL than with GA. This contradiction could be a consequence of the inherent limitations of the elastography technique that they used. The limitations of the quasi-static elastography in cervical tissue have already been addressed by several authors [16, 25, 147]. By this technique is not possible to quantify the stiffness in absolute values since the elastographic image is only a qualitative description of the tissue strain. Displacements are generated by a hand-induced displacement of the tissue using the probe, which in addition may not reach deep areas of the cervix [9]. In the work of Hernandez-Andrade *et al.* [27] the strain was assessed in two ROIs: the endocervical canal and the entire cervix. The large dimension of those ROIs compared to the one used in this study might affect the strain-rate value. It has been reported that the areas located directly under the probe have high strain-rate [25, 27, 147]. Many studies showed that the displacements are affected by the intensity and the direction of the pressure exerted [50, 238, 239]. Furthermore, the standardisation of the applied pressure to induce the displacements of the tissue is the main limitation of the technique [24, 25, 27, 142, 144]. Therefore, the strain depends on both the tissue elasticity and the force applied. As opposed to quasi-static elastography, SWE is based on the propagation of shear waves within the tissue. Although the pressure applied by the practitioner influences the SWE [240], it can be easier to control [241]. First, as the ultrasound beam creates the displacements, they are less user-dependent (i.e. more uniaxial) than those in hand-induced strain imaging [50]. Second, SWE has greater ability to target the area of evaluation. Ultrasound beams are successively focused at different depths to generate a quasi-plane shear wave that propagates through the tissue. Consequently, it can reach deeper areas of the cervix.

Currently, in the clinical practice, the only quantitative and objective parameter used to diagnose PTB is the CL measured by conventional endovaginal ultrasound. A weak correlation was found here between CL and cervical stiffness. Long cervices can be soft and CL alone cannot be used as a predictive parameter of delivery [242]. Our findings support the idea that CL and cervical stiffness might be independent. Therefore, measuring quantitatively and independently both parameters could increase the accuracy of the PTB diagnosis.

Regarding to the stiffness distribution within the cervix, significant variability within and between cervical regions was found. Our results show a longitudinally stiffness increment within the cervix, from external to internal parts (Figure 11.5, Table 11.3). Anterior compared to posterior part exhibits spatial variability too, but in smaller grade. The largest differences in mean values appear in the internal parts (regions A2 and A3), which present higher gradient, while external parts present the least (see Figure 11.2). This spatial variability is not surprising, and has been already reported by Carlson *et al.* [48]. In fact, the microstructure of the cervical ECM is composed of a dense, hydrated and highly cross-linked collagen network embedded in a viscous proteoglycan ground substance [2], far away from a homogeneous material, and therefore variability within and between cervical regions is expected. During normal pregnancy the cervical ECM remodels in preparation for labour, and several changes occur progressively in its structure, in particular in the collagen network [39]. The four cervical regions display different gradients, in particular the external part (regions A1 and A4) shows lesser stiffness gradient than the internal part. This different sensitivity may be related to the micro-architecture of the cervix, suggesting that the cervical ripening is heterogeneous in time within the tissue. However, more studies are needed to validate this hypothesis. In that vein, animal models present an opportunity for obtaining more understanding of the cervical remodelling process an its relation to SWE measurements. In the following chapter of this thesis, the results of an animal study developed according to that goal are presented.

In our opinion, anterior internal cervical lip (region A2) might be the best for cervical stiffness assessment. This region showed stronger association with gestational age than external part, and less internal variability than the internal posterior lip. Anterior cervical lip [147, 152] and *internal os* [155, 159] have been chosen for many authors to assess cervical stiffness. Furthermore, the anterior internal cervical lip (region A2) is close enough to the probe to guarantee shear wave propagation, and at the same time far from it to minimise the possible effects introduced by the pressure applied by the practitioner, which is impossible to avoid. Cervical tissue is a viscoelastic material, in which the elastic modulus is dependent on the frequency. In such a complex material, estimate the strain contrast imposed by the practitioner, unable to avoid in clinical practice, is an important requirement in the development of cervical elastography [37, 243]. Thus, in order to obtain reproducible measurements, the pressure applied on the cervix by the sonographer with the probe has to be minimal.

The main limitations of this study are related to the shear wave propagation and to the complex structure of cervical tissue. SWE relies on the propagation of shear waves to estimate the stiffness. Although it has been demonstrated its successful application to diseases diagnosis in many kind of soft tissues [244, 245], its potential application to cervical tissue still reminds unclear. Some assumptions, inappropriate for the cervix, are made to estimate the elasticity (Young's modulus): tissue is homogeneous, isotropic and semi-infinite [31]. Notwithstanding, cervical tissue is anisotropic, heterogeneous and its architecture small relative to the shear wavelengths that are characteristic in dynamic elastography

[32, 48, 231, 246]. Even though the election of a small ROI was based on that, allowing to assume homogeneous medium inside that ROI, future studies are necessary to understand shear waves-tissue interactions within this complex medium. These assumptions have motivated, in part, the development of the numerical approach that constitutes the main second part of this thesis. Its results will be presented in Chapters 13 and 14.

On the other hand, as the main aim of this study was to explore the feasibility of SWE to assess cervical ripening, a small sample size was employed. Thus, in order to generalise/extrapolate our finding to a general population, further studies with larger sample size would be required. We are confident in our preliminary findings, and SWE has high potential to objectively detect early cervical ripening in human pregnancy that leads to delivery. In a future, complete studies in a larger population must be performed to determine if cervical stiffness quantified by shear waves elastography is a reliable tool to predict vaginal delivery and eventually PTB.

11.4 Conclusions

The results of this study demonstrate that, first, cervical stiffness was more strongly associated with gestational age at examination and to interval from elastography examination to delivery than to cervical lenght. Secondly, it is possible to objectively quantify cervical stiffness during pregnancy by SWE. We have shown that the measurements taken by the same and by two different observers for different regions in the cervix are reliable and reproducible. Finally, stiffness anatomically varies in the cervix, there is a positive stiffness gradient from external to internal and from posterior to anterior parts.

SWE might provide additional information on the process of cervical effacement to that obtained from digital examination and conventional ultrasound. Further studies are needed to assess the feasibility of the technique in obstetric clinical applications, such as prediction of PTB or success in labour induction.

12

In-vivo evaluation of cervical remodelling during induced ripening in an animal model

In this chapter, we present the results of an *in-vivo* study in an animal model. Motivated by the promising results of the clinical study in women, the objective of this study is to provide physiologically relevant data during an objectively controlled cervical ripening, which could help to describe patterns of the maturation process by using shear wave elastography. In this animal study, the cervical remodelling was artificially induced with a dexamethasone injection and microscopically described by combining histology with two-photon excitation microscopy. Finally the reported micro-structural changes are linked to the cervical mechanical behaviour assessed by SWE.

Section 12.1 outlines the SWE results. The stiffness evolution during the induced cervical ripening and the repeatability of the SWE technique are presented. The results from a molecular assay of prostaglandins are depicted in Section 12.2. In Section 12.3, the cervical remodelling is described at the micro-scale. First, we show the histological results in Subsection 12.3.1. Second, Subsection 12.3.2 shows the results of the two-photon excitation microscopy analysis. Finally, the possible link between SWE measurements and cervical microstructure is discussed in Section 12.4.

12.1 Shear wave elastography

This study included 9 pregnant ewes. The characteristics of the animals are presented in Table 12.1. Cervical elastography could be performed in all cases ($n = 9$). A total of 378 ROIs were analysed for stiffness evaluation (9 animals x 7 measurements x 2 operators x 3

images/operator). During the last examination (24 hours after dexamethasone injection), one animal had to be removed from the study because no reliable measurement of cervical stiffness was obtained due to movements of the animal ($n = 6$ images, i.e., 1.6% of the total number). Images with strong artefacts, for which standard deviation within the ROI were higher than 30% of the nominal value, leading to apparent strong heterogeneities in the stiffness were rejected too ($n = 2$ images, i.e., 0.53% of the total number). No ewe showed any obvious sign of contraction or behavioural preparation for parturition (nesting behaviour, restlessness) during the experiment.

Characteristic	*Control group*	*Dexamethasone group*
Total population (number)	4	5
Gestational age (days)	127	127
Nulliparous (number)	3	4
Singleton pregnancy (number)	3	5

Table 12.1: *Characteristics of the study population.*

Figure 12.1 shows an example of the first ultrasound B-mode and elastographic images for two ewes (control and dexamethasone group), before dexamethasone was injected. Figure 12.1a was obtained in a control sheep, while Figure 12.1b corresponds to a sheep treated with dexamethasone. The results from the last measurement (after 24 hours) for the same animals are shown in Figure 12.2. The last stiffness measurement for the dexamethasone sheep (4.6 kPa $\pm$ 0.6 kPa) is significantly smaller than the initial one (8.9 kPa $\pm$ 1.6 kPa), and than the control one as well (10.2 kPa $\pm$ 0.5 kPa), while non-significant change is observed in the control sheep (10.4 kPa $\pm$ 0.7 kPa).

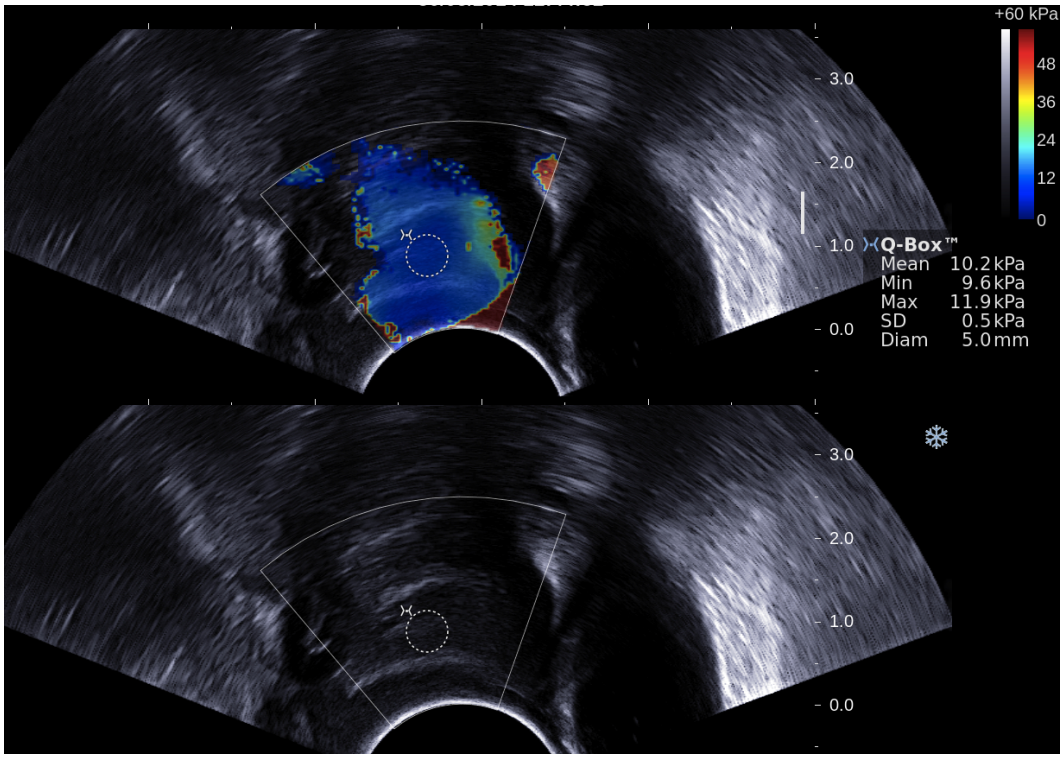

(a) Control animal

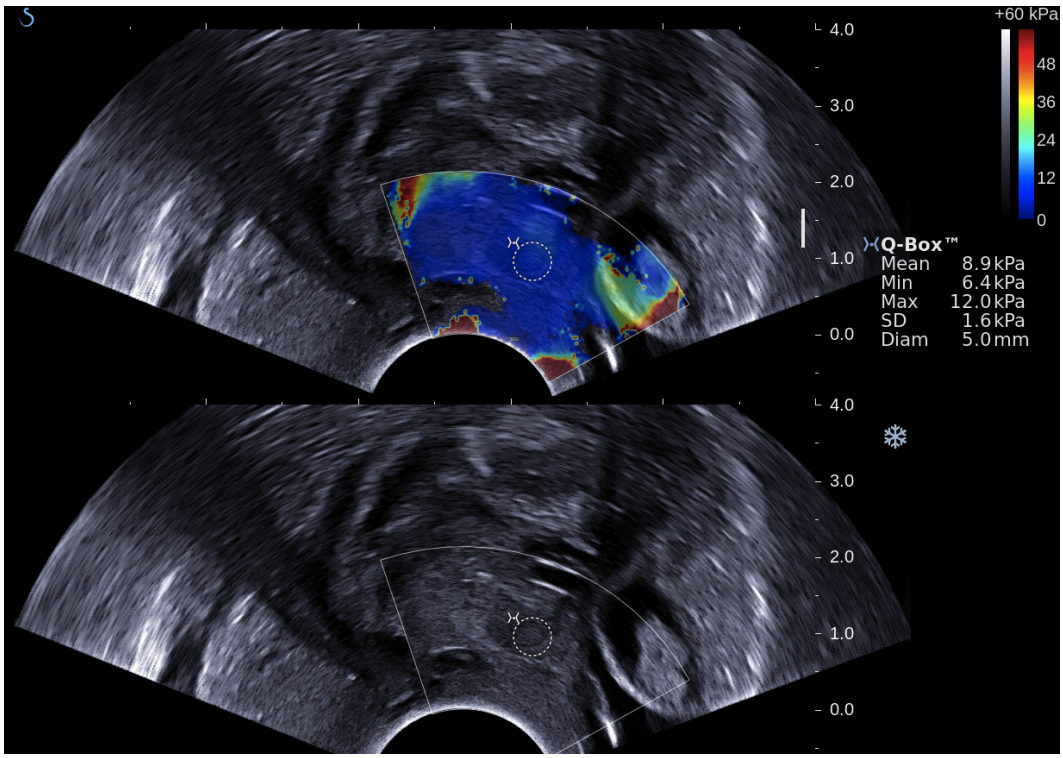

(b) Dexamethasone animal

Figure 12.1: *Elastography and Bmode images of the cervix in pregnant sheep at the beginning of the experiment, before dexamethasone was injected. (a) Control animal: stiffness 10.2 kPa ± 0.5 kPa, SWS 1.844 m/s ± 0.408 m/s. (b) Dexamethasone animal: stiffness 8.9 kPa ± 1.6 kPa, SWS 1.722 m/s ± 0.730 m/s.*

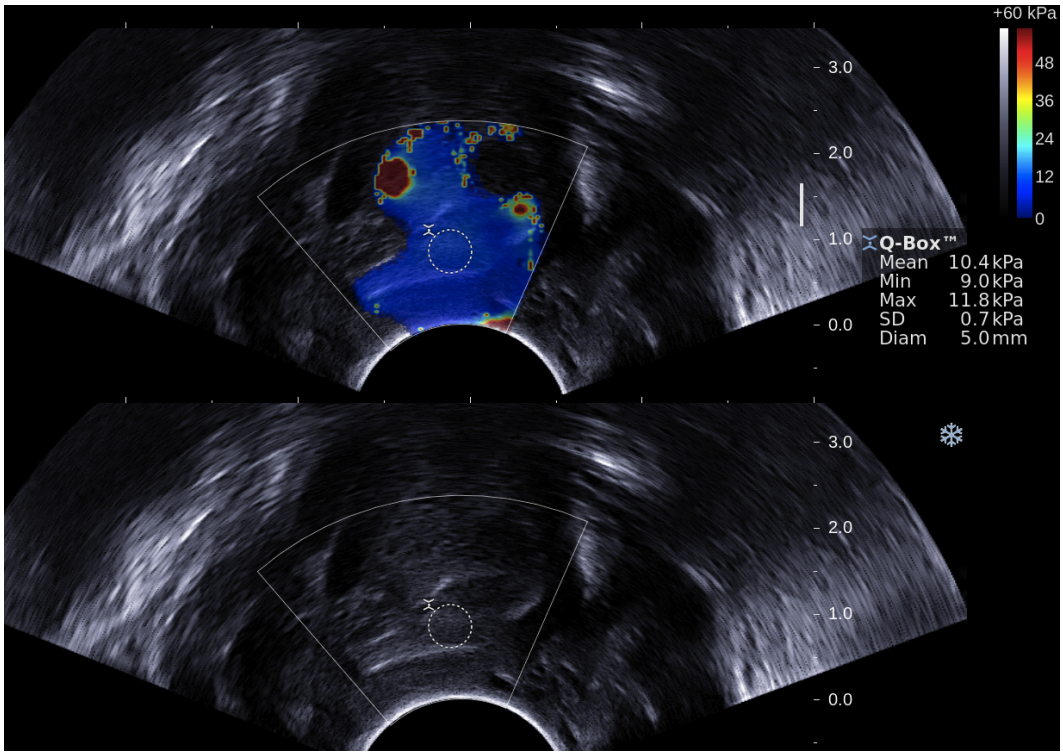

(a) Control animal

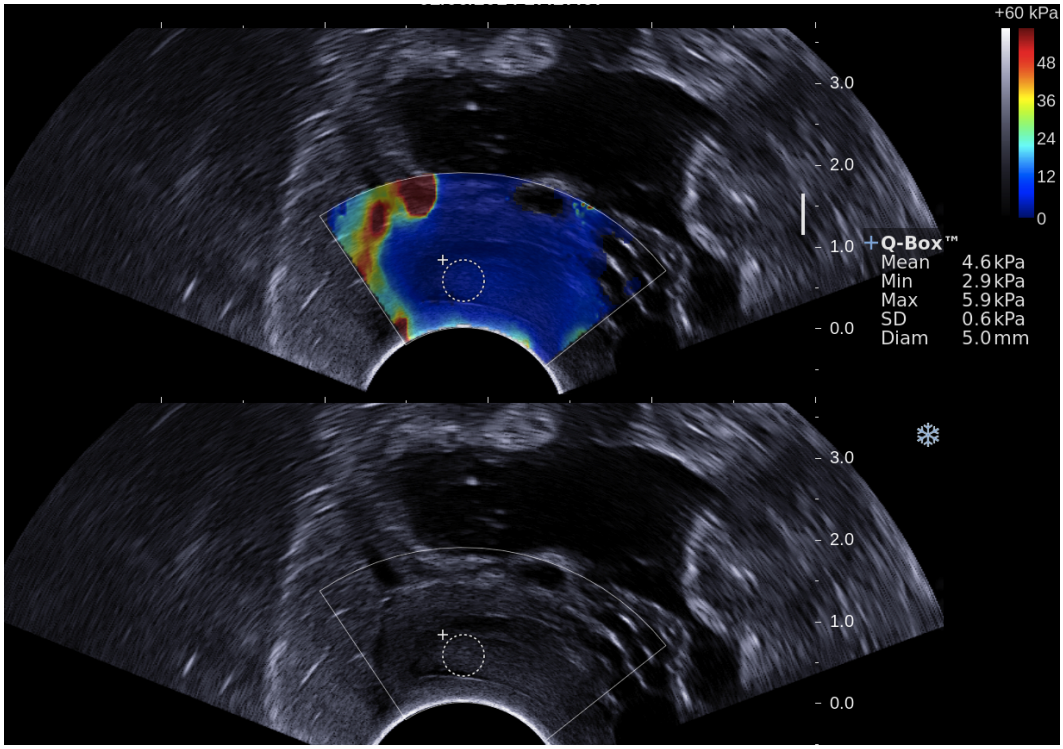

(b) Dexamethasone animal

Figure 12.2: *Elastography and Bmode images of the cervix in pregnant sheep at the end of the experiment, after 24 hours. (a) Control animal: stiffness 10.4 kPa ± 0.7 kPa, SWS 1.844 m/s ± 0.408 m/s. (b) Dexamethasone animal: stiffness 4.6 kPa ± 0.6 kPa, SWS 1.238 m/s ± 0.447 m/s.*

Figure 12.3 shows the distribution in form of box-and-whisker plots for each elastographic measurement time, and for both control and dexamethasone groups. In the dexamethasone group, stiffness values are significantly lower than the values measured in the control group. The minimum stiffness values correspond to the two last examinations (measurements taken after 20 and 24 hours). Since elasticity, E, is estimated from SWS, the same trends are found for both parameters (see Figure 12.4).

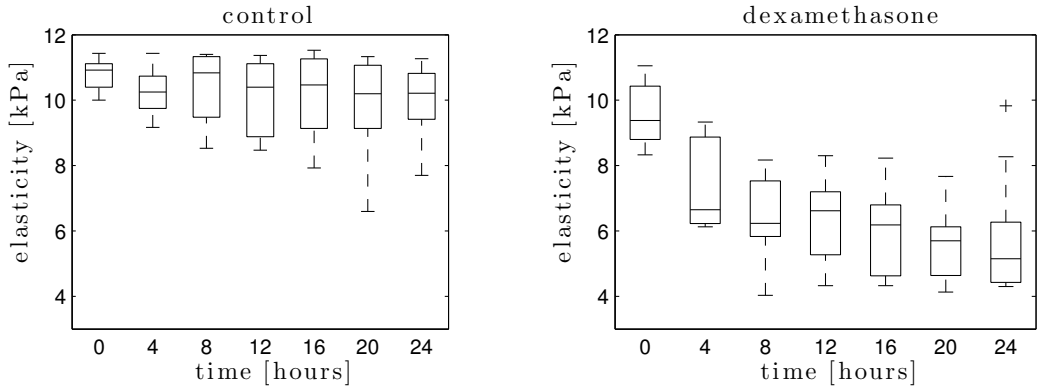

Figure 12.3: *Box-and-whisker plots of cervical stiffness measurements for the control (left) and dexamethasone group (right) in the 7 examinations performed over 24 hours. Median (lines within boxes), interquartile range (IQR, boxes) and extreme values (whiskers) are shown.*

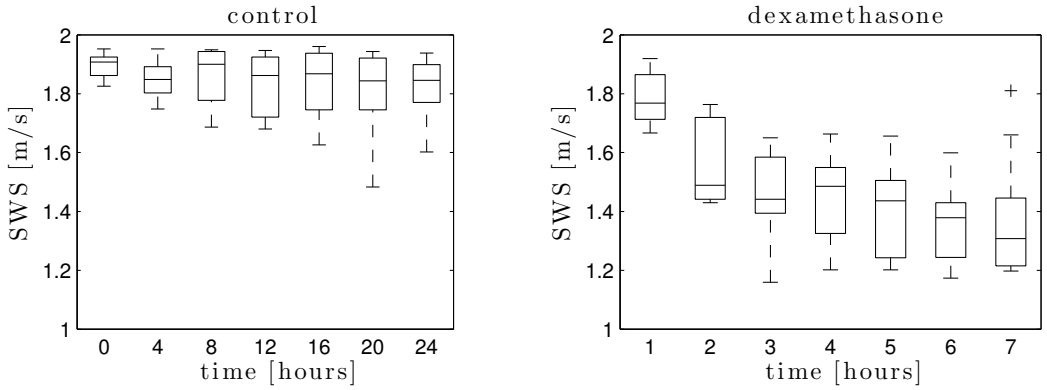

Figure 12.4: *Box-and-whisker plots of SWS measurements for the control (left) and dexamethasone group (right) in the 7 examinations performed over 24 hours. Median (lines within boxes), IQR (boxes) and extreme values (whiskers) are shown.*

The median initial stiffness and SWS values were not significantly different between groups (10.79 kPa $\pm$ 0.48 kPa, 1.897 m/s $\pm$ 0.4 m/s in control group versus 9.54 kPa $\pm$ 0.92 kPa, 1.783 m/s $\pm$ 0.554 m/s dexamethasone group, $p = 0.176$). In the dexamethasone group, stiffness and SWS decreased significantly with cervical maturation time, with a steep decrease within the first 4 hours (7.43 kPa $\pm$ 1.39 kPa, 1.574 m/s $\pm$ 0.681 m/s at 4 hours, $p < 0.05$) followed by a plateau. On the contrary, non significant trend was observed in the control group (last values 10.00 kPa $\pm$ 1.18 kPa, 1.826 m/s $\pm$ 0.627 m/s).

At 24 hours, the last SWS and consequently the average last stiffness value were significantly lower in treated versus non-treated animals (1.826 m/s $\pm$ 0.627 m/s and 10.00 kPa $\pm$ 1.18 kPa in control ewes versus 1.291 m/s $\pm$ 0.523 m/s and 5.00 kPa $\pm$ 0.82 kPa treated ewes, $p < 0.05$). Figure 12.5 shows a second order fit obtained for the stiffness and SWS versus cervical maturation time in the control ($R^2 = 95\%$) and dexamethasone group ($R^2 = 83\%$). It is worth pointing out stiffness and SWS values significantly decrease after the dexamethasone injection (starts), while they have a more constant trend in the control group (circles). Note that the dexamethasone group shows a significant higher negative slope ($0.0103t^2 - 0.3844t + 9.2147$) than the control group ($0.0014t^2 - 0.0648t + 10.7016$). When data were analysed using only the nulliparous animals, results were the same, and

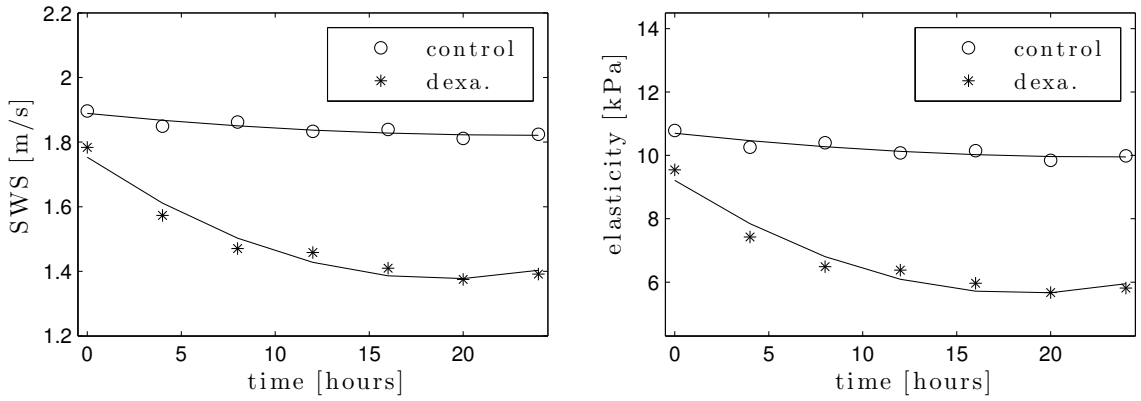

Figure 12.5: *Evolution of the average SWS and stiffness throughout 24 hours after the induction of cervical maturation by dexamethasone. The solid lines correspond to a second order fit of the stiffness values versus inducted time for both groups, control (blue) and dexamethasone (red).*

the elastographic profiles of the multiparous ewes closely matched that of the nulliparous ones. However, in the control group significant differences were found in elasticity between nulliparous and multiparous animals ($p = 0.0031$) when they were globally compared, whereas in the dexamethasone group stiffness measurements were not significantly different ($p = 0.22$).

Bland-Altman plots, demonstrating the degree of concordance between pairs of measurements made by the same and by two different observers, are given in Figure 12.6. There was no significant bias in any case because the difference between measurements remained stable as the average increased. The mean and standard deviation of differences appeared to be constant throughout the range of measurements for all comparisons. Note that the only few points where both operators do not agree are scattered between times and animals.

12.2 Induction of cervical ripening: Prostaglandin Assay

Results show that plasma PGE2 concentrations were not significantly different between groups at the beginning of the experiment (before dexamethasone injection). In contrast, as shown in Figure 12.7, there was a sharp and significant increase in PGE2 twenty-four hours

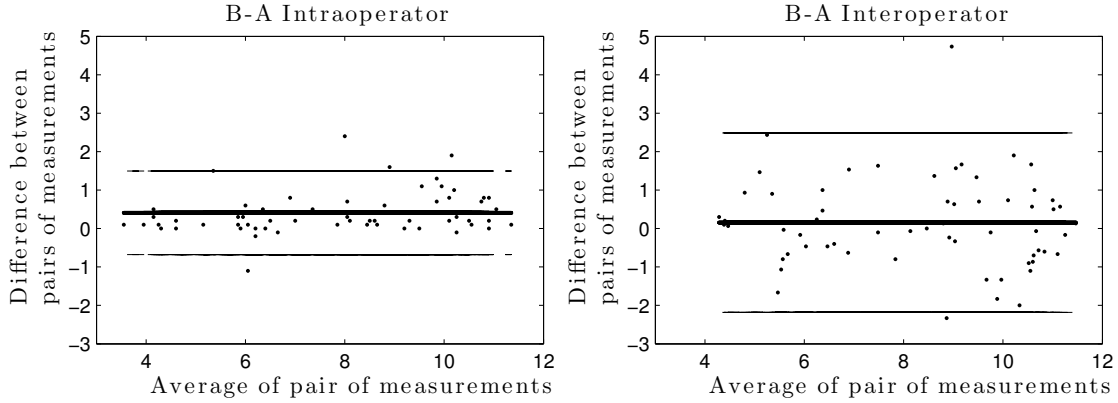

Figure 12.6: *Bland-Altman plots demonstrating degree of concordance between pairs of cervical elastography measurements obtained by the same (left) and by two different operators (right). Mean difference (solid line) and 95% limits of agreement (dashed lines) are shown.*

following dexamethasone treatment ($p < 0.01$), whereas values were not significantly different in the control group.

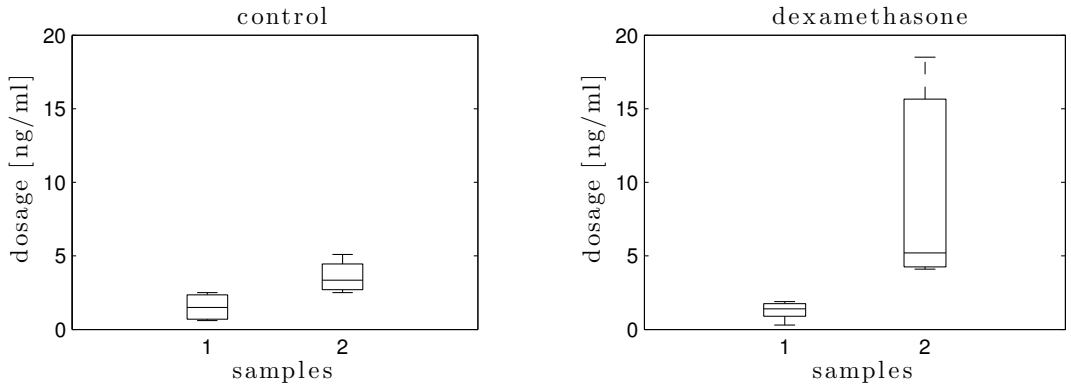

Figure 12.7: *Box-and-whisker plots of PGE2 and its metabolites in sheep serum just before the first elastographic exam and dexamethasone injection (sample 1) and at the end of the experiment just before euthanasia (sample 2), assayed via its metabolite PGEM with Cayman's Prostaglandin E Metabolite EIA Kit (Item No. 514531, Cayman chemical). Median (lines within boxes), IQR (boxes) and extreme values (whiskers) are shown.*

12.3 Micro-structural remodelling

12.3.1 Histology

The different structures identified by histological evaluation are shown in Figure 12.8. During the complete histological evaluation of the cervix, no systematic difference was observed between untreated and treated animals (see Figure 12.9). After hematoxylin-eosin-saffron (HES) staining, collagen fibres of the mucosal chorion and the submucosa appeared very similar between animals. Some inflammatory cells were present just beneath the mucosa and were consistently more numerous in treated animals compared to untreated ones

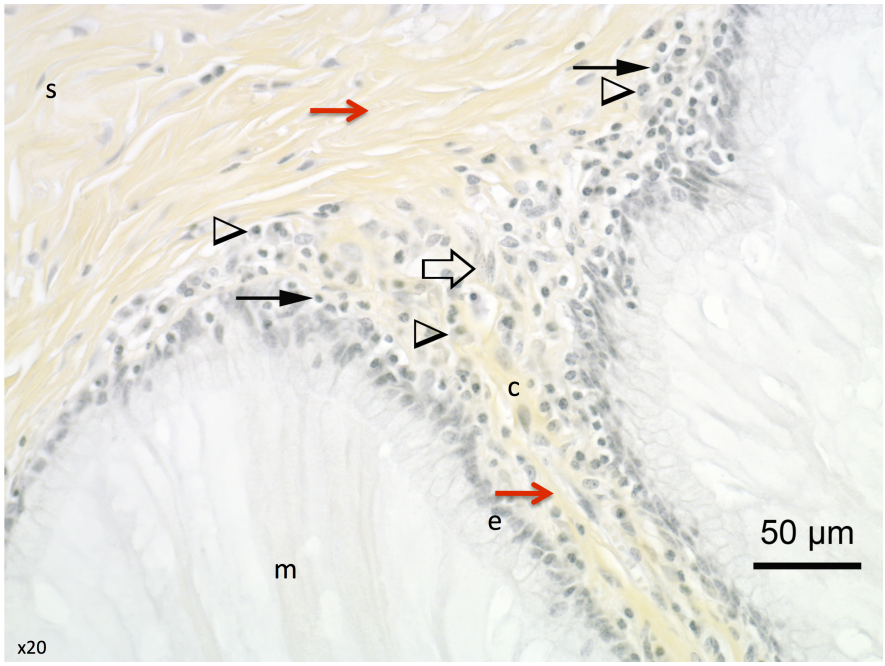

Figure 12.8: *Structures identified by histological evaluation in the cervical tissue. Mucous plug (m), epithelial cells (e), mucosal chorion (c), submucosa (s). Collagen fibres: red arrow; Macrophages: arrowhead; lymphocytes: solid arrow; fibroblasts: empty arrow.*

although some high inter-individual variability precluded any definitive conclusion. External diameter of the cervical mucosa tended to be higher in treated animals compared to untreated ones, respectively 7544 ± 337 and 6805 ± 327 μm, indicative of the relaxed gross appearance of the cervix in these animals (see Figure 12.10). No difference in the mucosal fold height was depicted between animal groups.

12.3.2 Second harmonic generation and two-photon fluorescence microscopy

2PF mucosal chorion and SHG imaging were performed simultaneously in 2 mm size regions covering the chorion, mucous plug and submucosa, with a spatial resolution of about 460nm (see Figure 12.11). Control and treated samples showed several differences, especially in the mucosal chorion, with consistency between different animals. Figure 12.12 shows zoomed images in control and treated samples and the corresponding 2D FT images, thresholded at 80% of their maximal intensity. SHG images in the control cases show well defined directional structures that are very reproducible from one region to another (Figure 12.12a,b), whereas the treated case shows more disorganised structures, at the scale of a few tens of μm up to 100 μm (Figure 12.12c,d).

12.4 Discussion

As it has been shown previously in this thesis in the human study (Chapter 11), cervical stiffness is continuously decreasing during pregnancy until the onset of labour, when dramatic changes in consistency lead to opening the cervix and allowing the fetus to pass. In

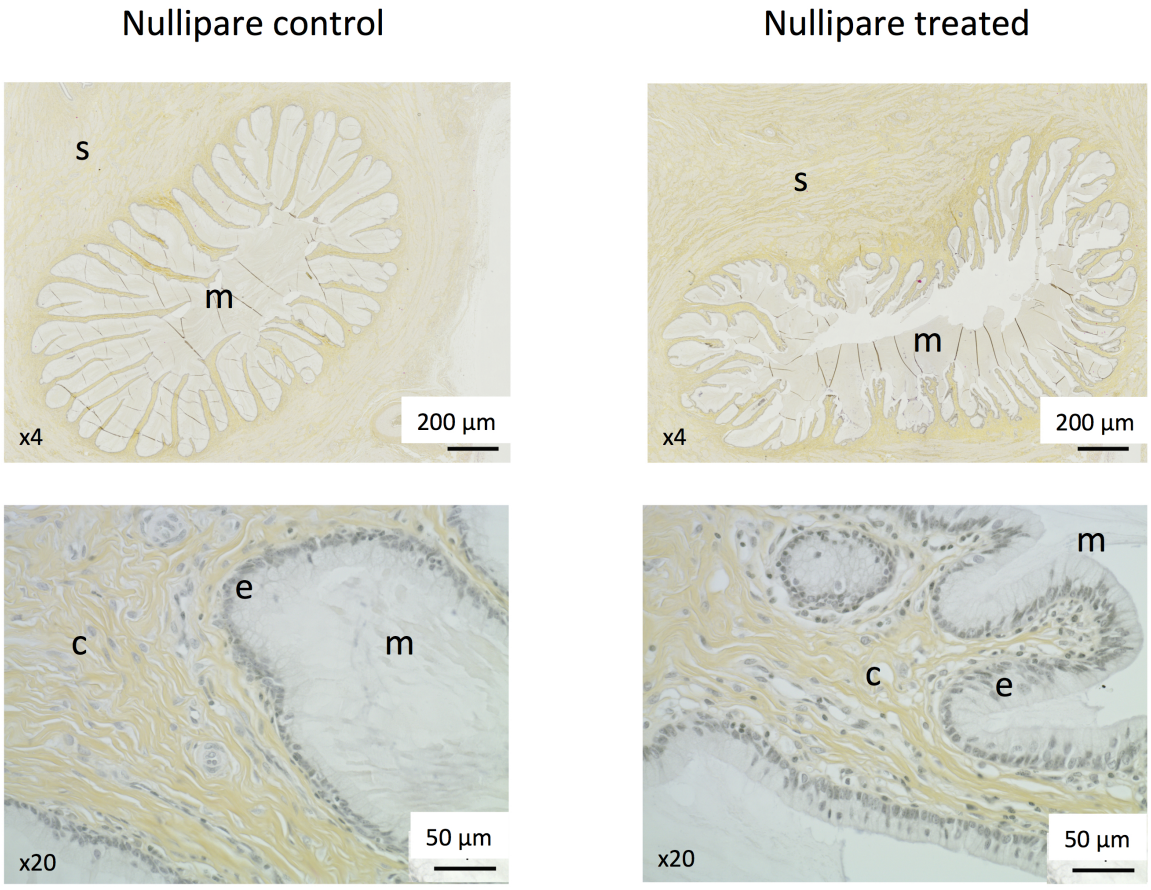

Figure 12.9: *Complete histological evaluation of the cervix. Mucous plug (m), epithelial cells (e), mucosal chorion (c), submucosa (s).*

Figure 12.10: *Measurement of the external diameter of the cervical mucosa (green line).*

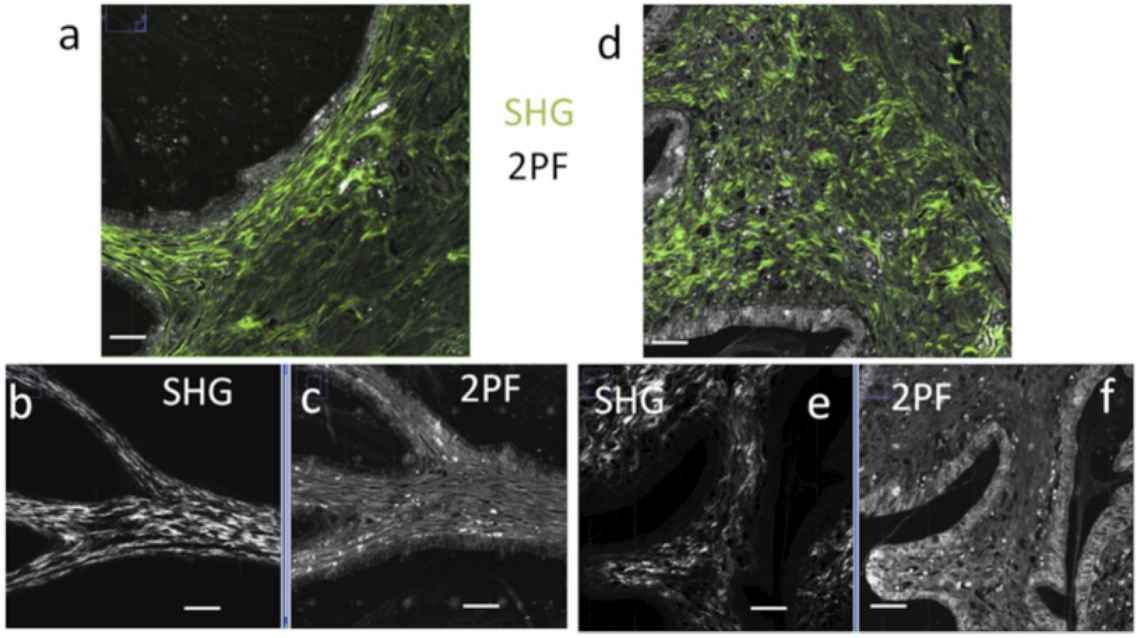

Figure 12.11: *SHG/2PF images. (a-c) control and (d-f) treated samples imaged in two photon microscopy, in the mucosal chorion/submucosa region of fixed slices. (a,d) Composite 2PF(grey)/SHG(green) image (scale bar: 100 μm). Separated SHG/2PF are shown in (b,c) and (e,f) inside the mucosal chorion (scale bar : 100 μm)*

the control animals, no statistical difference in cervical stiffness was observed at any time in this study. In addition, stiffness values matched those measured before the dexamethasone injection in the treated group. In contrast, cervical stiffness decreased significantly within 4 hours after induced cervical maturation by dexamethasone injection. This is consistent with the fact that cervical stiffness is significant reduced close to delivery. Previous studies have reported that cervical tissue is significantly softer at the end of the third trimester than at early pregnancy [27, 42, 51].

The cervix undergoes important changes during cervical ripening. This process involves catabolic processes leading to collagen degradation, inducing modifications of the collagen network, its geometrical configuration and mechanical properties within the cervical tissue. In this study, the changes in the mechanical properties of the tissue (measured with SWE) induced by the dexamethasone were associated with changes in the micro-structural organisation of the collagen matrix (measured with SHG and 2PF). Morphological features of the cervical collagen matrix changes during pregnancy encompass its transformation from an alienable fibrous matrix to an amorphous hydrated matrix capable of undergoing large distention [34]. SHG images exhibit collagen fibres assemblies with characteristic shapes similar to previous results on mice and humans [33, 75, 247]. While the submucosa region does not show significant morphological differences in the collagen fibres between the control and treated cases, the mucosal chorion is seen to undergo the strongest modifications. Fibre size and waviness as well as pore size are conserved throughout the mucosal chorion, with a more wavy and disorganised structure in treated samples (Figure 12.11d,e). Zoomed

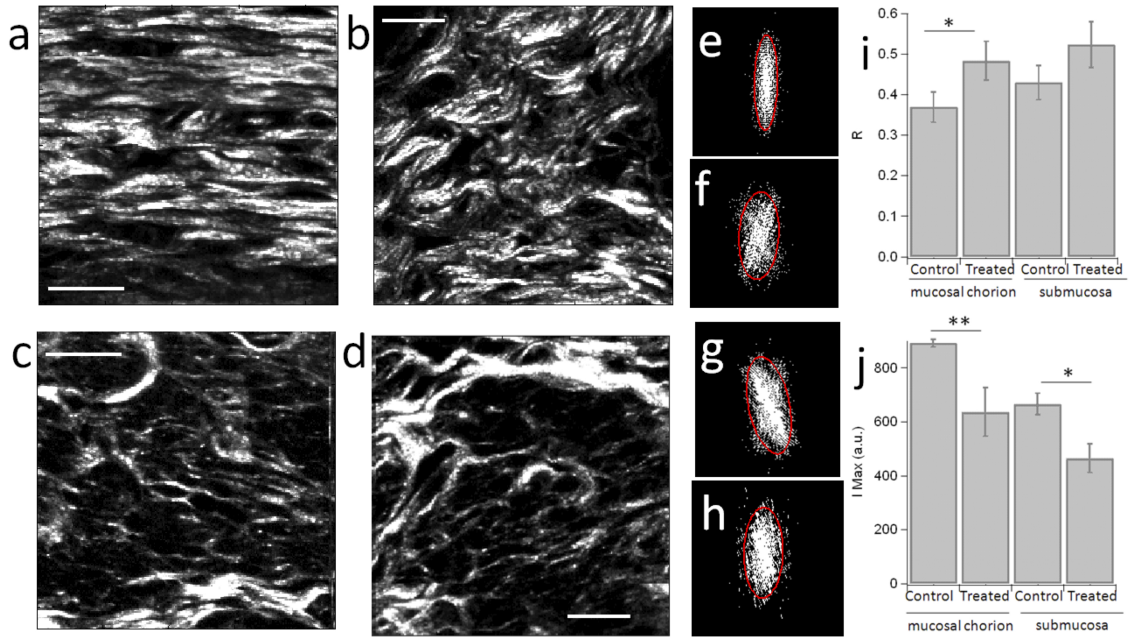

Figure 12.12: *Typical SHG zoomed images in the mucosal chorion region of (a) control and (b) treated samples, and in the submucosa region of (c) control and (d) treated sample. Scale bars: 20 μm. SHG ROI images are intentionally contrasted in order to enhance the visibility of the morphological differences between the control and treated samples. Corresponding 2D FT images, thresholded at 80% of their maximal intensity, are shown in (e-h) for (e) control-mucosal chorion (maximum intensity = 971 counts, R = 0.28), (f) treated-mucosal chorion (maximum intensity = 737 counts, R = 0.39), (g) control-submucosa (maximum intensity = 581 counts, R = 0.42), (h) treated-submucosa (maximum intensity = 412 counts, R = 0.43). Average values and standard deviations (plotted error bars) are given for 10 regions, measured from two different animals (Symbols * and ** indicate the significance level, $p < 0.05$ and $p < 0.01$, respectively)*

images in the control samples show well defined directional structures that are very similar from one region to another and from one animal to another in the mucosal chorion, while in the control sample, the fibers are seen to be well aligned and parallel (Figure 12.12a). The treated case shows more disorganised structures, at the scale of a few tens of μm up to 100 μm (Figure 12.12b). Note that there is no significant change in the fibre diameter, however fibre density is seen to slightly decrease in treated samples, with a visible change in waviness. In the submucosa region, for both control and treated samples, fibres are much more disorganised and heterogeneous in diameter, waviness and length (Figure 12.12c,d). In order to quantify the shape changes observed in the SHG images, 2D Fourier transform (FT) analysis of 10 ROI images size per region (chorion mucosa, submucosa) was performed in two different slices (e.g. two different animals). The size of these regions (typically 60 μm) was intentionally chosen such as to exhibit representative homogeneous structures, which were persistent in shapes over about a mm scale in the tissue SHG image. A 2D FT from aligned parallel fibres results in an elliptical shape, which orientation reflects the average direction of the fibres (given by its perpendicular direction), with a width that reflects the

extent of variations of the fibre directions along this average direction. This width is quantified by the ratio R between the ellipse short axis length and its long axis length. Figure 12.12e-h depicts typical ellipses obtained from thresholded 2D FT analysis for the SHG images shown in Figure 12.12a-d. A small R value means that fibres are very parallel to each other, while a high R value reflects more random orientations of fibres present in the image, including enhancements of waviness in the fibres shapes. Results (Figure 12.12i) show that R decreases from the control to the treated cases, both in the chorion mucosa and submucosa regions, with a more pronounced effect in the chorion mucosa. This reflects the loss of fibre directionality in the submucosa, as visible by the apparition of waviness. The treatment thus induces a clear disorganisation of collagen fibres at a scale of tens of μm (scale of the observed waviness of fibres in Figure 12.12b). In addition the SHG efficiency of collagen fibres is also seen to depend on the region and case. Maximum intensities (averaged over the 10 brightest pixels) were compared in the same ROI regions and previously analysed by 2D FT. Results depicted in Figure 12.12j show that the collagen SHG intensity significantly decreases from the control to treated region in both chorion mucosa and submucosa regions. These results are consistent with a more organised structure in the control chorion mucosa regions at the microscopic scale, where more parallel fibres lead to a more efficient build up of the coherent SHG signal and result in a higher intensity. This intensity effect also most probably reflects the loss of collagen density at a micro-metric scale. This microscopic scale observation is consistent with the degradation of the circumferential ring of collagen fibres observed in the cervix at the late stages of pregnancy in humans [33]. Overall, the quantitative changes in the mechanical properties proved by elastography seem to correspond to qualitative structural changes observed at the microscopic scale. This is in the agreement with the study [246], and seems to enforce the idea that straight and organised structures would favour more stiff mechanical properties. The relation between sub-micrometric resolution scale morphology and stiffness has been already evoked in previous work in other tissues such as collagen-rich tendons [248], liver [249] and prostate [250]. Similar results of cervix SHG imaging have been more recently obtained using endomicroscopy [75] and combined with B-mode ultrasound imaging and quantitative ultrasound (QUS) measurements, which corroborate it [247]. This supports the strong relation between collagen organisation and tissue mechanical properties, as also recently shown in various studies performed in collagenous tissues [251–253]. Despite the relationship between cervical micro-architecture and stiffness evidenced here, future works should focus on a longitudinal study to deeply explain this link between stiffness and the cervical remodelling.

2PF images show complementary information (Figure 12.11c,f). First, they show in clear contrast the contour of epithelial cells. They also exhibit fibrillar structures that are in close connection with collagen fibres. These fibres do not necessarily spatially overlap with collagen fibres, and could be assigned partially to elastin, with a structure visibly affected by the dexamethasone treatment since degradation appears. Even though the precise chemical identification of these structures is not known, their integrity is clearly seen to be affected

in the case of animals treated with dexamethasone. Both collagen and 2PF-active fibrillar structures would then be closely related to the mechanical properties of cervical tissues that are perceptible in elastography.

The morphology of collagen does not show any strong differences between control and animals treated with dexamethasone in histology results, in contrast to optical microscopy images. This is probably due to the different origin of the contrast and to the scale of observation, which is significantly larger in histology images. Histology results show that the external diameter of the cervical mucosa increases in treated animals compared to control ones (Figure 12.10). This is in agreement with previous observations [254]. It has been reported that the circumferential ring of collagen fibres presents in the cervix at early term disappears at later stages of pregnancy, close to delivery [33]. This phase of cervical remodelling gives the cervix the ability to dilate in response to uterine contractions of labour. The B-mode images presented in this study are consistent with this occurrence of remodelling. In the control group, as well as for the first measurement of the dexamethasone group, it is possible to identify some well defined structures in the rings that characterise the cervix of sheep. As soon as the dexamethasone starts to operate, these structures become diffused, being difficult to identify in the last measurements, when they practically disappear.

It is known that dexamethasone reaches its maximum effect between 2 and 3 hours following injection [255]. This has been reflected here by the fact that the highest drop in elasticity is observed in the first measurement after injection. This drop represents more than the half of the total stiffness reduction (total stiffness reduction 40.58%) as shown in Figure 12.5. The second order fit performed in the treated group confirms that dexamethasone effects are higher during the first hours.

Previous studies performed in humans suggest that ripened cervices are more like each other than are the unripened ones [48, 150]. This can be consistent with the fact that in the animals treated by dexamethasone elasticity measurements were not significantly different between nulliparous and multiparous animals, whereas the control group presented significant differences. However, in this study, no trend was observed in the dynamic range of stiffness. In sheep, fetal endogenous cortisol secretion rise only in the last two weeks of gestation whereas in humans, the rise starts from mid-pregnancy [256] and this may be the reason for this difference between observations in the present study and those in women.

The objective of this study was to explore the SWE method's feasibility and to describe the elastographic patterns of the cervical maturation, providing physiologically relevant data that could give insight into the microstructure-stiffness link. A comprehensive quantitative assessment of cervical ripening requires the calculation of the elastic moduli. As happened with the human clinical study, the main limitation of this study is related to the assumptions made for the assessment of stiffness from the shear wave speed values, namely a locally homogeneous, isotropic and semi-infinite medium. To estimate the elasticity, SWE technique relies on the assumption that the medium is locally homogeneous, isotropic and semi-infinite. However, at the beginning of this experiment, before cervical maturation was

induced by dexamethasone, collagen fibres may present a high orientation and thus these conditions might not have been satisfied. The cervix is heterogeneous, anisotropic and only a few times larger than shear wavelengths that are characteristic in SSI. However, all of the statistical tests have been done very carefully, and apply to the shear wave speed values as well as to the stiffness values. The ROIs assume small homogeneous areas and they allow the assessment of the ability of SWE to distinguish between ripened and unripened cervix by quantifying the elasticity. Further studies are required to judge the effect of the above parameters and to compare the findings in women. Experimentally, these morphological characteristics are difficult to investigate individually, and this motivates the use of a numerical model. which is the main core of the rest part of this thesis.

Finally, the viscoelastic nature of cervical tissue makes the elastic modulus dependent on the frequency [231]. This dependence on the frequency is numerically studied in this thesis and its results are presented in Chapter 13. This viscoelastic nature of soft tissues makes all elastography techniques be influenced by the pressure applied by the practitioner. Nevertheless, this issue can be easier to control in SWE [241]. As it has been already reported by the clinical human study presented in Chapter 11, SWE is less user-dependent, since the ultrasound beam creates the displacements and furthermore, can reach deeper areas of the cervix than quasi-static methods. In order to obtain reproducible measurements, the pressure applied on the cervix by the sonographer with the probe had to be minimal, and the ROI has to be placed away from the surface of the probe. The election of the second ring as ROI was based following these criteria. The second ring of collagen was chosen because it is an easy anatomical landmark and because it is located far enough from the cervical *os* so that the measurement could be minimally influenced by any pressure that could be exerted by the operator. It has been shown that, following these criteria SWE measurements were highly reproducible in all the cases.

12.5 Conclusions

An experimental protocol for monitoring the cervical stiffness during ripening has been developed. The combination of different tools as SWE, histology and two-photon excitation microscopy have provided physiologically relevant data for validating our mechanical remodelling hypothesis and linking it with SWE measurements. In particular, the principal findings of this study are that, first, shear waves elastography measurements using Supersonic Shear Imaging (SSI) technique were highly reproducible. We have shown that the stiffness measurements obtained by the same and by two different observers are reliable and reproducible. Second, stiffness of the uterine cervix changes throughout the maturation process artificially induced by the dexamethasone injection. In general, the control group (unripened cervix) presents the highest stiffness, and the lowest stiffness values correspond to a measurement closer to delivery in the labour induction group. Finally, the maturation process was validated by a significant increase in PGE2 twenty-four hours following dexamethasone treatment and by changes in the micro-structure of the tissue as observed by SHG

and 2PF images. It has been evidenced that, these changes at the microscopic scale during cervical remodelling may be partly responsible for the mechanical properties measured by elastography.

Objective measurements of stiffness reflect histological changes that could provide a measure of cervical ripening, and shear wave elastography may be a valuable method to objectively quantify the cervical stiffness. Standardisation of the cervical properties observed on elastography during pregnancy may help to guide the artificial labour induction and to diagnose preterm birth. Further studies are needed to relate shear wave propagation with histological and endocrine modifications in the cervix. For this purpose, animal models are necessary as they provide a means to generate physiologically relevant data that can then be evaluated in humans.

13

Viscoelastic description of cervical tissue

In this chapter, we describe the results of a numerical model that aimed at determining the viscoelasticity of cervical tissue from shear wave velocity using elementary rheological models. The results presented here constitute the first step of the numerical contribution of this thesis and were designed with the target of determining the most convenient excitation frequency and the best rheological law to describe the micro-structure of the cervix using shear waves. To this end, the dependency on the excitation frequency of the viscoelastic properties of cervical tissue is studied and the inverse problem is introduced to provide the most plausible rheological model that describes cervical tissue.

Section 13.1 shows the FDTD numerical shear wave propagation within the spatial media proposed to mimick cervical tissue. Section 13.2 presents the results for identifying viscoelastic parameters estimated by an inverse problem procedure. They are obtained by fitting the shear velocity dispersion curves with three proposed rheological laws. In Section 13.3, goodness-of-fit metrics are compared for the three models at a proposed frequency bandwidth and the plausibility of each rheological model is assessed by applying a stochastic model-class selection formulation. Finally, in Section 13.4, we discuss the ability of the proposed rheological laws to reproduce the simulated dispersion curves and thus to describe the viscoelastic behaviour of cervical tissue.

13.1 Numerical shear wave propagation

The cervical tissue was described at the micro-scale using the parametrized morphology model presented in Chapter 9. The values of the parameters that characterise the spatial model used in the simulations are summarised in Table 13.1. The Poisson's ratio, ν, can be

calculated from the Lamé parameters as $\nu = \frac{\lambda}{2(\lambda+\mu)}$. Note that the ECM or matrix material is described as a quasi-incompressible material ($\nu \approx 0.5$). The Poisson's ratio assumed here ($\nu = 0.499$) does not present any numerical problem in the simulations and corresponds to the range usually assumed in the literature to describe soft tissues [257].

Mechanics [kPa]	*Morphology* [μm]	*Composition* [%]
λ_{matrix}: $1.65 \cdot 10^6$	waviness: 15	hydration: 80
μ_{matrix}: 7.8	diameter: 5	fibrillar collagen: 20
λ_{fibres}: $1.73 \cdot 10^5$	gap: 1	GAG's: 1.5
μ_{fibres}: $7.7 \cdot 10^4$		cells: 8
		elastin: 2.5

Table 13.1: *Values of the different parameters, grouped into mechanics, morphology and composition, used in the FDTD simulations. Percentages are given with respect to dry tissue, except hydration and fibrillar collagen that refer to total tissue.*

Figure 13.1 shows the spatial media characterised by the paramaters listed in Table 13.1.

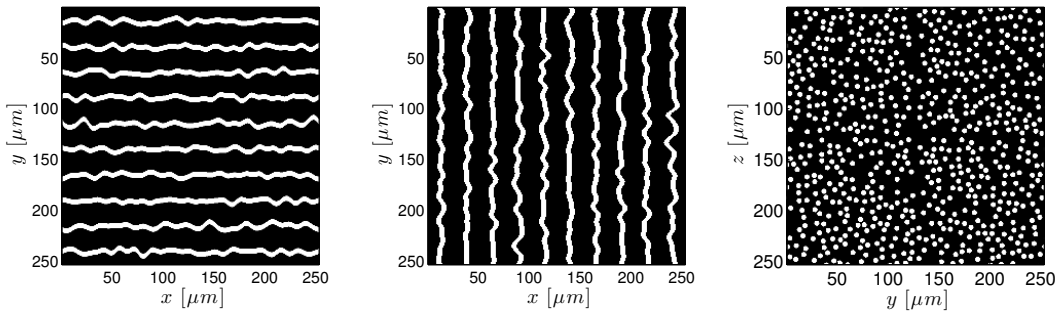

(a) (b) (c)

Figure 13.1: *Spatial media used in FDTD simulations: (a) longitudinal sections with fibres arranged in parallel and (b) perpendicular to the shear wave propagation, and (c) transversal section.*

Shear wave propagations within the spatial media of cervical tissue, shown in Figure 13.1, were numerically simulated by the heterogeneous FDTD numerical model described in Chapter 8. For each sample, a plane wave was transmitted through the medium from $x = 0$ μm to $x = 250$ μm. A simulation duration of 160 μs was chosen, which is enough time to guarantee most of the energy transmission within the proposed spatial media. The source was modelled as a broadband shear velocity pulse with a central frequency that ranges from 15 kHz to 200 kHz ($f = \{15, 25, 35, 50, 100, 150, 200\}$ kHz). Spatial and time discretizations were chosen following the stability conditions described in Section 8.2.3. The spatial resolution step was adjusted to 1 μm. At the frequency of 200 kHz, a spatial step of 1 μm corresponds to a discretization of 14 grid points per wavelength in the matrix material, which is therefore sufficient to describe the ultrasound propagation at the kHz range and to avoid the dispersion errors. The projection of the particle velocity, v_y, was recorded at each grid point. An example of the simulated shear wave propagation through the three spatial media after

60 μs of propagation is depicted in Figure 13.2 for the extreme excitation frequency values, namelv 15 and 200 kHz.

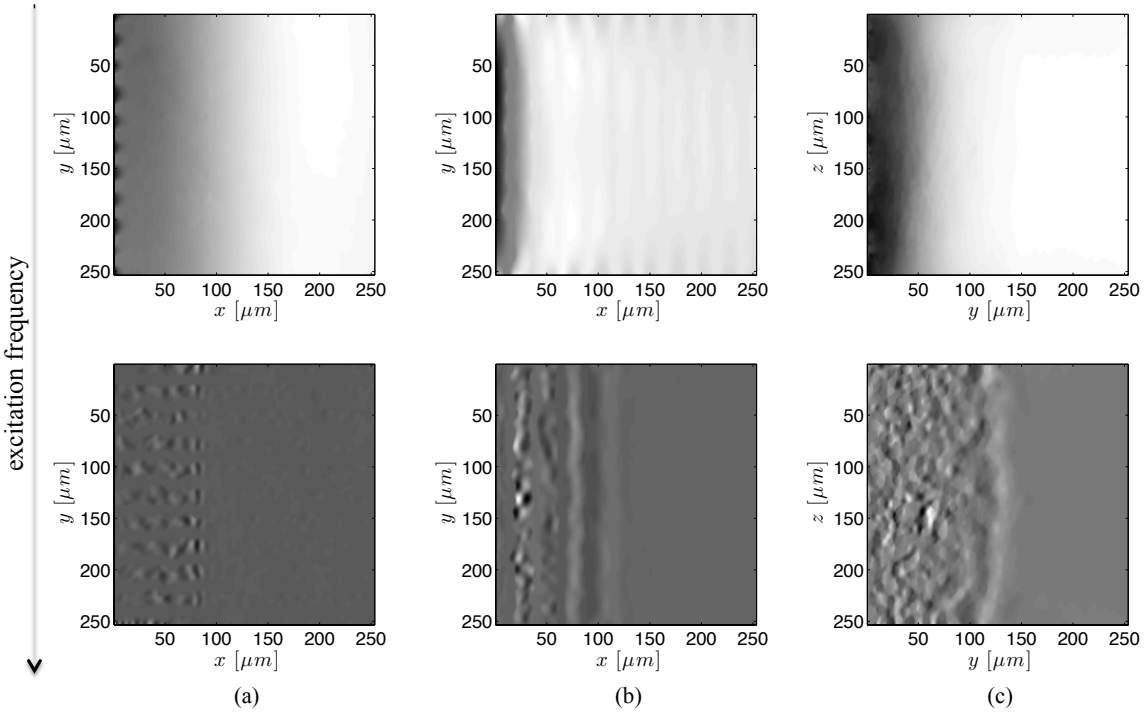

Figure 13.2: *Representation of FDTD simulated shear waves transmitted through the three spatial media of Figure 13.1 after 60 μs of propagation and excitation frequency that ranges from 15 kHz (upper graphs) to 200 kHz (bottom graphs). (a) Longitudinal section with fibres arranged in parallel to the shear wave propagation direction, (b) longitudinal section with fibres arranged in perpendicular to the shear wave propagation direction, and (c) transversal section.*

13.2 Estimation of viscoelasticity

From the simulated propagation movie, it is possible to extract the shear wave velocity dispersion curve by a phase difference algorithm. The procedure was explained in Section 10.2 and summarised in Figure 10.1.

Typical estimated shear wave phase velocities (dots), simulated with the extreme excitation frequency values, 15 kHz and 200 kHz, are depicted in Figure 13.3 as a function of frequency in the three spatial media. The lines are the optimal fits from the rheological laws of Equations (10.5)-(10.6). Similar dispersion curves were obtained by repeating the wave data acquisition for the whole excitation frequency range (from 15 kHz to 200 kHz) under monochromatic excitation. Figure 13.4 shows the associated spectral analysis corresponding to the extreme excitation frequency values and for each spatial model.

Both elasticity μ and viscosity η vary not only with the excitation frequency but also with the spatial medium and the rheological law that models the viscoelastic behaviour. Their dependence on the excitation frequency is plotted in Figure 13.5. Mean values, calculated from

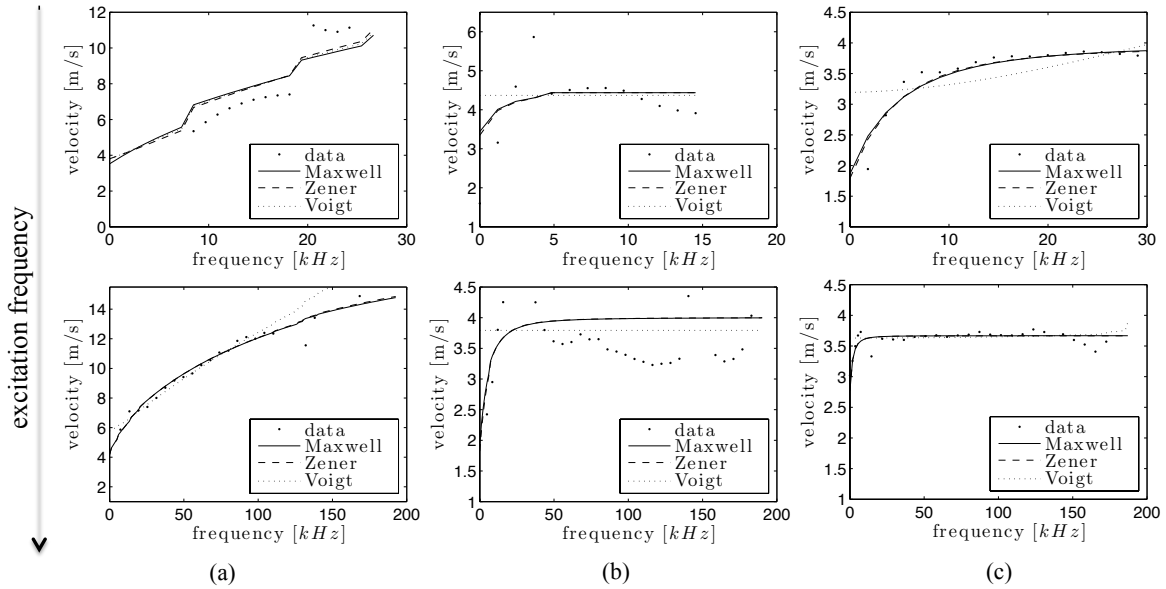

Figure 13.3: *Fitting of Maxwell, Zener and K-V models to the estimated dispersion curves, in the three spatial media at an excitation frequency that ranges from 15 kHz (upper graphs) to 200 kHz (bottom graphs). The line graphs represent the best fit of each model. (a) Longitudinal section with fibres arranged in parallel to the shear wave propagation direction, (b) longitudinal section with fibres arranged in perpendicular to the shear wave propagation direction, and (c) transversal section.*

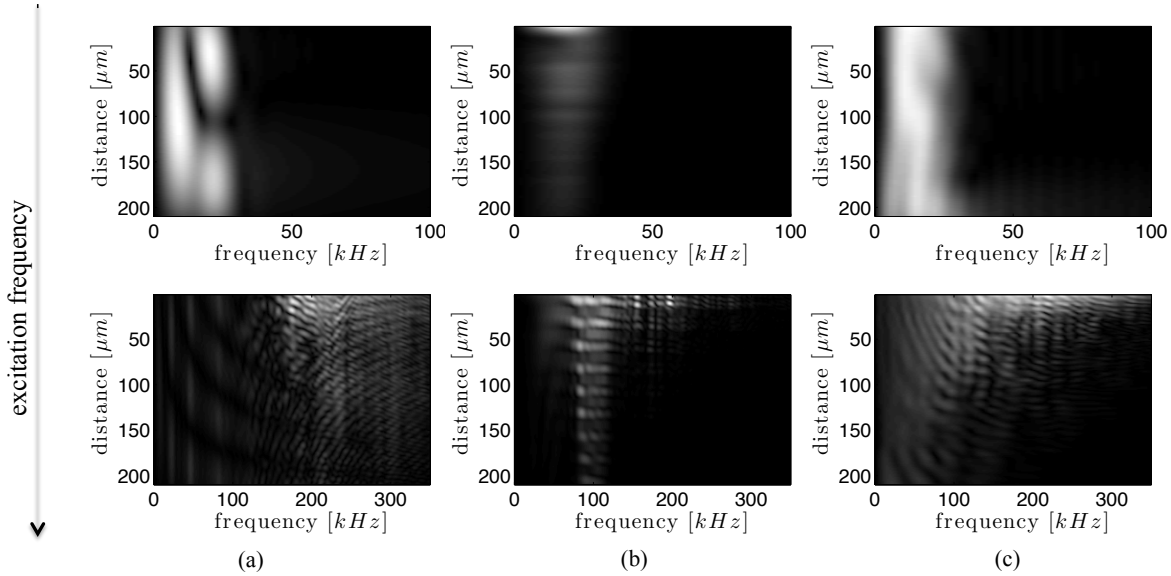

Figure 13.4: *Spectral analysis in the three spatial media for an excitation frequency that ranges from 15 kHz (upper graphs) to 200 kHz (bottom graphs). The power spectrum is described in grey scale, where white corresponds to the maximum and black represents zero energy. (a) Longitudinal section with fibres arranged in parallel to the shear wave propagation direction, (b) longitudinal section with fibres arranged in perpendicular to the shear wave propagation direction, and (c) transversal section.*

simulations on three different randomly created spatial media with similar characteristics, are represented. In the longitudinal sections, Maxwell and Zener laws do not considerably

differ in both elasticity and viscosity. This is not surprising since Zener's law represents a particular case of a general Maxwell's model. It is worth pointing out that both viscoelastic parameters are generally lower in the K-V law than in the other two.

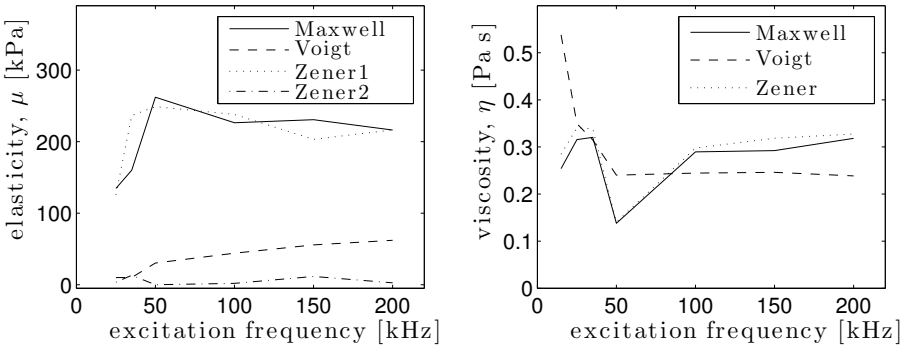

(a) Shear wave propagation along the fibres in the longitudinal profile ($\phi = 0^o$)

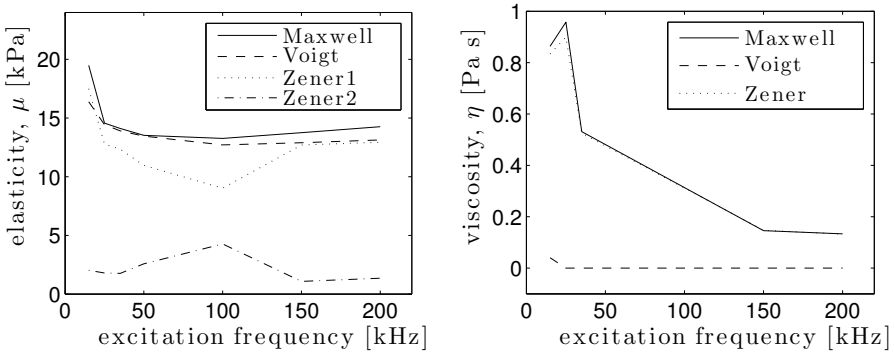

(b) Shear wave propagation across the fibres in the longitudinal profile ($\phi = 90^o$)

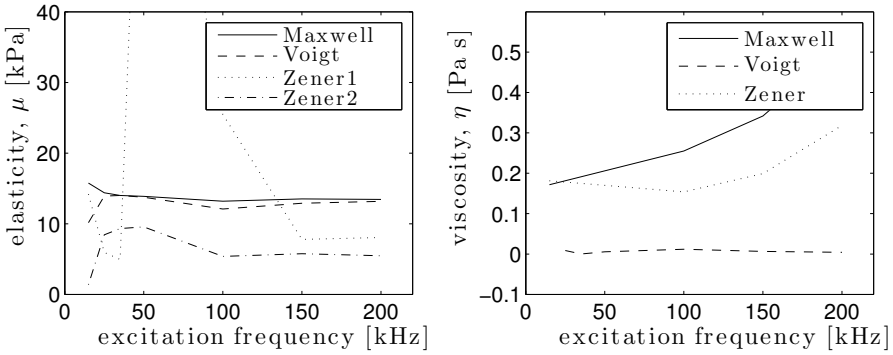

(c) Shear wave propagation through the transversal profile

Figure 13.5: *Evolution with the excitation frequency of the estimated parameters (elasticity, μ, and viscosity, η) in each rheological model, and employing the three proposed spatial media for the shear wave propagation.*

13.3 Rheological law selection

The probability density function of the different rheological laws and spatial media was computed for the excitation frequency range. Figures 13.6 and 13.7 show the PDF for the

extreme excitation frequency values, i.e., 15 kHz and 200 kHz, respectively. Since the PDF is a multidimensional function, only a slice along two parameters is represented and in the case of Zener model, which is defined by three parameters, only μ_1 and η are represented. The inspection of these plots reveals some local minima as valleys in the PDF, and variations of several orders of magnitude from good to bad reaction model parameters. This implies a bad conditioning of the reconstruction IP and justifies the use of advanced search algorithms such as genetic algorithms. The PDF for the other excitation frequencies present similar trends, but are not displayed here for sake of brevity.

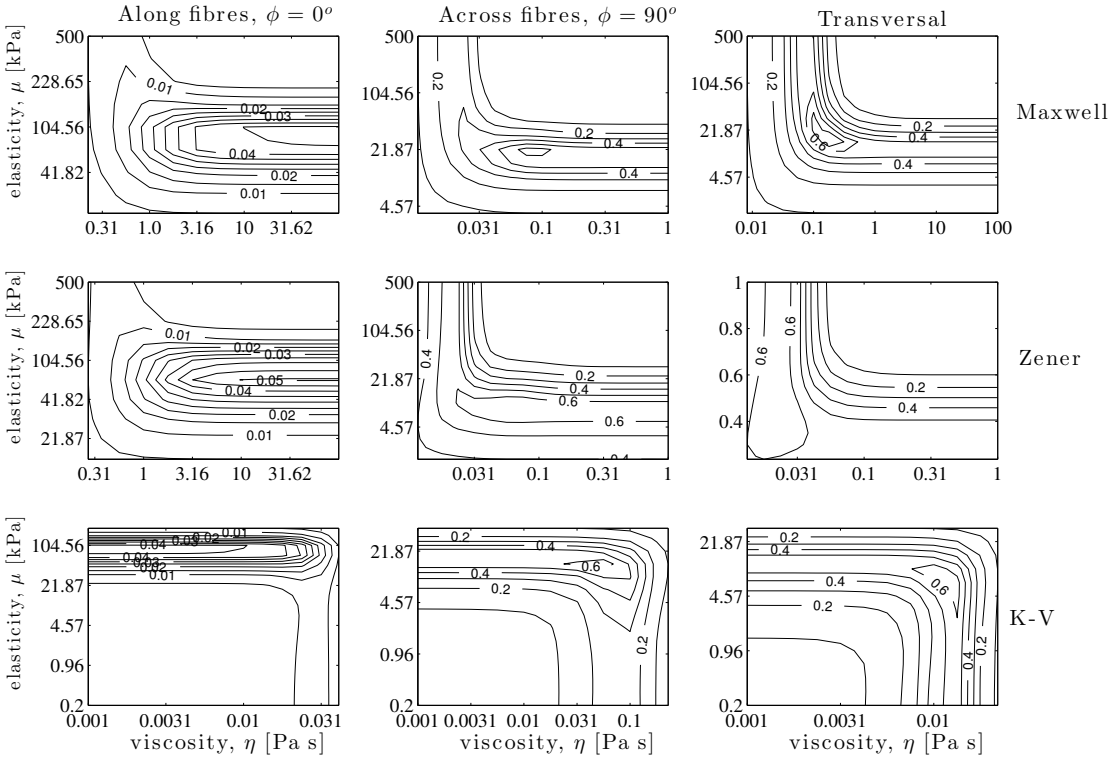

Figure 13.6: *Probability density* $(P(m)[\log_{10} - scale])$ *of the different rheological laws and spatial media, for an excitation frequency at 15 kHz.*

The plausibility of each rheological model was found by applying the stochastic model-class selection formulation described in Section 10.3.2. The posterior probability of every proposed rheological law is shown in Figure 13.8. The joint plausibility shows that the most plausible rheological model is Zener. It is closely followed by Maxwell, whereas K-V model is the less plausible. However, distinctions among these three rheological models depend on the load frequencies applied to the spatial media. Frequency determines which rheological model can be representative for the tissue. At higher frequencies, over 100 kHz, Maxwell's law rises probability while it drops in Zener's one. At 15 kHz excitation frequency, the probabilities of each rheological law are 31.09%, 37.00% and 31.92%, for Maxwell, Zener and K-V, respectively. At higher frequency, e.g. 200 kHz, these probabilities change to 34.94%, 41.91%

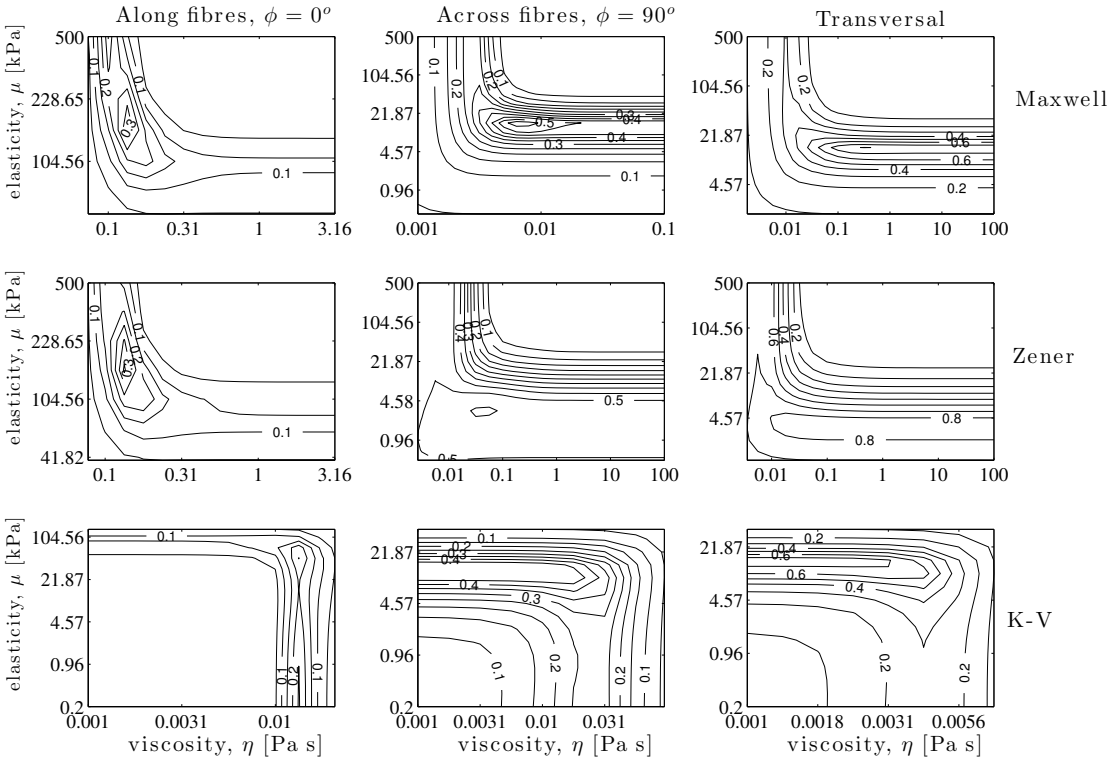

Figure 13.7: *Probability density* $(P(m)[\log_{10} - scale])$ *of the different rheological laws and spatial media, for an excitation frequency at 200 kHz.*

and 24.04%; which shows how Maxwell's law fits better at higher frequencies. Moreover, distinctions can be made depending on the spatial medium. At frequencies over 50 kHz, Maxwell's law is the most plausible model in the longitudinal section with the fibres arranged in perpendicular to the wave propagation direction ($\phi = 90^o$), and in the transversal section as well. However, for the shear wave propagation along the fibres in the longitudinal section ($\phi = 0^o$), the most plausible law is Zener, followed by K-V, which exceeds Maxwell plausibility. Notwithstanding, no rheological law may be able to fully represent tissue measurements over the entire frequency range. Different results were observed for lower frequencies (< 50 kHz), where it is not possible to identify one single law that dominates the viscoelastic behaviour in all the spatial media. The total plausibility over the complete excitation frequency range is shown in Table 13.2.

Spatial medium	Along fibres ($\phi = 0^o$)	Across fibres ($\phi = 90^o$)	Transversal	joint
Rheological law				
Maxwell	30.12%	29.79%	36.73%	32.21%
Zener	16.56%	53.66%	49.68%	39.97%
Voigt	53.32%	16.54%	13.59%	27.82%

Table 13.2: *Plausibility of rheological models over the complete excitation frequency range.*

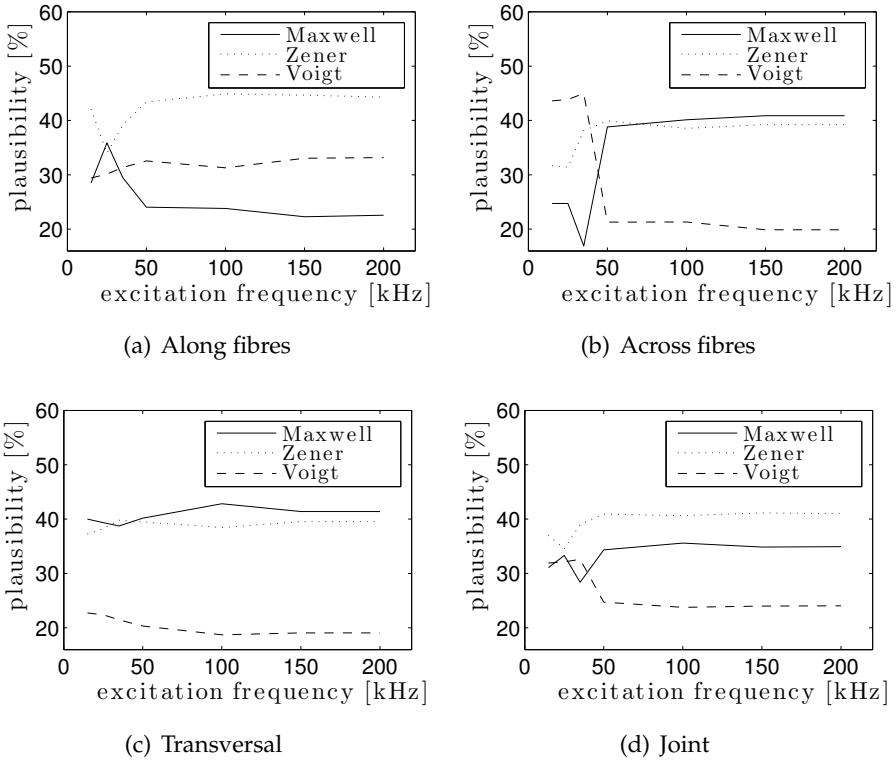

(a) Along fibres (b) Across fibres

(c) Transversal (d) Joint

Figure 13.8: *Plausibility of the proposed rheological models: Maxwell (solid line), K-V (dashed line) and Zener (dotted line); for the excitation frequency range. Values for longitudinal sections with shear wave propagation along ($\phi = 0^o$) and across the fibres ($\phi = 90^o$), transversal section, and joint plausibility for the three spatial media are plotted.*

13.4 Discussion

This study is aimed at understanding the shear waves-tissue interactions, which may determine the optimal excitation frequency and the rheological model, to finally characterise the viscoelasticity of cervical tissue. Modelling the complex rheological behaviour of cervical tissue is a challenging task and the choice of a model is a priori far from obvious. Here, such a model selection is based on the balance between the error and the complexity of the model. Therefore, the goal was determining which is the rheological law that, with less parameters (simplicity of the model) best describes (minimum model error) the viscoelastic behaviour of cervical tissue. Among the tested rheological models, the Zener law best reproduces the simulated dispersion data in cervical tissue, however is the most complex model too (more parameters). Moreover, Maxwell model is the simplest rheological law (defined by less parameters) that better characterises the viscoelastic behaviour of cervical tissue, contrarily to common belief in literature [221]. Results show that the dispersion data fit to the K-V law is poorer than the fits to the Maxwell and Zener laws. One reason for the poorer fit is that K-V model does not capture the quick increase in phase velocity often observed at low frequencies. Similar results have been reported previously for in-vivo studies performed on other kind of soft tissues [222]. Although initially conceived for cervical tissue, the results of the present study may be generalizable for collagenous tissues with a family of aligned

collagenous fibres. Even if soft tissues differ in structure and function, a common feature is that their gross mechanical behaviour is influenced by collagen and its interactions with other components of the tissue.

Results show that simulated measurement distortions from wave reflections bias modulus estimates in a manner that depends on the shear wavelength. Viscoelastic nature of cervical tissue and its heterogeneity influence the shear wave propagation and consequently the gross response of the tissue, as a consequence micro and macro mechanics may be different. Thus, the elastic modulus cannot be directly deduced from the shear group velocity as in homogeneous media, but is intrinsically related to the dispersion equation. Shear waves interact with collagen fibres (microscale), which determines macroscopic properties (centimetre scale), and are responsible for the mechanical behaviour of connective tissue. This supports the idea that a correct understanding of the tissue rheology is required to consistently quantify its viscoelastic properties. Figure 13.4 shows that each spatial medium has different dispersive effects, which determine the phase velocity. Bias is also shown to occur if the rheological model is not representative of the tissue at the excitation frequency used for measuring viscoelastic properties. The K-V model is the current default in elastography imaging, but recent studies [222, 244, 258] suggest a role for other models. In this study, both Maxwell and Zener models are representative for different frequency range. Currently, no rheological model is clearly able to model cervical tissue. The best rheological model will be the one that generates parameters that are reliably sensitive to the histological features that change during pregnancy [231].

From the results we can deduce not only the best rheological law to describe the spatial medium, but also its dependency on the frequency range and the most convenient excitation frequency. Our results suggest convergency at the high frequency response. Frequencies over 100 kHz allow to get viscoelastic parameters less dependent on the frequency. That supports the idea that wavelength may condition the interactions between shear waves and the microstructure of cervical tissue, and therefore viscoelastic properties. Notwithstanding, all current elastography techniques are characterised by a limited frequency band, below a few kHz and such a wavelength may constrain the sensitivity of the technique to the cervical microstructure and in particular, to the cervical remodelling.

To our knowledge there are no previous results reported in the literature on shear viscoelastic measurements in cervical tissue. In this chapter, the results were compared to viscoelastic studies in cervical tissue under compression [37, 243]. Both elasticity and viscosity increase significantly with frequency. Nevertheless, our results do not show an increasing viscosity in all the cases. Collagenous tissues exhibit multi-scale architecture and this complex structure originates multiple scattering effects at the microscopic level, which may condition the complex shear modulus and therefore, elasticity and viscosity. This apparent frequency dependence of viscosity is an evidence that the K-V model is incomplete. This model is shown to be the less plausible to represent cervical tissue in our study (see joint plausibility in Table 13.2). The higher elasticity value in the section with the fibres arranged

in parallel than in perpendicular has been reported too in the literature, not only for cervical tissue but also for ligaments and muscles [219, 259]. In addition, the simulated elasticity values correspond to the range of real values measured *in-vivo* in the women clinical study presented in Chapter 11.

The main limitations of this study are related to the dispersion curve estimation. The wave number is estimated as the slope from a linear regression analysis applied to the temporal phase of particle velocity measured along the propagation distance. However, the maximum distance where the linear fit can be performed depends on the wave amplitude and when the medium is not homogeneous and high dispersive, the phase gradient might not be constant along the propagation distance. Although the target of this study was to find the simplest rheological model to describe cervical tissue, the feasibility of more complex models should be test in a future.

Finally, the findings of this study have provided the needed information to design the numerical study about cervical remodelling, which is described in Chapter 14. The optimal rheological law and the frequency excitation, which guarantees microstructure-shear wave interactions, have been chosen according to the results presented here.

13.5 Conclusions

In this chapter, a numerical method to determine the viscoelastic properties in soft tissue has been developed by combining the solution of a inverse problem with FDTD simulations, applying genetic algorithms to minimise a cost function and using different rheological laws to model shear velocity in the tissue. Based on a stochastic model-class selection formulation, the Maxwell's law has been shown to be the simplest model that best describes cervical tissue. Furthermore, the changes with excitation frequency in the viscoelastic properties of cervical tissue were studied and dispersion curves from 15 to 200 kHz excitation frequency were characterised. It has been reported that wavelength may condition the shear waves-collagen interactions in the cervix, and therefore viscoelastic properties. Results show how measurement distortions from wave reflections bias modulus estimates in a manner that depends on the shear wavelength. Thus, wavelength and consequently frequency are determinant for micro-scale interrogation. Results suggest convergency at high frequency, and excitations over 100 kHz allow to get viscoelastic parameters less dependent on the frequency.

14

Mechanical assessment of cervical remodelling during pregnancy

This chapter presents the results of a numerical histo-mechanical model. The target of this study was to link variations in the microscopic histo-biomechanical process that characterise the cervical ripening with shear wave characteristics. Parametric simulations were carried out for a broad range of mechanical and geometrical parameters that are related to cervical remodelling.

Section 14.1 shows the FDTD numerical propagation within the spatial media proposed to describe cervical tissue. Section 14.2 presents the results from the parametric study, which is split into two parts. The results concerning the morphology are shown in Section 14.2.1. Section 14.2.2 shows the results from the parametric study focused on biomechanics. Finally, the principal findings are discussed in Section 14.3.

14.1 Numerical shear wave propagation

Using the heterogeneous FDTD numerical model described in Chapter 8, shear wave propagations within cervical tissue were numerically simulated. The cervical remodelling was simulated by the morphological and mixture-theory-based model described in Chapter 9. The ranges of the values of the different parameters used to define the spatial model and emulate the cervical maturation, grouped into mechanics, morphology and composition, were shown in Table 9.3. For each sample, a plane wave was transmitted through the spatial medium from $x = 0\ \mu m$ to $x = 250\ \mu m$. The source was modelled by a broadband shear velocity pulse characterised by a central frequency of 150 kHz. The choice of the excitation

frequency was based on the results presented in the previous chapter. Those results showed that wavelength and consequently frequency are determinant for micro-scale interrogation and that excitations over 100 kHz allow to get viscoelastic parameters less dependent on the frequency. Therefore, the chosen frequency in this study guarantees the microstructure-shear waves interactions and furthermore stable viscoelastic parameters.

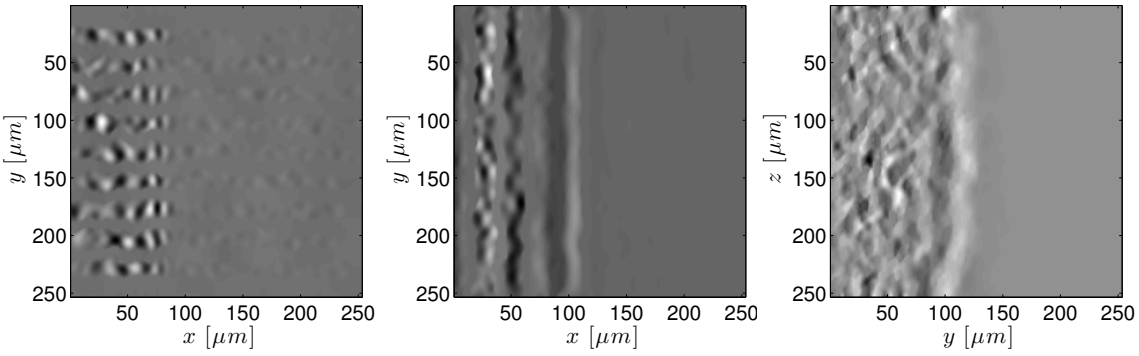

(a) (b) (c)

Figure 14.1: *Representation of FDTD simulated shear waves propagation, at time $t = 60$ μs, transmitted through the three spatial media: (a) longitudinal sections with fibres arranged in parallel and (b) perpendicular to the shear wave propagation direction, and (c) transversal section. In this example, the synthetic media are defined by 20% fibre fraction, standard deviation that characterises the waviness 15 μm, diameter of fibre 5 μm, gap between fibres 1 μm, $\mu_{fibres} = 5.2 \cdot 10^4$ kPa, $\mu_{matrix} = 7.15$ kPa, $\lambda_{fibres} = 1.21 \cdot 10^5$ kPa, $\lambda_{matrix} = 1.65 \cdot 10^6$ kPa.*

The spatial resolution step was adjusted to 1 μm and a simulation duration of 160 μs was chosen. The projection of the particle velocity, v_y, was recorded at each grid point. An example of the simulated shear waves propagation through the three spatial media, longitudinal sections with fibres parallel ($\phi = 0^o$) and perpendicular to the wave propagation direction ($\phi = 90^o$) and transversal section, at time of 60 μs is shown in Figure 14.1. The corresponding normalised received signals after 250 μm of propagation are depicted in Figure 14.2.

14.2 Parametric study of the cervical maturation

The simulated cervical maturation was mechanically characterised by shear wave simulations. The study can be divided into two different parametric studies: (i) morphology of collagen fibres and (ii) biochemical composition. Results show the dependence of viscoelastic parameters (elasticity and viscosity), the attenuation and the shear group velocity on the morphological and biomechanical parameters that mimic the cervical maturation. The viscoelastic parameters were estimated following the procedure explained in Section 10.2 and summarised in Figure 10.1, with the particularity that the chosen rheological model in this case was the Maxwell's law. Results shown in the previous chapter support the suitability of this model to describe cervical tissue at the chosen frequency.

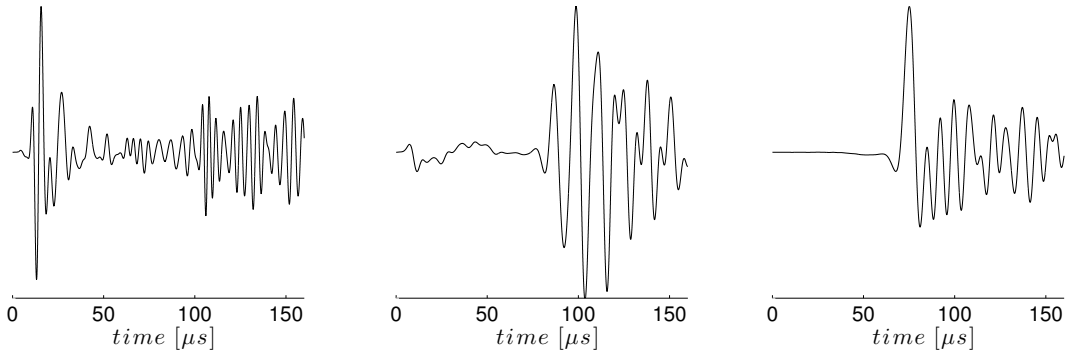

(a) (b) (c)

Figure 14.2: *Normalised received signal after 250 μm of propagation in the three spatial media: (a) longitudinal sections with fibres arranged in parallel and (b) perpendicular to the shear wave propagation direction, and (c) transversal section. In this example, the synthetic media are defined by 20% fibre fraction, standard deviation that characterises the waviness 15 μm, diameter of fibre 5 μm, gap between fibres 1 μm,* $\mu_{fibres} = 5.2 \cdot 10^4$ *kPa,* $\mu_{matrix} = 7.15$ *kPa,* $\lambda_{fibres} = 1.21 \cdot 10^5$ *kPa,* $\lambda_{matrix} = 1.65 \cdot 10^6$ *kPa.*

Due to the random nature of the numerical samples, we obtain a coherent value for each parameter by averaging over 3 equivalent randomly generated spatial models. Results are expressed as mean ± standard deviation.

14.2.1 Morphology

The parameters analysed in the morphological parametric study are related to the collagen network. The influence of waviness, diameter and gap between fibres were studied. Table 14.1 shows the values of the different parameters used for the simulation in this parametric study. Mechanics and composition are kept constant, while the parameters related to morphology vary between the proposed ranges.

Mechanics [kPa]	***Morphology* [μm]**	*Composition* [%]
λ_{matrix}: $1.65 \cdot 10^6$	waviness: $(5 - 45)$	hydration: 80
μ_{matrix}: 7.8	diameter: $(3 - 10)$	fibrillar collagen: 20
λ_{fibres}: $1.73 \cdot 10^5$	gap: $(1 - 4)$	GAGs: 1.5
μ_{fibres}: $7.7 \cdot 10^4$		cells: 8
		elastin: 2.5

Table 14.1: *Values of the different parameters, grouped into mechanics, morphology and composition, used in the FDTD simulations for the parametric study of the collagen morphology. Percentages are given with respect to dry tissue, except hydration and fibrillar collagen that refer to total tissue.*

Waviness of fibre

The influence of the fibre waviness on the mechanical behaviour of the tissue was evaluated by performing simulations for different waviness values in both longitudinal spatial media, i.e. with fibres arranged in parallel ($\phi = 0^o$) and perpendicular ($\phi = 90^o$) to the shear wave propagation direction. The value of the waviness (characterised by the standard deviation) ranged between 5 μm to 45 μm, with a step of 10 μm. Figure 14.3 shows the spatial media defined with this waviness range.

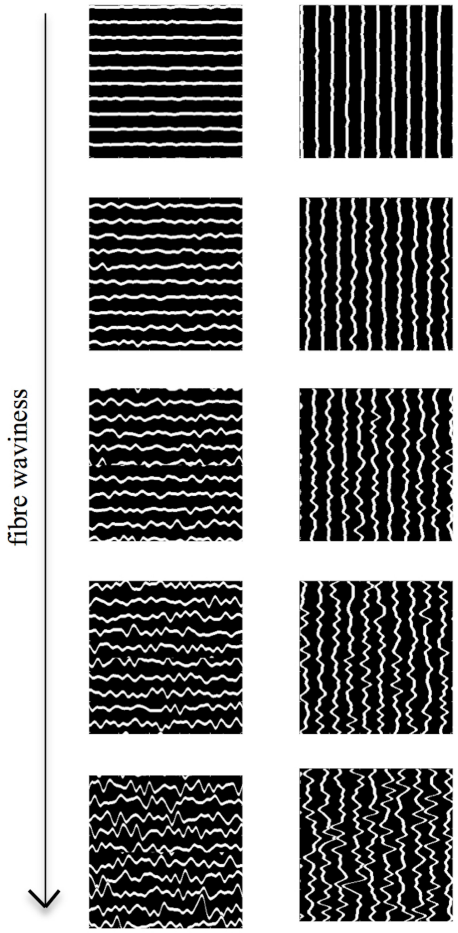

Figure 14.3: *Representation of the spatial media (longitudinal sections with fibres arranged in parallel and perpendicular to the shear wave propagation direction) defined for the waviness range [5-45] μm with a step increment of 10 μm.*

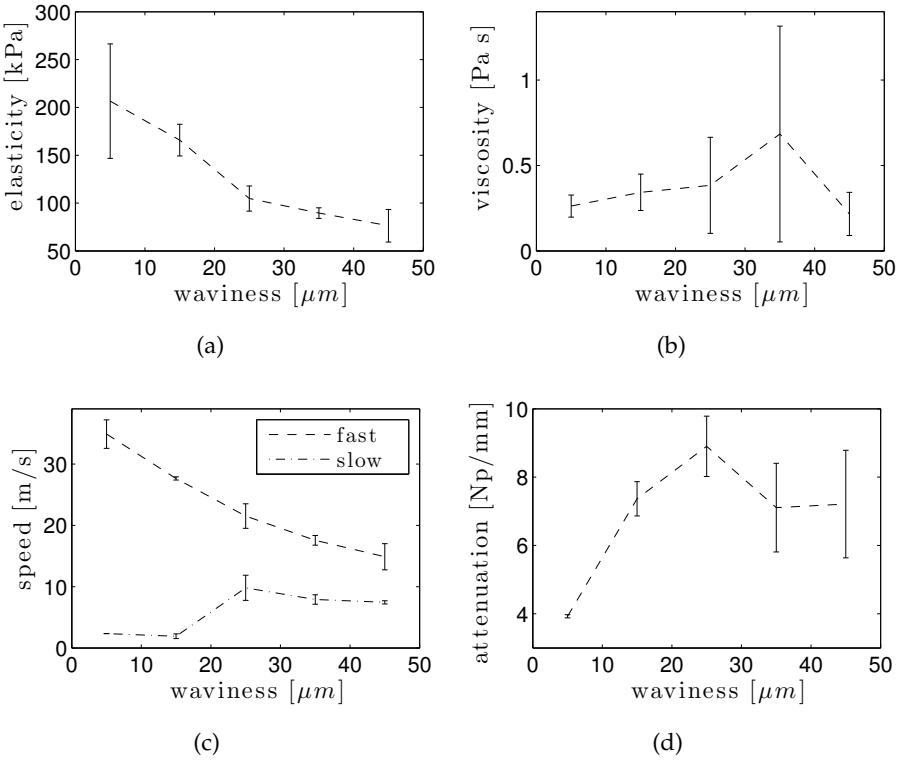

Figure 14.4: *Dependence on fibre waviness of (a) elasticity, (b) viscosity, (c) group velocity and (d) attenuation. Numerical simulations performed in the longitudinal profile with fibres arranged in parallel to the wave propagation direction ($\phi = 0^o$).*

The evolution of the studied parameters as function of waviness is depicted in Figures 14.4 and 14.5, for the longitudinal section with fibres parallel ($\phi = 0^o$) and perpendicular ($\phi = 90^o$) to the shear wave propagation direction, respectively. As can be observed in Figure 14.5, the elasticity positively depends on the fibre waviness for the profile with fibres perpendicular to the wave propagation direction ($\phi = 90^o$), while the opposite relation is obtained for the profile with the fibres arranged in parallel ($\phi = 0^o$). On the other hand, when the waviness of the collagen fibres increases, the viscosity decreases for the profile with fibres perpendicular to the shear wave propagation direction ($\phi = 90^o$). However, no significant trend is observed for the viscosity in the other longitudinal medium ($\phi = 0^o$).

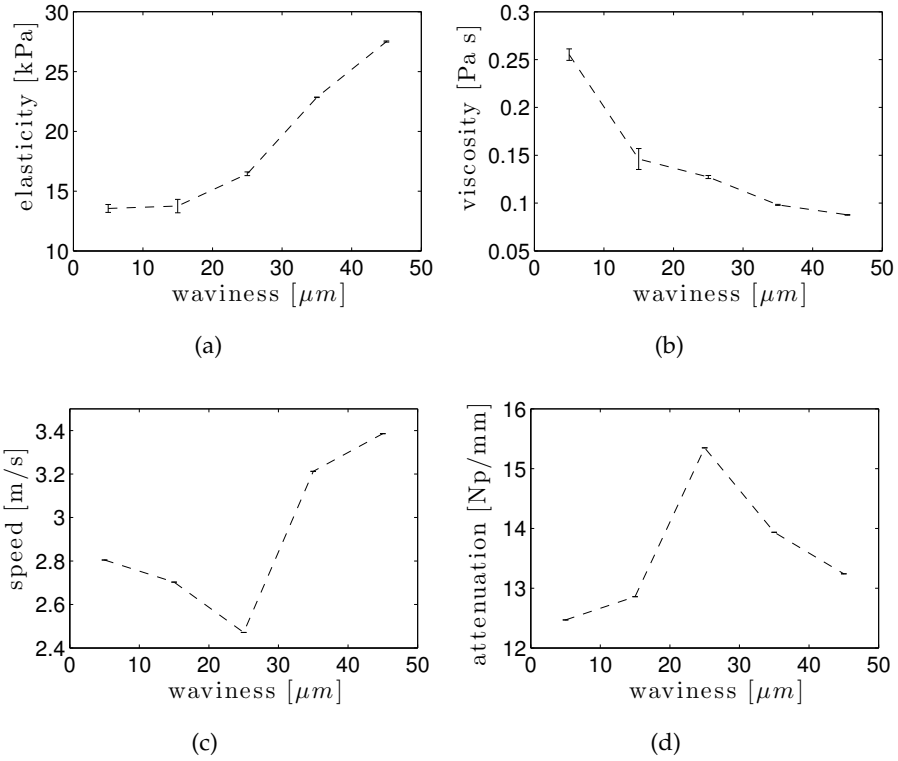

Figure 14.5: *Dependence on fibre waviness of (a) elasticity, (b) viscosity, (c) group velocity and (d) attenuation. Numerical simulations performed in the longitudinal profile with fibres arranged in perpendicular to the wave propagation direction ($\phi = 90^o$).*

The analysis of the group velocity shows that it is possible to identify two different waves, known as fast and slow waves, when shear waves propagate through the profile with fibres arranged in parallel to the propagation direction ($\phi = 0^o$). Only the fast wave, which is guided by the collagen fibres, presents a clear negative dependence on the fibre waviness (see Figure 14.4). The group velocity does not have a clear trend when the waves propagate through the profile with fibres arranged in perpendicular to the wave propagation direction ($\phi = 90^o$). Finally, no significant trend is observed for the attenuation in any of the cases. Although there is an increment in the attenuation for the profile with fibres parallel to the wave propagation direction, when fibres become more crimped the attenuation keeps stable.

Diameter of fibre

The effect of the diameter of fibre was studied for all considered spatial media, longitudinal and transversal sections, as it is depicted in Figure 14.6. In the spatial media used in the FDTD numerical simulations, the fibre thickness was increased from 3 μm to 10 μm with a step increment of 1 μm.

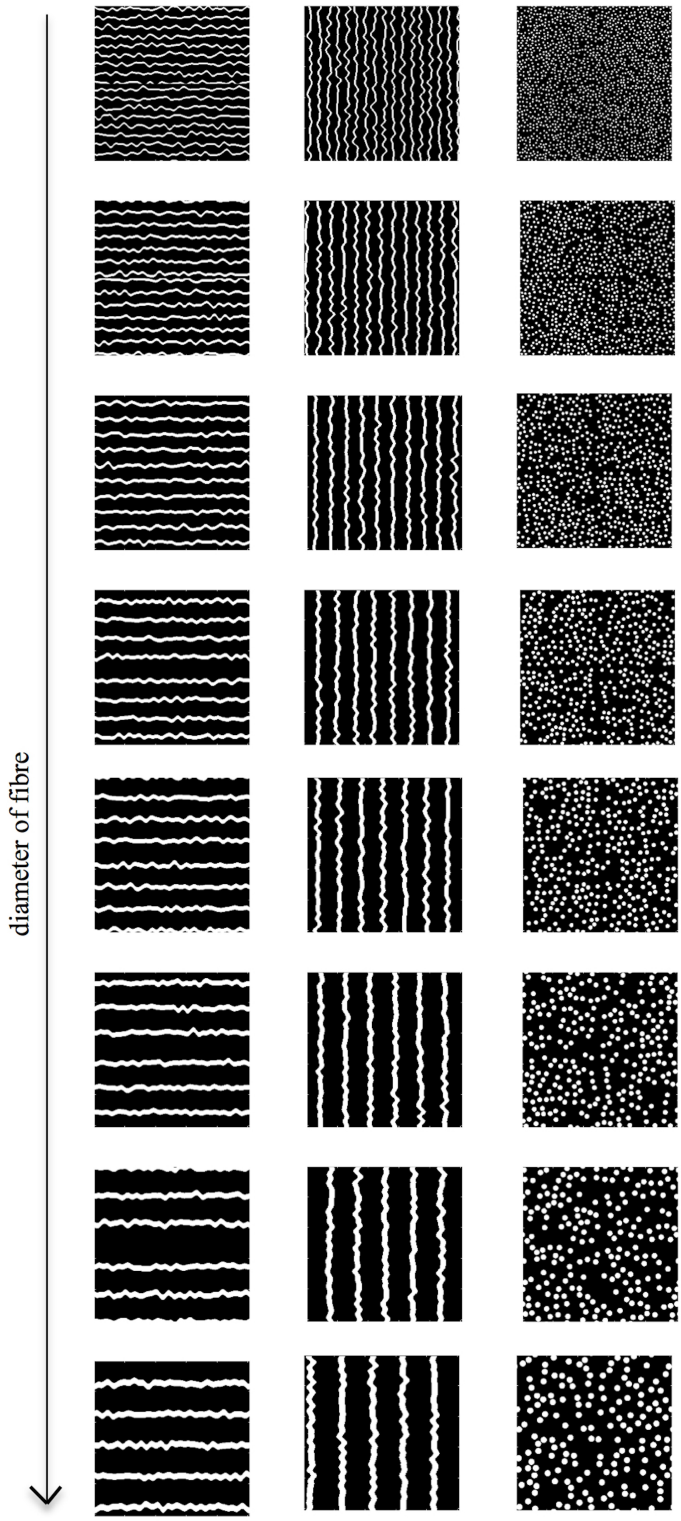

Figure 14.6: *Representation of the spatial media (longitudinal sections with fibres arranged in parallel and perpendicular to the shear wave propagation direction and transversal section) defined for the diameter range [3-10] μm with a step increment of 1 μm.*

Figures 14.7, 14.8 and 14.9 show the results for the three different spatial media: longitudinal with fibres parallel and perpendicular to the wave propagation direction and transversal section, respectively. A negative relationship is observed in all the cases for the elasticity, which decreases as the diameter of fibres increases. The elasticity drop in both longitudinal sections is higher than in the transversal profile. The behaviour observed in the case of viscosity is more random, since it fluctuates differently in the three spatial media. It presents opposite trend in the longitudinal sections: it increases for the profile with fibres arranged in parallel to the propagation direction and decreases when the fibres are arranged in perpendicular. Nevertheless, no clear trend is observed when the shear waves propagate through the transversal medium.

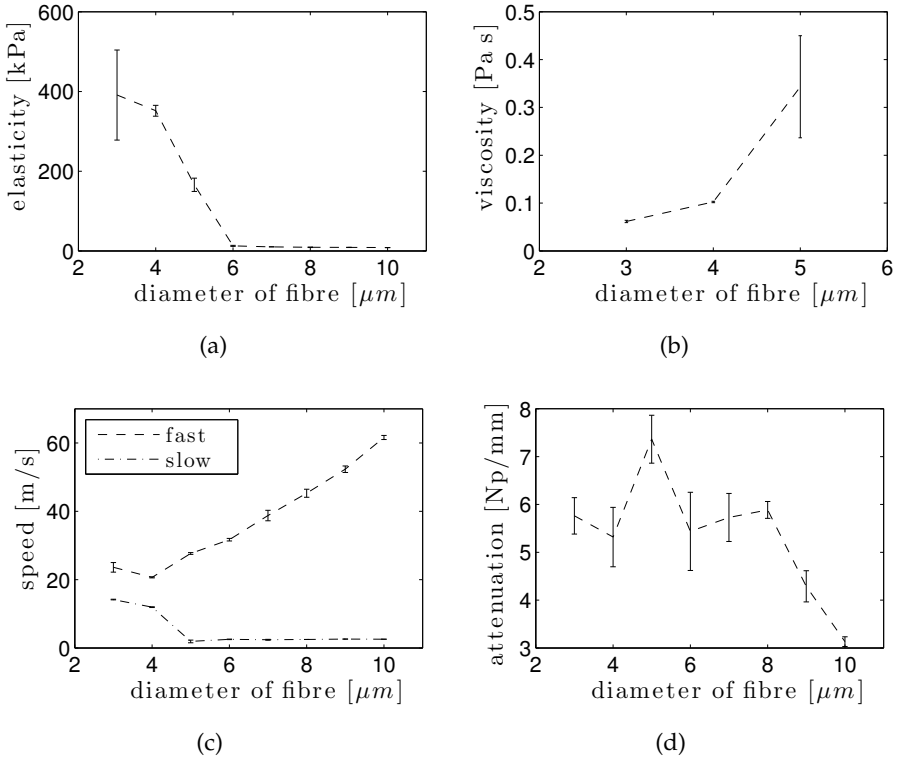

Figure 14.7: *(a) Elasticity, (b) viscosity, (c) group velocity and (d) attenuation evolutions as function of diameter of fibre. Numerical simulations performed in the longitudinal profile with fibres arranged in parallel to the wave propagation direction ($\phi = 0^o$).*

Regarding to group velocity, there is not any common evolution in the three spatial media. For the longitudinal section with fibres parallel to the propagation direction, a positive association is observed in the velocity for the fast wave, i.e. larger the diameter of fibres higher the velocity of the fast wave. As happened with the waviness dependence, only the fast wave presents a clear dependence on the fibre thickness (see Figure 14.7). In contrast, for propagations through the transversal section, the group velocity decreases as the diameter of fibres increases. No evident trend is observed in the longitudinal section with fibres arranged in perpendicular to the wave propagation direction.

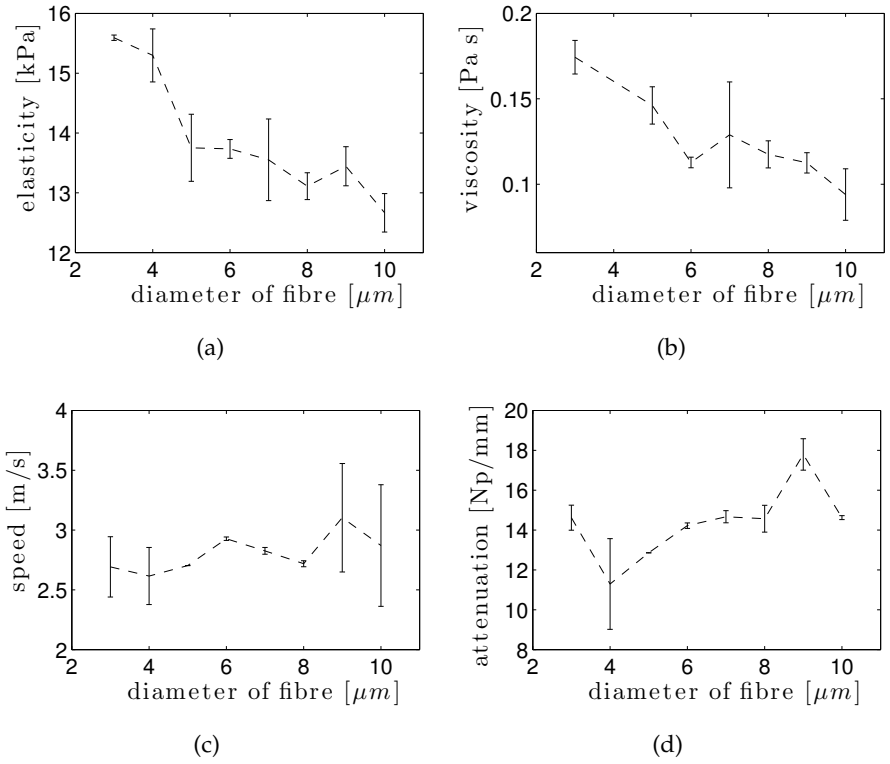

Figure 14.8: *(a) Elasticity, (b) viscosity, (c) group velocity and (d) attenuation evolutions as function of diameter of fibre. Numerical simulations performed in the longitudinal profile with fibres arranged in perpendicular to the wave propagation direction ($\phi = 90^o$).*

Finally, results show that attenuation increases in the transversal section for an increment in the diameter of fibre, while no clear trend is observed in any of the longitudinal sections.

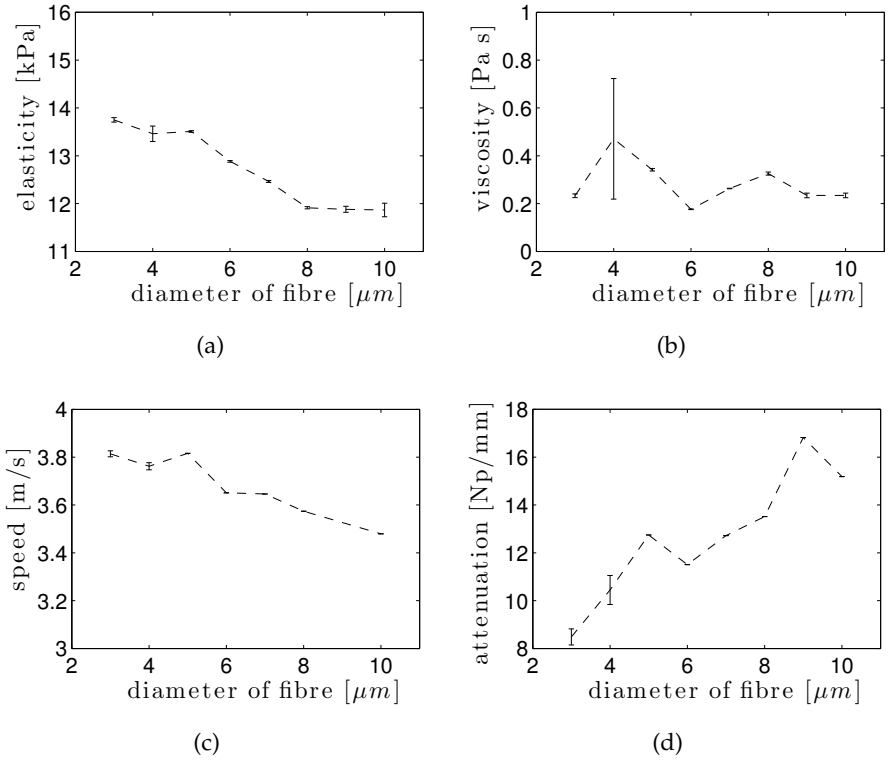

Figure 14.9: *(a) Elasticity, (b) viscosity, (c) group velocity and (d) attenuation evolutions as function of diameter of fibre. Numerical simulations performed in the transversal profile.*

Gap between fibres

Due to the geometric conditions to define both longitudinal spatial media, the separation between fibres and their thickness are directly related, i.e. an increment in the fibre thickness entails a pores rise. Thus, similar results are obtained in all the studied parameters with a pores increment and a thickness increment. However, the separation between fibres

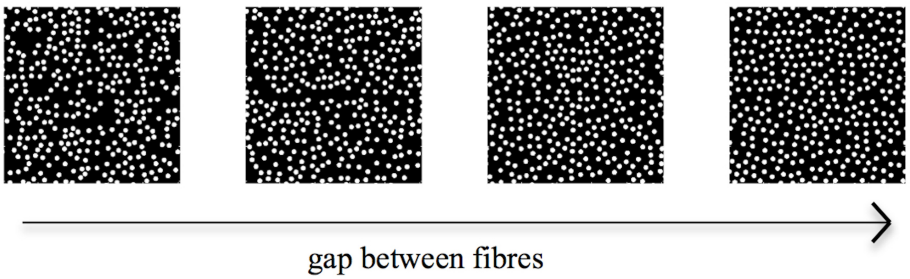

Figure 14.10: *Representation of the transversal spatial medium defined for the gap range [1-4] μm with a step increment of 1 μm.*

becomes a controllable parameter in the transversal section. For this case, simulations were

made for increasing values of the gap between fibres, ranging from 1 μm to 4 μm with an increment of 1 μm (see Figure 14.10).

Figure 14.11 shows the evolution of the different studied parameters (elasticity, viscosity, group velocity and attenuation) versus the separation between fibres. With the exception of attenuation, which drops versus the gap increment, the rest of the studied parameters do not highlight any particular trend.

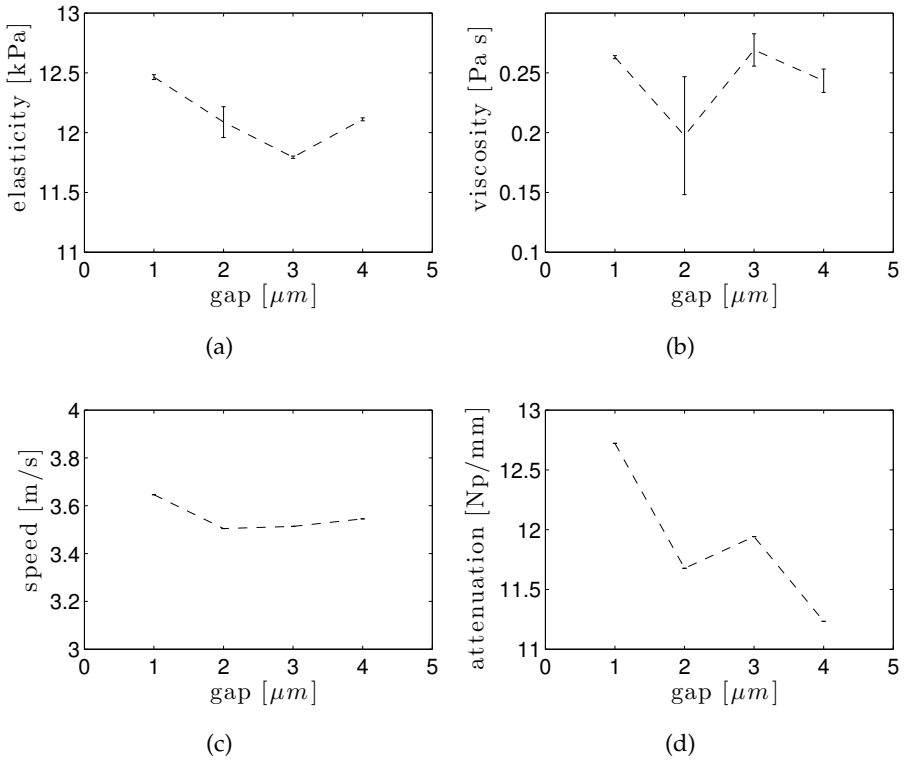

Figure 14.11: *Dependence on gap between fibres of (a) elasticity, (b) viscosity, (c) group velocity and (d) attenuation. Numerical simulations performed in the transversal profile.*

14.2.2 Biochemical composition and mechanics

The composition changes in the ECM during gestation were also simulated. Each constituent was independently studied, and thus only its concentration was changed to study its influence, keeping the concentration of the remaining constituents set to the concentration at early pregnancy. Because of the definition of the mixture-based model, a change in composition induces a change in the mechanical properties that characterise the model (see Section 9.3). The effective mechanical properties of each of the phases that characterise the spatial media (collagen fibres and matrix) are computed, inside a pixel, from the constituent concentrations ζ_i (%) and mechanical properties (λ_i, μ_i, γ_i, ρ_i), following mixture theory as, $(\lambda, \mu, \gamma, \rho) = \sum \zeta_i(\lambda_i, \mu_i, \gamma_i, \rho_i)$. Therefore, composition changes simulated here are reflected in the mechanical parameters. The values of the different parameters used in the numerical

simulations are summarised in Table 14.2. Parameters related to morphology are kept constant, while parameters related to mechanics and composition vary between the proposed ranges.

***Mechanics* [kPa]**	*Morphology* [μm]	***Composition* [%]**
λ_{matrix}: $(1.65 - 1.76) \cdot 10^6$	waviness: 15	hydration: $(80 - 85)$
μ_{matrix}: $(7.8 - 8.1)$	diameter: 5	fibrillar collagen: $(20 - 15)$
λ_{fibres}: $(1.21 - 1.73) \cdot 10^5$	gap: 1	GAGs: $(0.75 - 1.5)$
μ_{fibres}: $(5.2 - 7.7) \cdot 10^4$		cells: $(8 - 15)$
		elastin: 2.5

Table 14.2: *Values of the different parameters, grouped into mechanics, morphology and composition, used in the FDTD simulations for the parametric study of the biochemical composition. Percentages are given with respect to dry tissue, except hydration and fibrillar collagen that refer to total tissue.*

Tissue hydration

As it was described in Section 3.2.1, the water content during cervical maturation increases by approximately 5% at late in pregnancy. To analyse the influence of the tissue hydration, simulations were carried out for increasing values of the hydration, ranging from 80% to 85%. Figure 14.12 shows the spatial media used in the simulations.

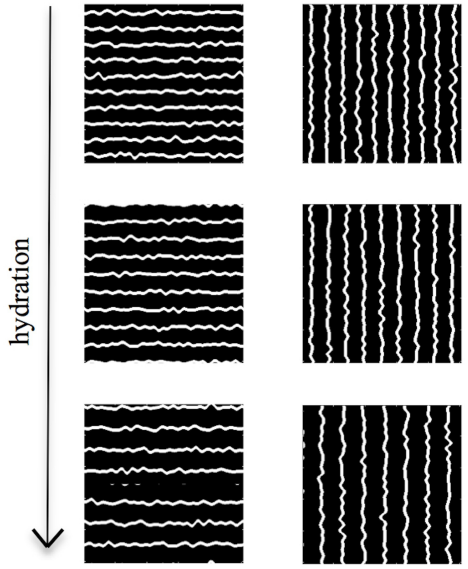

Figure 14.12: *Representation of the spatial media (longitudinal sections with fibres arranged in parallel and perpendicular to the propagation and transversal section) defined for the tissue hydration range: [80-85] % with an increment of 2.5 μm.*

Results are shown in Figures 14.13, 14.14 and 14.15, for propagations through the three spatial media. They show that, as a consequence of the hydration increment, the elasticity decreases in all the studied media. A drop in viscosity is observed in the section with fibres perpendicular to the wave propagation direction ($\phi = 0^o$) and in the transversal section, while the longitudinal section with fibres arranged in parallel does not present an evident trend.

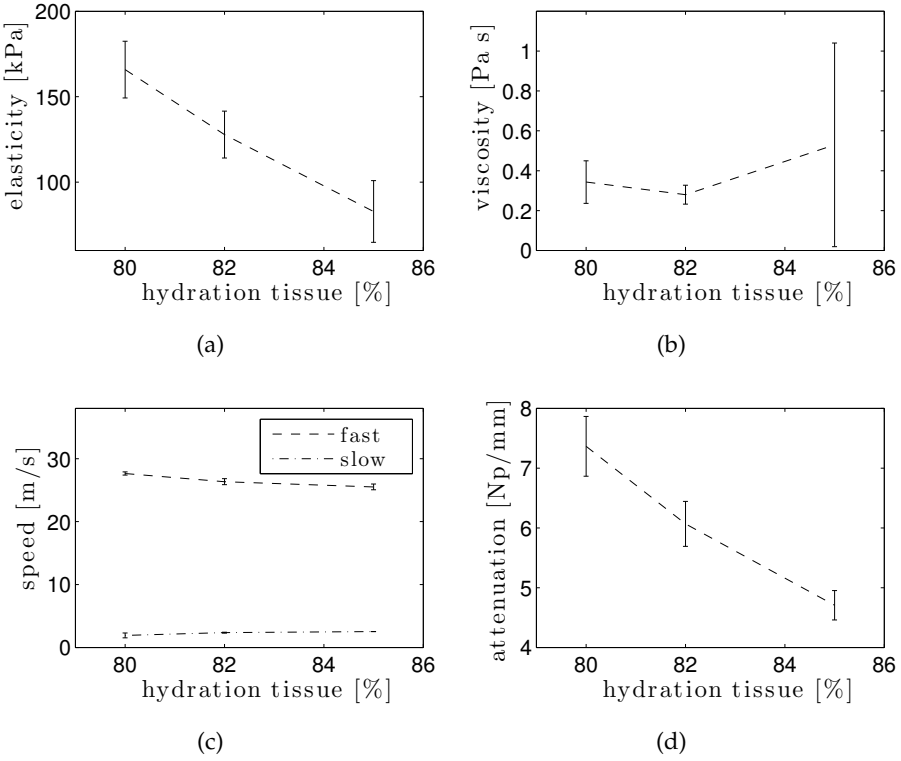

Figure 14.13: *Dependence on tissue hydration of (a) elasticity, (b) viscosity, (c) group velocity and (d) attenuation. Numerical simulations performed in the longitudinal profile with fibres arranged in parallel to the wave propagation direction ($\phi = 0^o$).*

Different evolutions are observed in the group velocity, depending on the considered spatial medium. As in previous results, in the longitudinal section with fibres arranged in parallel to the wave propagation direction, the fast and slow waves present different trends. While the fast wave propagates slower at higher level of hydration, the slow wave seems not to be influenced by the hydration level. Opposite evolutions are observed in the other two spatial media. Group velocity increases in the longitudinal profile with fibres arranged in parallel to the propagation direction and decreases in the transversal section.

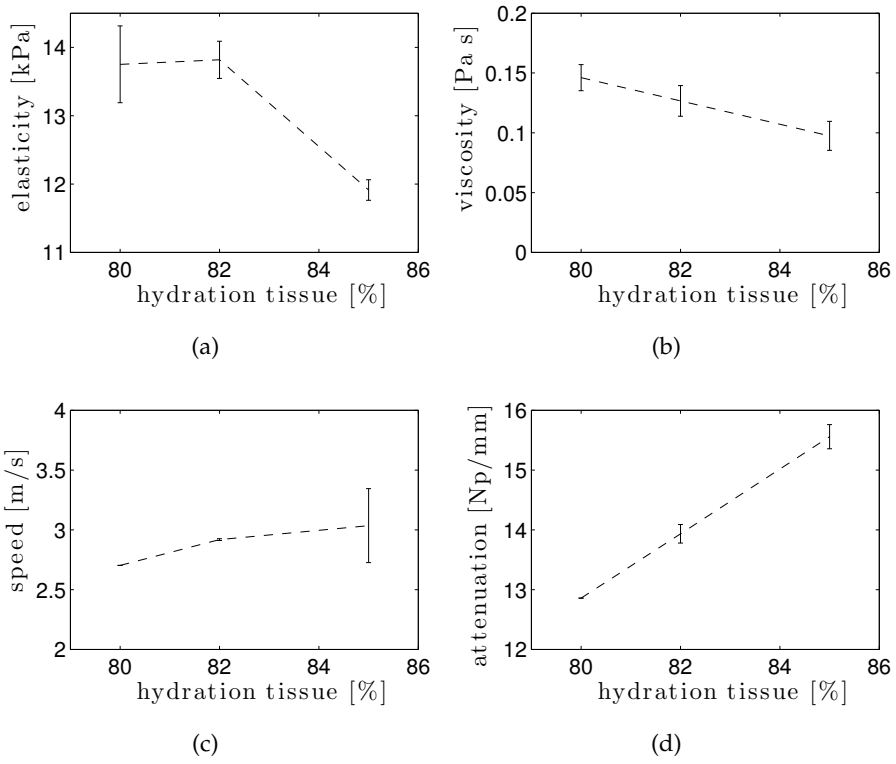

Figure 14.14: *Dependence on tissue hydration of (a) elasticity, (b) viscosity, (c) group velocity and (d) attenuation. Numerical simulations performed in the longitudinal profile with fibres arranged in perpendicular to the wave propagation direction ($\phi = 90^o$).*

The attenuation decreases with the hydration level in the longitudinal profile with fibres arranged in parallel and in the transversal section as well. The longitudinal profile with fibres arranged in perpendicular presents the opposite tendency.

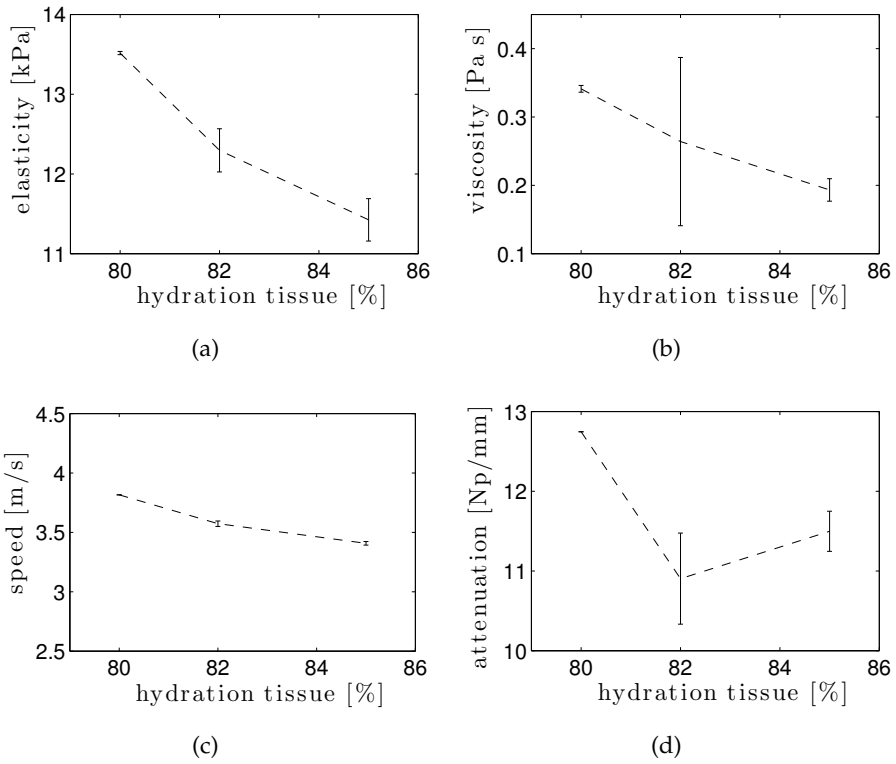

Figure 14.15: *Dependence on tissue hydration of (a) elasticity, (b) viscosity, (c) group velocity and (d) attenuation. Numerical simulations performed in the transversal profile.*

ECM constituents

The decrease in GAGs and the increase in cells concentrations, observed during pregnancy, were simulated decreasing the GAGs concentration from 1.5% to 0.75% and increasing the cells concentration from 8% to 15%, as shown in Table 14.2. The dependence of the studied parameters on cells and GAGs quantity was nearly similar for the three spatial media. Elasticity and velocity show the same relationship with the ECM constituents. They drop when the GAGs decrease, and rise with the cellular increment. Nevertheless, viscosity and attenuation present the opposite trend to elasticity and velocity. Both viscosity and attenuation decrease with the cellular increment and increase when GAGs drop. These associations are shown in Figure 14.16, which shows the evolution of the studied parameters with the increasing cells in the transversal section.

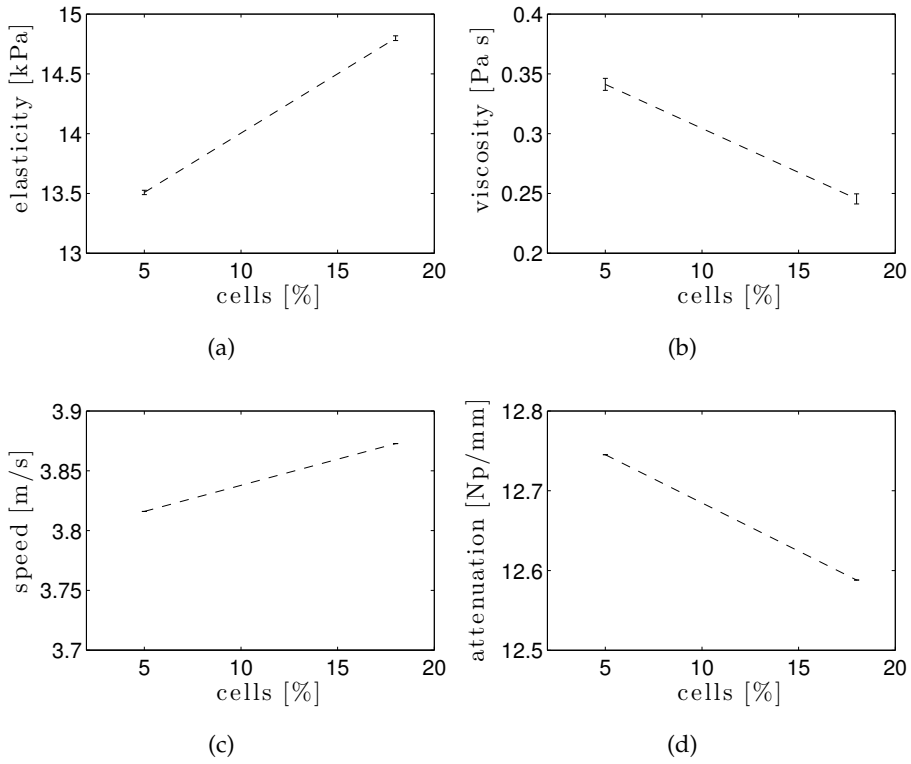

Figure 14.16: *Dependence on cells increment of (a) elasticity, (b) viscosity, (c) group velocity and (d) attenuation. Numerical simulations performed in the transversal profile.*

During pregnancy, collagen weakens up to 30% of its nominal strength (see Section 3.2). To simulate this drop in the collagen strength, the value of the Lamé's parameters of collagen fibres were decreased until 30% in the numerical model. Transversal section and longitudinal profile with fibres perpendicular to the wave propagation direction show similar dependence on collagen strength. Figure 14.17 shows the results for shear wave propagations through the transversal section. Attenuation and viscosity show a moderate increment when collagen strengthens, while elasticity depicts the opposite relationship. The group velocity does not show any clear dependence. The opposite tendencies to the ones that characterise transversal section and longitudinal with fibres arranged in perpendicular ($\phi = 90^o$) are found for all the parameters in the longitudinal profile with fibres parallel to the wave propagation direction (see Figure 14.18).

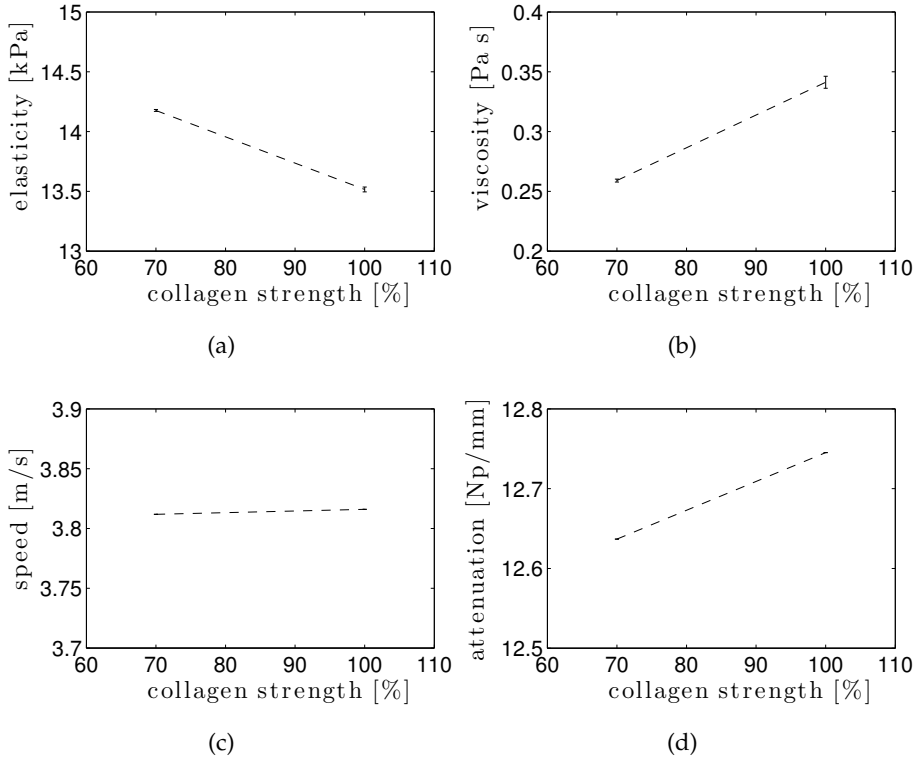

Figure 14.17: *Dependence on collagen strength of (a) elasticity, (b) viscosity, (c) group velocity and (d) attenuation. Numerical simulations performed in the transversal profile.*

14.3 Discussion

The main goal of this study was to link the variations of microscopic histological characteristics (both morphological and biochemical) with the macroscopic tissue-scale mechanical properties measurable by shear wave ultrasound. These relationships are briefly described in Figure 14.19. We have shown that the proposed multi-scale model composed of a FDTD algorithm, constitutive mixture theory and a collagen morphology model, quantitatively relates micro-scale histological characteristics with tissue-scale mechanical properties.

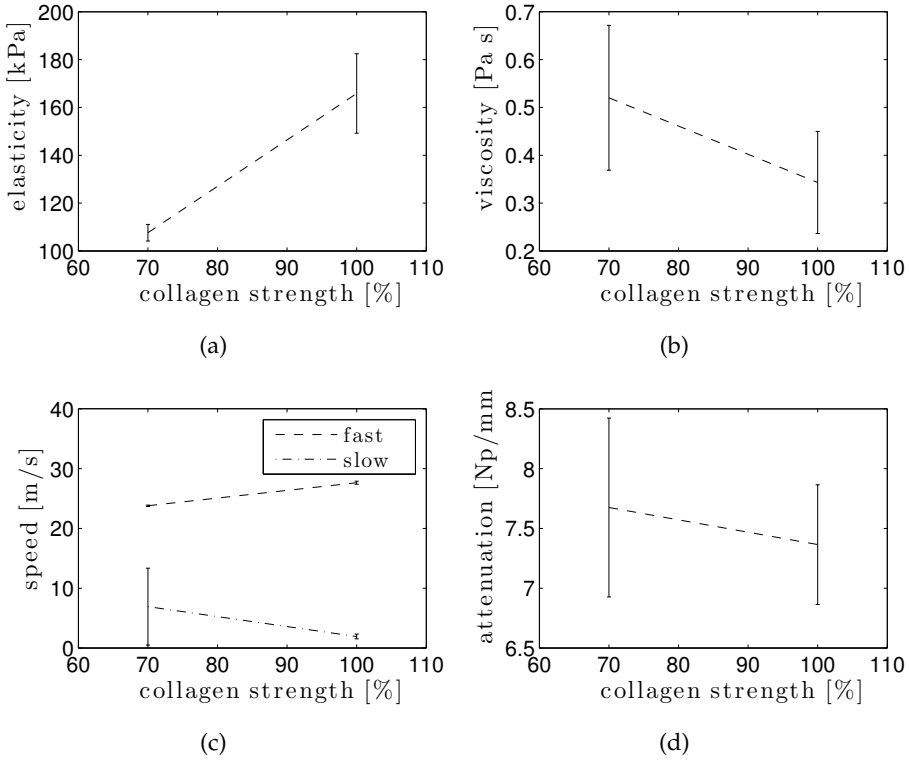

Figure 14.18: *Dependence on collagen strength of (a) elasticity, (b) viscosity, (c) group velocity and (d) attenuation. Numerical simulations performed in the longitudinal profile with fibres arranged in parallel to the wave propagation direction ($\phi = 0^o$).*

The main findings of this parametric study, related to the viscoelastic gross behaviour of cervical tissue during pregnancy, are summarised in Table 14.3. The results highlight the relevance of the proposed spatial media in the context of collagenous tissues. While such random media are obviously not supposed to mimic neither realistic soft tissue nor cervical one, they nonetheless present a similar viscoelastic behaviour to those observed from experimental results on cervical tissue [25, 69]. Simulated shear wave velocities ($\sim 2.2 - 3.8$ m/s) in longitudinal profiles with fibres disposed perpendicular to the wave propagation direction and in transversal media highly correlate to real shear wave velocities measured in human cervix [48, 150]. However, higher values were obtained for the longitudinal profile with fibres arranged in parallel to the propagation direction, where the guided waves that characterise this spatial profile may be responsible for these larger velocities. In addition, the viscoelastic nature of cervical tissue and its heterogeneity influence the shear wave propagation and consequently the gross response of the tissue, as it has been previously shown in this dissertation in Chapter 13. Therefore, to compare shear wave properties in cervical tissue all these features should be taken into account.

It has been shown that there is a drop in the elasticity during the gestation, represented here by different histological and morphological parameters that change during pregnancy. Spatial media were chosen to provide a random medium with controllable parameters, which describe the main aspects of the ECM and exhibits shear wave propagation. The

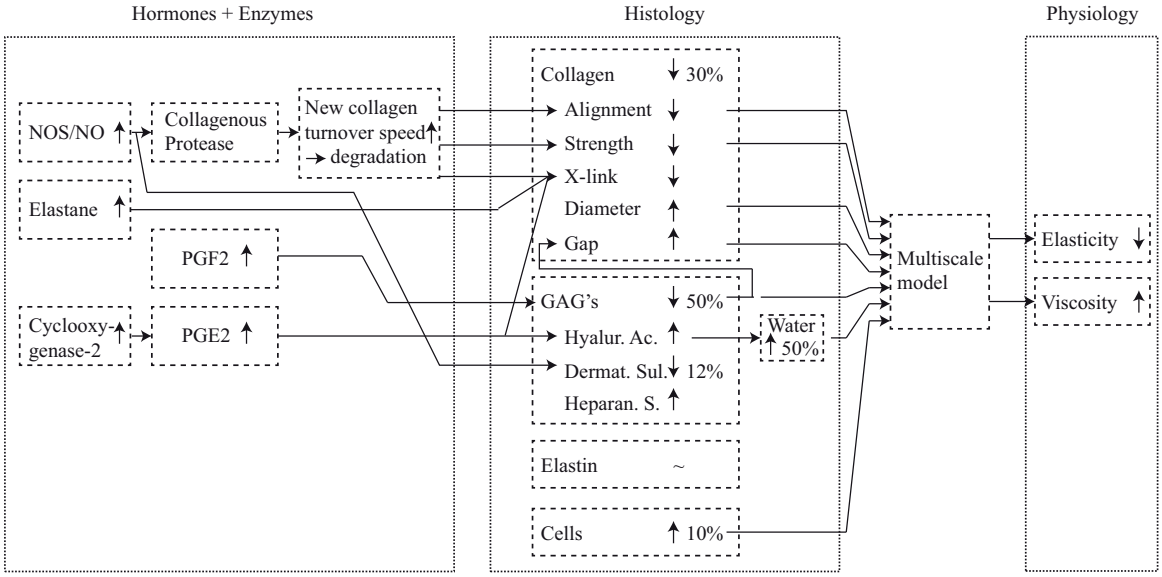

Figure 14.19: *Summary of the proposed multi-scale approach. The direction of the small arrows means the evolution of the substance quantity or parameters, i.e. ↑ increment, ↓ decrement, ∼ not change.*

objective of the spatial medium is to determine whether biomechanical properties of ECM, concretely the collagen, can provide more specific information about the gestation evolution. To achieve this goal, we strive to understand how the morphological changes that occur in the cervical ECM during pregnancy affect the biomechanical properties of the tissue. One can expect that specific morphological changes in the ECM could be monitored from the mechanical properties. The viscoelastic tendencies can be explained considering the microstructure of the tissue, i.e., the ECM, and thus, as expected, the elasticity mostly depends on the collagenous stroma of the tissue. Shear waves interact with collagen fibres (micro-scale), which determine macroscopic properties (centimetre scale) and are responsible for the mechanical behaviour of cervical tissue.

Histological (changes along gestation)	*Mechanical* (relative to histological)					
	μ [kPa]			η [Pa s]		
	transversal	$\phi = 90^o$	$\phi = 0^o$	transversal	$\phi = 90^o$	$\phi = 0^o$
Collagen waviness ↑	[-]	↑14:14.5	↓80:180	[-]	↓0.16:0.18	↑0.05:0.06
Collagen strength ↓	∼	∼	↓44:64	∼	∼	↑0.21:0.26
Collagen diameter ↑	↓1.7:1.8	↓2.7:3.3	↓130:325	∼	↓0.07:0.09	↑0.15:0.16
Collagen gap ↑	∼	↓2.7:3.3	↓130:325	∼	↓0.07:0.09	↑0.15:0.16
GAGs ↓	∼	∼	↓18:25	↓0.09:0.1	∼	↑0.05:0.13
Cells ↑	↑1.2:1.3	↑ 1.2:3.0	∼	↓0.09:0.1	∼	↑0.06:0.14
Hydration ↑ 5%	↓1.9:2.4	↓0.3:1.9	↓73:88	↓0.13:0.16	∼	↑0.28:0.58

Table 14.3: *Principal findings in the histo-mechanical parameter evolutions during gestation. Trends are indicated by: ↑ (increment), ↓ (drop) and ∼ (no variability). The notation ":" indicates the variability range of the properties in relative values.*

During the cervical remodelling the collagen structure disorganisation changes in a complex way. Collagen fibres turn thicker and more wavy as the gestation progresses in a transition from relatively straight fibres to wavy fibres, while pores between collagen fibres become larger and farther apart [34, 260]. Fibre morphology plays a prominent role in both mechanics and tissue-shear wave interactions. The maximum elasticity dependence is on the fibre appearance (diameter and waviness). Opposite trends are observed depending on the fibre orientation. When the fibres present a parallel orientation to the wave propagation direction (case of longitudinal medium $\phi = 0^o$) this dependence is positive. Two waves, a slow and a fast one, are distinguished for such a configuration. The fast wave corresponds to the wave guided by the fibres, while the slow wave is transmitted by the matrix material. This result indicates that the synthetic profiles developed here are able to capture the morphology of the collagen fibres at the micro-scale. As soon as the fibres are more straight, they guide the wave transmission, and consequently the velocity increases. In Figures 14.1 and 14.2 it is possible to appreciate these guided waves. However, for a perpendicular configuration of the fibres, a single wave front is received and elasticity increases when the fibres become more crimp. These waves guided along the fibres have already been observed in both hard [261] and soft tissues, such as ligament [235], cornea [262] and arteries [263].

Results from the parametric study of the morphology show the important role of the fibre morphology. On the one hand, that is reflected in the variability of the estimated parameters. Estimated viscoelastic parameters seem to have larger standard deviation for the spatial medium with fibres parallel to the wave propagation direction ($\phi = 0^o$). The randomly generated spatial media may be responsible for that higher variability. Results suggest that, in such a spatial configuration, the dependence on the collagen morphology is stronger than in the others spatial profiles. This fact is consequent with the results shown in Figure 14.17. In transversal section and longitudinal profile with fibres perpendicular to the propagation direction there is no significant positive dependence of the velocity on the collagen strength, while the fast wave guided by the fibres in the parallel profile ($\phi = 0^o$) presents a clear positive association (see Figure 14.18). On the other hand, no additional reliable conclusion can be taken from the standard deviation of the estimated parameters. Due to the numerical methodology proposed here, it seems awkward to provide a statistical analysis, since simulations do not take account any experimental variability that occurs in real measurements.

As has been previously suggested by various studies [38, 79, 80], the increment in water content and the spacing between collagen fibres should decrease the ultrasonic attenuation. Results in the transversal section and the longitudinal profile with parallel fibres are consistent with that. However, the increasing tissue hydration produces a rise in the ultrasonic attenuation for the spatial configuration with fibres disposed perpendicular to the wave propagation direction. That may be explained by the more dispersive behaviour of this medium. A water increment increases the spacing between fibres and consequently the

energy loss originated from the internal reflections too. It is worth pointing out that attenuation is always higher in the transverse and the longitudinal medium with perpendicular fibres ($\phi = 90^o$) than in the cases where the fibres are arranged in parallel to the wave propagation direction ($\phi = 0^o$). One process that significantly contributes to wave attenuation in soft tissues consists of mode conversion at interfaces involving abrupt changes in density and/or compressibility [264]. Abrupt differences in mechanical properties exist between the two materials considered in the spatial media, collagen and matrix, which furthermore exhibit disoriented interfaces. In both media, the number of different interfaces through which the wave is traveling is higher than in the parallel one, and consequently the energy loss too. The dispersive effects that collagen has in both media (transversal and perpendicular $\phi = 90^o$) are shown in Figure 14.17, where higher collagen strength values involve larger attenuation.

Currently, it is known that changes in biomechanical properties of cervical tissue are related to modifications of the microstructure. During the cervical maturation, the balance of the main biomechanical constituents of the cervical stroma is continually evolving. Histological and biochemical studies have provided insights in modifications of the ECM of the cervix in pregnancy and delivery [2, 15, 260]. These modifications are related to changes in the composition of GAGs, which involve the tissue remodelling, and are associated with increased tissue hydration, increased viscous behaviour and reduced stiffness in the course of pregnancy. Recent studies have shown that there is a progressively decrease in the stiffness of the cervix during gestation [51, 98, 154], which has been reported too in this thesis by using SWE in Chapter 11. In the present parametric study, an elasticity drop is shown for all the morphological variables studied. We have showed how elasticity decreases when the collagen fibres turn thicker and more wavy, the pores between collagen fibres become larger and separated, and when the hydration of the tissue rises. However, no clear change in the viscosity was observed, probably because the apparent loss modulus is originated from the absorption effects at the micro level, due to the impedance contrast between both materials along with the attenuation, rather than from the intrinsic viscosity. Hormonal processes may not be simultaneous but sequential, and generate competing trends in mechanical properties. Our model would help discriminating hormonal processes and explain non-monotonic evolutions of the different measurable viscoelastic parameters. Identify hormonal processes and correlate with non-monotonic mechanical evolutions will be the next goal.

The simulations support that collagen fibres are the main responsible for the mechanical behaviour of the cervix. Results show how the cervix mechanics is more sensitive to the modifications in the microstructure than to the ECM composition. Not only its quantitative variation, but also how the ECM constituents are responsible for the morphological changes that collagen suffers. In a collagenous tissue, the velocities of plane waves vary depending on their propagation directions, the stretch and preferred direction of fibres. Along the collagen fibres the shear wave is guided, modifying its propagation speed and generating dispersive effects. Diameter of fibres and/or pores between them, whose thickness is

smaller than or close to the shear wavelength, are structures that influence the propagation. This guided waves phenomenon characterises the collagenous tissue, and is clearly shown in the results. Consequently, the elastic modulus cannot be directly deduced from the shear group velocity as in homogeneous media, but is intrinsically related to the dispersion equation. As observed in the results, the group velocity and the elasticity do not always present the same tendency.

The election of the excitation frequency was based on the results from the study described in Chapter 13, which shows that viscoelastic parameters tend to converge for excitation frequencies over 100 kHz [231]. This frequency is rather high, and would thus be difficult to achieve in a real experiment, since all currently used elastography techniques are characterised by a limited frequency band [32]. Until today the potential application of elastography to cervical tissue still remains unclear since a number of inappropriate assumptions are made: tissue is homogeneous, isotropic and semi-infinite. Notwithstanding, cervical tissue is anisotropic, heterogeneous and its architecture small relative to the shear wavelengths that are characteristic in SWE. In this study, the main target was to evaluate if shear waves are sensitive enough to detect morphological changes in the microstructure of the cervical tissue. As the results presented in Chapter 13 show, the wavelength is a determinant issue to achieve that, since it may condition the interactions between shear waves and the microstructure of cervical tissue and hence viscoelastic properties. Micro structure-shear wave interactions are guaranteed in the present parametric study because the wavelength is of the same order of magnitude than collagen fibres [231]. Highlighting these interactions is the reason for choosing such a frequency.

The main limitations of this study are related to the 2-D spatial profiles and to the dispersion curve estimation. First, as was indicated in the previous chapter, the maximum distance where the linear fit to estimate the wave number can be performed depends on the wave amplitude, and when the medium is not homogeneous with high energy loss, the phase gradient might not be constant along the propagation distance. Second, the 2D nature of the model constitutes one of the main limitations of the proposed numerical simulation of the cervical remodelling. In that vein, a 3-D study would be necessary to achieve a complete understanding of the tissue-shear wave interactions and assess the importance of each morphological parameter.

14.4 Conclusions

In this study, we proposed a multi-scale approach that combines three elements: collagen morphology, wave-tissue interactions and constitutive mixture theory. In particular, we developed a parameterized micro-scale fibre geometry to study the role of collagenous fibre disorganisation during pregnancy. This work highlights the role of collagen architecture in soft tissue mechanics, and specifically, in the cervical tissue. Not only the mechanical parameters of the ECM constituents are responsible for the tissue behaviour, but also the morphology at the micro-scale. Results showed the ability of the proposed model to describe

the mechanical behaviour of the cervical tissue as a fibre-reinforced matrix, and that the shear wave propagation phenomena can be exploited to reconstruct the histo-mechanical properties of soft tissues. It is worth pointing out that the elasticity offers a good characterisation of the morphological changes in the microstructure that occurs during gestation. The combination of FDTD technique with a constitutive model based on mixture theory and the morphology description at the micro-scale quantitatively relates histological characteristics with mechanical properties that can be addressed by shear waves. The results reported here support the hypothesis that the cervical stiffness quantification can be an objective tool to predict the cervical ripening.

Part IV

CONCLUSIONS AND FUTURE WORKS

15

Conclusions and future works

The control of the cervical maturation has been considered for the last 30 years as one of the most pressing problems in obstetrics, and nowadays, its objective assessment is still a challenge. In this doctoral thesis, a rigorous approach to this problem has been developed to provide deeper knowledge about the mechanisms that take place in normal pregnancy and how to address them by shear waves. The methodology and the results presented in this dissertation were carefully designed to achieve that goal. First, we have verified that it is possible to objectively quantify cervical stiffness during normal pregnancy using shear wave elastography (SWE). The sensitivity and capability of the technique in assessing cervical maturation is shown in a preliminary study carried out in women with uncomplicated singleton pregnancies. Secondly, physiologically relevant data have been extracted from an animal model, which moreover allows to objectively define time control over the cervical maturation. The labour was artificially induced and the consequent changes in the mechanical properties of the cervical tissue were monitored by SWE. In addition, these elastographic measurements were associated with changes in the micro-structural organisation of the collagen matrix, which were reported by second harmonic generation (SHG) and two-photon fluorescence microscopy (2PF). We demonstrated that the cervical tissue of the animals to which the labour was induced present more disorganised structures at the micro-scale level and lower elasticity values. Thus, we have shown that these changes at the microscopic scale during cervical remodelling may be partly responsible for the variation of the mechanical properties measured by SWE. Finally, this hypothesized link between histology and shear wave elastography has been numerically validated. To this end, a computational

method to determine the viscoelastic properties of cervical tissue from shear wave propagation has been developed. We have shown that the combination of the finite difference time domain (FDTD) computational technique with a constitutive model based on mixture theory and the morphology description at the micro-scale, quantitatively relates histological characteristics with mechanical properties. Results reported in this thesis suggest that shear wave elastography may provide additional information on the process of cervical effacement to that obtained from digital examination and conventional ultrasound, and in a final step, help to guide the artificial labour induction and to diagnose spontaneous preterm birth (PTB).

In addition, the following relevant conclusions are also extracted from each of the investigated hypothesis and objectives proposed in Chapter 2. Their limitations and consequent future works are outlined too.

Gestational assessment

➥***Objective 1*:** Evaluate the shear wave elastography feasibility, sensitivity and capability for assessing cervical ripening.

The results exposed in **Chapter 11** have demonstrated the feasibility of cervical elasticity assessed by shear wave elastography as a valuable biomarker. We have shown that it is possible to objectively quantify cervical stiffness during pregnancy using shear wave elastography. A preliminary clinical study was designed in **Chapter 6** with the aim of providing *in-vivo* information about cervical elasticity throughout normal pregnancy. The cohort integrated in this study consisted of 42 uncomplicated singleton pregnant women, with gestational age from 6 to 41 weeks. Two expert practitioners performed SWE measurements, which provided us the needed data for evaluating the sensitivity and reliability of the SWE application to cervical tissue. Finally, the resulting elastographic maps allowed us to quantify cervical stiffness in four different region of the cervix, supplying fundamental experimental data for validating our first hypothesis.

Measurements taken by the same and by two different observers for different regions in the cervix were reliable and reproducible in all cases, showing the sensitivity of the technique in cervical tissue. A stronger correlation of gestational age with cervical stiffness than with cervical length was found in all the regions of the cervix. Moreover, the weakest correlation between the studied variables was found between cervical length and stiffness. These findings suggest that both variables may be independently used to predict cervical ripening. Finally, we have evidenced the stiffness variability within the cervix. Our results have revealed that stiffness anatomically varies in the cervix and there is a positive stiffness gradient from external to internal and from posterior to anterior parts. However, further studies are needed to confirm these preliminary findings in a larger cohort and to determine if cervical stiffness quantified by SWE is a reliable tool to predict vaginal delivery and eventually spontaneous PTB. Furthermore, in order to depict the relation between cervical remodelling and shear waves further studies aimed at understanding the mechanisms that take place

during gestation are needed. Unfortunately, having objectively defined time control over the cervical maturation may be difficult in humans. In that vein, an animal model, to generate physiologically relevant data that could then be evaluated in humans, is the second step that has been proposed in this thesis.

Understand changes in tissue micro-structure

➥***Objective 2*:** Propose a modelling approach to describe the histo-biomechanical changes of the cervical extracellular matrix during pregnancy and link them with shear wave propagation characteristics.

In this dissertation, we have shown that objective measurements of stiffness reflect histological changes that could provide a measure of cervical ripening and SWE may be a valuable method to objectively quantify the cervical stiffness. **Chapter 7** was devoted to the obtaining of relevant experimental observations that would allow to analyse the cervical remodelling by using SWE. In first place, we developed an experimental protocol for monitoring the cervical stiffness during ripening. An animal model, in particular sheep, and a method to artificially induce the labour (dexamethasone) were chosen to objectively define time control over the cervical maturation. The well explored physiology of ewes and their size similar to humans assisted us in using the tools developed for humans and, along with the artificially induced ripening, accurately controlling the variables. Secondly, we performed a prostaglandin assay in blood samples collected from all the animals, just before the induction of labour and at the end of the experiment, which served us to validate the induced cervical ripening. Finally, the micro-structure of cervical tissue was analysed with two different techniques, histology and two-photon excitation microscopy. This last step provided us physiologically relevant data for validating our mechanical remodelling hypothesis and linking it with SWE measurements.

Results from this animal study showed in **Chapter 12** suggest that the reported changes at the microscopic scale during cervical remodelling may be partly responsible for the mechanical properties measured by elastography. First, we have reported that stiffness of uterine cervix changes throughout the maturation process induced by the dexamethasone injection. In general, the control group (unripened cervix) presents the highest stiffness, and the lowest stiffness values correspond to a measurement closer to delivery in the labour induction group. The reproducibility of SWE was demonstrated by descriptive statistics, providing further support to our first objective. We showed again in this animal study that SWE measurements were highly reproducible. Secondly, the cervical ripening induced by the dexamethasone injection was confirmed by a significant increase in PGE2 twenty-four hours after dexamethasone treatment, whereas values were not significantly different in the control group. These findings provide an additional evidence to the fact that cervical ripening was successfully induced, in concordance with the stiffness decrement that was previously assessed by SWE measurements. Finally, changes at the micro-structure of the tissue were observed by SHG and 2PF, and linked with SWE measurements. Several differences

were found between treated and untreated animals. Control animals showed well defined directional structures, whereas the treated animals showed more disorganised structures, at the scale of few μm up to 100 μm.

Both animal and human experimental studies exhibit some common limitations that are related to the *in-vivo* application of SWE. Along with the small sample size, their main limitations are associated with the complex structure of cervical tissue and to the assumption made for the assessment of stiffness from the shear wave speed values. To estimate the elasticity, SWE relies on the assumption that the medium is locally homogeneous, isotropic and semi-infinite. However, this condition could not be always true. In the animal study, before cervical maturation was induced by dexamethasone and in the control group, collagen fibres may present a high orientation and thus these conditions might not have been satisfied. The same issue could happen in some of the patients in the human study, in particular in those with young gestational age, when the effects of the cervical remodelling (disorientation of the collagen network) may not be presented yet. Finally, in order to obtain reproducible measurements, the pressure applied on the cervix by the sonographer with the probe had to be minimal and the region of interest (ROI) had to be placed away from the surface of the probe. The nonlinearity introduced by the viscoelastic nature of the tissue is an issue very hard to avoid in clinical practice. However, like with any other imaging modality, there is a learning curve and a trained practitioner should guarantee the reproducibility. Further work in that vein should include a detailed investigation of the impact of these assumptions and underlying image artefacts. Moreover, further studies are needed to relate shear wave propagation with histological and endocrine modifications in the cervix and to compare the findings in women.

We principally attribute the elasticity reduction experimentally measured by SWE to the observed histological changes at the microstructure of the tissue. In a final step, the interactions between cervical microstructure and shear waves have been numerically analysed in **Chapter 14**. We have shown that histological characteristics, described by a model based on mixture theory and a parameterized morphology description, can be quantitatively relate to mechanical properties. Our results depict that the tissue mechanics is more sensitive to modifications in the microstructure than to the extracellular matrix (ECM) composition. Not only the quantitative variation of ECM constituents, but also how they are responsible for the morphological changes that collagen suffers during cervical remodelling. We have numerically shown that there is a drop in the elasticity during the gestation, represented in the proposed synthetic model by different histological and morphological parameters that change during pregnancy. It decreases when (1) the collagen fibres turn thicker and more wavy, (2) the pores between collagen fibres become larger and farther apart, and (3) when the hydration of the tissue rises.

A synthetic description of cervical tissue, able to capture the main features of the ECM, was developed in **Chapter 9**. We generated 2D spatial media to describe the micro-structure

of cervical tissue and feed a FDTD model to simulate shear wave propagation through cervical tissue. These media describe the cervical stroma as a fibre-reinforced material, made of collagenous fibres surrounded by a matrix. These spatial media were defined by: (1) three different profiles, which model the different zones that are present in the collagen network of the cervical ECM; (2) a parameterized micro-scale fibre geometry, which allows to study the role of collagenous fibre disorganisation; and (3) the mechanical properties of the ECM constituents, which are incorporated into the model by a mixture-theory-based model. The advantage of such a definition is that it allows to individually study the morphological, compositional and mechanical features of the cervix, difficult to do it experimentally.

Mechanical reconstruction from ultrasound

➥***Objective 3*:** Evaluate the feasibility of elementary rheological models to describe the viscoelastic behaviour of cervical tissue and explore the possibility of quantifying both cervical elasticity and viscosity from shear wave velocities.

It has been showed that shear wave propagation is properly simulated by FDTD technique. In **Chapter 8** we have proposed and implemented the FDTD technique to describe shear wave propagation. A model that describes shear wave propagation through heterogeneous media by varying the properties as a piece-wise constant function at each discretization element was developed. An advantage of using the FDTD simulation technique is that no physical simplifying approximations are made; indeed, propagation includes refraction, diffraction, and multiple reflections. Moreover, the FDTD simulations can be used both to show the interaction between shear waves and the hierarchical structure of connective tissues and to study the mechanical properties of soft tissues.

In **Chapter 13**, the dependency on the excitation frequency of the viscoelastic properties of cervical tissue was studied. We have shown that the Maxwell's law is the most feasible to describe the viscoelastic behaviour of cervical tissue between three elementary proposed rheological laws, contrarily to common belief in literature. This finding shows that the viscoelastic nature of cervical tissue and its heterogeneity influence the shear wave propagation and consequently the gross response of the tissue and, as a consequence micro and macro mechanics may be different. Thus, the elastic modulus cannot be directly deduced from the shear group velocity as in homogeneous media, but is intrinsically related to the dispersion equation. Our numerical results report that the shear wave propagation phenomena can be exploited to infer the histo-mechanical properties of cervical tissue. Shear waves interact with collagen fibres (micro-scale), which determine macroscopic properties (centimetre scale), and are responsible for the mechanical behaviour of connective tissue. Furthermore, our results suggest that the estimated parameters are more stables at high frequency, and excitations over 100 kHz allow to get viscoelastic parameters less dependent on the frequency.

The developed numerical approach to determine viscoelastic properties in soft tissue was presented in **Chapter 10**. From the FDTD shear wave propagation the dispersion velocity can be obtained by a phase-difference algorithm. We proposed then to fit this shear phase

velocity with three well-known rheological laws using a model-based IP applying genetic algorithms. The last methodological step consists of finding the plausibility of each rheological law, in the sense of probability to well describe the viscoelastic behaviour of cervical tissue, by applying a stochastic model-class selection formulation.

The main limitations of this approach are related to the dispersion curve calculation. The wave number is estimated from a linear fit of the phase along the propagation distance. However, the wave amplitude conditions the maximum distance where this linear fit can be performed, and when the medium is highly dispersive the phase gradient might not be constant along the propagation distance. Ongoing theoretical work related to this modelling approach includes a further analysis of the phase velocity and amplitude-frequency dependence to study the wave propagation phenomena within more complex media than those used here. Future research in that vein should be conducted, especially on the feasibility of approaching the viscoelastic response of cervical tissue with a more complex rheological law, along with the possibility of widening the frequency range to lower frequencies. Finally, in a future the FDTD model and the space medium should be extended to the third dimension and a 3D study should be performed to achieve a complete understanding of the tissue-shear wave interactions and assess the importance of each morphological parameter.

16

Conclusiones y trabajos futuros

El control de la maduración del cuello del útero se considera en los últimos 30 años como uno de los problemas más acusados en obstetricia, y hoy en día, su evaluación objetiva es aún un reto. En esta tesis doctoral se ha desarrollado un enfoque riguroso a este problema para proporcionar un conocimiento más profundo acerca de los mecanismos que se producen durante el embarazo normal y la forma de abordarlos usando ondas mecánicas de cizalla. La metodología y los resultados presentados en esta tesis han sido cuidadosamente diseñados para conseguir ese objetivo. En primer lugar, se ha verificado que es posible cuantificar objetivamente la rigidez del cuello uterino durante el proceso de gestación normal usando la técnica de elastografía basada en ondas de cizalla. La sensibilidad y la capacidad de dicha técnica para evaluar la maduración cervical se muestra en un estudio preliminar llevado a cabo en mujeres con embarazos únicos sin complicaciones. En segundo lugar, se han obtenido datos fisiológicos relevantes de un modelo animal, que además permite definir objetivamente el control del tiempo sobre la maduración cervical. El parto fue artificialmente inducido y los consecuentes cambios en las propiedades mecánicas del tejido cervical se controlaron y midieron mediante elastografía basada en ondas de cizalla. Además, estas medidas elastográficas fueron asociadas con cambios en la organización de la microestructura de la red de colágeno, que fueron descritos por dos técnicas de imagen (generación del segundo armónico y microscopía de fluorescencia de dos fotones). Se demostró que el tejido del cuello del útero de los animales a los que se les indujo el parto presentan estructuras más desorganizadas a nivel de micro-escala y menores valores de elasticidad. Por lo tanto, con este estudio demostramos que estos cambios en la micro-escala del tejido durante el proceso de remodelación del cuello del útero pueden ser parcialmente responsables de

las variaciones en las propiedades mecánicas medidas mediante la elastografía. Finalmente, este supuesto enlace entre histología y elastografía se ha validado numéricamente. Con este fin, se ha desarrollado una metodología computacional para determinar las propiedades viscoelásticas del tejido cervical usando ondas de cizalla. Se ha demostrado que la combinación de la técnica de las diferencias finitas en el dominio del tiempo con un modelo constitutivo basado en la teoría de mezclas y la descripción de la morfología en la micro-escala del tejido, relaciona de forma cuantitativa características histológicas con propiedades mecánicas. Los resultados presentados en esta tesis sugieren que la elastografía basada en ondas de cizalla puede proporcionar información adicional a la que se puede obtener por palpación y ultrasonidos convencionales al proceso de maduración cervical, y como último paso, ayudar en el diseño de la inducción artificial del parto y en el diagnóstico del parto prematuro.

Además, las siguientes conclusiones también se han extraído de cada una de las hipótesis investigadas y los objetivos propuestos en el Capítulo 2. Sus limitaciones y los futuros trabajos que han surgido también se describen a continuación.

Evaluación de la gestación

➥***Objetivo 1*:** Evaluar la viabilidad, sensibilidad y capacidad de la elastografía basada en ondas de cizalla para cuantificar la maduración del cuello del útero.

Los resultados expuestos en el **Capítulo 11** han demostrado la viabilidad como biomarcador de la elastografía basada en ondas de cizalla para evaluar la elasticidad cervical. Se ha demostrado que es posible cuantificar objetivamente la rigidez cervical durante el embarazo usando la elastografía basada en ondas de cizalla. Un estudio clínico preliminar fue diseñado en el **Capítulo 6** con el fin de proporcionar información *in-vivo* sobre la elasticidad cervical durante el proceso de embarazo normal. La población incluida en el estudio consistió en 42 mujeres embarazadas sin complicaciones, con una edad gestacional de 6-41 semanas. Dos expertos ginecólogos realizaron las mediciones de elastografía, lo que nos aportó los datos necesarios para evaluar la sensibilidad y la fiabilidad de la aplicación de las ondas de cizalla en el tejido cervical. Finalmente, los mapas elastográficos resultantes permitieron cuantificar la rigidez del cuello uterino en cuatro regiones diferentes del mismo, proporcionando los datos experimentales fundamentales para la validación de la primera hipótesis que se plantea en esta tesis.

Las medidas tomadas por el mismo médico y por dos médicos diferentes en las distintas regiones del cuello uterino fueron fiables y reproducibles en todos los casos, lo que demuestra la sensibilidad de la técnica en el tejido cervical. Se encontró una correlación más fuerte de la edad gestacional con la rigidez del cuello uterino que con la longitud del mismo. Por otra parte, la correlación más débil entre las variables estudiadas se encontró entre la longitud cervical y la rigidez. Estos hallazgos sugieren que ambas variables se pueden utilizar de forma independiente para predecir la maduración cervical. Finalmente, se aportaron evidencias de la variabilidad anatómica de la rigidez en el cuello uterino. Nuestros resultados han revelado que la rigidez varía anatómicamente en el cuello uterino y que existe un

gradiente de rigidez positivo de la parte externa a la interna y de la posterior a la anterior. Sin embargo, se necesitan más estudios para confirmar estos resultados preliminares en un estudio más amplio con más individuos, para determinar si la rigidez cervical medida mediante la elastografía basada en ondas de cizalla es una herramienta fiable para predecir el parto vaginal espontáneo y eventualmente el parto prematuro. Además, más estudios son necesarios para describir la relación entre el proceso de remodelación del cuello del útero y las ondas de cizalla y comprender los mecanismos que tienen lugar durante la gestación. Desafortunadamente, controlar objetivamente la maduración cervical en el tiempo puede ser difícil en los seres humanos. Para afrontar eso, el segundo paso propuesto en esta tesis es un modelo animal que permita generar datos fisiológicamente relevantes que podrían ser evaluados a posteriori en los seres humanos.

Comprender los cambios en la micro-estructura del tejido cervical

➥***Objetivo* 2:** Proponer una estrategia para modelar los cambios histo-mecánicos de la matriz extracelular del cuello uterino durante el embarazo y vincularlos con las características de propagación de las ondas de cizalla.

En esta tesis, hemos demostrado que las mediciones objetivas de la rigidez reflejan cambios histológicos que podrían proporcionar una medida de la maduración cervical y que la elastografía basada en ondas de cizalla puede ser un valioso método para cuantificar objetivamente la rigidez del cuello uterino. El **Capítulo 7** se ha dedicado a obtener las observaciones experimentales pertinentes que permitan analizar el proceso de remodelación del cuello del útero utilizando la elastografía basada en ondas de cizalla. En primer lugar, se ha diseñado un protocolo experimental para realizar el seguimiento de la rigidez cervical durante la maduración del cuello uterino. Un modelo animal, en particular ovejas, y un método artificial para inducir el parto (dexametasona) fueron elegidos para controlar objetivamente el tiempo y la maduración cervical. La fisiología bien conocida de las ovejas y su tamaño similar a los humanos permitió el uso de las herramientas desarrolladas para las mujeres y, junto con la maduración inducida artificialmente, controlar con precisión todas las variables. En segundo lugar, se realizó un ensayo de prostaglandinas en muestras de sangre tomadas en todos los animales, justo antes de la inducción del parto y al final del experimento, lo que sirvió para validar que la maduración cervical había sido correctamente inducida. Por último, la micro-estructura del tejido cervical se analizó con dos técnicas diferentes, histología y microscopía de excitación de dos fotones. Este último paso proporcionó datos fisiológicamente relevantes para validar la hipótesis de la remodelación mecánica y su vinculación con las mediciones de elastografía.

Los resultados de este estudio en animales se muestran en el **Capítulo 12** y sugieren que los cambios observados en la escala microscópica del tejido durante el proceso de remodelación del cuello uterino pueden ser, en parte, responsables de las propiedades mecánicas medidas con la elastografía. En primer lugar, se ha demostrado que la rigidez del cuello

uterino cambia a lo largo del proceso de maduración inducido por la inyección de dexametasona. En general, el grupo control (cuello uterino no maduro) presenta la rigidez más alta, y los valores de rigidez más bajos corresponden a la medición más cercana al parto en el grupo al que se le indujo el parto. La reproducibilidad de la elastografía basada en ondas de cizalla fue demostrada con estadística descriptiva, respaldando el primer objetivo previamente validado en mujeres. Se demostró de nuevo en este estudio en animales la reproducibilidad de la elastografía basada en ondas de cizalla. En segundo lugar, la maduración del cuello uterino inducida por la inyección de dexametasona fue confirmada por un incremento significativo en PGE2 24 horas después de inducir el parto, mientras que esos valores no mostraron diferencias significativas en los animales del grupo control. Estos hallazgos proporcionan evidencias adicionales a que el parto fue satisfactoriamente inducido, y concuerdan con la reducción en elasticidad previamente medida por la elastografía. Finalmente, los cambios en la micro-estructura del tejido fueron descritos mediante técnicas no lineales de imagen (generación del segundo armónico y microscopía de fluorescencia de dos fotones) y correlacionados con las medidas elastográficas. Se encontraron acusadas diferencias entre los animales a los que se les indujo el parto y los animales control. Los animales del grupo control mostraron estructuras direccionales bien definidas, mientras que los animales a los que se les indujo el parto presentaron estructuras más desorganizadas a una escala microscópica (1-100 μm).

Ambos estudios experimentales, tanto en animales como en mujeres, presentan limitaciones comunes que estás relacionadas con la aplicación *en-vivo* de la elastografía basada en ondas de cizalla. Junto con el tamaño reducido de la población de estudio, las principales limitaciones se asocian con la estructura compleja del tejido cervical y con las hipótesis asumidas para calcular la rigidez a partir de la velocidad de las ondas de cizalla. Para calcular la rigidez, la técnica de elastografía basada en ondas de cizalla se basa en la hipótesis de que el medio es localmente homogéneo, isotrópico y semi-infinito. Sin embargo, estas condiciones puede que no sean satisfechas siempre. En el estudio animal, antes de inducir el parto y en el grupo control, las fibras de colágeno podrían presentar una orientación altamente definida y por tanto las condiciones anteriores pueden no ser satisfechas del todo. El mismo problema podría pasar en algunas de las pacientes del estudio clínico, en particular en aquellas mujeres con corta edad gestacional, cuando los efectos de la remodelación del cuello uterino (desorganización de la red de colágeno) pueden no haber comenzado. Por último, para obtener reproducibilidad en las medidas, la presión aplicada con la sonda tiene que ser mínima y la región de interés se debe colocar alejada de la superficie de la sonda. Los efectos no lineales introducidos por la naturaleza viscoelástica del tejido son difíciles de evitar en la práctica. Sin embargo, como en toda técnica clínica de imagen, existe una curva de aprendizaje, y un médico entrenado para ello garantizará la reproducibilidad de las medidas. En relación a estas limitaciones, futuros estudios debería ser realizados para investigar

el impacto de las hipótesis asumidas y estudiar los posibles artefactos que se pueden producir en las imágenes. Además, estudios adicionales son necesarios para poder relacionar la propagación de las ondas de cizalla con los cambios histológicos y compararlos con mujeres.

La disminución de la elasticidad medida mediante la elastografía se atribuye principalmente a los cambios histológicos observados en la micro-estructura del tejido. Como último paso, se han analizado numéricamente las interacciones entre la micro-estructura del tejido y las ondas de cizalla en el **Capítulo 14**. Se ha mostrado que las características histológicas, descritas mediante un modelo basado en la teoría de mezclas y en un modelo parametrizado de la morfología, se pueden relacionar cuantitativamente con las propiedades mecánicas. Los resultados muestran que la mecánica del tejido es más sensible a las modificaciones en la micro-estructura que a los cambios en la composición de la matriz extracelular. No sólo los cambios en la composición, sino también cómo estos cambios son responsables de las variaciones en la morfología del colágeno durante la remodelación del cuello uterino. Se ha mostrado numéricamente que existe una caída en la elasticidad durante la gestación, caracterizada por diferentes parámetros histológicos y morfológicos que varían durante el embarazo en el modelo sintético propuesto. La elasticidad decrece cuando (1) las fibras de colágeno se vuelven más onduladas y aumentan de espesor, (2) la separación entre ellas aumenta y las fibras se separan, y (3) cuando la hidratación del tejido aumenta.

En el **Capítulo 9** se ha desarrollado un modelo para describir el tejido del cuello uterino que captura las principales características de la matriz extracelular. Se han generado medios espaciales bidimensionales que describen la micro-estructura del tejido cervical y se usan para simular la propagación de ondas de cizalla mediante la técnica de las diferencias finitas. Estos modelos espaciales describen el tejido cervical como un material compuesto de fibras reforzadas, formado por fibras de colágeno rodeadas por una matriz. Estos perfiles quedan definidos completamente por tres elementos: (1) tres secciones diferentes, que simulan las diferentes zonas que presenta la red de colágeno en el cuello uterino; (2) una geometría parametrizada de las fibras de colágeno, que permite estudiar el papel de la desorganización de las fibras de colágeno; y (3) las propiedades mecánicas de los constituyentes de la matriz extracelular, que se incorporan al modelo usando la teoría de mezclas. La ventaja de los medios espaciales definidos de esta particular forma es que permiten estudiar individualmente la morfología, composición y mecánica del cérvix, difícil de hacer experimentalmente.

Reconstrucción de las propiedades mecánicas mediante ultrasonidos

➥***Objetivo 3*:** Evaluar la viabilidad que tienen los modelos reológicos elementales para describir el comportamiento viscoelástico del tejido cervical y explorar la posibilidad de cuantificar la elasticidad y la viscosidad a partir de la velocidad de las ondas de cizalla.

Se ha demostrado que la propagación de ondas de cizalla se puede simular correctamente usado la técnica de las diferencias finitas. En el **Capítulo 8** se ha propuesto e implementado dicha técnica para describir la propagación de las ondas de cizalla. Para ello, se ha desarrollado un modelo que permite describir la propagación de las ondas de cizalla en un medio heterogéneo, en el que las variables se definen como funciones constantes en cada elemento. Una ventaja de usar la técnica de las diferencias finitas en el dominio del tiempo es que no se hace ninguna simplificación en la propagación de la onda, incluyendo refracciones, difracciones y múltiples reflexiones. Además, las simulaciones se pueden usar tanto para mostrar las interacciones entre las ondas de cizalla y la estructura multiescala de los tejidos blandos, como para estudiar las propiedades mecánicas de los tejidos.

La dependencia de las propiedades viscoelásticas de la frecuencia de excitación se ha estudiado en el **Capítulo 13**. Se ha mostrado que el modelo más plausible, de entre tres modelos elementales propuestos, para describir la viscoelasticidad del tejido cervical es el modelo reológico de Maxwell, contrariamente a la creencia común en la literatura. Estos resultados demuestran que la naturaleza viscoelástica del tejido cervical y su heterogeneidad influye en la propagación de las ondas de cizalla y por tanto en la respuesta global del tejido, y por consiguiente la micro y macro mecánica del tejido pueden diferir. El módulo elástico por tanto no se puede deducir directamente de la velocidad de grupo como en un medio homogéneo y está intrínsecamente relacionado con la ecuación de dispersión. Los resultados numéricos mostrados en esta tesis muestran que el fenómeno de propagación de ondas puede ser usado para evaluar las propiedades histológicas y mecánicas del tejido cervical. Las ondas de cizalla interaccionan con las fibras de colágeno (micro-escala), lo que determina las propiedades macroscópicas (escala centimétrica), y por tanto el comportamiento mecánico del tejido. Además, estos resultados sugieren que los parámetros estimados son más estables a altas frecuencias, y para excitaciones por encima de los 100 kHz los parámetros viscoelásticos son menos dependientes de la frecuencia.

La estrategia numérica desarrollada en esta tesis para determinar las propiedades viscoelásticas de los tejidos blandos se ha descrito en el **Capítulo 10**. A partir de la simulación mediante diferencias finitas de la propagación de las ondas de cizalla se puede obtener la velocidad de dispersión mediante un algoritmo basado en la diferencia de fase. Después, se proponen tres leyes reológicas bien conocidas para describir esta velocidad de fase previamente calculada, cuyos parámetros se definen mediante el problema inverso usando algoritmos genéticos. El último paso consiste en encontrar la plausibilidad de cada ley reológica propuesta, en el sentido de la probabilidad que posee para describir el comportamiento viscoelástico de tejido cervical, mediante la aplicación de una formulación estocástica de selección de clases.

Las principales limitaciones de este enfoque están relacionados con el cálculo de la curva de dispersión. El número de onda se estima a partir de un ajuste lineal de la fase a lo largo de la distancia de propagación. Sin embargo, la amplitud de onda condiciona la distancia

máxima en que este ajuste lineal puede llevarse a cabo, y cuando el medio es altamente dispersivo el gradiente de fase podría no ser constante a lo largo de la distancia de propagación. Trabajos futuros relacionados con esta metodología deberían incluir un análisis adicional de la dependencia de la frecuencia de velocidad de fase y la amplitud, y estudiar los fenómenos de propagación de ondas en medios más complejos que los que se han utilizados aquí. Adicional investigación en esta dirección debe llevarse a cabo, especialmente sobre la viabilidad de describir la respuesta viscoelástica del tejido cervical mediante una ley reológica más compleja, junto con la posibilidad de ampliar la gama de frecuencias a un registro más bajo. Finalmente, en un futuro, el modelo numérico de diferencias finitas y el medio espacial que describe el tejido deberían extenderse a la tercera dimensión y realizar un estudio en tres dimensiones para lograr una comprensión completa de las interacciones entre el tejido y las ondas de cizalla y valorar la importancia de cada parámetro morfológico.

Part V

APPENDICES

A

Contributions

The outcomes from this dissertation and other contributions of the PhD fellow are partially reflected in the refereed journals papers, book chapters and international conferences listed below.

- Refereed journal publications:
  - L. Peralta, E. Mourier, C. Richard, G. Charpigny, T. Larcher, D. Aït-Belkacem, N.K. Balla, S. Brasselet, M. Tanter, M. Muller, and P. Chavatte-Palmer, "Validation of Shear Wave Elastography to assess cervical stiffness in vivo using a sheep model of induced cervical ripening," *Submitted to PloS one (under review)*, 2015.
  - L. Peralta, F.S Molina, J. Melchor, L.F. Gómez, P. Massó, J. Florido. and G. Rus, "Transient elastography to assess the cervical ripening during pregnancy: A preliminary study," *Ultraschall in der Medizin/European Journal of Ultrasound*, 2015–In press.
  - L. Peralta, G. Rus, N. Bochud, and F.S. Molina, "Assessing viscoelasticity of shear wave propagation in cervical tissue by multiscale computational simulation," *Journal of Biomechanics*, vol. 48, no. 9, pp. 1549–1556, 2015.
  - L. Peralta, G. Rus, N. Bochud, and F.S. Molina, "Mechanical assessment of cervical remodelling in pregnancy: insight from a synthetic model," *Journal of Biomechanics*, vol. 48, no. 9, pp. 1557–1565, 2015.
  - L. Peralta, E. Mourier, C. Richard, P. Chavette-Palmer, M. Muller, M. Tanter, and G. Rus, "117 in vivo evaluation of the cervical stiffness evolution during induced labor in ewes using elastography," *Reproduction, Fertility and Development*, vol. 27, no. 1, pp. 150–151, 2015.

- L. M. Peralta, G. Rus, N. Bochud, J. M. Melchor, J. Chiachío, M. Chiachío, J. Florido, and F. Molina, "A multiscale mechanical model for the cervical tissue," *Journal of Biomechanics*, vol. 45, p. S475, 2012.
- N. Bochud, J.M. Melchor, L.M. Peralta, J. Chiachío, M. Chiachío, G. Rus, M. González-Andrades, and M. Alaminos, "Ultrasonic Monitoring of the decellularization process of porcine corneal stroma," *Journal of Biomechanics*, vol. 45, p. S435, 2012.
- J. Chiachío, M. Chiachío, G. Rus, N. Bochud, L.M. Peralta, and J.M. Melchor, "A stochastic model for tissue consistence evolution based on the inverse problem," *Journal of Biomechanics*, vol. 45, p. S652, 2012.

- Book chapters:
  - R. Muñoz, G. Rus, N. Bochud, D. Barnard, J. Melchor, J. Chiachío, M. Chiachío, S. Cantero, A. Callejas, L. Peralta and J. Bond. Nonlinear ultrasonics as an early damage signature. *In: Emerging Design Solutions in Structural Health Monitoring Systems, Advances in Civil and Industrial Engineering Series* (September 2014), Ed. IGI Global.

- Patents:
  - G. Rus, N. Bochud, J. Melchor, J. Florido and L. Peralta, "Torsional wave transducer – Transductor de ondas de torsión," Dec. 20 2012. WO Patent App. PCT/ES2012/070,380.

- International conferences:
  - J. Melchor, L. Peralta, G. Rus, N. Saffari and J. Soto, "Single-transmitter on nonlinear mixing to measure acoustic nonlinearity," *International Congress on Ultrasonics*, Metz (France), May 10–15, 2015.
  - L. Peralta, E. Mourier, C. Richard, P. Chavette-Palmer, M. Muller, M. Tanter, and G. Rus, "In vivo evaluation of the cervical stiffness evolution during induced labor in ewes using elastography," *41st Annual Conference of the International Embryo Transfer Society*, Versailles (France), January 10–13, 2015.
  - R. Muñoz, N. Bochud, G. Rus, L. Peralta, J. Melchor, J. Chiachío, M. Chiachío and L.J. Bond, "Model-based damage evaluation of layered CFRP structures," *In 41ST Annual Review of Progress in Quantitative Nondestructive Evaluation*, Idaho (USA), July 20–25, 2014.
  - G. Rus, F.S. Molina, L. Peralta, J. Florido, J. Melchor, A. Gómez, N. Bochud, J. Chiachío. and M. Chiachío, "Mechanical characterization of cervical tissue by shear wave ultrasound," *7th World Congress of Biomechanics*, Boston (USA), July 6–11, 2014.

- L. Peralta, G. Rus, N. Bochud, J. Melchor, J. Chiachío, M. Chiachío, "FDTD simulations for ultrasound propagation in a 2-D cervical tissue model," *2nd International Work-Conference on Bioinformatics and Biomedical Engineering*, Granada (Spain), April 7–9, 2014.
- L. Peralta, N. Bochud, G. Rus, "Mechanical characterization of cervical tissue by ultrasound," *Congress on Numerical Method in engineering*, Bilbao (Spain), June 25–28, 2013.
- A. Gómez, G. Rus, J. Suárez, D. Arcoya, N. Bochud, J. Melchor, L. Peralta, J. Chiachío and M. Chiachío, "Biomechanical shear moduli recovery from ultrasound in multilayered half-space media," *International Congress on Ultrasonics*, Singapore, May 2–5, 2013.
- L. Peralta, G. Rus, J. Florido and F.S. Molina, "Multiscale mechanical model for the cervical tissue," *European Congress on Computational Methods in Applied Sciences and Engineering*, Vienna (Austria), September 10–14, 2012.
- L. M. Peralta, G. Rus, N. Bochud, J. M. Melchor, J. Chiachío, M. Chiachío, J. Florido, and F. Molina, "A multiscale mechanical model for the cervical tissue," *18th Congress of the European Society of Biomechanicss*, Lisbon (Portugal), July 1–4, 2012.
- N. Bochud, J.M. Melchor, L.M. Peralta, J. Chiachío, M. Chiachío, G. Rus, M. González-Andrades, and M. Alaminos, "Ultrasonic Monitoring of the decellularization process of porcine corneal stroma," *18th Congress of the European Society of Biomechanicss*, Lisbon (Portugal), July 1–4, 2012.
- J. Chiachío, M. Chiachío, G. Rus, N. Bochud, L.M. Peralta, and J.M. Melchor, "A stochastic model for tissue consistence evolution based on the inverse problem," *18th Congress of the European Society of Biomechanicss*, Lisbon (Portugal), July 1–4, 2012.

References

[1] M. House, D. L. Kaplan, and S. Socrate, "Relationships between mechanical properties and extracellular matrix constituents of the cervical stroma during pregnancy," *Seminars in perinatology*, vol. 33, no. 5, pp. 300–307, 2009.

[2] K. Myers, S. Socrate, D. Tzeranis, and M. House, "Changes in the biochemical constituents and morphologic appearance of the human cervical stroma during pregnancy," *European Journal of Obstetrics & Gynecology and Reproductive Biology*, vol. 144, pp. S82–S89, 2009.

[3] P. C. Leppert and J. F. Woessner, *The extracellular matrix of the uterus, cervix and fetal membranes: synthesis, degradation and hormonal regulation*. Perinatology Press, 1991.

[4] L. Liu, S. Oza, D. Hogan, J. Perin, I. Rudan, J. E. Lawn, S. Cousens, C. Mathers, and R. E. Black, "Global, regional, and national causes of child mortality in 2000–13, with projections to inform post-2015 priorities: an updated systematic analysis," *The Lancet*, 2014.

[5] J. Bryce, R. E. Black, and C. G. Victora, "Millennium development goals 4 and 5: progress and challenges," *BMC medicine*, vol. 11, no. 1, p. 225, 2013.

[6] World Health Organization, "World health assembly closes." http://www.who.int/mediacentre/news/releases/2014/WHA-20140524/en/, September 2014.

[7] World Health Organization, "Preterm birth." http://who.int, November 2014.

[8] World Health Organization, "Born too soon: the global action report on preterm birth," 2012.

[9] V. Berghella, "Post-term pregnancy," *Obstetric Evidence Based Guidelines*, p. 183, 2007.

[10] A. K. Sue-A-Quan, M. E. Hannah, M. M. Cohen, G. A. Foster, and R. M. Liston, "Effect of labour induction on rates of stillbirth and cesarean section in post-term pregnancies," *Canadian Medical Association Journal*, vol. 160, no. 8, pp. 1145–1149, 1999.

[11] L. Sanchez-Ramos, F. Olivier, I. Delke, and A. M. Kaunitz, "Labor induction versus expectant management for postterm pregnancies: A systematic review with meta-analysis," *Obstetrics & Gynecology*, vol. 101, no. 6, pp. 1312–1318, 2003.

[12] World Health Organization, "Who recommendations for induction of labour," 2011.

[13] J. A. Martin, B. E. Hamilton, S. J. Ventura, M. J. Osterman, and T. Mathews, "Births: final data for 2011," *National Vital Statistics Report*, vol. 62, no. 1, pp. 1–90, 2013.

[14] A. Kwee, M. L. Bots, G. H. Visser, and H. W. Bruinse, "Obstetric management and outcome of pregnancy in women with a history of caesarean section in the netherlands," *European Journal of Obstetrics & Gynecology and Reproductive Biology*, vol. 132, no. 2, pp. 171–176, 2007.

[15] N. Uldbjerg, G. Ekman, A. Malmström, B. Sporrong, U. Ulmsten, and L. Wingerup, "Biochemical and morphological changes of human cervix after local application of prostaglandin E, in pregnancy," *The Lancet*, vol. 317, no. 8214, pp. 267–268, 1981.

[16] H. Feltovich and T. J. Hall, "Quantitative imaging of the cervix: setting the bar," *Ultrasound in Obstetrics & Gynecology*, vol. 41, no. 2, pp. 121–128, 2013.

[17] E. H. Bishop, "Pelvic scoring for elective induction," *Obstetrics & Gynecology*, vol. 24, no. 2, pp. 266–268, 1964.

[18] D. G. E. Kolkman, C. J. M. Verhoeven, S. J. Brinkhorst, J. A. M. van der Post, E. Pajkrt, B. C. Opmeer, and B. W. J. Mol, "The bishop score as a predictor of labor induction success: a systematic review," *American journal of perinatology*, vol. 30, no. 08, pp. 625–630, 2013.

[19] R. Gomez, M. Galasso, R. Romero, M. Mazor, Y. Sorokin, L. Goncalves, and M. Treadwell, "Ultrasonographic examination of the uterine cervix is better than cervical digital examination as a predictor of the likelihood of premature delivery in patients with preterm labor and intact membranes," *American journal of obstetrics and gynecology*, vol. 171, no. 4, pp. 956–964, 1994.

[20] J. D. Iams, R. L. Goldenberg, P. J. Meis, B. M. Mercer, A. Moawad, A. Das, E. Thom, D. McNellis, R. L. Copper, F. Johnson, *et al.*, "The length of the cervix and the risk of spontaneous premature delivery," *New England Journal of Medicine*, vol. 334, no. 9, pp. 567–573, 1996.

[21] E. Celik, M. To, K. Gajewska, G. C. S. Smith, and K. H. Nicolaides, "Cervical length and obstetric history predict spontaneous preterm birth: development and validation of a model to provide individualized risk assessment," *Ultrasound in obstetrics & gynecology*, vol. 31, no. 5, pp. 549–554, 2008.

[22] G. K. Pandis, A. T. Papageorghiou, V. G. Ramanathan, M. O. Thompson, and K. H. Nicolaides, "Preinduction sonographic measurement of cervical length in the prediction of successful induction of labor," *Ultrasound in obstetrics & gynecology*, vol. 18, no. 6, pp. 623–628, 2001.

[23] C. J. M. Verhoeven, B. C. Opmeer, S. G. Oei, V. Latour, J. A. M. van Der Post, and B. W. J. Mol, "Transvaginal sonographic assessment of cervical length and wedging for predicting outcome of labor induction at term: a systematic review and meta-analysis," *Ultrasound in Obstetrics & Gynecology*, vol. 42, no. 5, pp. 500–508, 2013.

[24] M. Swiatkowska-Freund and K. Preis, "Elastography of the uterine cervix: implications for success of induction of labor," *Ultrasound in Obstetrics & Gynecology*, vol. 38, no. 1, pp. 52–56, 2011.

[25] F. S. Molina, L. F. Gómez, J. Florido, M. C. Padilla, and K. H. Nicolaides, "Quantification of cervical elastography: a reproducibility study," *Ultrasound in Obstetrics & Gynecology*, vol. 39, no. 6, pp. 685–689, 2012.

[26] M. R. Khalil, P. Thorsen, and N. Uldbjerg, "Cervical ultrasound elastography may hold potential to predict risk of preterm birth," *Dan Med J*, vol. 60, no. 1, p. A4570, 2013.

[27] E. Hernandez-Andrade, S. S. Hassan, H. Ahn, S. J. Korzeniewski, L. Yeo, T. Chaiworapongsa, and R. Romero, "Evaluation of cervical stiffness during pregnancy using semiquantitative ultrasound elastography," *Ultrasound in Obstetrics & Gynecology*, vol. 41, no. 2, pp. 152–161, 2013.

[28] E. Mazza, A. Nava, M. Bauer, R. Winter, M. Bajka, and G. A. Holzapfel, "Mechanical properties of the human uterine cervix: an in vivo study," *Medical image analysis*, vol. 10, no. 2, pp. 125–136, 2006.

[29] R. C. Booi, P. L. Carson, M. O'Donnell, M. A. Roubidoux, A. L. Hall, and J. M. Rubin, "Characterization of cysts using differential correlation coefficient values from two dimensional breast elastography: preliminary study," *Ultrasound in medicine & biology*, vol. 34, no. 1, pp. 12–21, 2008.

[30] M. Muller, J. L. Gennisson, T. Deffieux, M. Tanter, and M. Fink, "Quantitative viscoelasticity mapping of human liver using supersonic shear imaging: Preliminary in vivo feasability study," *Ultrasound in medicine & biology*, vol. 35, no. 2, pp. 219–229, 2009.

[31] J. L. Gennisson, T. Deffieux, M. Fink, and M. Tanter, "Ultrasound elastography: Principles and techniques," *Diagnostic and interventional imaging*, vol. 94, no. 5, pp. 487–495, 2013.

[32] T. K. Yasar, T. J. Royston, and R. L. Magin, "Wideband MR elastography for viscoelasticity model identification," *Magnetic Resonance in Medicine*, vol. 70, no. 2, pp. 479–489, 2013.

[33] M. L. Akins, K. Luby-Phelps, R. A. Bank, and M. Mahendroo, "Cervical softening during pregnancy: regulated changes in collagen cross-linking and composition of matricellular proteins in the mouse," *Biology of reproduction*, vol. 84, no. 5, pp. 1053–1062, 2011.

[34] M. Mahendroo, "Cervical remodeling in term and preterm birth: insights from an animal model," *Reproduction*, vol. 143, no. 4, pp. 429–438, 2012.

[35] L. Peralta, M. Mourier, C. Richard, G. Charpigny, T. Larcher, D. Aït-Belkacem, N. Balla, S. Brasselet, M. Tanter, M. Muller, and P. Chavatte-Palmer, "Validation of shear wave elastography to assess cervical stiffness in vivo using a sheep model of induced cervical ripening," *Plos One*, 2015.

[36] I. Sack, B. Beierbach, J. Wuerfel, D. Klatt, U. Hamhaber, S. Papazoglou, P. Martus, and J. Braun, "The impact of aging and gender on brain viscoelasticity," *Neuroimage*, vol. 46, no. 3, pp. 652–657, 2009.

[37] M. Z. Kiss, M. A. Hobson, T. Varghese, J. Harter, M. A. Kliewer, E. M. Hartenbach, and J. A. Zagzebski, "Frequency-dependent complex modulus of the uterus: preliminary results," *Physics in medicine and biology*, vol. 51, no. 15, p. 3683, 2006.

[38] B. L. McFarlin, T. A. Bigelow, Y. Laybed, W. O'Brien, M. L. Oelze, and J. Abramowicz, "Ultrasonic attenuation estimation of the pregnant cervix: a preliminary report," *Ultrasound in Obstetrics & Gynecology*, vol. 36, no. 2, pp. 218–225, 2010.

[39] B. Timmons, M. Akins, and M. Mahendroo, "Cervical remodeling during pregnancy and parturition," *Trends in Endocrinology & Metabolism*, vol. 21, no. 6, pp. 353–361, 2010.

[40] W. R. Barone, A. J. Feola, P. A. Moalli, and S. D. Abramowitch, "Viscoelastic behavior of the rat uterine cervix at mid-pregnancy," in *ASME 2010 Summer Bioengineering Conference*, pp. 697–698, American Society of Mechanical Engineers, 2010.

[41] H. Feltovich, T. J. Hall, and V. Berghella, "Beyond cervical length: emerging technologies for assessing the pregnant cervix," *American journal of obstetrics and gynecology*, vol. 207, no. 5, pp. 345–354, 2012.

[42] E. Mazza, M. Parra-Saavedra, M. Bajka, E. Gratacos, K. Nicolaides, and J. Deprest, "In vivo assessment of the biomechanical properties of the uterine cervix in pregnancy," *Prenatal diagnosis*, vol. 34, no. 1, pp. 33–41, 2014.

[43] D. N. Danforth, "The morphology of the human cervix," *Clinical obstetrics and gynecology*, vol. 26, no. 1, pp. 7–13, 1983.

[44] T. Rechberger, S. R. Abramson, and J. Woessner, "Onapristone and prostaglandin e2 induction of delivery in the rat in late pregnancy: a model for the analysis of cervical softening," *American journal of obstetrics and gynecology*, vol. 175, no. 3, pp. 719–723, 1996.

[45] M. S. Mahendroo, A. Porter, D. W. Russell, and R. A. Word, "The parturition defect in steroid 5α-reductase type 1 knockout mice is due to impaired cervical ripening," *Molecular Endocrinology*, vol. 13, no. 6, pp. 981–992, 1999.

[46] L. Hee, "Overview of the methods available for biomechanical testing of the uterine cervix in vivo," *Acta obstetricia et gynecologica Scandinavica*, vol. 93, no. 12, pp. 1219–1237, 2014.

[47] L. C. Carlson, S. T. Romero, M. L. Palmeri, A. Muñoz del Rio, S. M. Esplin, V. M. Rotemberg, T. J. Hall, and H. Feltovich, "Changes in shear wave speed pre and post induction of labor: a feasibility study," *Ultrasound in Obstetrics & Gynecology*, 2014.

[48] L. C. Carlson, H. Feltovich, M. L. Palmeri, J. J. Dahl, A. Munoz Del Rio, and T. J. Hall, "Estimation of shear wave speed in the human uterine cervix," *Ultrasound in Obstetrics & Gynecology*, vol. 43, no. 4, pp. 452–458, 2014.

[49] J. Bercoff, M. Tanter, and M. Fink, "Supersonic shear imaging: a new technique for soft tissue elasticity mapping," *Ultrasonics, Ferroelectrics, and Frequency Control, IEEE Transactions on*, vol. 51, no. 4, pp. 396–409, 2004.

[50] J. Bamber, D. Cosgrove, C. Dietrich, J. Fromageau, J. Bojunga, F. Calliada, V. Cantisani, J. Correas, M. D'Onofrio, E. Drakonaki, *et al.*, "EFSUMB guidelines and recommendations on the clinical use of ultrasound elastography. Part 1: Basic principles and technology," *Ultraschall Med*, vol. 34, no. 2, pp. 169–184, 2013.

[51] S. Badir, E. Mazza, R. Zimmermann, and M. Bajka, "Cervical softening occurs early in pregnancy: characterization of cervical stiffness in 100 healthy women using the aspiration technique," *Prenatal diagnosis*, vol. 33, no. 8, pp. 737–741, 2013.

[52] A. Sarvazyan and C. Hill, "Physical chemistry of the ultrasound-tissue intereaction," *Hill CR, Bamber JC, ter HaarGR,(eds) Physical Principles of Medical Ultrasonics. 2nd ed. Chichester: John Wiley*, pp. 223–235, 2004.

[53] A. Singer and J. A. Jordan, *The Cervix*. Wiley Online Library, 2nd ed., 2006.

[54] P. Fratzl, *Collagen: structure and mechanics*. Springer Science & Business Media, 2008.

[55] R. M. Aspden, "Collagen organisation in the cervix and its relation to mechanical function," *Collagen and related research*, vol. 8, no. 2, pp. 103–112, 1988.

[56] S. Weiss, T. Jaermann, P. Schmid, P. Staempfli, P. Boesiger, P. Niederer, R. Caduff, and M. Bajka, "Three-dimensional fiber architecture of the nonpregnant human uterus determined ex vivo using magnetic resonance diffusion tensor imaging," *The Anatomical Record Part A: Discoveries in Molecular, Cellular, and Evolutionary Biology*, vol. 288, no. 1, pp. 84–90, 2006.

[57] M. L. Akins, K. Luby-Phelps, and M. Mahendroo, "Second harmonic generation imaging as a potential tool for staging pregnancy and predicting preterm birth," *Journal of biomedical optics*, vol. 15, no. 2, pp. 026020–026020, 2010.

[58] W. C. Dale and E. Baer, "Fibre-buckling in composite systems: a model for the ultrastructure of uncalcified collagen tissues," *Journal of Materials Science*, vol. 9, no. 3, pp. 369–382, 1974.

[59] S. P. Magnusson, K. Qvortrup, J. O. Larsen, S. Rosager, P. Hanson, P. Aagaard, M. Krogsgaard, and M. Kjaer, "Collagen fibril size and crimp morphology in ruptured and intact achilles tendons," *Matrix biology*, vol. 21, no. 4, pp. 369–377, 2002.

[60] M. P. E. Wenger, L. Bozec, M. A. Horton, and P. Mesquida, "Mechanical properties of collagen fibrils," *Biophysical journal*, vol. 93, no. 4, pp. 1255–1263, 2007.

[61] L. M. Peralta, G. Rus, N. Bochud, J. M. Melchor, J. Chiachío, M. Chiachío, J. Florido, and F. Molina, "A multiscale mechanical model for the cervical tissue," *Journal of Biomechanics*, vol. 45, p. S475, 2012.

[62] P. C. Leppert, S. Keller, J. Cerreta, Y. Hosannah, and I. Mandl, "The content of elastin in the uterine cervix," *Archives of biochemistry and biophysics*, vol. 222, no. 1, pp. 53–58, 1983.

[63] P. C. Leppert, J. M. Cerreta, and I. Mandl, "Orientation of elastic fibers in the human cervix," *American journal of obstetrics and gynecology*, vol. 155, no. 1, pp. 219–224, 1986.

[64] M. M. Koenders, L. Yang, R. G. Wismans, K. O. van der Werf, D. P. Reinhardt, W. Daamen, M. L. Bennink, P. J. Dijkstra, T. H. van Kuppevelt, and J. Feijen, "Microscale

mechanical properties of single elastic fibers: the role of fibrillin–microfibrils," *Biomaterials*, vol. 30, no. 13, pp. 2425–2432, 2009.

[65] K. G. Danielson, H. Baribault, D. F. Holmes, H. Graham, K. E. Kadler, and R. V. Iozzo, "Targeted disruption of decorin leads to abnormal collagen fibril morphology and skin fragility," *The Journal of cell biology*, vol. 136, no. 3, pp. 729–743, 1997.

[66] K. M. Myers, H. Feltovich, E. Mazza, J. Vink, M. Bajka, R. J. Wapner, T. J. Hall, and M. House, "The mechanical role of the cervix in pregnancy," *Journal of biomechanics*, 2015.

[67] N. Uldbjerg, G. Ekman, A. Malmstrom, K. Olsson, and U. Ulmsten, "Ripening of the human uterine cervix related to changes in collagen, glycosaminoglycans, and collagenolytic activity," *Obstet. Gynecol*, vol. 147, pp. 662–666, 1983.

[68] K. Yoshida, C. Reeves, J. Vink, J. Kitajewski, R. Wapner, H. Jiang, S. Cremers, and K. Myers, "Cervical collagen network remodeling in normal pregnancy and disrupted parturition in Antxr2 deficient mice," *Journal of biomechanical engineering*, vol. 136, no. 2, p. 021017, 2014.

[69] K. M. Myers, A. P. Paskaleva, M. House, and S. Socrate, "Mechanical and biochemical properties of human cervical tissue," *Acta Biomaterialia*, vol. 4, no. 1, pp. 104–116, 2008.

[70] T. Rechberger, N. Uldbjerg, and H. Oxlund, "Connective tissue changes in the cervix during normal pregnancy and pregnancy complicated by cervical incompetence.," *Obstetrics & Gynecology*, vol. 71, no. 4, pp. 563–567, 1988.

[71] L. K. Petersen and N. Uldbjerg, "Cervical collagen in non-pregnant women with previous cervical incompetence," *European Journal of Obstetrics & Gynecology and Reproductive Biology*, vol. 67, no. 1, pp. 41–45, 1996.

[72] R. Garfield, G. Saade, C. Buhimschi, I. Buhimschi, L. Shi, S. Shi, and K. Chwalisz, "Control and assessment of the uterus and cervix during pregnancy and labour," *Human Reproduction Update*, vol. 4, no. 5, pp. 673–695, 1998.

[73] M. Iwahashi, Y. Muragaki, A. Ooshima, and N. Umesaki, "Decreased type I collagen expression in human uterine cervix during pregnancy," *The Journal of Clinical Endocrinology & Metabolism*, vol. 88, no. 5, pp. 2231–2235, 2003.

[74] Y. Gan, W. Yao, K. M. Myers, J. Y. Vink, R. J. Wapner, and C. P. Hendon, "Analyzing three-dimensional ultrastructure of human cervical tissue using optical coherence tomography," *Biomedical Optics Express*, vol. 6, no. 4, pp. 1090–1108, 2015.

[75] Y. Zhang, M. L. Akins, K. Murari, J. Xi, M.-J. Li, K. Luby-Phelps, M. Mahendroo, and X. Li, "A compact fiber-optic SHG scanning endomicroscope and its application to visualize cervical remodeling during pregnancy," *Proceedings of the National Academy of Sciences*, vol. 109, no. 32, pp. 12878–12883, 2012.

[76] C. S. Buhimschi, N. Sora, G. Zhao, and I. A. Buhimschi, "Genetic background affects the biomechanical behavior of the postpartum mouse cervix," *American journal of obstetrics and gynecology*, vol. 200, no. 4, pp. 434–e1, 2009.

[77] E. El Maradny, N. Kanayama, H. Kobayashi, B. Hossain, S. Khatun, S. Liping, T. Kobayashi, and T. Terao, "The role of hyaluronic acid as a mediator and regulator of cervical ripening.," *Human reproduction*, vol. 12, no. 5, pp. 1080–1088, 1997.

[78] R. Osmers, W. Rath, M. A. Pflanz, W. Kuhn, H.-W. Stuhlsatz, and M. Szeverényi, "Glycosaminoglycans in cervical connective tissue during pregnancy and parturition.," *Obstetrics & Gynecology*, vol. 81, no. 1, pp. 88–92, 1993.

[79] T. A. Bigelow, B. L. McFarlin, W. D. O'Brien Jr, and M. L. Oelze, "In vivo ultrasonic attenuation slope estimates for detecting cervical ripening in rats: Preliminary results," *The Journal of the Acoustical Society of America*, vol. 123, no. 3, pp. 1794–1800, 2008.

[80] Y. Labyed, T. A. Bigelow, and B. L. McFarlin, "Estimate of the attenuation coefficient using a clinical array transducer for the detection of cervical ripening in human pregnancy," *Ultrasonics*, vol. 51, no. 1, pp. 34–39, 2011.

[81] M. O'Connell, J. Tidy, S. Wisher, N. Avis, B. Brown, and S. Lindow, "An in vivo comparative study of the pregnant and nonpregnant cervix using electrical impedance measurements," *BJOG: An International Journal of Obstetrics & Gynaecology*, vol. 107, no. 8, pp. 1040–1041, 2000.

[82] M. O'Connell, N. Avis, B. Brown, S. Killick, and S. Lindow, "Electrical impedance measurements: an objective measure of prelabor cervical change," *Journal of Maternal-Fetal and Neonatal Medicine*, vol. 14, no. 6, pp. 389–391, 2003.

[83] S. V. Gandhi, D. Walker, P. Milnes, S. Mukherjee, B. H. Brown, and D. O. Anumba, "Electrical impedance spectroscopy of the cervix in non-pregnant and pregnant women," *European Journal of Obstetrics & Gynecology and Reproductive Biology*, vol. 129, no. 2, pp. 145–149, 2006.

[84] R. P. Jokhi, B. H. Brown, and D. O. Anumba, "The role of cervical electrical impedance spectroscopy in the prediction of the course and outcome of induced labour," *BMC pregnancy and childbirth*, vol. 9, no. 1, p. 40, 2009.

[85] Y. Chan, W. Lam, T. Lau, S. Wong, C. Li, and C. Metreweli, "Cervical assessment by magnetic resonance imaging–its relationship to gestational age and interval to delivery.," *The British journal of radiology*, vol. 71, no. 842, pp. 155–159, 1998.

[86] M. House, M. O'Callaghan, S. Bahrami, D. Chelmow, J. Kini, D. Wu, S. Patz, and R. A. Bhadelia, "Magnetic resonance imaging of the cervix during pregnancy: effect of gestational age and prior vaginal birth," *American journal of obstetrics and gynecology*, vol. 193, no. 4, pp. 1554–1560, 2005.

[87] B. M. de Tejada, D. L. Faltin, K. Kinkel, M.-J. Guittier, M. Boulvain, and O. Irion, "Magnetic resonance imaging of the cervix in women at high risk for preterm delivery," *Journal of Maternal-Fetal and Neonatal Medicine*, vol. 24, no. 11, pp. 1392–1397, 2011.

[88] M. Lucovnik, R. J. Kuon, and R. E. Garfield, "Assessment of parturition with cervical light-induced fluorescence and uterine electromyography," *Computational and mathematical methods in medicine*, vol. 2013, 2013.

[89] D. Schlembach, L. MacKay, L. Shi, W. L. Maner, R. E. Garfield, and H. Maul, "Cervical ripening and insufficiency: from biochemical and molecular studies to in vivo clinical examination," *European Journal of Obstetrics & Gynecology and Reproductive Biology*, vol. 144, pp. S70–S76, 2009.

[90] H. Maul, G. Olson, C. T. Fittkow, G. R. Saade, and R. E. Garfield, "Cervical light-induced fluorescence in humans decreases throughout gestation and before delivery: preliminary observations," *American journal of obstetrics and gynecology*, vol. 188, no. 2, pp. 537–541, 2003.

[91] C. T. Fittkow, H. Maul, G. Olson, E. Martin, L. B. MacKay, G. R. Saade, and R. E. Garfield, "Light-induced fluorescence of the human cervix decreases after prostaglandin application for induction of labor at term," *European Journal of Obstetrics & Gynecology and Reproductive Biology*, vol. 123, no. 1, pp. 62–66, 2005.

[92] N. Afzali, M. Mohajeri, A. Malek, and A. Alamatian, "Cervical gland area: a new sonographic marker in predicting preterm delivery," *Archives of gynecology and obstetrics*, vol. 285, no. 1, pp. 255–258, 2012.

[93] K. Yoshimatsu, T. Sekiya, K. Ishihara, T. Fukami, T. Otabe, and T. Araki, "Detection of the cervical gland area in threatened preterm labor using transvaginal sonography in the assessment of cervical maturation and the outcome of pregnancy.," *Gynecologic and obstetric investigation*, vol. 53, no. 3, pp. 149–156, 2001.

[94] C. Pires, A. Moron, R. Mattar, A. Diniz, S. Andrade, and L. Bussamra, "Cervical gland area as an ultrasonographic marker for preterm delivery," *International Journal of Gynecology & Obstetrics*, vol. 93, no. 3, pp. 214–219, 2006.

[95] N. Tateyama, H. Asakura, and T. Takeshita, "Correlation between an absence of cervical gland area on transvaginal sonography and cervical mucus hyaluronic acid levels in women with threatened preterm delivery," *Journal of perinatal medicine*, vol. 41, no. 2, pp. 151–157, 2013.

[96] R. Hornung, S. Spichtig, A. Baños, M. Stahel, R. Zimmermann, and M. Wolf, "Frequency-domain near-infrared spectroscopy of the uterine cervix during regular pregnancies," *Lasers in medical science*, vol. 26, no. 2, pp. 205–212, 2011.

[97] A. Baños, M. Wolf, C. Grawe, M. Stahel, D. Haensse, D. Fink, and R. Hornung, "Frequency domain near-infrared spectroscopy of the uterine cervix during cervical ripening," *Lasers in surgery and medicine*, vol. 39, no. 8, pp. 641–646, 2007.

[98] L. Peralta, F. S. Molina, J. Melchor, L. F. Gómez, P. Massó, J. Florido, and G. Rus, "Transient elastography to assess the cervical ripening during pregnancy: A preliminary study," *Ultraschall in der Medizin*, 2015.

[99] M. Bauer, E. Mazza, M. Jabareen, L. Sultan, M. Bajka, U. Lang, R. Zimmermann, and G. A. Holzapfel, "Assessment of the in vivo biomechanical properties of the human uterine cervix in pregnancy using the aspiration test: a feasibility study," *European Journal of Obstetrics & Gynecology and Reproductive Biology*, vol. 144, pp. S77–S81, 2009.

[100] S. Badir, M. Bajka, and E. Mazza, "A novel procedure for the mechanical characterization of the uterine cervix during pregnancy," *Journal of the mechanical behavior of biomedical materials*, vol. 27, pp. 143–153, 2013.

[101] T. Kuwata, S. Matsubara, N. Taniguchi, A. Ohkuchi, T. Ohkusa, and M. Suzuki, "A novel method for evaluating uterine cervical consistency using vaginal ultrasound gray-level histogram," *Journal of perinatal medicine*, vol. 38, no. 5, pp. 491–494, 2010.

[102] W. Stein, L. Hellmeyer, S. Schmidt, and I. Tekesin, "Intraobserver and interobserver reliability of transvaginal cervical length measurements and quantitative ultrasound tissue characterization of the cervix in the second and third trimester of pregnancy.," *Ultraschall in der Medizin (Stuttgart, Germany: 1980)*, vol. 32, pp. E169–74, 2011.

[103] I. Tekesin, L. Hellmeyer, G. Heller, A. Römer, M. Kühnert, and S. Schmidt, "Evaluation of quantitative ultrasound tissue characterization of the cervix and cervical length in the prediction of premature delivery for patients with spontaneous preterm labor," *American journal of obstetrics and gynecology*, vol. 189, no. 2, pp. 532–539, 2003.

[104] I. Tekesin, D. Wallwiener, and S. Schmidt, "The value of quantitative ultrasound tissue characterization of the cervix and rapid fetal fibronectin in predicting preterm delivery," *Journal of perinatal medicine*, vol. 33, no. 5, pp. 383–391, 2005.

[105] D. Cabrol, D. Jannet, R. Le Houezec, W. Dudzik, E. Bonoris, and L. Cedard, "Mechanical properties of the pregnant human uterine cervix use of an instrument to measure the index of cervical distensibility," *Gynecologic and obstetric investigation*, vol. 29, no. 1, pp. 32–36, 1990.

[106] R. Kiwi, M. R. Neuman, I. R. Merkatz, M. A. Selim, and A. Lysikiewicz, "Determination of the elastic properties of the cervix.," *Obstetrics & Gynecology*, vol. 71, no. 4, pp. 568–574, 1988.

[107] L. Hee, D. Liao, P. Sandager, H. Gregersen, and N. Uldbjerg, "Cervical stiffness evaluated in vivo by endoflip in pregnant women," *PloS one*, vol. 9, no. 3, p. e91121, 2014.

[108] D. Cabrol, B. Carbonne, D. Jannet, C. Baton, E. Bonoris, W. Dudzik, and R. Lehouezec, "Prognostic value of cervical distensibility index measurement in the outcome of pregnancies with threatened premature labor," *Gynecologic and obstetric investigation*, vol. 32, no. 1, pp. 28–32, 1991.

[109] D. Cabrol, B. Carbonne, C. Ledieu, and F. Lussiana, "Relationship between mechanical properties of the uterine cervix and occurrence of postdate pregnancy," *Gynecologic and obstetric investigation*, vol. 32, no. 1, pp. 36–38, 1991.

[110] D. Cosgrove, F. Piscaglia, J. Bamber, J. Bojunga, J. Correas, O. Gilja, A. Klauser, I. Sporea, F. Calliada, V. Cantisani, *et al.*, "EFSUMB guidelines and recommendations on the clinical use of ultrasound elastography. Part 2: Clinical applications," *Ultraschall Med*, vol. 34, no. 3, pp. 238–253, 2013.

[111] C. A. Elsberg, *Dr. Edwin Smith surgical papyrus and the diagnosis and treatment of injuries to the skull and spine 5000 years ago*. Charles Albert Elsberg, 1931.

[112] K. Parker, M. Doyley, and D. Rubens, "Corrigendum: Imaging the elastic properties of tissue: the 20 year perspective," *Physics in Medicine and Biology*, vol. 57, no. 16, p. 5359, 2012.

[113] J. Ophir, I. Cespedes, H. Ponnekanti, Y. Yazdi, and X. Li, "Elastography: a quantitative method for imaging the elasticity of biological tissues," *Ultrasonic imaging*, vol. 13, no. 2, pp. 111–134, 1991.

[114] L. Wilson, D. Robinson, and M. Dadd, "Elastography-the movement begins," *Physics in medicine and biology*, vol. 45, no. 6, p. 1409, 2000.

[115] H. Morikawa, K. Fukuda, S. Kobayashi, H. Fujii, S. Iwai, M. Enomoto, A. Tamori, H. Sakaguchi, and N. Kawada, "Real-time tissue elastography as a tool for the non-invasive assessment of liver stiffness in patients with chronic hepatitis c," *Journal of gastroenterology*, vol. 46, no. 3, pp. 350–358, 2011.

[116] A. Itoh, E. Ueno, E. Tohno, H. Kamma, H. Takahashi, T. Shiina, M. Yamakawa, and T. Matsumura, "Breast disease: Clinical application of us elastography for diagnosis 1," *Radiology*, vol. 239, no. 2, pp. 341–350, 2006.

[117] B. S. Garra, E. I. Cespedes, J. Ophir, S. R. Spratt, R. A. Zuurbier, C. M. Magnant, and M. F. Pennanen, "Elastography of breast lesions: initial clinical results.," *Radiology*, vol. 202, no. 1, pp. 79–86, 1997.

[118] R. M. Lerner, K. J. Parker, J. Holen, R. Gramiak, and R. C. Waag, "Sono-elasticity: medical elasticity images derived from ultrasound signals in mechanically vibrated targets," in *Acoustical imaging*, pp. 317–327, Springer, 1988.

[119] M. Fatemi and J. F. Greenleaf, "Ultrasound-stimulated vibro-acoustic spectrography," *Science*, vol. 280, no. 5360, pp. 82–85, 1998.

[120] L. Sandrin, M. Tanter, J.-L. Gennisson, S. Catheline, and M. Fink, "Shear elasticity probe for soft tissues with 1-D transient elastography," *Ultrasonics, Ferroelectrics, and Frequency Control, IEEE Transactions on*, vol. 49, no. 4, pp. 436–446, 2002.

[121] K. Nightingale, M. S. Soo, R. Nightingale, and G. Trahey, "Acoustic radiation force impulse imaging: in vivo demonstration of clinical feasibility," *Ultrasound in medicine & biology*, vol. 28, no. 2, pp. 227–235, 2002.

[122] L. Gao, K. J. Parker, S. Alam, D. Rubens, and R. M. Lerner, "Theory and application of sonoelasticity imaging," *International journal of imaging systems and technology*, vol. 8, no. 1, pp. 104–109, 1997.

[123] S. F. Levinson, M. Shinagawa, and T. Sato, "Sonoelastic determination of human skeletal muscle elasticity," *Journal of biomechanics*, vol. 28, no. 10, pp. 1145–1154, 1995.

[124] L. Taylor, B. Porter, D. Rubens, and K. Parker, "Three-dimensional sonoelastography: principles and practices," *Physics in medicine and biology*, vol. 45, no. 6, p. 1477, 2000.

[125] G. Torr, "The acoustic radiation force," *American Journal of Physics*, vol. 52, no. 5, pp. 402–408, 1984.

[126] G. Rus, "Nature of acoustic nonlinear radiation stress," *Applied Physics Letters*, vol. 105, no. 12, p. 121904, 2014.

[127] W. Nyborg, "Acoustic streaming," *Physical acoustics*, vol. 2, no. Pt B, p. 265, 1965.

[128] M. Fatemi, L. E. Wold, A. Alizad, and J. F. Greenleaf, "Vibro-acoustic tissue mammography," *Medical Imaging, IEEE Transactions on*, vol. 21, no. 1, pp. 1–8, 2002.

[129] F. Mitri, B. Davis, J. Greenleaf, and M. Fatemi, "In vitro comparative study of vibro-acoustography versus pulse-echo ultrasound in imaging permanent prostate brachytherapy seeds," *Ultrasonics*, vol. 49, no. 1, pp. 31–38, 2009.

[130] S. Catheline, F. Wu, and M. Fink, "A solution to diffraction biases in sonoelasticity: the acoustic impulse technique," *The Journal of the Acoustical Society of America*, vol. 105, no. 5, pp. 2941–2950, 1999.

[131] L. Castéra, J. Vergniol, J. Foucher, B. Le Bail, E. Chanteloup, M. Haaser, M. Darriet, P. Couzigou, and V. de Lédinghen, "Prospective comparison of transient elastography, fibrotest, apri, and liver biopsy for the assessment of fibrosis in chronic hepatitis c," *Gastroenterology*, vol. 128, no. 2, pp. 343–350, 2005.

[132] L. Sandrin, B. Fourquet, J.-M. Hasquenoph, S. Yon, C. Fournier, F. Mal, C. Christidis, M. Ziol, B. Poulet, F. Kazemi, *et al.*, "Transient elastography: a new noninvasive method for assessment of hepatic fibrosis," *Ultrasound in medicine & biology*, vol. 29, no. 12, pp. 1705–1713, 2003.

[133] J. Bercoff, S. Chaffai, M. Tanter, L. Sandrin, S. Catheline, M. Fink, J. Gennisson, and M. Meunier, "In vivo breast tumor detection using transient elastography," *Ultrasound in medicine & biology*, vol. 29, no. 10, pp. 1387–1396, 2003.

[134] K. R. Nightingale, M. L. Palmeri, R. W. Nightingale, and G. E. Trahey, "On the feasibility of remote palpation using acoustic radiation force," *The Journal of the Acoustical Society of America*, vol. 110, no. 1, pp. 625–634, 2001.

[135] T. Shiina, K. R. Nightingale, M. L. Palmeri, T. J. Hall, J. C. Bamber, R. G. Barr, L. Castera, B. I. Choi, Y.-H. Chou, D. Cosgrove, *et al.*, "WFUMB guidelines and recommendations for clinical use of ultrasound elastography: Part 1: Basic principles and terminology," *Ultrasound in Medicine & Biology*, 2015.

[136] W. Meng, G. Zhang, C. Wu, G. Wu, Y. Song, and Z. Lu, "Preliminary results of acoustic radiation force impulse (arfi) ultrasound imaging of breast lesions," *Ultrasound in medicine & biology*, vol. 37, no. 9, pp. 1436–1443, 2011.

[137] L. Zhai, J. Madden, W.-C. Foo, M. L. Palmeri, V. Mouraviev, T. J. Polascik, and K. R. Nightingale, "Acoustic radiation force impulse imaging of human prostates ex vivo," *Ultrasound in medicine & biology*, vol. 36, no. 4, pp. 576–588, 2010.

[138] B. J. Fahey, M. L. Palmeri, and G. E. Trahey, "Frame rate considerations for real-time abdominal acoustic radiation force impulse imaging," *Ultrasonic imaging*, vol. 28, no. 4, pp. 193–210, 2006.

[139] K. Nightingale, S. McAleavey, and G. Trahey, "Shear-wave generation using acoustic radiation force: in vivo and ex vivo results," *Ultrasound in medicine & biology*, vol. 29, no. 12, pp. 1715–1723, 2003.

[140] J. Melchor and G. Rus, "Torsional ultrasonic transducer computational design optimization," *Ultrasonics*, vol. 54, no. 7, pp. 1950–1962, 2014.

[141] A. Thomas, "Imaging of the cervix using sonoelastography," *Ultrasound in obstetrics & gynecology*, vol. 28, no. 3, pp. 356–357, 2006.

[142] A. Thomas, S. Kümmel, O. Gemeinhardt, and T. Fischer, "Real-time sonoelastography of the cervix: tissue elasticity of the normal and abnormal cervix," *Academic radiology*, vol. 14, no. 2, pp. 193–200, 2007.

[143] M. Maurer, S. Badir, M. Pensalfini, M. Bajka, P. Abitabile, R. Zimmermann, and E. Mazza, "Challenging the in-vivo assessment of biomechanical properties of the uterine cervix: A critical analysis of ultrasound based quasi-static procedures," *Journal of biomechanics*, vol. doi:10.1016/j.jbiomech.2015.02.038, 2015.

[144] A. Fruscalzo and R. Schmitz, "Quantitative cervical elastography in pregnancy," *Ultrasound in Obstetrics & Gynecology*, vol. 40, no. 5, pp. 612–612, 2012.

[145] L. Hee, P. Sandager, O. Petersen, and N. Uldbjerg, "Quantitative sonoelastography of the uterine cervix by interposition of a synthetic reference material," *Acta obstetricia et gynecologica Scandinavica*, vol. 92, no. 11, pp. 1244–1249, 2013.

[146] A. Fruscalzo, A. P. Londero, and R. Schmitz, "Quantitative cervical elastography during pregnancy: influence of setting features on strain calculation," *Journal of Medical Ultrasonics*, pp. 1–8, 2015.

[147] A. Fruscalzo, R. Schmitz, W. Klockenbusch, and J. Steinhard, "Reliability of cervix elastography in the late first and second trimester of pregnancy," *Ultraschall in der Medizin-European Journal of Ultrasound*, vol. 33, no. 07, pp. E101–E107, 2012.

[148] A. Fruscalzo, A. Londero, C. Fröhlich, U. Möllmann, and R. Schmitz, "Quantitative elastography for cervical stiffness assessment during pregnancy," *BioMed research international*, vol. 2014, 2014.

[149] A. Al Naimi, M. Fittschen, and F. Bahlmann, "Measuring cervical strain with tissue doppler imaging depending on the shape and placement of the region of interest and its correlation with cervical consistency index," *European Journal of Obstetrics & Gynecology and Reproductive Biology*, vol. 179, pp. 246–250, 2014.

[150] L. C. Carlson, H. Feltovich, M. L. Palmeri, A. Munoz del Rio, and T. J. Hall, "Statistical analysis of shear wave speed in the uterine cervix," *Ultrasonics, Ferroelectrics, and Frequency Control, IEEE Transactions on*, vol. 61, no. 10, pp. 1651–1660, 2014.

[151] E. Hernandez-Andrade, R. Romero, S. J. Korzeniewski, H. Ahn, A. Aurioles-Garibay, M. Garcia, A. G. Schwartz, L. Yeo, T. Chaiworapongsa, and S. S. Hassan, "Cervical strain determined by ultrasound elastography and its association with spontaneous preterm delivery," *Journal of perinatal medicine*, vol. 42, no. 2, pp. 159–169, 2014.

[152] K. Köbbing, A. Fruscalzo, K. Hammer, M. Möllers, M. Falkenberg, R. Kwiecien, W. Klockenbusch, and R. Schmitz, "Quantitative elastography of the uterine cervix as a predictor of preterm delivery," *Journal of Perinatology*, vol. 34, pp. 774–780, 2014.

[153] F. D. Öcal, Y. Cekmez, E. Erdogdu, M. Gezer, I. Fanuscu, H. Özkan, O. F. Kara, and T. Kücüközkan, "The utility of cervical elastosonography in prediction of cervical insufficiency: cervical elastosonography and cervical insufficiency," *The Journal of Maternal-Fetal & Neonatal Medicine*, no. 0, pp. 1–7, 2014.

[154] M. Parra-Saavedra, L. Gomez, A. Barrero, G. Parra, F. Vergara, and E. Navarro, "Prediction of preterm birth using the cervical consistency index," *Ultrasound in Obstetrics & Gynecology*, vol. 38, no. 1, pp. 44–51, 2011.

[155] S. Wozniak, P. Czuczwar, P. Szkodziak, P. Milart, E. Wozniakowska, and T. Paszkowski, "Elastography in predicting preterm delivery in asymptomatic, low-risk women: a prospective observational study," *BMC pregnancy and childbirth*, vol. 14, no. 1, p. 238, 2014.

[156] H. S. Hwang, I. S. Sohn, and H. S. Kwon, "Imaging analysis of cervical elastography for prediction of successful induction of labor at term," *Journal of Ultrasound in Medicine*, vol. 32, no. 6, pp. 937–946, 2013.

[157] A. Fruscalzo, A. Londero, C. Frohlich, M. Meyer-Wittkopf, and R. Schmitz, "Quantitative elastography of the cervix for predicting labor induction success," *Ultraschall Med*, 2014.

[158] L. Hee, C. K. Rasmussen, J. M. Schlütter, P. Sandager, and N. Uldbjerg, "Quantitative sonoelastography of the uterine cervix prior to induction of labor as a predictor of cervical dilation time," *Acta obstetricia et gynecologica Scandinavica*, vol. 93, no. 7, pp. 684–690, 2014.

[159] S. Pereira, A. P. Frick, L. C. Poon, A. Zamprakou, and K. H. Nicolaides, "Successful induction of labor: prediction by preinduction cervical length, angle of progression and cervical elastography," *Ultrasound in Obstetrics & Gynecology*, vol. 44, no. 4, pp. 468–475, 2014.

[160] R. M. Christensen, *Theory of viscoelasticity*. Mineola, New York: Dover Publications, Inc., 2012.

[161] W. Flügge, *Viscoelasticity*. New York: Springer, 1975.

[162] J. Cohen, "Statistical power analysis," *Current directions in psychological science*, pp. 98–101, 1992.

[163] L. J. Cronbach, "Coefficient alpha and the internal structure of tests," *psychometrika*, vol. 16, no. 3, pp. 297–334, 1951.

[164] G. Darren and P. Mallery, "SPSS for windows step by step: A simple guide and reference," 1999.

[165] G. C. l. Liggins, "Premature parturition after infusion of corticotrophin or cortisol into foetal lambs," *The Journal of endocrinology*, vol. 42, no. 2, p. 323, 1968.

[166] L. Ingoldby and P. Jackson, "Induction of parturition in sheep," *In Practice*, vol. 23, no. 4, pp. 228–231, 2001.

[167] G. N. Purohit, C. Shekher, P. Kumar, K. Solanki, *et al.*, "Induced termination of pregnancy in domestic farm animals," *Iranian J. Appl. Anim. Sci*, vol. 2, pp. 1–12, 2012.

[168] G. W. Halbert, H. Dobson, J. S. Walton, and B. C. Buckrell, "The structure of the cervical canal of the ewe," *Theriogenology*, vol. 33, no. 5, pp. 977–992, 1990.

[169] J. R. Challis, S. G. Matthews, W. Gibb, and S. J. Lye, "Endocrine and paracrine regulation of birth at term and preterm 1," *Endocrine reviews*, vol. 21, no. 5, pp. 514–550, 2000.

[170] A. A. Calder, "Prostaglandins and biological control of cervical function," *Australian and New Zealand journal of obstetrics and gynaecology*, vol. 34, no. 3, pp. 347–351, 1994.

[171] I. Freund, M. Deutsch, and A. Sprecher, "Connective tissue polarity. Optical second-harmonic microscopy, crossed-beam summation, and small-angle scattering in rat-tail tendon," *Biophysical journal*, vol. 50, no. 4, pp. 693–712, 1986.

[172] P. J. Campagnola, A. C. Millard, M. Terasaki, P. E. Hoppe, C. J. Malone, and W. A. Mohler, "Three-dimensional high-resolution second-harmonic generation imaging of endogenous structural proteins in biological tissues," *Biophysical journal*, vol. 82, no. 1, pp. 493–508, 2002.

[173] R. M. Williams, W. R. Zipfel, and W. W. Webb, "Interpreting second-harmonic generation images of collagen I fibrils," *Biophysical journal*, vol. 88, no. 2, pp. 1377–1386, 2005.

[174] P. P. Provenzano, K. W. Eliceiri, J. M. Campbell, D. R. Inman, J. G. White, and P. J. Keely, "Collagen reorganization at the tumor-stromal interface facilitates local invasion," *BMC medicine*, vol. 4, no. 1, p. 38, 2006.

[175] M. Strupler, M. Hernest, C. Fligny, J.-L. Martin, P.-L. Tharaux, and M.-C. Schanne-Klein, "Second harmonic microscopy to quantify renal interstitial fibrosis and arterial remodeling," *Journal of biomedical optics*, vol. 13, no. 5, pp. 054041–054041, 2008.

[176] O. Nadiarnykh, R. B. LaComb, M. A. Brewer, and P. J. Campagnola, "Alterations of the extracellular matrix in ovarian cancer studied by second harmonic generation imaging microscopy," *BMC cancer*, vol. 10, no. 1, p. 94, 2010.

[177] P. Campagnola, "Second harmonic generation imaging microscopy: applications to diseases diagnostics," *Analytical chemistry*, vol. 83, no. 9, pp. 3224–3231, 2011.

[178] K. Tilbury, C.-H. Lien, S.-J. Chen, and P. J. Campagnola, "Differentiation of col I and col III isoforms in stromal models of ovarian cancer by analysis of second harmonic generation polarization and emission directionality," *Biophysical journal*, vol. 106, no. 2, pp. 354–365, 2014.

[179] B. R. Masters, P. So, and E. Gratton, "Multiphoton excitation fluorescence microscopy and spectroscopy of in vivo human skin.," *Biophysical journal*, vol. 72, no. 6, p. 2405, 1997.

[180] A. Diaspro and M. Robello, "Two-photon excitation of fluorescence for three-dimensional optical imaging of biological structures," *Journal of Photochemistry and Photobiology B: Biology*, vol. 55, no. 1, pp. 1–8, 2000.

[181] H. Maul, G. Saade, and R. E. Garfield, "Prediction of term and preterm parturition and treatment monitoring by measurement of cervical cross-linked collagen using

light-induced fluorescence," *Acta obstetricia et gynecologica Scandinavica*, vol. 84, no. 6, pp. 534–536, 2005.

[182] S. K. Chang, M. Y. Dawood, G. Staerkel, U. Utzinger, E. N. Atkinson, R. R. Richards-Kortum, and M. Follen, "Fluorescence spectroscopy for cervical precancer detection: Is there variance across the menstrual cycle?," *Journal of Biomedical Optics*, vol. 7, no. 4, pp. 595–602, 2002.

[183] K. Noguchi, Y. R. Gel, E. Brunner, and F. Konietschke, *nparLD: An R software package for the nonparametric analysis of longitudinal data in factorial experiments*, 2012.

[184] J. Martin Bland and D. Altman, "Statistical methods for assessing agreement between two methods of clinical measurement," *The lancet*, vol. 327, no. 8476, pp. 307–310, 1986.

[185] J. H. McDonald, *Handbook of biological statistics*, vol. 2. Sparky House Publishing Baltimore, MD, 2009.

[186] A. L. Fetter and J. D. Walecka, *Theoretical mechanics of particles and continua*. Courier Dover Publications, 2003.

[187] A. Hosokawa, "Ultrasonic pulse waves in cancellous bone analyzed by finite-difference time-domain methods," *Ultrasonics*, vol. 44, pp. e227–e231, 2006.

[188] A. Hosokawa, "Development of a numerical cancellous bone model for finite-difference time-domain simulations of ultrasound propagation," *Ultrasonics, Ferroelectrics, and Frequency Control, IEEE Transactions on*, vol. 55, no. 6, pp. 1219–1233, 2008.

[189] J. Francés, S. Bleda, A. Márquez, C. Neipp, S. Gallego, B. Otero, and A. Beléndez, "Performance analysis of sse and avx instructions in multi-core cpus and gpu computing on fdtd scheme for solid and fluid vibration problems," *The Journal of Supercomputing*, vol. 70, no. 2, pp. 514–526, 2014.

[190] H. T. Banks, S. Hu, and Z. R. Kenz, "A brief review of elasticity and viscoelasticity," tech. rep., DTIC Document, 2010.

[191] L. A. Renteira and J. M. P. Oria, "A modified finite differences method for analysis of ultrasonic propagation in nonhomogeneous media," *Journal of Computational Acoustics*, vol. 18, no. 01, pp. 31–45, 2010.

[192] T. D. Mast, L. M. Hinkelman, L. A. Metlay, M. J. Orr, and R. C. Waag, "Simulation of ultrasonic pulse propagation, distortion, and attenuation in the human chest wall," *The Journal of the Acoustical Society of America*, vol. 106, no. 6, pp. 3665–3677, 1999.

[193] J. Virieux, "P-SV wave propagation in heterogeneous media: Velocity-stress finite-difference method," *Geophysics*, vol. 51, no. 4, pp. 889–901, 1986.

[194] P. Fellinger, R. Marklein, K. J. Langenberg, and S. Klaholz, "Numerical modeling of elastic wave propagation and scattering with EFIT-elastodynamic finite integration technique," *Wave motion*, vol. 21, no. 1, pp. 47–66, 1995.

[195] R. W. Graves, "Simulating seismic wave propagation in 3d elastic media using staggered-grid finite differences," *Bulletin of the Seismological Society of America*, vol. 86, no. 4, pp. 1091–1106, 1996.

[196] J. Sochacki, R. Kubichek, J. George, W. Fletcher, and S. Smithson, "Absorbing boundary conditions and surface waves," *Geophysics*, vol. 52, no. 1, pp. 60–71, 1987.

[197] F. Schubert, A. Peiffer, B. Köhler, and T. Sanderson, "The elastodynamic finite integration technique for waves in cylindrical geometries," *The Journal of the Acoustical Society of America*, vol. 104, no. 5, pp. 2604–2614, 1998.

[198] S. Vesentini, C. F. Fitié, F. M. Montevecchi, and A. Redaelli, "Molecular assessment of the elastic properties of collagen-like homotrimer sequences," *Biomechanics and modeling in mechanobiology*, vol. 3, no. 4, pp. 224–234, 2005.

[199] M. J. Buehler, "Atomistic and continuum modeling of mechanical properties of collagen: elasticity, fracture, and self-assembly," *Journal of Materials Research*, vol. 21, no. 08, pp. 1947–1961, 2006.

[200] T. C. Gasser, R. W. Ogden, and G. A. Holzapfel, "Hyperelastic modelling of arterial layers with distributed collagen fibre orientations," *Journal of the royal society interface*, vol. 3, no. 6, pp. 15–35, 2006.

[201] J. Humphrey, "Remodeling of a collagenous tissue at fixed lengths," *Journal of biomechanical engineering*, vol. 121, no. 6, pp. 591–597, 1999.

[202] M. Comninou and I. V. Yannas, "Dependence of stress-strain nonlinearity of connective tissues on the geometry of collagen fibres," *Journal of Biomechanics*, vol. 9, no. 7, pp. 427–433, 1976.

[203] K. Garikipati, S. Göktepe, and C. Miehe, "Elastica-based strain energy functions for soft biological tissue," *Journal of the Mechanics and Physics of Solids*, vol. 56, no. 4, pp. 1693–1713, 2008.

[204] R. Grytz and G. Meschke, "Constitutive modeling of crimped collagen fibrils in soft tissues," *Journal of the mechanical behavior of biomedical materials*, vol. 2, no. 5, pp. 522–533, 2009.

[205] F. Cacho, P. J. Elbischger, J. F. Rodriguez, M. Doblare, and G. A. Holzapfel, "A constitutive model for fibrous tissues considering collagen fiber crimp," *International Journal of Non-Linear Mechanics*, vol. 42, no. 2, pp. 391–402, 2007.

[206] Y. Lanir, "Constitutive equations for fibrous connective tissues," *Journal of biomechanics*, vol. 16, no. 1, pp. 1–12, 1983.

[207] E. Kuhl, K. Garikipati, E. M. Arruda, and K. Grosh, "Remodeling of biological tissue: mechanically induced reorientation of a transversely isotropic chain network," *Journal of the Mechanics and Physics of Solids*, vol. 53, no. 7, pp. 1552–1573, 2005.

[208] P. J. Elbischger, H. Bischof, P. Regitnig, and G. A. Holzapfel, "Automatic analysis of collagen fiber orientation in the outermost layer of human arteries," *Pattern analysis and applications*, vol. 7, no. 3, pp. 269–284, 2004.

[209] L. M. Peralta Pereira, "Mechanical characterization of cervical tissue," Master's thesis, Universidad de Granada, 2013.

[210] M. Abramowitz, I. A. Stegun, *et al.*, *Handbook of mathematical functions*, vol. 1. Dover New York, 1972.

[211] J. Gosline, M. Lillie, E. Carrington, P. Guerette, C. Ortlepp, and K. Savage, "Elastic proteins: biological roles and mechanical properties," *Philosophical Transactions of the Royal Society B: Biological Sciences*, vol. 357, no. 1418, pp. 121–132, 2002.

[212] M.-T. Sheu, J.-C. Huang, G.-C. Yeh, and H.-O. Ho, "Characterization of collagen gel solutions and collagen matrices for cell culture," *Biomaterials*, vol. 22, no. 13, pp. 1713–1719, 2001.

[213] K. R. Kirker and G. D. Prestwich, "Physical properties of glycosaminoglycan hydrogels," *Journal of Polymer Science Part B: Polymer Physics*, vol. 42, no. 23, pp. 4344–4356, 2004.

[214] M. Shayegan and N. R. Forde, "Microrheological characterization of collagen systems: from molecular solutions to fibrillar gels," *PloS one*, vol. 8, no. 8, p. e70590, 2013.

[215] L. Bozec, G. van der Heijden, and M. Horton, "Collagen fibrils: nanoscale ropes," *Biophysical journal*, vol. 92, no. 1, pp. 70–75, 2007.

[216] Z. A. Saddiq, J. C. Barbenel, and M. H. Grant, "The mechanical strength of collagen gels containing glycosaminoglycans and populated with fibroblasts," *Journal of Biomedical Materials Research Part A*, vol. 89, no. 3, pp. 697–706, 2009.

[217] A. M. Collinsworth, S. Zhang, W. E. Kraus, and G. A. Truskey, "Apparent elastic modulus and hysteresis of skeletal muscle cells throughout differentiation," *American Journal of Physiology-Cell Physiology*, vol. 283, no. 4, pp. C1219–C1227, 2002.

[218] J. M. Carcione, *Wave fields in real media: Wave propagation in anisotropic, anelastic, porous and electromagnetic media*, vol. 38. Elsevier, 2007.

[219] S. Catheline, J. L. Gennisson, G. Delon, M. Fink, R. Sinkus, S. Abouelkaram, and J. Culioli, "Measurement of viscoelastic properties of homogeneous soft solid using transient elastography: An inverse problem approach," *The Journal of the Acoustical Society of America*, vol. 116, no. 6, pp. 3734–3741, 2004.

[220] A. I. Malkin, A. Y. Malkin, and A. I. Isayev, *Rheology: concepts, methods, and applications*. ChemTec Publishing, 2006.

[221] S. Chen, M. Fatemi, and J. F. Greenleaf, "Quantifying elasticity and viscosity from measurement of shear wave speed dispersion," *The Journal of the Acoustical Society of America*, vol. 115, no. 6, pp. 2781–2785, 2004.

[222] D. Klatt, U. Hamhaber, P. Asbach, J. Braun, and I. Sack, "Noninvasive assessment of the rheological behavior of human organs using multifrequency mr elastography: a study of brain and liver viscoelasticity," *Physics in medicine and biology*, vol. 52, no. 24, p. 7281, 2007.

[223] G. Rus and R. Gallego, "Optimization algorithms for identification inverse problems with the boundary element method," *Engineering Analysis with Boundary Elements*, vol. 26, no. 4, pp. 315–327, 2002.

[224] G. Rus, S.-Y. Lee, and R. Gallego, "Defect identification in laminated composite structures by bem from incomplete static data," *International journal of solids and structures*, vol. 42, no. 5, pp. 1743–1758, 2005.

[225] R. Palma, G. Rus, and R. Gallego, "Probabilistic inverse problem and system uncertainties for damage detection in piezoelectrics," *Mechanics of Materials*, vol. 41, no. 9, pp. 1000–1016, 2009.

[226] G. Rus, R. Palma, and J. Pérez-Aparicio, "Experimental design of dynamic model-based damage identification in piezoelectric ceramics," *Mechanical Systems and Signal Processing*, vol. 26, pp. 268–293, 2012.

[227] N. Bochud, *Signal processing-based identification of pathology using ultrasonics*. PhD thesis, Universidad de Granada, 2014.

[228] G. Rus, R. Palma, and J. Pérez-Aparicio, "Optimal measurement setup for damage detection in piezoelectric plates," *International Journal of Engineering Science*, vol. 47, no. 4, pp. 554–572, 2009.

[229] A. Tarantola, *Inverse Problem Theory*. SIAM, 2005.

[230] N. Bochud and G. Rus, "Probabilistic inverse problem to characterize tissue-equivalent material mechanical properties," *Ultrasonics, Ferroelectrics, and Frequency Control, IEEE Transactions on*, vol. 59, no. 7, pp. 1443–1456, 2012.

[231] L. Peralta, G. Rus, N. Bochud, and F. Molina, "Assessing viscoelasticity of shear wave propagation in cervical tissue by multiscale computational simulation," *Journal of biomechanics*, vol. 48, no. 9, pp. 1549–1556, 2015.

[232] Hazewinkel and e. Michiel, *"Joint distribution", Encyclopedia of Mathematics*. Springer ISBN 978-1-55608-010-4, 2001.

[233] I. M. Sobol, "On the distribution of points in a cube and the approximate evaluation of integrals," *USSR Computational Mathematics and Mathematical Physics*, vol. 7, no. 4, pp. 86–112, 1967.

[234] M. Tanter, J. Bercoff, A. Athanasiou, T. Deffieux, J. L. Gennisson, G. Montaldo, M. Muller, A. Tardivon, and M. Fink, "Quantitative assessment of breast lesion viscoelasticity: initial clinical results using supersonic shear imaging," *Ultrasound in medicine & biology*, vol. 34, no. 9, pp. 1373–1386, 2008.

[235] J. Brum, M. Bernal, J. L. Gennisson, and M. Tanter, "In vivo evaluation of the elastic anisotropy of the human achilles tendon using shear wave dispersion analysis," *Physics in medicine and biology*, vol. 59, no. 3, p. 505, 2014.

[236] L. Peralta, E. Mourier, C. Richard, P. Chavette-Palmer, M. Muller, M. Tanter, and G. Rus, "117 in vivo evaluation of the cervical stiffness evolution during induced labor in ewes using elastography," *Reproduction, Fertility and Development*, vol. 27, no. 1, pp. 150–151, 2015.

[237] J. L. Gennisson, M. Muller, P. Gabor, R. Frydman, D. Musset, M. Tanter, and O. Ami, "Quantification of elasticity changes in the myometrium during labor using supersonic shear imaging: A feasibility study," *Ultrasonics*, vol. 56, pp. 183–188, 2015.

[238] V. Shamdasani and Y. Kim, "Two-dimensional autocorrelation method for ultrasound-based strain estimation," in *Engineering in Medicine and Biology Society, 2004. IEMBS'04. 26th Annual International Conference of the IEEE*, vol. 1, pp. 1380–1383, IEEE, 2004.

[239] S. Kim, S. R. Aglyamov, S. Park, M. O'Donnell, and S. Y. Emelianov, "An autocorrelation-based method for improvement of sub-pixel displacement estimation in ultrasound strain imaging," *Ultrasonics, Ferroelectrics, and Frequency Control, IEEE Transactions on*, vol. 58, no. 4, pp. 838–843, 2011.

[240] S. Wojcinski, K. Brandhorst, G. Sadigh, P. Hillemanns, and F. Degenhardt, "Acoustic radiation force impulse imaging with virtual touch tissue quantification: measurements of normal breast tissue and dependence on the degree of pre-compression," *Ultrasound in medicine & biology*, vol. 39, no. 12, pp. 2226–2232, 2013.

[241] D. Melodelima, J. C. Bamber, F. A. Duck, and J. A. Shipley, "Transient elastography using impulsive ultrasound radiation force: a preliminary comparison with surface palpation elastography," *Ultrasound in medicine & biology*, vol. 33, no. 6, pp. 959–969, 2007.

[242] N. Melamed, L. Hiersch, N. Domniz, A. Maresky, R. Bardin, and Y. Yogev, "Predictive value of cervical length in women with threatened preterm labor," *Obstetrics & Gynecology*, vol. 122, no. 6, pp. 1279–1287, 2013.

[243] R. J. DeWall, T. Varghese, M. A. Kliewer, J. M. Harter, and E. M. Hartenbach, "Compression-dependent viscoelastic behavior of human cervix tissue," *Ultrasonic imaging*, vol. 32, no. 4, pp. 214–228, 2010.

[244] Y. Wang and M. F. Insana, "Viscoelastic properties of rodent mammary tumors using ultrasonic shear-wave imaging," *Ultrasonic imaging*, vol. 35, no. 2, pp. 126–145, 2013.

[245] W. A. Berg, D. O. Cosgrove, C. J. Doré, F. K. Schäfer, W. E. Svensson, R. J. Hooley, R. Ohlinger, E. B. Mendelson, C. Balu-Maestro, M. Locatelli, *et al.*, "Shear-wave elastography improves the specificity of breast US: the BE1 multinational study of 939 masses," *Radiology*, vol. 262, no. 2, pp. 435–449, 2012.

[246] L. Peralta, G. Rus, N. Bochud, and F. Molina, "Mechanical assessment of cervical remodelling in pregnancy: insight from a synthetic model," *Journal of biomechanics*, vol. 48, no. 9, pp. 1557–1565, 2015.

[247] L. M. Reusch, H. Feltovich, L. C. Carlson, G. Hall, P. J. Campagnola, K. W. Eliceiri, and T. J. Hall, "Nonlinear optical microscopy and ultrasound imaging of human cervical structure," *Journal of biomedical optics*, vol. 18, no. 3, pp. 031110–031110, 2013.

[248] I. Gusachenko, V. Tran, Y. G. Houssen, J.-M. Allain, and M.-C. Schanne-Klein, "Polarization-resolved second-harmonic generation in tendon upon mechanical stretching," *Biophysical journal*, vol. 102, no. 9, pp. 2220–2229, 2012.

[249] G. Isgro, V. Calvaruso, L. Andreana, T. V. Luong, M. Garcovich, P. Manousou, A. Alibrandi, S. Maimone, L. Marelli, N. Davies, *et al.*, "The relationship between transient elastography and histological collagen proportionate area for assessing fibrosis in chronic viral hepatitis," *Journal of gastroenterology*, vol. 48, no. 8, pp. 921–929, 2013.

[250] J. Tang, Y. Zhang, M.-B. Zhang, Y.-M. Li, X. Fei, and Z.-G. Song, "Tissue elasticity displayed by elastography and its correlation with the characteristics of collagen type I and type III in prostatic stroma," *Asian journal of andrology*, vol. 16, no. 2, p. 305, 2014.

[251] P. Friedl, K. Wolf, G. Harms, and U. H. Andrian, "Biological second and third harmonic generation microscopy," *Current Protocols in Cell Biology*, pp. 4–15, 2007.

[252] C. B. Raub, J. Unruh, V. Suresh, T. Krasieva, T. Lindmo, E. Gratton, B. J. Tromberg, and S. C. George, "Image correlation spectroscopy of multiphoton images correlates with collagen mechanical properties," *Biophysical journal*, vol. 94, no. 6, pp. 2361–2373, 2008.

[253] D. Aït-Belkacem, M. Guilbert, M. Roche, J. Duboisset, P. Ferrand, G. Sockalingum, P. Jeannesson, and S. Brasselet, "Microscopic structural study of collagen aging in isolated fibrils using polarized second harmonic generation," *Journal of biomedical optics*, vol. 17, no. 8, pp. 0805061–0805063, 2012.

[254] E. Aughey, A. Calder, J. Coutts, R. Fleming, T. McManus, and C. Munro, "Pregnancy-associated changes in the physical and microscopic characteristics of the ovine cervix.," *Journal of anatomy*, vol. 136, no. Pt 2, p. 389, 1983.

[255] G. Hochhaus, J. Barth, S. Al-Fayoumi, S. Suarez, H. Derendorf, R. Hochhaus, and H. Möllmann, "Pharmacokinetics and pharmacodynamics of dexamethasone sodium-m-sulfobenzoate (ds) after intravenous and intramuscular administration: a comparison with dexamethasone phosphate (dp)," *The Journal of Clinical Pharmacology*, vol. 41, no. 4, pp. 425–434, 2001.

[256] M. Silver, "Prenatal maturation, the timing of birth and how it may be regulated in domestic animals," *Experimental physiology*, vol. 75, no. 3, pp. 285–307, 1990.

[257] U. Hamhaber, F. Grieshaber, J. Nagel, and U. Klose, "Comparison of quantitative shear wave MR-elastography with mechanical compression tests," *Magnetic Resonance in Medicine*, vol. 49, no. 1, pp. 71–77, 2003.

[258] M. Orescanin, M. A. Qayyum, K. S. Toohey, and M. F. Insana, "Dispersion and shear modulus measurements of porcine liver," *Ultrasonic imaging*, vol. 32, no. 4, pp. 255–266, 2010.

[259] J. L. Gennisson, S. Catheline, S. Chaffaı, and M. Fink, "Transient elastography in anisotropic medium: application to the measurement of slow and fast shear wave speeds in muscles," *The Journal of the Acoustical Society of America*, vol. 114, no. 1, pp. 536–541, 2003.

[260] H. Feltovich, K. Nam, and T. J. Hall, "Quantitative ultrasound assessment of cervical microstructure," *Ultrasonic imaging*, vol. 32, no. 3, pp. 131–142, 2010.

[261] F. Mézière, M. Muller, B. Dobigny, E. Bossy, and A. Derode, "Simulations of ultrasound propagation in random arrangements of elliptic scatterers: occurrence of two longitudinal waves," *The Journal of the Acoustical Society of America*, vol. 133, no. 2, pp. 643–652, 2013.

[262] T.-M. Nguyen, M. Couade, J. Bercoff, and M. Tanter, "Assessment of viscous and elastic properties of sub-wavelength layered soft tissues using shear wave spectroscopy: theoretical framework and in vitro experimental validation," *Ultrasonics, Ferroelectrics, and Frequency Control, IEEE Transactions on*, vol. 58, no. 11, pp. 2305–2315, 2011.

[263] M. Bernal, I. Nenadic, M. W. Urban, and J. F. Greenleaf, "Material property estimation for tubes and arteries using ultrasound radiation force and analysis of propagating modes," *The Journal of the Acoustical Society of America*, vol. 129, no. 3, pp. 1344–1354, 2011.

[264] E. L. Madsen, H. J. Sathoff, and J. A. Zagzebski, "Ultrasonic shear wave properties of soft tissues and tissuelike materials," *The Journal of the Acoustical Society of America*, vol. 74, no. 5, pp. 1346–1355, 1983.